# CONTENT

# СОДЕРЖАНИЕ

# The influence of pulse current on drop transfer during double-electrode gas surfacing

**Sergey K. Elsukov**[*1], PhD (Engineering),
assistant professor of Chair "Welding Production Equipment and Technology"
**Ilya V. Zorin**[2], Doctor of Sciences (Engineering), Associate Professor,
professor of Chair "Welding Production Equipment and Technology"
**Dmitry S. Nesin**, postgraduate student

*Volgograd State Technical University, Volgograd (Russia)*

**E-mail:** serzh.elsukov@yandex.ru

[1]ORCID: https://orcid.org/0000-0002-4965-8028
[2]ORCID: https://orcid.org/0000-0002-9912-2598

*Abstract:* The application of a circuit with a common pulse current source for surfacing with two electrode wires increases the energy efficiency of the arc process and the welding arc technological properties, but requires a more detailed study of the influence of the mode parameters on its stability. In this regard, this paper focuses on studying the dynamics of formation and transfer of metal drops under various modes of pulsed power supply of the welding arc. Using high-speed video filming of the welding arc and synchronized recording of current and voltage signals, a mode was set (average current value was 250 A, maximum current value in pulse was 600 A, arc voltage was ~30 V), which ensured a stable process of transfer of electrode metal by a drop common to two wires without short circuits. It was found that the common drop under the action of electrodynamic forces acquires centripetal acceleration, which contributes to its directed transfer to the weld pool and allows minimizing the amount of spatter on the surface of the base metal. Using mathematical modeling, the nature of the interaction of welding arcs on two wires was confirmed and it was found that even at the stage of the current pulse "hot" phase (600 A, $t$=0.8 s), the arc pressure on the plate surface is less than when welding with one wire at direct current. The identified effect is associated with a change in the direction of the plasma flow to perpendicular to the wire axis due to an increase in the electrodynamic attractive force of the magnetic fields around the two wire conductors. Together with a decrease in the arc temperature and pressure on the plate surface during the "heat input control" phase of the current pulse (180 A, $t$=1.4 s), this should help to reduce the heat input and the depth of penetration of the base metal, and, consequently, reduce the degree of dilution of the deposited alloy by the substrate metal. The latter is especially relevant when solving problems of creating a technology for surfacing of relatively thin layers of corrosion-resistant alloys, in particular, on the surface of petrochemical equipment products.

*Keywords:* double-electrode surfacing; pulse-arc process; welding arc; drop transfer; numerical simulation.

*For citation:* Elsukov S.K., Zorin I.V., Nesin D.S. The influence of pulse current on drop transfer during double-electrode gas surfacing. *Frontier Materials & Technologies*, 2025, no. 2, pp. 9–18. DOI: 10.18323/2782-4039-2025-2-72-1.

## INTRODUCTION

The quality and service reliability of products in the metallurgical and mechanical engineering industries are largely determined by the level of development of technological processes of welding and surfacing. As a result, the priority task is the continuous improvement of welding technologies aimed at developing methods to increase the productivity of these processes and improve the properties of welded joints and deposited metal. One of these methods is double-electrode welding and surfacing, when the wire electrodes are connected to a common power source [1; 2]. It is widely used both for welding thick-walled structures and for forming a layer of high-tin bronze on steel [3] and corrosion-resistant deposited

coatings [4], which expands the technological capabilities of welding production.

Using mathematical modeling methods, it was found that the plasma temperature of a double-electrode arc is generally lower compared to a single-electrode process, its maximum temperature and arc pressure on the surface of the weld pool are also lower [5]. At the same time, the average temperature of the electrode metal is lower [6]. In the case of double-electrode surfacing, the heat flow into the product is reduced [7], which helps to reduce the deformation of the surfacing product. A similar result can be achieved by applying current pulses to the arc using special control algorithms [8–10], which is currently widely implemented in serially produced semi-

automatic machines and has actually become the basic solution for single-electrode mechanized welding and surfacing in shielding gases. Existing equipment for using pulse current with two electrode wires has been industrially mastered for the process of two-arc welding "tandem", when each wire is connected to a separate power source [11–13].

The use of a circuit with a common power supply for two electrode wires [14] increases both the energy efficiency of the arc process and its manufacturability, since its implementation does not require equipping each electrode wire with a feed mechanism and additional equipment. The existing positive experience of using double-electrode surfacing to form corrosion-resistant cladding coatings is based on the use of relatively low arc voltage values, which ensures the transfer of electrode metal in the mode of forming a so-called "common" drop for two melting electrode wires and minimizes the share of the base metal in the deposit one to 30 % [15].

The use of a common pulse current source for surfacing with two electrode wires is of interest, which will make it possible to develop the advantages of the double-electrode scheme in improving the technological properties of the arc (the quality of the transfer of electrode metal in the arc, heat input into the base metal, etc.). For this reason, it is necessary to study the influence of both the main parameters of the mode and the pulse current on the arc.

The relevance of this topic is also caused by the necessity of improving the quality of welding and surfacing processes when assimilating new products at petrochemical engineering enterprises and solving the problems they face in technological advancement. This will improve the quality of deposited coatings, reduce costs and increase the efficiency of production processes.

The aim of this work is to determine the optimal mode of pulsed power supply of the welding arc during double-electrode surfacing, ensuring the formation of a common drop and its directed transfer into the weld pool without short-circuiting the arc gap.

## METHODS

### Modernization of welding equipment

For the experimental studies, the Lorch S8 Pulse XT semiautomatic pulse welding machine (Germany) was retrofitted with a pair of rollers (manufactured using FDM printing) with two identical V-shaped grooves for use in the feed mechanism of two wires with a diameter of 1.6 mm at the same time, which were fed through a fluoroplastic flexible tube into an external current-supplying unit equipped with a water-cooled nozzle. The "Pulse" program was selected in the semiautomatic machine settings.

### Experimental facility and measurements

The scheme of arc surfacing process study (Fig. 1) included an iSpeedy 50MT13M-SE high-speed photography system (China) and a LA-20USB multichannel analog-to-digital converter (Russia) for monitoring voltage and current changes over time with a sampling frequency of 5 kHz.

The obtained oscillograms were processed in specialized PowerGraph 3.3 Pro software.

The high-speed photography system included a camera connected to a laptop via a 10 Gbps Ethernet interface and specialized iSpeedyPro software, which was used to configure the camera operating mode parameters and perform primary processing of the obtained video signal. The camera has an extended high-speed memory of 64 GB. A special housing was used to protect the camera and the front lens from welding spatter. Video recording of the welding arc zone was performed at a speed of 5000 frames per second. The shooting direction was perpendicular to the connecting line between the two welding wires. High-speed arc frames were synchronized with the recording of electrical signals, which made it possible to compare the dynamics of drop formation and transfer in the arc with changes in current and voltage in it.

### Surfacing parameters

Surfacing was performed on St3sp plates of $200 \times 100 \times 10$ mm in size moved at a surfacing speed of 13 m/h by a special mechanism relative to a stationary welding head. Surfacing in pulse mode was performed at a current of $I$=280 A and a voltage of $U_{arc}$=24 V with a center-to-center distance of $b$=6 mm. An AG ER-347Si (Sv-08H19N10G2B) welding wire with a diameter of 1.6 mm and a mixture of argon and carbon dioxide (97.5 % + 2.5 %) were used. The gas mixture flow rate was 25–30 l/min.

### Arc mathematical modeling

For a more visual and comprehensive assessment of the electro- and thermal-physical processes occurring in the welding arc under the influence of pulse current, mathematical modeling was performed in the Comsol Multiphysics software package. The approach to creating a welding arc model used in the work is based on a system of interrelated equations describing the complex interaction of hydrodynamic, electromagnetic and thermal processes in a plasma discharge, as well as on the fundamental laws of conservation of mass, momentum and energy, supplemented by the equations of electrodynamics for a conducting medium[1]. The hydrodynamic part of the model considers plasma as a viscous electrically conductive liquid, the movement of which is determined by the balance of the forces of pressure, viscosity and electromagnetic action. Electromagnetic processes are described taking into account the generation of a magnetic field by the arc current and its reverse effect on the distribution of charged particles. Thermal effects include Joule heating, convective and conductive heat transfer, and radiation energy losses. The arc length was set in the model according to high-speed video footage ($l_{arc}$=6 mm).

---

[1] *Elsukov S.K. Povyshenie effektivnosti dvukhelektrodnoy naplavki v zashchitnykh gazakh khromonikelevykh austenitnykh staley na detali neftekhimicheskogo oborudovaniya [Improving the efficiency of two-electrode surfacing in protective gases of chromium-nickel austenitic steels on petrochemical equipment parts], diss. kand. tekhn. nauk. Volgograd, 2023. 143 p. EDN: MEZKRU.*
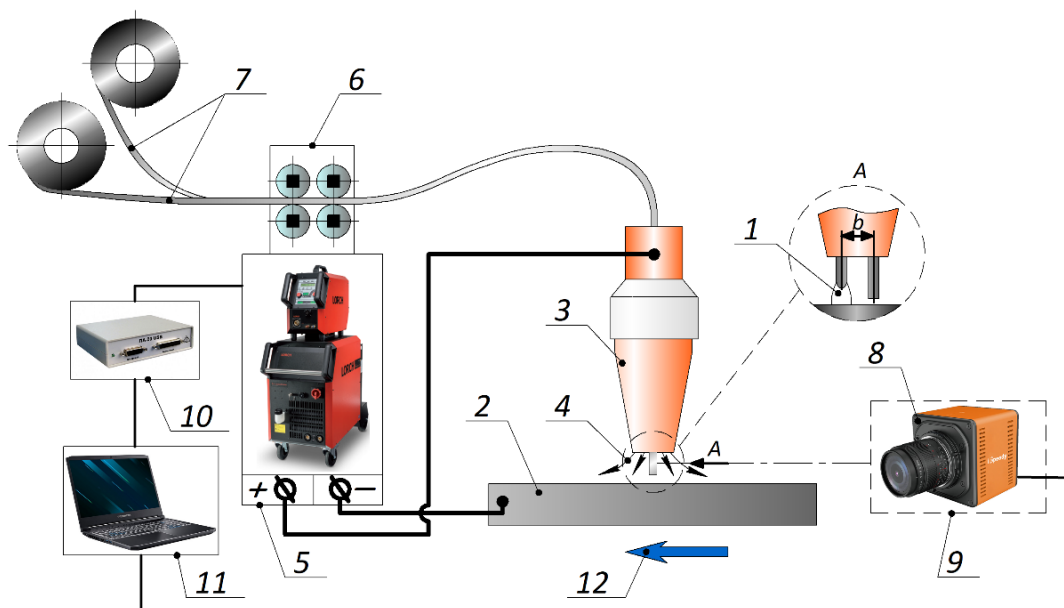
**Fig. 1.** *Scheme of the study of the welding arc reaction zone in the process of double-electrode pulsed surfacing:*
*1 – welding arc; 2 – deposited plate; 3 – shielding gas supply nozzle;*
*4 – shielding gas flow; 5 – semiautomatic welding machine; 6 – feed mechanism; 7 – welding wires;*
*8 – high-speed camera; 9 – protective camera housing; 10 – analog-to-digital converter;*
*11 – computer; 12 – plate movement direction*
**Рис. 1.** *Схема исследования реакционной зоны сварочной дуги в процессе двухэлектродной импульсной наплавки:*
*1 – сварочная дуга; 2 – наплавляемая пластина; 3 – сопло подачи защитного газа;*
*4 – поток защитного газа; 5 – сварочный полуавтомат; 6 – подающий механизм; 7 – сварочные проволоки;*
*8 – высокоскоростная камера; 9 – защитный корпус камеры; 10 – аналого-цифровой преобразователь;*
*11 – компьютер; 12 – направление перемещения пластины*

The model is based on a number of reasonable assumptions, including the assumption of local thermodynamic equilibrium of the plasma, the laminar nature of the flow, and neglect of phase transition processes in electrode materials. The relationship between the equations was ensured through the constitutive relations for the thermophysical and electrodynamic properties of the plasma, which made it possible to create a closed system for the numerical solution. This approach allowed studying the influence of various welding arc parameters on the temperature distribution, pressure, and flow rates in its plasma column.

**RESULTS**

Analysis of the modulated current oscillogram obtained at a welding wire feed rate of 2 m/min shows that the average welding current was 280 A at a modulation frequency of ~333 Hz (Fig. 2).

Large droplets are simultaneously formed at the ends of the welding wires (Fig. 3, frame *a*), which are held by surface tension forces and attracted by the action of electrodynamic force (Fig. 3, frames *b*, *c*). At the moment of frame *d*, the droplets at the ends of the wires merge, one of the droplets flows to the other. The resulting common drop of electrode metal closes on the surface of the weld pool and passes into it (Fig. 3, frame *e*).

A further increase in current to 280 A disrupts the stability of the drop transfer process and the formation of a common drop, which is pushed toward the current-carrying tip (Fig. 4).

When using the pulse welding mode at a wire feed speed of 2 m/min and an arc voltage of 24 V, the average current value reached 280 A. In this mode, the Lorch S8 Pulse XT current source generates a complex-shaped pulse signal (Fig. 5). At the beginning of each pulse, the current strength sharply increases to 620 A and is maintained at this level for 3 ms. Then, smoothly decreasing over 5 ms, it reaches 200 A, after which it decreases at the same speed to the base value of 60 A. The pulse repetition frequency is 105 Hz, ensuring the stability of the welding process.

During the analysis of the obtained frames of the arc zone with its pulsed power supply, it was found that at the moment of the current pulse, the detachment of welding droplets from the electrode does not occur (Fig. 6, frame *b*), unlike the single-electrode process. Instead, the pulse energy is spent on the formation of large droplets, which, as they grow, merge into a common drop. The transition of the common drop occurs through a short circuit (Fig. 6, frame *d*), which is similar to the nature of drop transfer when using direct current.

The obtained results do not allow revealing fully the capabilities of the pulsed power supply of the welding arc due to the preservation of the mode of drop transfer through their short circuits on the surface of the weld pool. To prevent this, it is possible to increase the arc length by setting
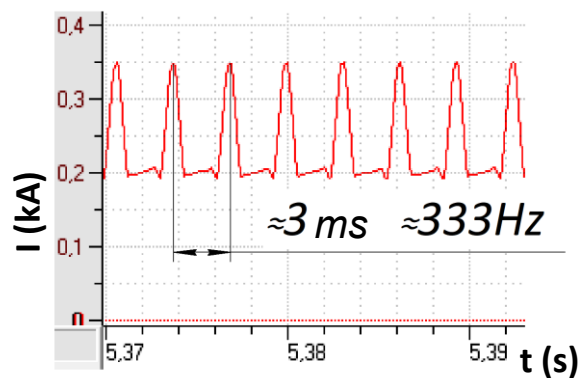
***Fig. 2.*** *External appearance of the oscillogram of the modulated current of the Lorch S8 Pulse XT power supply*
***Рис. 2.*** *Внешний вид осциллограммы модулированного тока источника питания Lorch S8 Pulse XT*
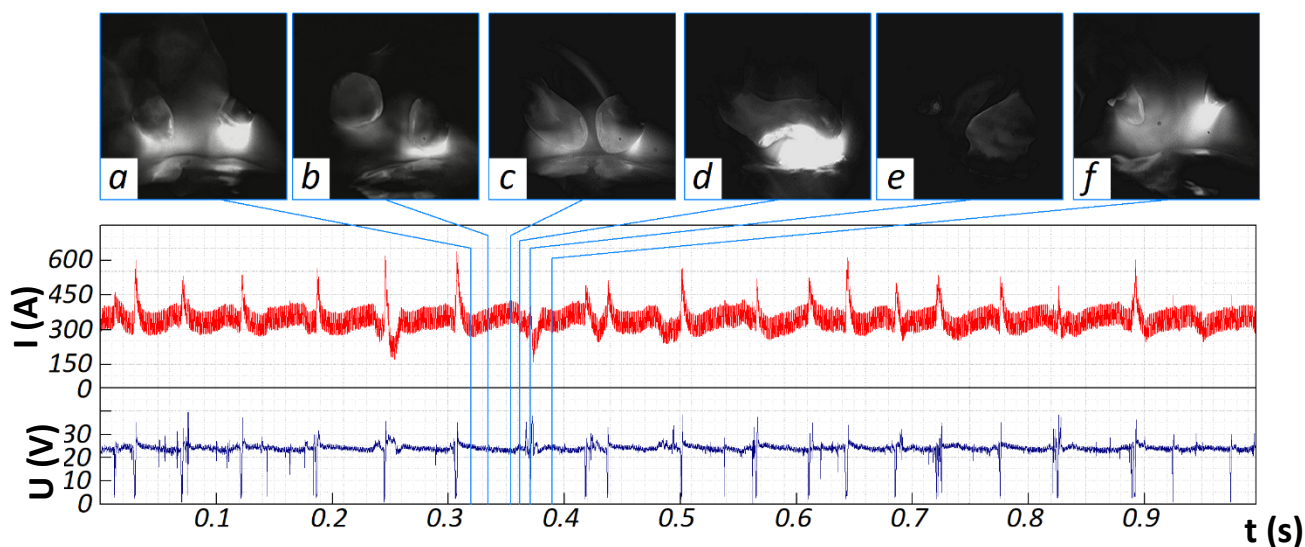


***Fig. 3.*** *External appearance of the oscillogram of the direct current and voltage*
*and high-speed video footage (I=280 A; U$_{arc}$=23 V)*
***Рис. 3.*** *Внешний вид осциллограммы постоянного тока и напряжения,*
*а также кадры высокоскоростной видеосъемки (I=280 А; U$_{д}$=23 В)*
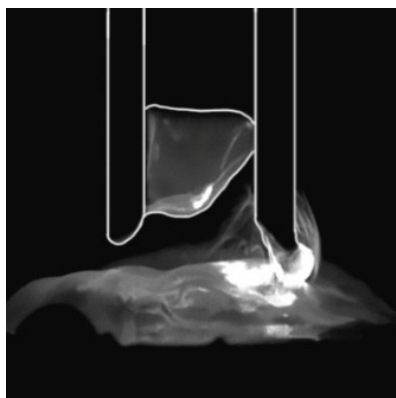


***Fig. 4.*** *Displacement of the common drop to the upper part of the arc reaction zone*
***Рис. 4.*** *Оттеснение общей капли в верхнюю часть реакционной зоны дуги*
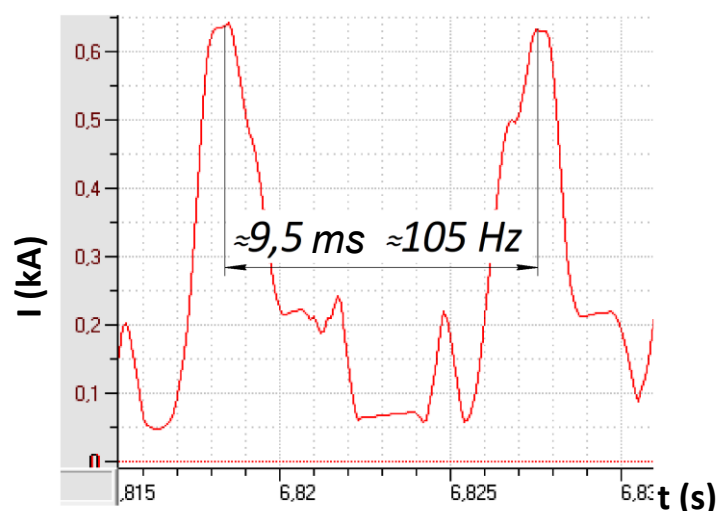
*Fig. 5. External appearance of the oscillogram of the pulse current of the Lorch S8 Pulse XT power supply*
*Рис. 5. Внешний вид осциллограммы импульсного тока источника питания Lorch S8 Pulse XT*
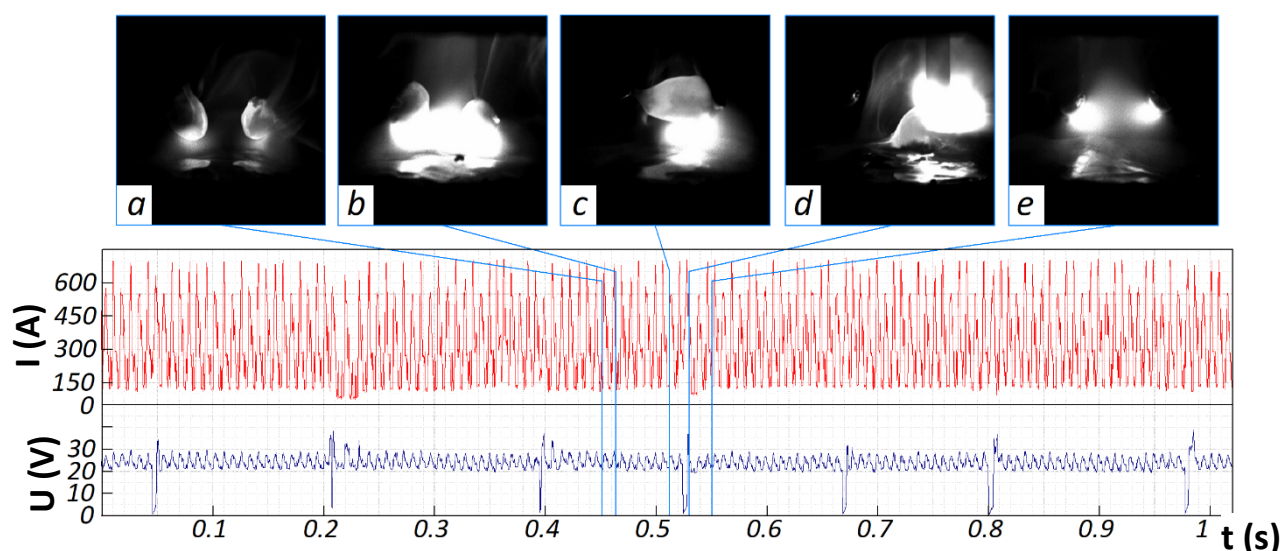


*Fig. 6. External appearance of the oscillogram of the pulse current*
*and voltage and high-speed video footage (I=280 A; $U_{arc}$=24 V)*
*Рис. 6. Внешний вид осциллограммы импульсного тока и напряжения,*
*а также кадры высокоскоростной видеосъемки (I=280 А; $U_д$=24 В)*

an increased voltage value (for example, up to 30 V) on the welding semiautomatic device. In this case, the drop transfer process begins with the alternating existence of the arc on the ends of the welding wires (Fig. 7, frames *a*, *b*). The arc movement frequency is on average 150 Hz, which corresponds to the current pulses generated by the power source. As the droplets grow (Fig. 7, frames *c*, *d*), after about 100 ms, the arc switches to the mode of simultaneous melting of the wires, and as the volume of the droplets increases, they merge into a common drop after 50 ms. After that, a large common drop flows to the end of one of the wires and goes into the weld pool. The duration of the overall cycle of drop formation and transfer is approximately 300 ms. The transition of the drop into the weld pool differs from the transition during direct current welding: at the moment of detachment, a powerful current pulse imparts additional centripetal acceleration to the drop (Fig. 7, frame *e*). This mode is characterized by the absence of short circuits of the common drop, which allows minimizing the amount of spatter on the base metal surface. Therefore, this surfacing mode is the most promising. A further increase in the current strength to 350 A in the welding current source, according to the obtained oscillogram, occurs due to an increase in the pulse frequency to 166 Hz and an increase in the base current strength to 120 A.
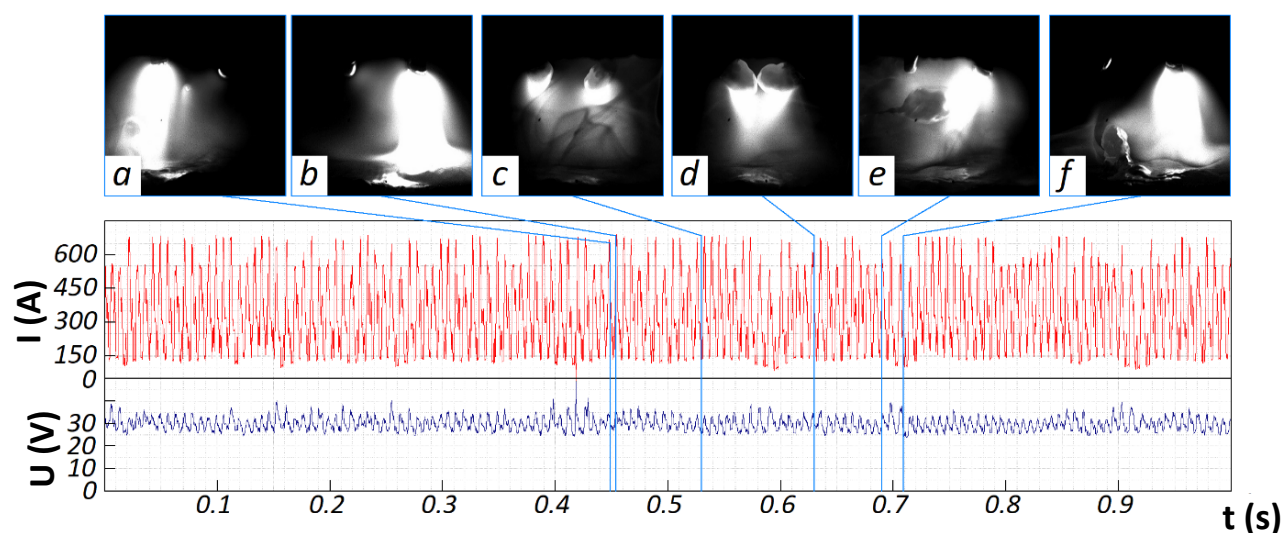
*Fig. 7. External appearance of the oscillogram of the pulse current
and voltage and high-speed video footage (I=280 A; U$_{arc}$=30 V)*
*Рис. 7. Внешний вид осциллограммы импульсного тока и напряжения,
а также кадры высокоскоростной видеосъемки (I=280 А; U$_{д}$=30 В)*

An increase in the current strength leads to an increase in the electrodynamic force, which tends to attract the droplets to each other. The resulting force at the moment of the pulse swings them, due to which the drops vibrate on the end of the electrode and detach asynchronously. This leads to the fact that at the moment when the droplet shifts to the axis of symmetry of the electrode, under the action of the pinch effect, the current pulse detaches it, imparting a rotational motion. When colliding into a common drop, they break up due to their high speed, which disrupts the drop transfer process (Fig. 8).

It follows from the simulation results that a typical current pulse begins with a smooth linear increase from 85 to 600 A in 1.5 ms. At this point, the maximum temperature region moves up the electrode axis, as the intersection point of the opposing flows does, while their intensity increases (Fig. 9, frame a). The pressure distribution in the pulse current arc differs from that in the direct current arc. As the pulse increases, two zones of maximum pressure are formed: in the anode spot region – 620 Pa and in the zone of intersection of flows at an angle of ≈130° – 517 Pa (Fig. 9, frame e).

After the current stabilizes for 0.8 ms at 600 A (the "hot" pulse phase), the plasma flow acquires a perpendicular direction relative to the wire axis due to an increase in the electrodynamic attractive force. The temperature near the anode spot reaches its maximum – 24,987 K (Fig. 9, frame b). The increased density of current vector lines is also observed in this area. The pressure on the surface of the model plate is 826 Pa (Fig. 9, frame f), which is lower[2]

than the arc pressure value during single-wire welding with direct current (about 1000 Pa).

Then the current value decreases linearly to 180 A in 0.7 ms (the "heat input control" phase) and is maintained at this level for 1.4 ms. At this stage, the arc temperature decreases, and the zone of maximum heating shifts closer to the surface of the plate (15,209 K) (Fig. 9, frame c). The plasma flow stops deviating to the upper part of the arc. The pressure on the surface of the plate decreases to 329 Pa (Fig. 9, frame g).

The final phase is a pause of 3.3 ms at a current value of 85 A (the "cold" phase). At this point, the minimum pressure is recorded – 76 Pa, and the temperature field retains a structure (Fig. 9, frames d, h) similar to the previous phase. Then the cycle repeats.

**DISCUSSION**

Analyzing the obtained results, it can be concluded that the nature of drop transfer in the modulated current mode is generally similar to the transfer during surfacing with direct current of reverse polarity. The average time of electrode drop transfer was 320 ms, which is comparable with previously obtained data [15]; therefore, there is no advantage of arc supply with modulated current over direct current.

Assessing the results obtained when supplying the arc with pulse current, one should note an interesting feature of the transition of the total drop into the weld pool with centripetal acceleration under the influence of the pinch effect that occurs at the moment of reaching the highest power of the current pulse (at 600 A). As a result, the drop, rotating, enters the weld pool exactly along the axis of the welding wire. This allows avoiding a common defect – crystallized splashes and drops of electrode metal on the surface of the product both in double-electrode welding in a shielding gas and in single-electrode welding [16]. A further increase in current (up to 350 A) disrupts the stability of

---

[2] *Elsukov S.K. Povyshenie effektivnosti dvukhelektrodnoy naplavki v zashchitnykh gazakh khromonikelevykh austenitnykh staley na detali neftekhimicheskogo oborudovaniya [Improving the efficiency of two-electrode surfacing in protective gases of chromium-nickel austenitic steels on petrochemical equipment parts], diss. kand. tekhn. nauk. Volgograd, 2023. 143 p. EDN: MEZKRU.*
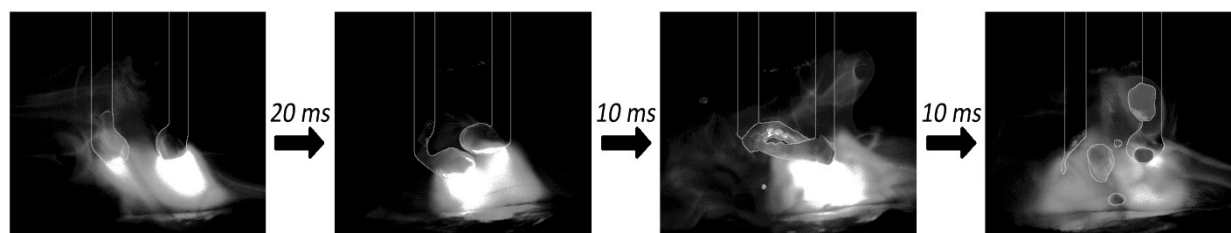
**Fig. 8.** *Cross-movement of electrode drops with drop transfer disruption (I=350 A; $U_{arc}$=30 V)*
**Рис. 8.** *Перекрестное перемещение электродных капель с нарушением каплепереноса (I=350 A; $U_д$=30 В)*
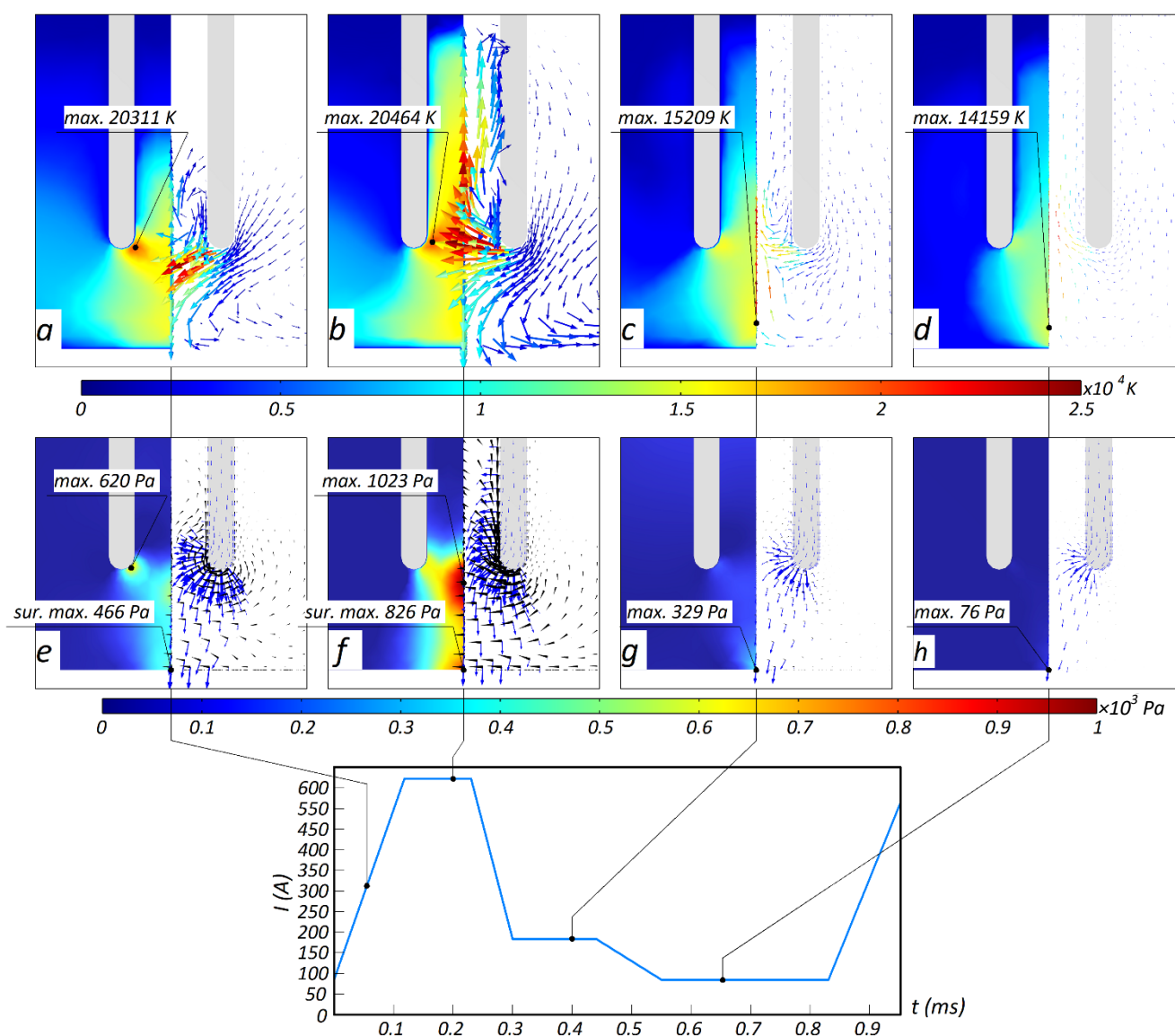


**Fig. 9.** *Distribution of temperature in the model arc, direction and plasma flow rate (**a**–**d**);*
*distribution of arc pressure, current density vector (blue arrows)*
*and Lorentz force vector (black triangles) (**e**–**h**) depending on the phase of the current pulse cycle*
**Рис. 9.** *Распределение температуры в модельной дуге, направления и скорости плазменного потока (**a**–**d**);*
*распределение давления дуги, вектора плотности тока (синие стрелки)*
*и вектора силы Лоренца (черные треугольники) (**e**–**h**) в зависимости от фазы цикла импульса тока*

the formation of a common drop, which was also observed when using carbon dioxide as a shielding gas [17]. Therefore, the use of this mode for surfacing is impractical.

Mathematical modeling confirmed the nature of the interaction of welding arcs on two wires and found that even at the stage of the "hot" phase of the current pulse (600 A, $t$=0.8 s), the arc pressure on the plate surface is less than when welding with one wire at direct current. The identified effect is associated with a change in the flow direction to perpendicular to the wire axis due to an increase in the electrodynamic force of attraction of magnetic fields around two wire conductors. Together with a decrease in the arc temperature and pressure on the plate surface in the "cold" phase of the current pulse (180 A, $t$=1.4 s), this should help to reduce heat input and the depth of penetration of the base metal, and, consequently, reduce the degree of dilution of the deposited alloy by the substrate metal. The latter is especially relevant when solving problems related to the creation of a technology for surfacing relatively thin layers of corrosion-resistant alloys, in particular, on the surface of petrochemical equipment products.

One of the prospects for developing the method under consideration is more precise control of heat input into the product by changing the pulse frequency or using the "double pulse" program [18]. Both in the case of using direct current and when using the pulse mode, the anode-to-cathode distance has a significant influence on the process of double-electrode surfacing, which also requires further study.

**CONCLUSIONS**

It has been found that the use of pulse current in double-electrode surfacing makes it possible to expand the area of existence of electrode metal transfer by common drops from 24 to 30 V in the absence of arc gap short circuits. At the moment of drop detachment, a powerful current pulse (~600 A) imparts additional centripetal acceleration to the drop directed toward the surface of the weld pool, which virtually eliminates metal spatter.

The conducted mathematical modeling of pulse arc surfacing with a consumable electrode allowed identifying the dynamics of temperature and pressure changes in various pulse phases, which is important for further optimization of the process.

**REFERENCES**

1. Malinovska E., Pavelka V. Characteristics of welded joints produced by two wire submerged-arc welding. *Welding International*, 1990, vol. 4, no. 2, pp. 157–163. DOI: 10.1080/09507119009447698.

2. Zorin I.V., Elsukov S.K., Sokolov G.N., Dubtsov Yu.N., Lysak V.I., Kharlamov V.O. Investigation of the alloy Inconel 625 deposition process by a split electrode. *Svarochnoe proizvodstvo*, 2018, no. 11, pp. 9–15. EDN: YULCSL.

3. Maydanchuk T.B., Ilyushenko V.M., Bondarenko A.N. Improving the quality of bimetallic compounds during submerged deposition of high-lead bronze on steel.

*Avtomaticheskaya svarka*, 2015, no. 5-6, pp. 42–45. EDN: TVOTMJ.

4. Mastenko V.Yu. Method of automatic two-electrode surfacing with submerged wires. *Remont. Vosstanovlenie. Modernizatsiya*, 2006, no. 8, pp. 8–10. EDN: HVBRIP.

5. Wang Xiaoli, Zhang Qi, Liu Yangsen, Luo Chengfu, Hu Qingxian. Impact of welding current on arc physical characteristics in single-power, double-wire, single-arc gas metal arc welding. *Welding in the World*, 2025, no. 2, pp. 1–12. DOI: 10.1007/s40194-025-01982-y.

6. Jie Xu, Yiming Ma, Lin Wang, Xu Lu. Numerical simulation of arc and metal transfer behaviors in double-wire gas metal arc welding. *Welding in the World*, 2022, vol. 66, no. 12, pp. 2521–2531. DOI: 10.1007/s40194-022-01381-7.

7. Ding Xueping, Li Huan, Wei Huiliang, Liu Jiquan. Numerical analysis of arc plasma behavior in double-wire GMAW. *Vacuum*, 2016, vol. 124, pp. 46–54. DOI: 10.1016/j.vacuum.2015.11.006.

8. Krampit A.G., Zernin E.A., Krampit M.A. Modern methods of pulsed-arc MIG/MAG welding. *Tekhnologii i materialy*, 2015, no. 1, pp. 4–11. EDN: TUHYSL.

9. Rezende R.F., Arias A.R., Lima II E.J., Coelho F.G.F. Pulsed GMAW-based WAAM – Influence of droplet detachment mode on the geometry and mechanical properties of 308 L stainless steel. *Journal of Advanced Joining Processes*, 2025, vol. 11, article number 100286. DOI: 10.1016/j.jajp.2025.100286.

10. Zhao Yangyang, Lee Phill-Seung, Chung Hyun. Effect of pulsing parameters on drop transfer dynamics and heat transfer behavior in pulsed gas metal arc welding. *International Journal of Heat and Mass Transfer*, 2019, vol. 129, pp. 1110–1122. DOI: 10.1016/j.ijheatmasstransfer.2018.10.037.

11. Liu Guonqiang, Han Siyuan, Tang Xinhua, Cui Haichao. Effects of torch configuration on arc interaction behaviors and weld defect formation mechanism in tandem pulsed GMAW. *Journal of Manufacturing Processes*, 2021, vol. 62, pp. 729–742. DOI: 10.1016/j.jmapro.2021.01.007.

12. Ueyama T., Ohnawa T., Nakata K., Tanaka M. Occurrence of arc interaction in tandem pulsed gas metal arc welding. *Science and Technology of Welding and Joining*, 2007, vol. 12, no. 6, pp. 523–529. DOI: 10.1179/174329307X173715.

13. Wu Kaiyuan, Wang Jiajia, Yin Tong, He Zuwei, Liang Zhuoyong. Double arc interference and dynamic behavior characteristics of double wire double-pulsed GMAW. *The International Journal of Advanced Manufacturing Technology*, 2018, vol. 95, pp. 991–1002. DOI: 10.1007/s00170-017-1269-y.

14. Motta M.F., Dutra J.C. Effects of the variables of the double wire MIG/MAG process with insulated potentials on the weld bead geometry. *Welding international*, 2006, vol. 20, no. 10, pp. 785–793. DOI: 10.1533/weli.2006.20.10.785.

15. Elsukov S.K., Zorin I.V, Fastov S.A., Lysak V.I. Applications of split electrode for surfacing in argon-carbonacid mixtures of corrosion-resistant steel. *Svarka i diagnostika*, 2023, no. 2, pp. 37–40. EDN: CYLBIS.

16. Potapevskiy A.G., Saraev Yu.N., Chinakhov D.A. *Svarka staley v zashchitnykh gazakh plavyashchimsya elektrodom. Tekhnika i tekhnologiya budushchego* [Welding of steels in protective gases with a melting electrode. Engineering and technology of the future]. Tomsk, Izdatelstvo Tomskogo politekhnicheskogo universiteta Publ., 2012. 208 p.

17. Spitsyn V.V. Metal transfer and arc gorenje during welding with a split electrode in $CO_2$. *Svarochnoe proizvodstvo*, 1969, no. 4, pp. 5–7.

18. Yao Ping, Zhou Kang, Huang Shuwei. Process and parameter optimization of the double-pulsed GMAW process. *Metals*, 2019, vol. 9, no. 9, article number 1009. DOI: 10.3390/met9091009.

## СПИСОК ЛИТЕРАТУРЫ

1. Malinovska E., Pavelka V. Characteristics of welded joints produced by two wire submerged-arc welding // Welding International. 1990. Vol. 4. № 2. P. 157–163. DOI: 10.1080/09507119009447698.

2. Зорин И.В., Елсуков С.К., Соколов Г.Н., Дубцов Ю.Н., Лысак В.И., Харламов В.О. Исследование процесса наплавки расщепленным электродом сплава Inconel 625 // Сварочное производство. 2018. № 11. С. 9–15. EDN: YULCSL.

3. Майданчук Т.Б., Илюшенко В.М., Бондаренко А.Н. Улучшение качества биметаллического соединения при наплавке под флюсом высокооловянной бронзы на сталь // Автоматическая сварка. 2015. № 5-6. С. 42–45. EDN: TVOTMJ.

4. Мастенко В.Ю. Способ автоматической двухэлектродной наплавки проволоками под флюсом // Ремонт. Восстановление. Модернизация. 2006. № 8. С. 8–10. EDN: HVBRIP.

5. Wang Xiaoli, Zhang Qi, Liu Yangsen, Luo Chengfu, Hu Qingxian. Impact of welding current on arc physical characteristics in single-power, double-wire, single-arc gas metal arc welding // Welding in the World. 2025. № 2. P. 1–12. DOI: 10.1007/s40194-025-01982-y.

6. Xu Jie, Ma Yiming, Wang Lin, Lu Xu. Numerical simulation of arc and metal transfer behaviors in double-wire gas metal arc welding // Welding in the World. 2022. Vol. 66. № 12. P. 2521–2531. DOI: 10.1007/s40194-022-01381-7.

7. Ding Xueping, Li Huan, Wei Huiliang, Liu Jiquan. Numerical analysis of arc plasma behavior in double-wire GMAW // Vacuum. 2016. Vol. 124. P. 46–54. DOI: 10.1016/j.vacuum.2015.11.006.

8. Крампит А.Г., Зернин Е.А., Крампит М.А. Современные способы импульсно-дуговой MIG/MAG сварки // Технологии и материалы. 2015. № 1. С. 4–11. EDN: TUHYSL.

9. Rezende R.F., Arias A.R., Lima II E.J., Coelho F.G.F. Pulsed GMAW-based WAAM – Influence of droplet detachment mode on the geometry and mechanical properties of 308 L stainless steel // Journal of Advanced Joining Processes. 2025. Vol. 11. Article number 100286. DOI: 10.1016/j.jajp.2025.100286.

10. Zhao Yangyang, Lee Phill-Seung, Chung Hyun. Effect of pulsing parameters on drop transfer dynamics and heat transfer behavior in pulsed gas metal arc welding // International Journal of Heat and Mass Transfer. 2019. Vol. 129. P. 1110–1122. DOI: 10.1016/j.ijheatmasstransfer.2018.10.037.

11. Liu Guonqiang, Han Siyuan, Tang Xinhua, Cui Haichao. Effects of torch configuration on arc interaction behaviors and weld defect formation mechanism in tandem pulsed GMAW // Journal of Manufacturing Processes. 2021. Vol. 62. P. 729–742. DOI: 10.1016/j.jmapro.2021.01.007.

12. Ueyama T., Ohnawa T., Nakata K., Tanaka M. Occurrence of arc interaction in tandem pulsed gas metal arc welding // Science and Technology of Welding and Joining. 2007. Vol. 12. № 6. P. 523–529. DOI: 10.1179/174329307X173715.

13. Wu Kaiyuan, Wang Jiajia, Yin Tong, He Zuwei, Liang Zhuoyong. Double arc interference and dynamic behavior characteristics of double wire double-pulsed GMAW // The International Journal of Advanced Manufacturing Technology. 2018. Vol. 95. P. 991–1002. DOI: 10.1007/s00170-017-1269-y.

14. Motta M.F., Dutra J.C. Effects of the variables of the double wire MIG/MAG process with insulated potentials on the weld bead geometry // Welding international. 2006. Vol. 20. № 10. P. 785–793. DOI: 10.1533/weli.2006.20.10.785.

15. Елсуков С.К., Зорин И.В, Фастов С.А., Лысак В.И. Применение расщепленного электрода для наплавки в аргоноуглекислотных смесях коррозионностойкой стали // Сварка и диагностика. 2023. № 2. С. 37–40. EDN: CYLBIS.

16. Потапьевский А.Г., Сараев Ю.Н., Чинахов Д.А. Сварка сталей в защитных газах плавящимся электродом. Техника и технология будущего. Томск: Издательство Томского политехнического университета, 2012. 208 с.

17. Спицын В.В. Перенос металла и горение дуги при сварке расщепленным электродом в $CO_2$ // Сварочное производство. 1969. № 4. С. 5–7.

18. Yao Ping, Zhou Kang, Huang Shuwei. Process and parameter optimization of the double-pulsed GMAW process // Metals. 2019. Vol. 9. № 9. Article number 1009. DOI: 10.3390/met9091009.

# Влияние импульсного тока на каплеперенос при двухэлектродной наплавке в газах

*Елсуков Сергей Константинович*[*1], кандидат технических наук,
доцент кафедры «Оборудование и технология сварочного производства»
*Зорин Илья Васильевич*[2], доктор технических наук, доцент,
профессор кафедры «Оборудование и технология сварочного производства»
*Несин Дмитрий Сергеевич*, аспирант

*Волгоградский государственный технический университет, Волгоград (Россия)*

*E-mail: serzh.elsukov@yandex.ru

[1]ORCID: https://orcid.org/0000-0002-4965-8028
[2]ORCID: https://orcid.org/0000-0002-9912-2598

*Аннотация:* Применение для наплавки двумя электродными проволоками схемы с общим источником импульсного тока повышает энергоэффективность дугового процесса и технологические свойства сварочной дуги, но требует более детального изучения влияния параметров режима на ее стабильность. В связи с этим в данной работе основное внимание уделено изучению динамики формирования и переноса металлических капель при различных режимах импульсного питания сварочной дуги. С использованием скоростной видеосъемки сварочной дуги и синхронизированной записи сигналов тока и напряжения установлен режим (среднее значение тока 250 А, максимальное в импульсе 600 А, напряжение на дуге ~30 В), который обеспечивает стабильный процесс переноса электродного металла общей для двух проволок капель без образования коротких замыканий. Обнаружено, что общая капля под действием электродинамических сил приобретает центростремительное ускорение, что способствует ее направленному переносу в сварочную ванну и позволяет максимально снизить количество брызг на поверхности основного металла. С использованием математического моделирования был подтвержден характер взаимодействия сварочных дуг на двух проволоках и установлено, что даже на стадии «горячей» фазы импульса тока (600 А, $t$=0,8 с) давление дуги на поверхность пластины меньше, чем при сварке одной проволокой на постоянном токе. Выявленный эффект связан с изменением направления плазменного потока на перпендикулярное к оси проволоки вследствие увеличения электродинамической силы притяжения магнитных полей вокруг двух проволочных проводников. В совокупности со снижением температуры дуги и давления на поверхность пластины в фазе «контроля тепловложения» импульса тока (180 А, $t$=1,4 с) это должно способствовать уменьшению тепловложения и глубины проплавления основного металла, а следовательно, уменьшить степень разбавления наплавляемого сплава металлом подложки. Последнее особенно востребовано при решении задач по созданию технологии наплавки относительно тонких слоев из коррозионностойких сплавов, в частности, на поверхности изделий нефтехимического оборудования.

*Ключевые слова:* двухэлектродная наплавка; импульсно-дуговой процесс; сварочная дуга; каплеперенос; численное моделирование.

# Effects of extrusion on Young's modulus and internal friction of magnesium alloys with various long period ordered structure content

*Vladimir V. Kaminskii**[1,2,5], PhD (Physics and Mathematics),
Head of laboratory of Institute of Advanced Data Transfer Systems
*Dmitrii A. Kalganov*[2,6], junior researcher of Laboratory
of Diffraction Methods for Investigation of Real Crystal-Structures
*Maksim V. Dorogov*[1,7], PhD (Physics and Mathematics),
assistant professor of Institute of Advanced Data Transfer Systems
*Sergei A. Philippov*[2,3,8], researcher of Laboratory of Diffraction Methods for Investigation
of Real Crystal-Structures, assistant professor of Higher School of Mechanics and Control Processes
*Alexey E. Romanov*[1,4,9], Doctor of Sciences (Physics and Mathematics), Professor,
chief researcher of Institute of Advanced Data Transfer Systems

[1]*ITMO University, St. Petersburg (Russia)*
[2]*Ioffe Institute of the RAS, St. Petersburg (Russia)*
[3]*Peter the Great St. Petersburg Polytechnic University, St. Petersburg (Russia)*
[4]*Togliatti State University, Togliatti (Russia)*

**E-mail:** vvkaminskii@itmo.ru

[5]ORCID: https://orcid.org/0000-0002-4388-2459
[6]ORCID: https://orcid.org/0000-0003-1986-3693
[7]ORCID: https://orcid.org/0000-0001-5987-3357
[8]ORCID: https://orcid.org/0000-0002-7784-555X
[9]ORCID: https://orcid.org/0000-0003-3738-408X

*Abstract:* The relevance of this work stems from the growing interest in magnesium alloys with long period ordered structure (LPSO) due to their unique mechanical properties. Investigating the effect of extrusion on Young's modulus and internal friction of such alloys provides a deeper understanding of their mechanical behaviour, which is important for the development of new materials with improved performance properties. This research explores the effect of warm extrusion on the structure, dynamic Young's modulus and internal friction of magnesium alloys containing varying amounts of LPSO phases. Alloys in the Mg–Zn–Y system with estimated LPSO phase contents of 0, 50 and 100 % vol. were analysed using the composite piezoelectric oscillator technique at 100 kHz. The results demonstrate that the Young's modulus increases with higher LPSO content, driven by the enhanced stiffness and strong interatomic bonding of the LPSO phases. Extrusion leads to a 3 % decrease in Young's modulus along the direction parallel to its axis for all samples. This effect is explained by the formation of an elongated texture and an increase in the dislocation density. Internal friction measurements revealed a rise in amplitude-independent internal friction post-extrusion, suggesting higher dislocation density, while the critical strain amplitude decreased in alloys with higher LPSO content. Additionally, Young's modulus softening was reduced after extrusion, primarily due to dislocation-induced hardening. These findings shed light on the mechanical properties of Mg–Zn–Y alloys with LPSO structures, emphasising the effects of extrusion and phase content on their dynamic behaviour.

*Keywords:* magnesium alloys; long-period stacking-ordered structure; LPSO; internal friction; Young's modulus; microplasticity.

## INTRODUCTION

Magnesium alloys with a long-period stacking ordered (LPSO) structure represent a unique class of materials that have attracted the attention of researchers and engineers due to their outstanding mechanical properties. Yosihito Kawamura first proposed the characteristics of the constituents and methods for preparation of LPSO magnesium ternary alloys [1]. Team of authors from the Magnesium Research Center is the most active in the development of these nanostructured materials and the publication of new

papers to date. These alloys combine the lightness of magnesium with increased strength, creep resistance, and improved damping characteristics [1–3]. The most studied materials in this category are alloys based on Mg–Zn–Y, the LPSO structure in them is characterised by a periodic alternation of layers with different atomic stacking sequence. Mg–Zn–Y ternary compounds crystallise in different phases depending on the Zn–Y ratio and solidification methods [4]. Common types of LPSO phases in these alloys are 18R (rhombohedral structure with a period of 18 layers) and 14H (hexagonal structure with a period of 14 layers). These phases in the Mg–Zn–Y system are formed by adding a few atomic percent of zinc and yttrium (Zn/Y ratio of ~1) to magnesium alloy by rapid solidification [1]. LPSO phases significantly increase the strength of Mg–Zn–Y alloys due to an ordered structure that impedes the movement of dislocations, creates barriers at interfaces, promotes dispersion hardening and grain size reduction, and suppresses strain twinning. Of particular interest is the fracture mechanism of these alloys, which differs significantly from that of classical alloys due to the formation of so-called "kink bands" [5].

Magnesium alloys with LPSO structure are hardened after extrusion [6]. For example, in a study [7], a cast alloy with 88 % LPSO content ($Mg_{88}Zn_4Y_7$) had a low tensile strength (yield strength) of about 140 MPa at room temperature. After extrusion, the strength increased significantly. At an extrusion ratio of 10:1, the strength reached 460 MPa at room temperature, which is more than three times higher than that of the cast alloy. The strengthening occurs because the extrusion aligns the LPSO phase along the extrusion direction, preventing basal slip and increasing strength. In addition, the kink bands formed during extrusion create additional boundaries that effectively prevent dislocation movement, further contributing to the strength improvement. Although it is known that the LPSO phase increases the strength of the alloy and extrusion further enhances this strengthening, the exact mechanisms (e. g., dislocation interaction with the LPSO phase) require further clarification.

Typically, the mechanical properties of magnesium alloys with LPSO structures are studied using standard methods (tensile, fatigue and hardness tests) [8] as well as more specialised methods (acoustic emission, in situ observations) [9]. These methods provide comprehensive information on the strength, ductility, fatigue characteristics and microstructure of alloys. A relatively new avenue of research of alloys containing LPSO has been the investigation of the high-frequency damping and the effective elastic modulus [10].

The aim of our work is to investigate the effect of extrusion on the mechanical properties of magnesium alloys with LPSO structures using a composite piezoelectric oscillator method at a frequency of 100 kHz.

## METHODS

### Composite piezoelectric oscillator method

The main method of investigation in this work is the composite piezoelectric oscillator (CPO) technique [11]. The CPO method is based on measuring the reso-

nant frequencies of a material sample excited by a piezoelectric transducer. The composite oscillator consists of two parts: a piezoelectric element (quartz) and the sample under study, which are mechanically connected using a cyanoacrylate adhesive. When an alternating voltage is applied to the piezoelectric element, mechanical vibrations are generated and transmitted to the sample. Analysis of the resonant frequencies and damping of oscillations (internal friction (IF), decrement) of the CPO allows for the determination of the Young's modulus (modulus of elasticity at low-amplitude vibrational deformation) and IF of the sample based on the following relationships:

$$m_{osc}\delta_{osc} = m_q\delta_q + m_s\delta_s ;$$
$$m_{osc}f_{osc} = m_qf_q + m_sf_s ,$$
(1)

where $m_{osc}$ is mass of the entire oscillator;
$m_q$ is mass of the quartz;
$m_s$ is mass of the sample;
$\delta_{osc}$ is damping of oscillations of the entire oscillator;
$\delta_q$ is damping of oscillations of the quartz;
$\delta_s$ is damping of oscillations of the sample;
$f_{osc}$ is oscillation frequency of the entire oscillator;
$f_q$ is oscillation frequency of the quartz;
$f_s$ is oscillation frequency of the sample.

The equation for determining the Young's modulus:

$$E = 4\rho l^2 f_s^2$$
, (2)

where $\rho$ is density of the material under study;
$l$ is length of the sample.

By measuring the change in resonant frequency, the Young's modulus and IF of the material can be determined at various temperatures and loads (strain amplitudes). The strain amplitude in the experiments varied from $2\times10^{-7}$ to $2\times10^{-4}$, and the temperature ranged from 80 to 320 K with a heating/cooling rate of 2 K/min. It should be noted that IF characterises the material's ability to dissipate mechanical vibration energy. It manifests as a damping of the oscillation amplitude and is expressed through the damping decrement or logarithmic decrement. The logarithmic decrement $\delta$ (defined as $\delta=\Delta W/2W$, where $\Delta W$ is the energy dissipated per cycle; $W$ is the maximum stored oscillation energy) served as a measure of internal friction. Young's modulus characterises the ratio of stress to strain in the approximation of uniaxial tension or compression. Studying both of these characteristics simultaneously at various strain amplitudes over a wide temperature range provides integrated information on the mechanical processes occurring in the samples.

The Young's modulus softening was measured based on the dynamic modulus at the amplitude-independent stage $E_i$, and modulus on strain dependency at the high amplitude stage $E(\varepsilon)$, as given by equation:

$$\frac{\Delta E}{E} = \frac{E_i - E(\varepsilon)}{E_i} .$$
(3)

The study of internal friction and dislocation modulus softening in metals by CPO method is considered in detail in the works by Lebedev et al. [12–14].

**Research materials and supporting methods**

The objects of study in this work were a set of polycrystalline samples of Mg–Zn–Y-based alloys, both before and after extrusion, with varying LPSO content: 0, 50, and 100 % (volume fraction). These alloys were obtained from Kumamoto University, Japan. Their nominal chemical compositions (in at. %), confirmed by inductively coupled plasma spectroscopy, are as follows: Mg99.2Zn0.2Y0.6 (LPSO-0 %), Mg93Zn2.5Y4.5 (LPSO-50 %), and Mg85Zn6Y9 (LPSO-100 %). Using a diamond saw, the samples were shaped into parallelepipeds with dimensions of $2 \times 3 \times 24.5$ mm$^3$. For all extruded samples, the longest direction coincided with the extrusion direction. This shape was chosen based on formula (2) to ensure resonance in the quartz-sample system.

As a complementary method, scanning electron microscopy (SEM) (MIRA III Tescan), optical microscopy (MET-5t Altami), and X-ray powder diffraction (MD-10 Radikon) were used to investigate the microstructure. SEM images and X-ray diffraction pattern were obtained from an orthogonal (smallest) cross-section of the parallelepiped sample. The sample surfaces were polished in isopropyl alcohol using sandpaper up to 1 μm grit. X-ray diffraction (XRD) data were obtained by rotating the samples around ω at a speed of 10 min$^{-1}$, using monochromatized by LiF(200) CrKa$_\alpha$ radiation.

**RESULTS**

The obtained X-ray diffractograms (Fig. 1 a, 1 b) are satisfactorily described within the framework of three structures with different parameters: distorted hexagonal lattice of alpha magnesium (P63/mmc a=3.19 c=5.18), cubic W-phase and hexagonal phase. All samples are characte-rised by a complex diffraction pattern of the indicated structures in the region of 30–40 deg. The sample of LPSO-0 % as-cast alloy shows increased intensity in the direction 0 0 0 2 (2θ=34.59°) and the sample of LPSO-50 % as-cast alloy shows increased intensity in the direction 1 1 −2 0 (2θ=58.36°).

The main feature of extruded samples vs cast ones is the pronounced texture in the basal planes of the magnesium hexagonal lattice, which corresponds to the 1 0 −1 0 peak in Fig. 1 b. It can also be observed that the LPSO-0 % and LPSO-50 % samples, reoriented with an extinction of 0 0 0 2 and 1 1 −2 0 peaks correspondingly (Fig. 1 b).

SEM micro-images of as-cast and extruded samples show the presence of blocks of different contrast in the backscattered electron mode for LPSO-50 % and LPSO-100 % (Fig. 2). The LPSO-50 % sample includes at least three different types of grains in terms of contrast.

As a result of the work, the temperature dependencies of the Young's modulus of Mg-Zn-Y alloys with varying LPSO content, both before and after extrusion, were determined (Fig. 3). It can be observed that the Young's modulus of the samples after extrusion decreases by an average of 3 % for 0 %, 50 %, and 100 % LPSO content. Despite the fact that the measurement error for Young's modulus is 0.001 % (this is true for the already fixed sample), it can reach 1 % when the sample is re-glued. We tried to increase the accuracy by repeatedly repeating the experiment on different samples. The values of Young's modulus at room temperature were as follows: for 0 % LPSO before extrusion is 44.2 GPa, after is 42.6 GPa; for 50 % LPSO before extrusion is 49.8 GPa, after is 48.5 GPa; for 100 % LPSO before extrusion is 57.2 GPa, after is 55.6 GPa. Young's modulus increases with decreasing temperature.

Fig. 4 shows the amplitude dependences of internal friction for samples before and after extrusion. It is possible to see the increase of internal friction in the samples
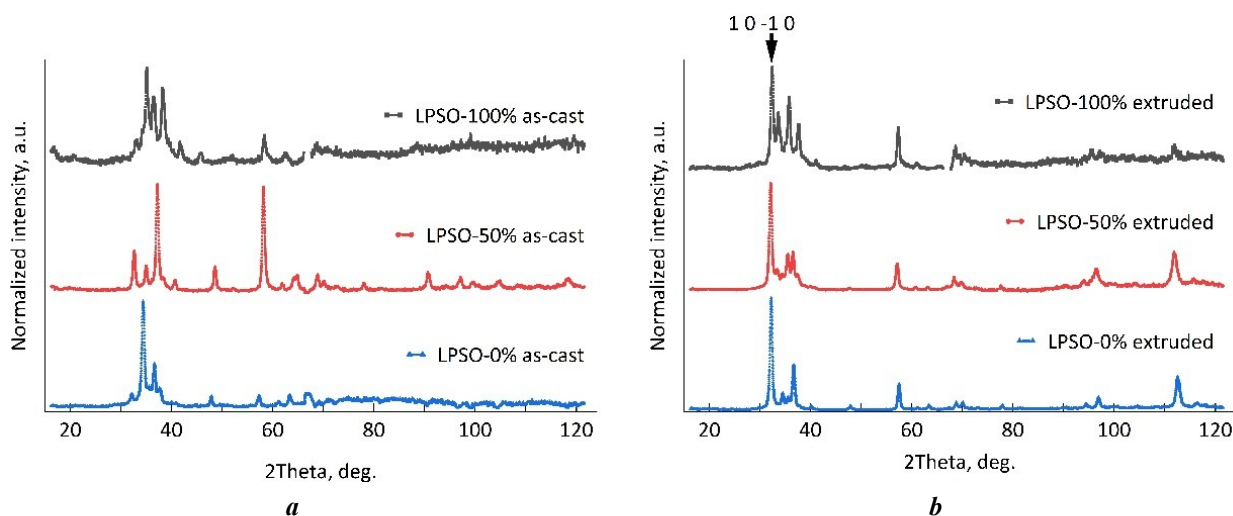


*Fig. 1. X-ray diffraction patterns on as-cast (**a**) and extruded (**b**) LPSO samples*
*Рис. 1. Рентгеновские дифракционные картины на литых (**a**) и экструдированных (**b**) ДПС образцах*

*a*

*b*

*c*

*d*

*e*

*f*
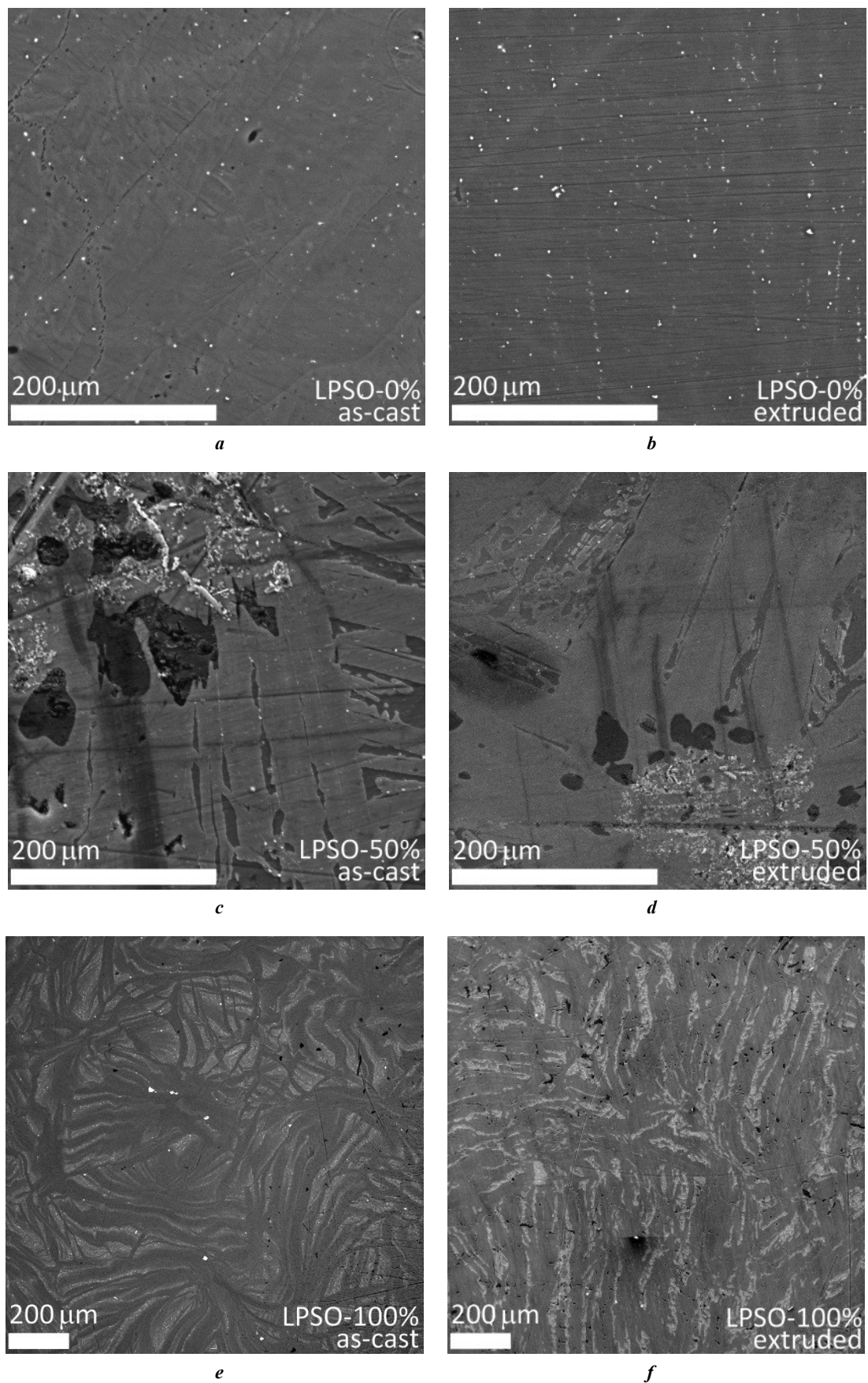
***Fig. 2.*** *SEM microimages for as-cast (**a, c, e**) and extruded (**b, d, f**) LPSO samples obtained*
*in backscattered electron contrast mode*
***Рис. 2.*** *РЭМ микроизображения для литых (**a, c, e**) и экструдированных (**b, d, f**) ДПС образцов,*
*полученные в режиме сопоставления отраженных электронов*
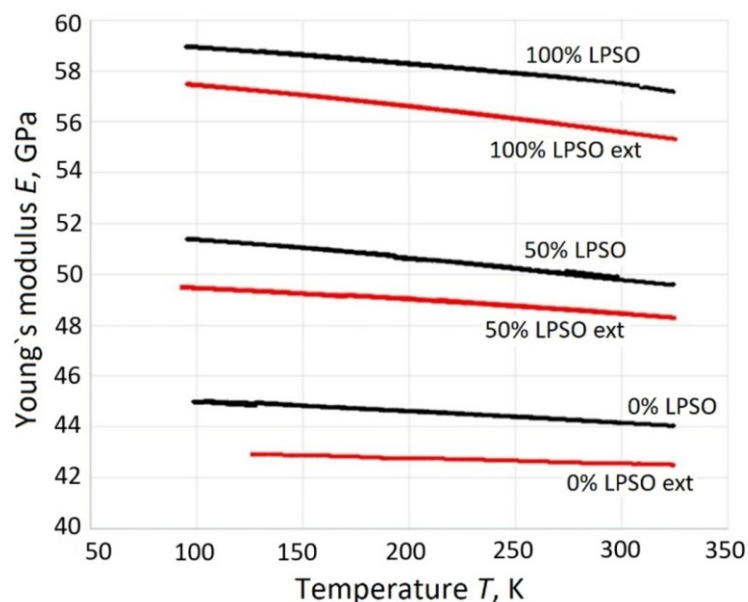
***Fig. 3.*** *Temperature dependence of Young's modulus of magnesium alloys*
*with different content of LPSO structures before and after extrusion*
***Рис. 3.*** *Температурная зависимость модуля Юнга магниевых сплавов*
*с различным содержанием ДПС структур до и после экструзии*

after extrusion, the increase of internal friction is also observed with the increase of the content of LPSO phases in the alloy. The amplitude dependent (ADIF) and amplitude independent (AIIF) part of internal friction is clearly visible in these relationships, for understanding the inset in Fig. 4 is presented. AIIF increases with increase in LPSO content but more increase occurs after extrusion. ADIF behaves differently without a pronounced pattern. In samples with LPSO content of 50 % and 100 %, a significant decrease in the critical strain amplitude can be observed, $\varepsilon_c$.

In Fig. 5 shows the amplitude dependences of Young's modulus softening, before and after extrusion. After extrusion, the modulus softening decreased significantly. Before extrusion, one can observe an increase in Young's modulus softening with increasing LPSO content of phases.

**DISCUSSION**

The X-ray diffraction peaks of the samples (Fig. 1) in the investigated range correspond to known crystal structures [4]. The texture of the samples corresponding to the phase-contrast images (Fig. 2 a, c, e) is preserved in the plane normal to the extrusion direction (Fig. 2 b, d, f). However, for all phases, the orientation of the crystal structure under shear deformation is observed (Fig. 1 b, 1 0 −1 0 peak).

The results show that the Young's modulus of magnesium alloys with LPSO structures increases with higher LPSO content (Fig. 3). Young's modulus values at a fixed strain amplitude grow with increasing volume fraction of the LPSO phase. This occurs because LPSO phases have strong interatomic bonds and increase

the stiffness of the alloy. The reasons for the decrease in Young's modulus after extrusion are varied. For example, during extrusion, a texture is formed in the material where most crystallites are oriented in a specific manner (e. g., basal planes (0001) align parallel to the extrusion direction), as confirmed by X-ray results (Fig. 1). In the direction parallel to the extrusion axis, the Young's modulus may decrease due to the predominant orientation of basal planes, which have a lower $E$ modulus along the c-axis [15]. In the perpendicular direction, the Young's modulus may, conversely, increase. In our case, texture may play a key role since measurements are conducted parallel to the extrusion axis.

In alloys with LPSO structures, extrusion can also lead to partial destruction or changes in the shape of LPSO phases [16]. These phases play a crucial role in strengthening the material, and their degradation can reduce the overall Young's modulus. In our experiments, the SEM results (Fig. 2) show changes in the shape of the blocks containing LPSO structures. Extrusion also induces significant plastic deformation, resulting in the accumulation of dislocations and the formation of kink band [17]. These defects reduce the elastic properties of the material as they create regions with reduced stiffness. The increase of AIIF (Fig. 4) just indirectly indicates the increase of dislocation density. Extrusion typically leads to grain refinement through dynamic recrystallisation [18]. Although grain size reduction increases strength and plasticity, it can reduce the Young's modulus due to the increased volume of grain boundaries, which have lower elasticity than the bulk crystallites [19].

The amplitude dependences of internal friction were taken at room temperature, Fig. 4. Based on classical works [20], the amplitude dependence of internal friction is related
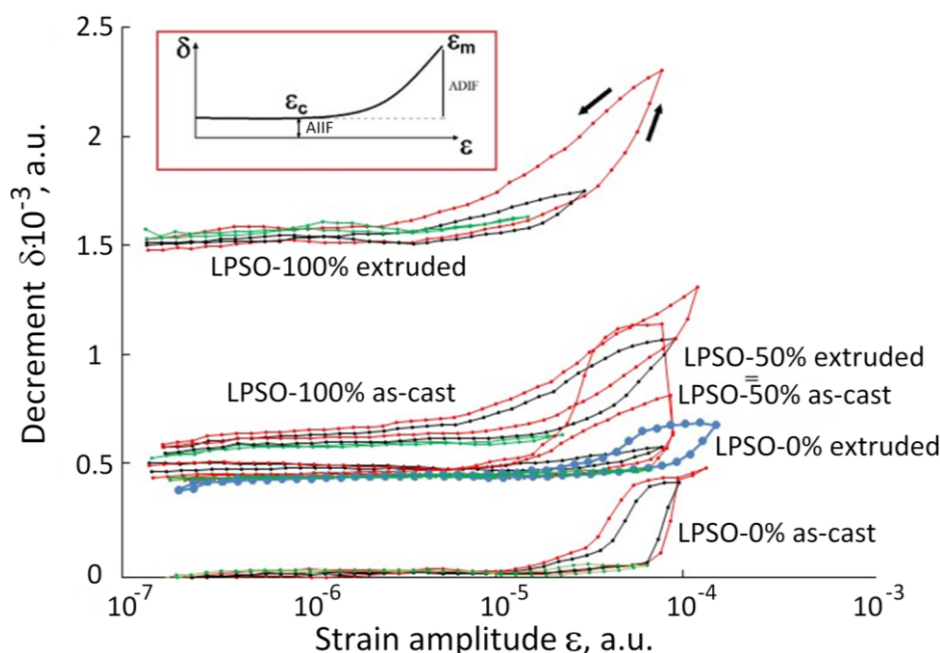
***Fig. 4.** Amplitude dependence of internal friction in the Mg–Y–Zn alloy
with different content of LPSO structures (LPSO – 0 %, LPSO – 50 %, LPSO – 100 %) before and after extrusion.
Consequent loading cycles with increasing $\varepsilon_m$ are marked in red, green and black, respectively.
The curve for 0 % LPSO after extrusion is highlighted in blue. Inset – schematic illustration of the amplitude –
independent internal friction (AIIF) and amplitude – dependent friction (ADIF).
$\varepsilon_c$ is the critical strain amplitude delineating these two regimes.
The arrows indicate the direction of the forward and backward run in the global loading cycle*
***Рис. 4.** Амплитудная зависимость внутреннего трения в сплаве Mg–Y–Zn
с различным содержанием ДПС структур (ДПС – 0 %, ДПС – 50 %, ДПС – 100 %) до и после экструзии.
Последовательные циклы нагружения с ростом $\varepsilon_m$ обозначены красным, зеленым и черным цветом соответственно.
Кривая для содержания ДПС 0 % после экструзии выделена синим цветом. Вставка – схематическое изображение
амплитудно-независимого внутреннего трения (AIIF) и амплитудно-зависимого трения (ADIF).
$\varepsilon_c$ – критическая амплитуда деформации, разграничивающая эти два режима.
Стрелки указывают направление прямого и обратного хода в глобальном цикле нагружения*

to the movement of dislocations in the material, where AIIF reflects the density of dislocations, ADIF reflects the movement of dislocation segments, and $\varepsilon_c$ is related to the detachment of dislocations (their segments) from the anchoring points. It should be noted that AIIF increases with increasing LPSO content, but to a greater extent the increase occurs after extrusion, which is associated with an increase in dislocation density. ADIF behaves differently and a precise interpretation of the observed phenomenon requires a more detailed study. Also in the present work, we will only emphasize the observed phenomenon of the decrease of the critical strain amplitude in samples with high content of LPSO phases further this phenomenon should be discussed more fully.

In Fig. 5 it can be seen that the Young's modulus softening over a wide range of amplitudes is smaller for the samples after extrusion. This can be explained by several reasons, but the main one is hardening due to dislocations. During extrusion, the material undergoes significant plastic deformation, which leads to an increase in dislocation density, as evidenced by the increase in AIIF in the post-extrusion samples. The high dislocation density may make it difficult for dislocations

to move during subsequent loading, which reduces the contribution of dislocation mechanisms to Young's modulus softening. The effect of LPSO phase changes on the decrease in Young's modulus softening after extrusion is not significant, which can be confirmed by the changes in Young's modulus softening in samples with 0 % LPSO phase content. In summary, the main reason for the decrease in Young's modulus softening after extrusion is the increase in dislocation density.

## CONCLUSIONS

The study demonstrates that the Young's modulus of Mg–Zn–Y alloys increases with higher LPSO content due to the strong interatomic bonds of LPSO phases. However, extrusion reduces the Young's modulus by approximately 3 %, attributed to texture formation, partial degradation of LPSO phases, and increased dislocation density. Internal friction measurements reveal a rise in amplitude-independent internal friction after extrusion, indicating higher dislocation density, while the critical strain amplitude decreases in alloys with higher LPSO content. Extrusion also reduces Young's modulus softening, primarily
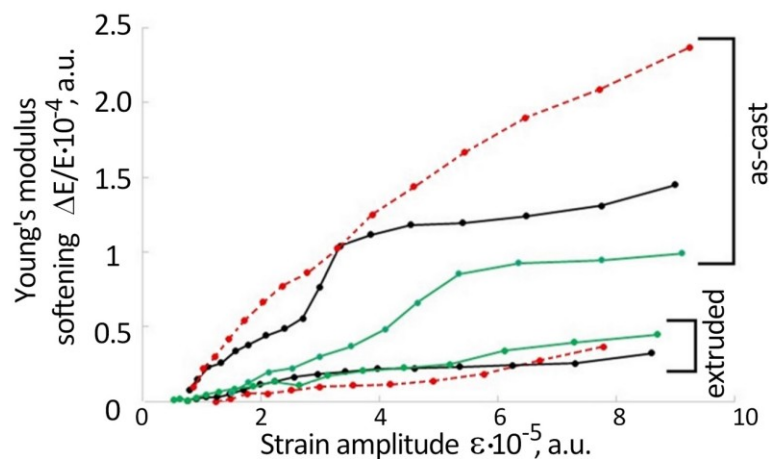
***Fig. 5.*** *Amplitude dependence of the softening of Young's modulus for alloys*
*with different LPSO content before and after extrusion.*
*Green line samples with 0 % LPSO, black line with 50 % LPSO, red-dashed line with 100 % LPSO*
***Рис. 5.*** *Амплитудная зависимость дефекта модуля Юнга для сплавов*
*с различным содержанием ДПС до и после экструзии.*
*Зеленая линия – образцы с 0 % ДПС, черная линия – с 50 % ДПС, красная пунктирная линия – со 100 % ДПС*

due to dislocation-induced hardening. Microstructural changes, such as grain refinement and kink band formation, further influence the mechanical properties. These findings underscore the importance of LPSO content and extrusion processes in optimising the mechanical behaviour of magnesium alloys.

## REFERENCES

1. Kawamura Y., Hayashi K., Inoue A., Masumoto T. Rapidly solidified powder metallurgy $Mg_{97}Zn_1Y_2$ alloys with excellent tensile yield strength above 600 MPa. *Materials Transactions*, 2001, vol. 42, no. 7, pp. 1172–1176. DOI: 10.2320/matertrans.42.1172.

2. Cao Furong, Liang Jinrui, Xu Panning, Xu Guangming. Microstructural Evolution, Mechanical Property, and Strengthening in a Lightweight Mg-Y-Zn-Mn Alloy Fabricated by Multidirectional Forging and Hot Rolling. *Journal of Materials Engineering and Performance*, 2024. DOI: 10.1007/s11665-024-10221-2.

3. Jiang We, Zou Chunming, Chen Yang, Wei Zunjie. The effect of pressure-induced $Mg_{64}Zn_{15}Y_{21}$ phase on the mechanical properties of Mg–Zn–Y alloy. *Journal of Alloys and Compounds*, 2020, vol. 840, article number 155682. DOI: 10.1016/j.jallcom.2020.155682.

4. Deng D.W., Kuo K.H., Luo Z.P., Miller D.J., Kramer M.J., Dennis K.W. Crystal structure of the hexagonal $Zn_3MgY$ phase. *Journal of Alloys and Compounds*, 2004, vol. 373, no. 1-2, pp. 156–160. DOI: 10.1016/j.jallcom.2003.10.039.

5. Kaminskii V.V., Abe E., Kawamura Y., Dorogin L.M., Romanov A.E. Kinking in LPSO Mg-Zn-Y alloys and other layered materials. *Reviews on Advanced Materials and Technologies*, 2022, vol. 4, no. 2, pp. 15–31. DOI: 10.17586/2687-0568-2022-4-2-15-31.

6. Liu Wei, Zhao Yuhang, Zhang Yuntao, Shuai Chuan, Chen Liwen, Huang Zhiquan, Hou Hua. Deformation-induced dynamic precipitation of 14H-LPSO structure and its effect on dynamic recrystallization in hot-extruded Mg-Y-Zn alloys. *International Journal of Plasticity*, 2023, vol. 164, article number 103573. DOI: 10.1016/j.ijplas.2023.103573.

7. Hagihara K., Kinoshita A., Sugino Y., Yamasaki M., Kawamura Y., Yasuda H.Y., Umakoshi Y. Effect of long-period stacking ordered phase on mechanical properties of Mg–Zn–Y extruded alloy. *Acta Materialia*, 2010, vol. 58, no. 19, pp. 6282–6293. DOI: 10.1016/j.actamat.2010.07.050.

8. Xu D.K., Liu L., Xu Y.B., Han E.H. The fatigue crack propagation behavior of the forged Mg–Zn–Y–Zr alloy. *Journal of Alloys and Compounds*, 2007, vol. 431, no. 1-2, pp. 107–111. DOI: 10.1016/j.jallcom.2006.05.043.

9. Janeček M., Král R., Dobroň P., Chmelik F., Supik V., Hollander F. Mechanisms of plastic deformation in AZ31 magnesium alloy investigated by acoustic emission and transmission electron microscopy. *Materials Science and Engineering: A*, 2007, vol. 462, no. 1-2, pp. 311–315. DOI: 10.1016/j.msea.2006.01.172.

10. Kalganov D.A., Philippov S.A., Kaminskii V.V., Ivanov A.Yu., Zasypkin S.V., Merson D.L., Dorogov M.V. Low Amplitude Nonlinear Damping and Effective Modulus in Magnesium Alloys Containing Long-Period Stacking Ordered Structures. *Reviews on Advanced Materials and Technologies*, 2025, vol. 7, no. 1, pp. 63–70. DOI: 10.17586/2687-0568-2025-7-1-63-70.

11. Robinson W.H., Edgar A. The Piezoelectric Method of Determining Mechanical Damping at Frequencies of 30 to 200 KHz. *IEEE Transactions on Sonics and Ultrasonics*, 1974, vol. 21, no. 2, pp. 98–105. DOI: 10.1109/T-SU.1974.29798.

12. Lebedev A.B., Kustov S.B., Kardashev B.K. Acousto-plastic effect in the active deformation and creep of aluminum. *Fizika tverdogo tela*, 1987, vol. 29, no. 12, pp. 3563–3569.

13. Kaufmann H.J., Pal-Val P.P. Interaction of dislocations with localized pinning points in high-purity molybdenum

single crystals. *Physica Status Solidi (A)*, 1980, vol. 62, no. 2, pp. 569–575. DOI: 10.1002/pssa.2210620226.

14. Pal-Val P., Vatazhuk O., Ostapovets A., Král L., Pinc J. Thermoactivated Dislocation Motion in Rolled and Extruded Magnesium: Data of the Low-Temperature Acoustic Experiment. *Metals*, 2021, vol. 11, no. 10, article number 1647. DOI: 10.3390/met11101647.

15. Wang Zixuan, Zheng Jie, Jia Leichen, Liu Waner, Huang Youwang, Yan Zhaoming, Zhang Zhimin, Xue Yong. Abnormal texture formation and mechanical anisotropy of pre-aging extruded Mg-Gd-Y-Zn-Zr alloy with large-scale. *Journal of Materials Research and Technology*, 2022, vol. 20, pp. 2771–2783. DOI: 10.1016/j.jmrt.2022.08.069.

16. Chen Tao, Chen Zhiyang, Shao Jianbo, Wang Renke, Mao Longhui, Liu Chuming. Evolution of LPSO phases in a Mg-Zn-Y-Gd-Zr alloy during semi-continuous casting, homogenization and hot extrusion. *Materials & Design*, 2018, vol. 152, pp. 1–9. DOI: 10.1016/j.matdes.2018.04.070.

17. Wang Jie, Zhu Gaoming, Wang Leyun, Zhang Xianbing, Knezevic M., Zeng Xiaoqin. Strengthening mechanisms, hardening/softening behavior, and microstructure evolution in an LPSO magnesium alloy at elevated temperatures. *Materials Characterization*, 2023, vol. 203, article number 113066. DOI: 10.1016/j.matchar.2023.113066.

18. Yoshimoto S., Yamasaki M., Kawamura Y. Microstructure and mechanical properties of extruded Mg-Zn-Y alloys with 14H long period ordered structure. *Materials Transactions*, 2006, vol. 47, no. 4, pp. 959–965. DOI: 10.2320/matertrans.47.959.

19. Liu Wei, Su Yu, Zhang Yuntao, Chen Liwen, Hou Hua, Zhao Yuhong. Dissolution and reprecipitation of 14H-LPSO structure accompanied by dynamic recrystallization in hot-extruded $Mg_{89}Y_4Zn_2Li_5$ alloy. *Journal of Magnesium and Alloys*, 2023, vol. 11, no. 4, pp. 1408–1421. DOI: 10.1016/j.jma.2022.03.018.

20. Yin Wujun, Briffod F., Shiraiwa T., Enoki M. Mechanical properties and failure mechanisms of Mg-Zn-Y alloys with different extrusion ratio and LPSO volume fraction. *Journal of Magnesium and Alloys*, 2022, vol. 10, no. 8, pp. 2158–2172. DOI: 10.1016/j.jma.2022.02.004.

phase // Journal of Alloys and Compounds. 2004. Vol. 373. № 1-2. P. 156–160. DOI: 10.1016/j.jallcom.2003.10.039.

5. Kaminskii V.V., Abe E., Kawamura Y., Dorogin L.M., Romanov A.E. Kinking in LPSO Mg-Zn-Y alloys and other layered materials // Reviews on Advanced Materials and Technologies. 2022. Vol. 4. № 2. P. 15–31. DOI: 10.17586/2687-0568-2022-4-2-15-31.

6. Liu Wei, Zhao Yuhang, Zhang Yuntao, Shuai Chuan, Chen Liwen, Huang Zhiquan, Hou Hua. Deformation-induced dynamic precipitation of 14H-LPSO structure and its effect on dynamic recrystallization in hot-extruded Mg-Y-Zn alloys // International Journal of Plasticity. 2023. Vol. 164. Article number 103573. DOI: 10.1016/j.ijplas.2023.103573.

7. Hagihara K., Kinoshita A., Sugino Y., Yamasaki M., Kawamura Y., Yasuda H.Y., Umakoshi Y. Effect of long-period stacking ordered phase on mechanical properties of Mg–Zn–Y extruded alloy // Acta Materialia. 2010. Vol. 58. № 19. P. 6282–6293. DOI: 10.1016/j.actamat.2010.07.050.

8. Xu D.K., Liu L., Xu Y.B., Han E.H. The fatigue crack propagation behavior of the forged Mg–Zn–Y–Zr alloy // Journal of Alloys and Compounds. 2007. Vol. 431. № 1-2. P. 107–111. DOI: 10.1016/j.jallcom.2006.05.043.

9. Janeček M., Král R., Dobroň P., Chmelik F., Supik V., Hollander F. Mechanisms of plastic deformation in AZ31 magnesium alloy investigated by acoustic emission and transmission electron microscopy // Materials Science and Engineering: A. 2007. Vol. 462. № 1-2. P. 311–315. DOI: 10.1016/j.msea.2006.01.172.

10. Kalganov D.A., Philippov S.A., Kaminskii V.V., Ivanov A.Yu., Zasypkin S.V., Merson D.L., Dorogov M.V. Low Amplitude Nonlinear Damping and Effective Modulus in Magnesium Alloys Containing Long-Period Stacking Ordered Structures // Reviews on Advanced Materials and Technologies. 2025. Vol. 7. № 1. P. 63–70. DOI: 10.17586/2687-0568-2025-7-1-63-70.

11. Robinson W.H., Edgar A. The Piezoelectric Method of Determining Mechanical Damping at Frequencies of 30 to 200 KHz // IEEE Transactions on Sonics and Ultrasonics. 1974. Vol. 21. № 2. P. 98–105. DOI: 10.1109/T-SU.1974.29798.

12. Лебедев А.Б., Кустов С.Б., Кардашев Б.К. Акустопластический эффект при активном деформировании и ползучести алюминия // Физика твердого тела. 1987. Т. 29. № 12. С. 3563–3569.

13. Kaufmann H.J., Pal-Val P.P. Interaction of dislocations with localized pinning points in high-purity molybdenum single crystals // Physica Status Solidi (A). 1980. Vol. 62. № 2. P. 569–575. DOI: 10.1002/pssa.2210620226.

14. Pal-Val P., Vatazhuk O., Ostapovets A., Král L., Pinc J. Thermoactivated Dislocation Motion in Rolled and Extruded Magnesium: Data of the Low-Temperature Acoustic Experiment // Metals. 2021. Vol. 11. № 10. Article number 1647. DOI: 10.3390/met11101647.

15. Wang Zixuan, Zheng Jie, Jia Leichen, Liu Waner, Huang Youwang, Yan Zhaoming, Zhang Zhimin, Xue Yong. Abnormal texture formation and mechanical anisotropy of pre-aging extruded Mg-Gd-Y-Zn-Zr alloy with large-scale // Journal of Materials Research and Technology. 2022. Vol. 20. P. 2771–2783. DOI: 10.1016/j.jmrt.2022.08.069.

16. Chen Tao, Chen Zhiyang, Shao Jianbo, Wang Renke, Mao Longhui, Liu Chuming. Evolution of LPSO

## СПИСОК ЛИТЕРАТУРЫ

1. Kawamura Y., Hayashi K., Inoue A., Masumoto T. Rapidly solidified powder metallurgy $Mg_{97}Zn_1Y_2$ alloys with excellent tensile yield strength above 600 MPa // Materials Transactions. 2001. Vol. 42. № 7. P. 1172–1176. DOI: 10.2320/matertrans.42.1172.

2. Cao Furong, Liang Jinrui, Xu Panning, Xu Guangming. Microstructural Evolution, Mechanical Property, and Strengthening in a Lightweight Mg-Y-Zn-Mn Alloy Fabricated by Multidirectional Forging and Hot Rolling // Journal of Materials Engineering and Performance. 2024. DOI: 10.1007/s11665-024-10221-2.

3. Jiang We, Zou Chunming, Chen Yang, Wei Zunjie. The effect of pressure-induced $Mg_{64}Zn_{15}Y_{21}$ phase on the mechanical properties of Mg–Zn–Y alloy // Journal of Alloys and Compounds. 2020. Vol. 840. Article number 155682. DOI: 10.1016/j.jallcom.2020.155682.

4. Deng D.W., Kuo K.H., Luo Z.P., Miller D.J., Kramer M.J., Dennis K.W. Crystal structure of the hexagonal $Zn_3MgY$

phases in a Mg-Zn-Y-Gd-Zr alloy during semi-continuous casting, homogenization and hot extrusion // Materials & Design. 2018. Vol. 152. P. 1–9. DOI: 10.1016/j.matdes.2018.04.070.

17. Wang Jie, Zhu Gaoming, Wang Leyun, Zhang Xianbing, Knezevic M., Zeng Xiaoqin. Strengthening mechanisms, hardening/softening behavior, and microstructure evolution in an LPSO magnesium alloy at elevated temperatures // Materials Characterization. 2023. Vol. 203. Article number 113066. DOI: 10.1016/j.matchar.2023.113066.

18. Yoshimoto S., Yamasaki M., Kawamura Y. Microstructure and mechanical properties of extruded Mg-Zn-Y alloys with 14H long period ordered structure // Materials Transactions. 2006. Vol. 47. № 4. P. 959–965. DOI: 10.2320/matertrans.47.959.

19. Liu Wei, Su Yu, Zhang Yuntao, Chen Liwen, Hou Hua, Zhao Yuhong. Dissolution and reprecipitation of 14H-LPSO structure accompanied by dynamic recrystallization in hot-extruded $Mg_{89}Y_4Zn_2Li_5$ alloy // Journal of Magnesium and Alloys. 2023. Vol. 11. № 4. P. 1408–1421. DOI: 10.1016/j.jma.2022.03.018.

20. Yin Wujun, Briffod F., Shiraiwa T., Enoki M. Mechanical properties and failure mechanisms of Mg-Zn-Y alloys with different extrusion ratio and LPSO volume fraction // Journal of Magnesium and Alloys. 2022. Vol. 10. № 8. P. 2158–2172. DOI: 10.1016/j.jma.2022.02.004.

# Влияние экструзии на модуль Юнга и внутреннее трение в магниевых сплавах с различным содержанием длиннопериодной слоистой структуры

**Каминский Владимир Владимирович**[*,1,2,5], кандидат физико-математических наук,
заведующий лабораторией института перспективных систем передачи данных
**Калганов Дмитрий Александрович**[2,6], младший научный сотрудник
лаборатории дифракционных методов исследования реальной структуры кристаллов
**Дорогов Максим Владимирович**[1,7], кандидат физико-математических наук,
доцент института перспективных систем передачи данных
**Филиппов Сергей Анатольевич**[2,3,8], научный сотрудник лаборатории дифракционных методов исследования
реальной структуры кристаллов, доцент высшей школы механики и процессов управления
**Романов Алексей Евгеньевич**[1,4,9], доктор физико-математических наук, профессор,
главный научный сотрудник института перспективных систем передачи данных

[1]*Университет ИТМО, Санкт-Петербург (Россия)*
[2]*Физико-технический институт им. А.Ф. Иоффе РАН, Санкт-Петербург (Россия)*
[3]*Санкт-Петербургский политехнический университет Петра Великого, Санкт-Петербург (Россия)*
[4]*Тольяттинский государственный университет, Тольятти (Россия)*

[*]**E-mail:** vvkaminskii@itmo.ru

[5]ORCID: https://orcid.org/0000-0002-4388-2459
[6]ORCID: https://orcid.org/0000-0003-1986-3693
[7]ORCID: https://orcid.org/0000-0001-5987-3357
[8]ORCID: https://orcid.org/0000-0002-7784-555X
[9]ORCID: https://orcid.org/0000-0003-3738-408X

*Аннотация:* Проведение исследования обусловлено растущим прикладным интересом к получению и исследованию механических свойств новых магниевых сплавов, содержащих длиннопериодную слоистую структуру (ДПС). Исследование влияния обработки теплой экструзией на модуль Юнга и внутреннее трение позволит в большей мере понять поведение данных материалов под действием различных механических напряжений, что важно для улучшения их функциональных характеристик. Представлены результаты влияния теплой экструзии на структуру, эффективный модуль Юнга и внутреннее трение в сплавах с различным содержанием фазы ДПС. Сплавы в системе Mg–Zn–Y с содержанием ДПС 0, 50 и 100 % об. были изучены с использованием пьезоэлектрического составного вибратора на частотах, близких к 100 кГц. Полученные результаты показали увеличение модуля Юнга с ростом содержания ДПС, обусловленное большей жесткостью и сильной межатомной связью в этой структуре. Экструзия вызвала уменьшение модуля Юнга на 3 % вдоль направления обработки. Этот эффект объясняется формированием удлиненной микротекстуры, преимущественной ориентацией в фазах альфа-магния и ДПС, а также возрастанием плотности подвижных дислокаций. Нелинейная часть внутреннего трения возрастала в результате экструзии благодаря увеличению плотности вовлеченных дислокаций. В то же время критическая амплитуда деформации уменьшалась с увеличением доли ДПС. Кроме того, выявлено снижение дефекта модуля Юнга после экструзии, что объясняется преимущественно дислокационным упрочнением. Полученные данные позволяют с большим пониманием взглянуть на деформационное поведение сплавов Mg–Zn–Y с ДПС, а также на влияние на него обработки теплой экструзией.

*Ключевые слова:* сплавы магния; длиннопериодная слоистая структура; ДПС; внутреннее трение; модуль Юнга; микропластичность.

**Togliatti State University** is a participant in the Priority-2030 program of strategic academic leadership, a flagship university in the Samara region, a center for innovative and technological development of the region.

Togliatti State University was created in 2001 by merging Togliatti Polytechnic Institute (founded in 1951 as a branch of Kuibyshev Industrial Institute) and Togliatti branch of Samara State Pedagogical University (founded in 1987).

### Togliatti State University today

– More than 22,000 students of all modes of study.

– Ten institutes implementing more than 170 higher education programs for 25 integrated groups of training areas, advanced technologies research institute, Zhiguli Valley Institute of Additional Education, military training center.

– 38 resource centers with up-to-date facilities and equipment created since 2011.

– Accreditation in eight systems for standard testing, research, and engineering.

– Main areas: advanced digital, intelligent manufacturing technologies, robotic systems, advanced materials and design methods, environmentally friendly and resource-saving energy engineering, personalized medicine, countering industrial threats.

### University main achievements

– Ongoing project and professional practical activity was introduced for 100 % of full-time undergraduate/specialist students.

– Four mega-grants were implemented according to the Resolutions of the Government of the Russian Federation dated April 9, 2010 No. 219 and No. 220 – three laboratories in the field of physical materials science and nanotechnology (with the invitation of leading scientists), as well as an innovation technology center were created. The latter was transformed into a university innovation technopark.

– A member of the extraterritorial scientific and educational center "Engineering of the Future".

– An initiator of the formation of eight consortiums, which brought together 69 organizations, including 36 universities, six scientific partners, among which there are three organizations of the Russian Academy of Sciences.

– A twice winner of the RF Government award in the field of quality (2009, 2019).

– An Online Higher Education System promoted under the Rosdistant brand was created. The project is the winner of the Project Olympus competition of the Analytical Center under the Government of the Russian Federation in the Project Management in the System of Higher Education and Science nomination (2019).

# Ductility, bending and wrapping ability relationship in wires made of electromagnetically cast ultrafine grained Al–0.5Fe and Al–0.5Fe–0.3Cu alloys

*Andrey E. Medvedev*\*[1,3], PhD (Physics and Mathematics), senior researcher
*Olga O. Zhukova*[1,4], engineer-researcher
*Darya D. Fedotova*[1,5], master, 4th category operator
of the Research Laboratory "Metals and Alloys under Extreme Conditions"
*Elvira D. Khafizova*[1,6], PhD (Physics and Mathematics), senior researcher
*Mikhail M. Motkov*[2,7], PhD (Engineering), senior researcher
*Maxim Yu. Murashkin*[1,8], PhD (Engineering), senior researcher

[1]*Ufa University of Science and Technology, Ufa (Russia)*
[2]*Siberian Federal University, Krasnoyarsk (Russia)*

\***E-mail:** medvedevandreyrf@gmail.com

[3]ORCID: https://orcid.org/0000-0002-8616-0042
[4]ORCID: https://orcid.org/0000-0002-1879-9389
[5]ORCID: https://orcid.org/0009-0000-7526-8309
[6]ORCID: https://orcid.org/0000-0002-4618-412X
[7]ORCID: https://orcid.org/0009-0007-1272-3993
[8]ORCID: https://orcid.org/0000-0001-9950-0336

*Abstract:* The research status on such functional properties, as bending capability, wrapping capability and ductility of conductive Al–Fe and Al–Fe–Cu alloys wires is uncertain. Bending and wrapping capability is determined by the industrial standards while no attempts were made to study the relation between them and ductility of the Al alloys wires, paying even less attention to the ultrafine-grained Al-based wires, produced by electromagnetic casting and equal-channel angular pressing. In this study alloys with two different chemical compositions (Al–0.5 wt. % Fe and Al–0.5 wt. % Fe–0.3 wt. % Cu) and two different casting methods (casting into electromagnetic mold and continuous casting and rolling) were used. Part of the wires for the study was prepared by cold drawing (CD), the other part – by the combination of the equal-channel angular pressing by the Conform scheme and cold drawing (ECAP-C+CD) to obtain coarse grained (CG) and ultrafine grained (UFG) structures, respectively. Annealing at 230 °C for 1 h was carried out to evaluate the thermal stability of the wires. It was shown that the correlation between ductility (elongation to failure), number of wraps and number of bends (both before the first crack and before complete failure of the specimen) may differ depending on the deformation value, deformation scheme, and amount of alloying elements of the alloy wire, as well as ability to form solid solutions.

*Keywords:* Al alloy; Al–Fe; Al–Fe–Cu; electromagnetic casting; continuous casting and rolling; equal-channel angular pressing; cold drawing; elongation to failure; ductility; wire bending; wire wrapping; fracture analysis.

*Acknowledgments:* The work was supported by the Russian Science Foundation, grant number 20-79-10133, https://rscf.ru/project/20-79-10133/.

The research part of the work was carried out on the equipment of the Core Facility Centre "Nanotech" of Ufa University of Science and Technology.

The authors express their gratitude to Professor V.N. Timofeev (Siberian Federal University) for providing the research material.

*For citation:* Medvedev A.E., Zhukova O.O., Fedotova D.D., Khafizova E.D., Motkov M.M., Murashkin M.Yu. Ductility, bending and wrapping ability relationship in wires made of electromagnetically cast ultrafine grained Al–0.5Fe and Al–0.5Fe–0.3Cu alloys. *Frontier Materials & Technologies*, 2025, no. 2, pp. 29–38. DOI: 10.18323/2782-4039-2025-2-72-3.

## INTRODUCTION

Aluminium and aluminium alloys are among the most widespread materials in different areas of industry. The increased use of the aluminium and its alloys is dictated by their increasing competitiveness with copper alloys. Low cost, high availability, sufficient mechanical strength and electrical conductivity, coupled with high ductility and corrosion resistance ensure the growing presence of these alloys in different areas of industrial complex [1].

Aluminium and its alloys possess a few properties, and their importance and acceptable levels depend on

their application. Hence, for electrical wires and cables the electrical conductivity, mechanical strength, and ductility are the most important [2]. Electrical conductivity is the primary factor here since it determines the ability to transfer electrical current, thus the most important property for the electrical wire. Mechanical strength is important in applications that involve any notable value of stress applied to the wire or cable, such as the overhead powerlines. The ductility determines the level of deformation that wire, or cable can endure before cracking or failure, thus meaning how flexible it is for different ways of mount.

Most often research papers only present the ductility of the studied material, which is insufficient for complex evaluation of the material functional properties. It is true that wires and cables used in the electrical industry in most cases are subjected to static load schemes, meaning tensile tests are the fastest way to obtain the experimental data that would be enough for most of the applications. However, in some real-life application cases such parameters, as fatigue [3], number of bends [4], winding capability [5] and fretting resistance [6] do matter. In terms of practical application, every important parameter should be evaluated, since there is no direct correlation of the different properties between each other.

For the overhead powerlines and other applications that withstand cyclic loads, fatigue tests are required. The fatigue tests are expensive and time-consuming, so they are not implemented in cases when the wire or cable has only static loads, or is only deformed once (for example, during mounting). For these cases, the ability to withstand bending and wrapping has higher importance [7].

The research on the matter of bending and wrapping capabilities of conductive aluminium alloys is very scarce. The values of these parameters are most often dictated by standards, such as ISO 7801:1984 "Wire. Bending test method" or ISO 7802:2013 "Metallic materials. Wire. Wrapping test". These standards determine the minimal amount of bends or wraps that the material should withstand in order to pass the bar, with no regard to the ductility of the material. However, as it was mentioned in the previous paragraph, the relationship between these parameters is of high interest.

Of particular interest are the alloys with an ultrafine-grained (UFG) structure formed in conductive materials by severe plastic deformation (SPD) methods. These materials usually demonstrate a very favorable "strength – electrical conductivity" combination, but ductility does not always exceed that of analogs produced by conventional methods [8]. In this regard, the study of the behavior of wires with a UFG structure, which have high strength and good electrical conductivity along with acceptable wrapping and bending abilities is very important for assessing their further use to produce conductors with a new level of properties, as well as the suitability of such conductors for installation. According to the results of our recent studies, Al–Fe aluminium alloys with the UFG structure demonstrate a combination of "strength-electrical conductivity-heat resistance" that is not competed by aluminum alloys of other alloying systems as Al–Mg–Si and Al–Zr etc., widely used in the cable industry [9].

The purpose of this study is to establish the relation (or absence of it) between ductility (total elongation to failure), bending and wrapping capabilities of the electrically conductive wires made of Al–Fe and Al–Fe–Cu aluminium alloys in both coarse-grained and ultrafine-grained states.

## METHODS

Two different alloys – Al–0.5 wt. % Fe and Al–0.5 wt. % Fe–0.3 wt. % Cu – were picked for the study. These alloys have chemical composition similar to that of commercial 8176 [10] and 8030 alloy [11], respectively. The alloys were produced via casting into electromagnetic mold (electromagnetic casting, EMC) for the purpose of fine chemical composition control and identical casting conditions. For the comparison part of the Al–0.5 wt. % Fe alloy samples were produced via continuous casting and rolling method (CCR), conventionally used for aluminium alloys. The chemical composition of the alloys is presented in Table 1. CCR alloy was chosen as a one to be compared with, since it is produced by the conventional technique, contrary to Al–0.5Fe (EMC) and Al–0.5Fe–0.3Cu (EMCM) alloys, produced via relatively new method of casting into electromagnetic mold. As established by the authors in the course of their previous studies, although the addition of 0.3 % Cu adds mechanical strength and thermal stability to the alloy, it also requires a very careful approach in terms of obtaining and processing, thus the EMC method was applied to it [12].

*Table 1. Chemical composition of alloys of the Al–Fe system, wt. %*
*Таблица 1. Химический состав сплавов системы Al–Fe, вес. %*

| Alloy | Alloy designation | Si | Fe | Cu | Σ(Mg, Zn, V) | Al |
|---|---|---|---|---|---|---|
| **Al–0.5Fe** | EMC | 0.04 | 0.50 | 0.01 | <0.01 | Rem |
| **Al–0.5Fe** | CCR | 0.06 | 0.48 | 0.01 | <0.20 | Rem |
| **Al–0.5Fe–0.3Cu** | EMCM | 0.02 | 0.50 | 0.30 | <0.01 | Rem |

Samples of the alloys studied were subjected to two different deformation treatments: cold drawing (CD) and combination of the equal-channel angular pressing (by the Conform scheme [13]) and cold drawing. The ECAP by the Conform scheme (ECAP-C) includes placing a wire rod of 11 mm in diameter into a pressing channel comprised of a running wheel die with the pressure arranged along working surfaces. Friction resistance forces a wire rod going from a running wheel die into a channel formed by a pressure arrangement and a gauge, coupling at a certain angle ψ with a wheel die. Shear straining occurs at an intersection of these channels (deformation zone). An intersection angle of channels ψ constituted 120° with four processing cycles. A wire rod was rotated around the axis by +90° after each ECAP-C cycle (route B_c), at room temperature (RT). As a result of ECAP-C processing, samples with a cross section of 10×10 mm and a length of at least 100 mm were obtained.

During the CD the samples were subjected to cold deformation on a laboratory drawing machine with a drawing ratio of 13.5 (relative compression ~75 %). As a result of the CD, wire samples with a diameter of 3 mm were obtained. Samples of the original wire rod were also subjected to CD using similar conditions.

Annealing at 230 °C for 1 h was carried out in an atmosphere Nabertherm B180 (Germany) furnace according to the IEC 62641:2023.

JEOL JSM 6940LV (Japan) was used to perform scanning electron microscopy. Additional fracture analysis was conducted in order to provide insight into the fracture behavior of the EMCM alloy.

To obtain statistically reliable results, tensile tests were carried out on three samples for each state on a universal tensile testing machine Instron 5982 (USA) at RT. The strain rate of 100 mm/min (for wire samples after cold drawing according to ASTM A931-96). Based on the test results, the values of elongation to failure (δ) were determined. The tensile tests were carried out on the samples after cold drawing (CD), after ECAP-C and cold drawing (ECAP-C+CD), as well as after annealing.

The bending tests were conducted according to ISO 7801:1984. For each state at least 3 samples were tested. On the special testing rig each sample was tested, and the number of bends until first crack (C) and until complete failure (F) was recorded.

The wrapping tests were conducted according to ISO 7802-2013. The requirements of the GOST 10447-93 were also noted. At least one sample was tested for each state. Wire samples of 3 mm in diameter were tightly wrapped around steel rod of 3 mm in diameter with the rate of no more than 1 s$^{-1}$. For passing the test each sample should withstand at least 5 turns, where 1 turn is equivalent for the 360° rotation. Different standards have different regulations for the acceptable number of wraps, from 5 (according to GOST 10447-93) up to 16 (according to ISO 7802:2013). Authors have made the conclusion based on the test results, that in case of 5 successful wraps, further wrapping goes unobstructed, until some major microdefect is presented, or the experimenter runs out of testing material. In this study authors took the regulations presented in GOST 10447-93.

## RESULTS

### Wrapping, bending and tensile tests assessment

Fig. 1 demonstrates the view of the samples after bending and wrapping tests. It may be noted that the fracture of the bending sample occurs not in the region of the bending, but at the periphery of it. Surface of the samples after both types of tests contains no visible defects.

Table 2 contains the results of the tensile, bending and wrapping tests of all studied materials: EMC, CCR and EMCM. Cold drawing provides the ductility (elongation to failure) of about 5 % on average in all alloys' samples, except for the EMCM alloy, where its average level is 2 %. According to IEC 62641:2023 the minimum elongation to failure of aluminium wires is 1.7 % for the cold-drawn state and 3.5 % for the annealed state. All the alloys studied have passed the 2 % elongation to failure mark. Some of the alloys surpass even the requirements for the annealed wires.

Combined ECAP-C+CD in low-Fe alloy, such as EMC and CCR, results in decreased, relatively to CD, level of ductility. Since these alloys could be considered as technically pure aluminium, they act like one, and an increase in the deformation value leads to the aforementioned results.
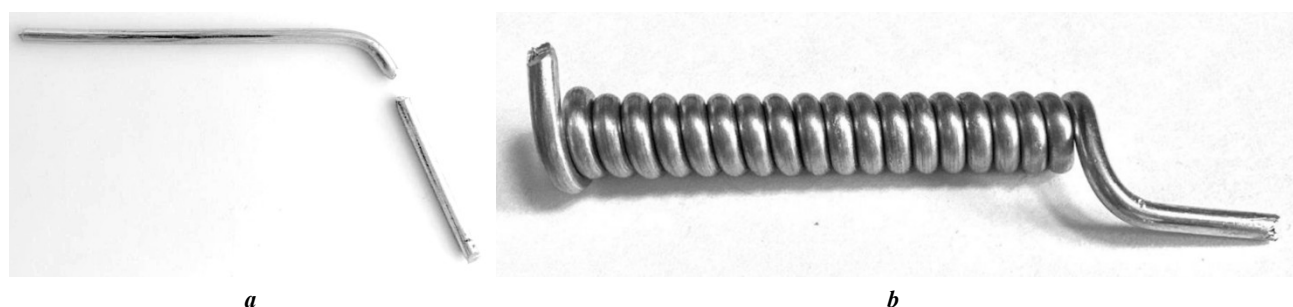


***Fig. 1.*** *Samples after bending (**a**) and wrapping (**b**) tests.*
*Both samples are made of wire of 3 mm diameter*
***Рис. 1.*** *Внешний вид образца после испытаний на перегибы (**a**) и навивы (**b**).*
*Оба образца изготовлены из проволоки диаметром 3 мм*

*Table 2. Results of the wrapping, bending and tensile tests*
*Таблица 2. Результаты испытаний на навивы, перегибы и растяжение*

| Alloy | State | Wrapping | | | Bending | | Ductility |
|---|---|---|---|---|---|---|---|
| | | Total number | Meeting requirements of GOST 10447-93 | Meeting requirements of ISO 7802:2013 | Until the first crack, C | Until complete failure, F | Elongation to failure, % |
| EMC | CD | >16 | yes | yes | 8–9 | 11–13 | 4.9±0.4 |
| | CD+230 °C | >16 | yes | yes | 7–8 | 12–13 | 3.8±0.7 |
| | ECAP-C+CD | >16 | yes | yes | 9 | 12 | 2.8±0.2 |
| | ECAP-C+CD+230 °C | >16 | yes | yes | 7 | 10–11 | 2.5±0.3 |
| CCR | CD | >16 | yes | yes | 8–11 | 9–15 | 5.6±0.4 |
| | CD+230 °C | >16 | yes | yes | 6–11 | 14–16 | 3.2±0.5 |
| | ECAP-C+CD | >16 | yes | yes | 9–10 | 12–14 | 2.7±0.2 |
| | ECAP-C+CD+230 °C | >16 | yes | yes | 8 | 11–14 | 2.2±0.7 |
| EMCM | CD | >16 | yes | yes | 6–9 | 7–10 | 2.3±0.4 |
| | CD+230 °C | >16 | yes | yes | 9 | 11–13 | 3.1±0.3 |
| | ECAP-C+CD | 0 | no | no | 1 | 1 | 2.7±0.5 |
| | ECAP-C+CD+230 °C | >16 | yes | yes | 10–12 | 14–30 | 7.2±3.7 |

The most notable difference between CD and ECAP-C+CD is observed in the EMCM sample. The introduction of the ECAP-C stage significantly increases the elongation to failure, but at a level that lies within the error value. Still, the total elongation to failure of the EMCM samples is higher than 2 %, which is considered to be sufficient for practical applications according to IEC 62641:2023. In EMC and CCR alloys, contrary to the EMCM, the annealing at 230 °C after CD and ECAP-C+CD results in a small, but notable decrease in ductility.

Table 2 contains, in addition to ductility data, results of the wrapping tests of the studied alloys. The only exception for the successful wrapping tests passage (the minimum amount of wraps is 5 according to the GOST 10447-93) was demonstrated by the EMCM alloy in the ECAP-C+CD state. Not a single wrap was possible to make since the wire was fracturing upon wrapping. In the CD state, however, the wire made of EMCM alloy demonstrated the sufficient number of wraps. Although elongation to failure of the EMCM alloy sample in the ECAP-C+CD state is relatively high, it has no direct correlation with the wrapping ability. The EMCM alloy in ECAP-C+CD state after annealing does pass the wrapping test. However, the first wraps were partially cracked, and only after a couple of wraps did the test continue smoothly.

Table 2 shows the number of bends before the first crack ($C$) and before complete failure ($F$). The values related to the elongation to failure of these wires are also given. It is more reasonable to assess the ability of

the wire to bends by the number of bends $C$, and not $F$ – if the spread of $C$ values is insignificant, then the spread of parameter $F$ can reach several tens of units, especially in the annealed state.

Most of the wires in the studied states meet this criterion, except for EMCM alloy in the ECAP-C+CD state – the wire in this state is so brittle that it fails already at the first bend on each of the studied samples.

With the increase of the parameters $C$ and $F$, in most cases the parameter δ (ductility) also increases, especially in the annealed states. However, this correlation is not straightforward. The most striking illustration is the ECAP-C+CD state of the EMCM alloy – despite the acceptable level of δ of 2.7±0.5 %, the wire in this state does not withstand even one bend. At the same time, the EMCM wire in the CD state, characterized by similar values of δ (2.3±0.4%), not only surpasses the ECAP-C+CD state in the parameters $C$ and $F$, but also successfully meets the requirements of ISO 7801:1984 and IEC 62641:2023.

**Fracture analysis of the EMC and EMCM alloys**

The fracture surface of the EMC alloy in the CD state (Fig. 2) has clearly a ductile nature. Surface has a break line across the fracture surface (Fig. 2 a, b). On one side of the break line there are round dimples, characteristic for the ductile fracture (Fig. 2 c), on the other – lamellar patterns (Fig. 2 d). These patterns formed as a result of compression of the parts of the sample during the last cycles of the bending test, when the crack has already formed and

developed, and parts of the sample were freely moving against each other.

The fracture surfaces of the EMCM alloy in a CD state, as well as EMC alloy in the ECAP-C+CD state are similar in nature (which is expected given these states have similar $F$ value (Table 2), thus they are not presented in the study.

The bending sample of the EMCM alloy after ECAP-C and CD, however, has different fracture behavior, images of which are presented in Fig. 3. The sample was barely able to withstand one bend (Table 2), cracking during it and completely fracturing upon the second bend. Three areas of the fracture surface (Fig. 3 a) correspond to the first crack (1), fracture area (2) and the break area (3). Judging from the number of bends one would expect the fragile nature of the fracture, but the fracture analysis indicates the opposite – the fracture surface consists of dimples (Fig. 3 c, d), although they much shallower than that of the other samples (Fig. 2). Process, similar to one in cold-drawn EMC alloy sample (Fig. 2 d), occurs in the fracture area – two parts of the sample compressed against each other, crumpling and smoothing the dimpled surface (Fig. 3 d).

## DISCUSSION

The research literature on the subject is very scarce, making this study somewhat unique. The general requirements for the wires are given in standards (ISO 7801:1984, IEC 62641:2023, ISO 7802-2013, GOST 10447-93), but they operate independently, having no connections with each other. However, it would be useful to find out if there
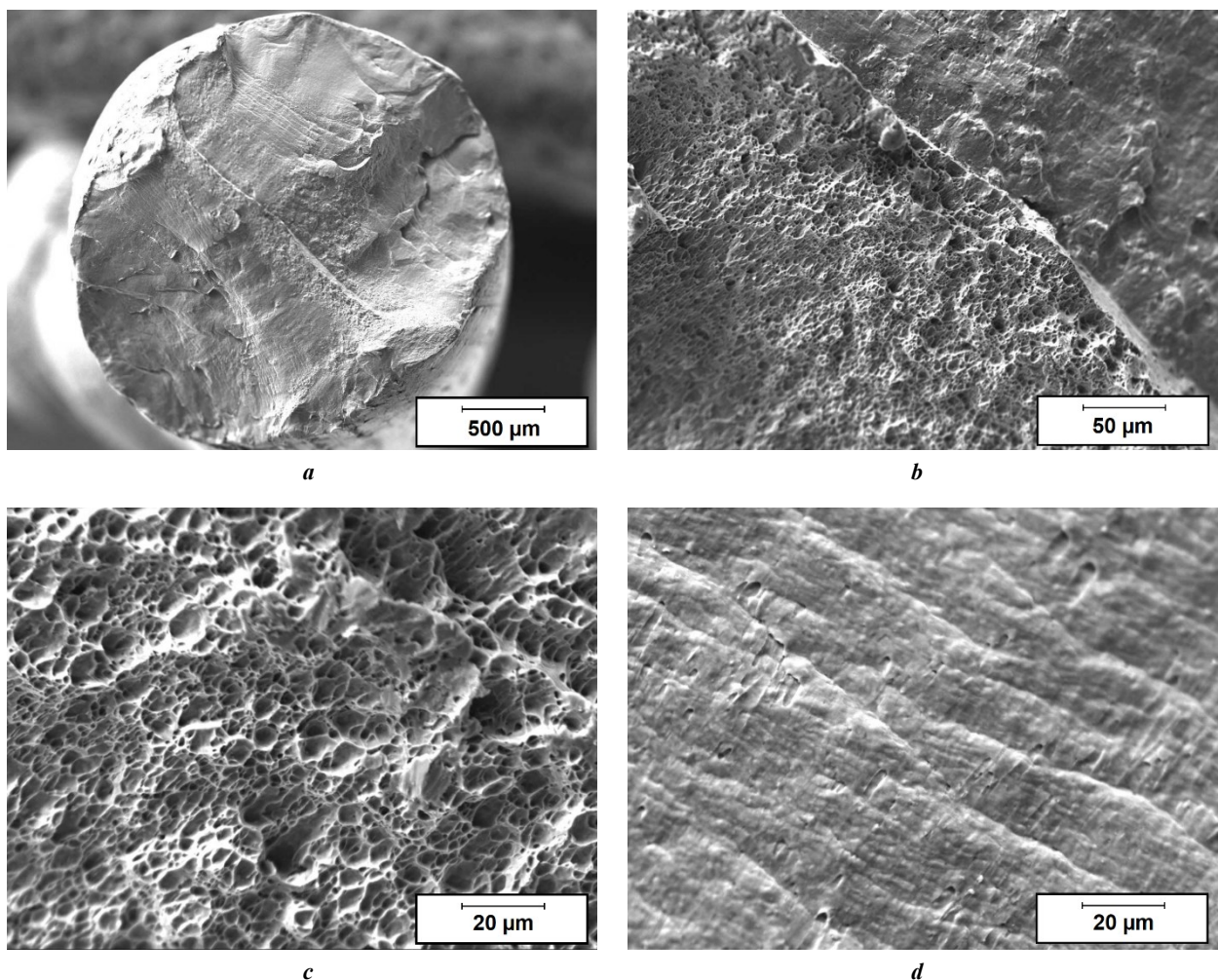


*Fig. 2. Fracture surface of the bending tests sample of the EMC alloy in the CD state, SEM:*
*a – overview of the fracture surface;*
*b – the border between the last and second-to-last fracture areas;*
*c – magnified image of the actual fracture surface, dimples are visible;*
*d – magnified image of the second-to-last fracture surface, dimples are smoothened by the smashing of the parts of the bending sample*
*Рис. 2. Поверхность излома образца из сплава ЭМК в состоянии ХВ после испытаний на перегибы, СЭМ:*
*a – обзор поверхности излома;*
*b – граница между последней и предпоследней зонами излома;*
*c – увеличенное изображение фактической поверхности излома, видны ямки;*
*d – увеличенное изображение предпоследней поверхности излома, ямки сглажены за счет сминания частей образца*
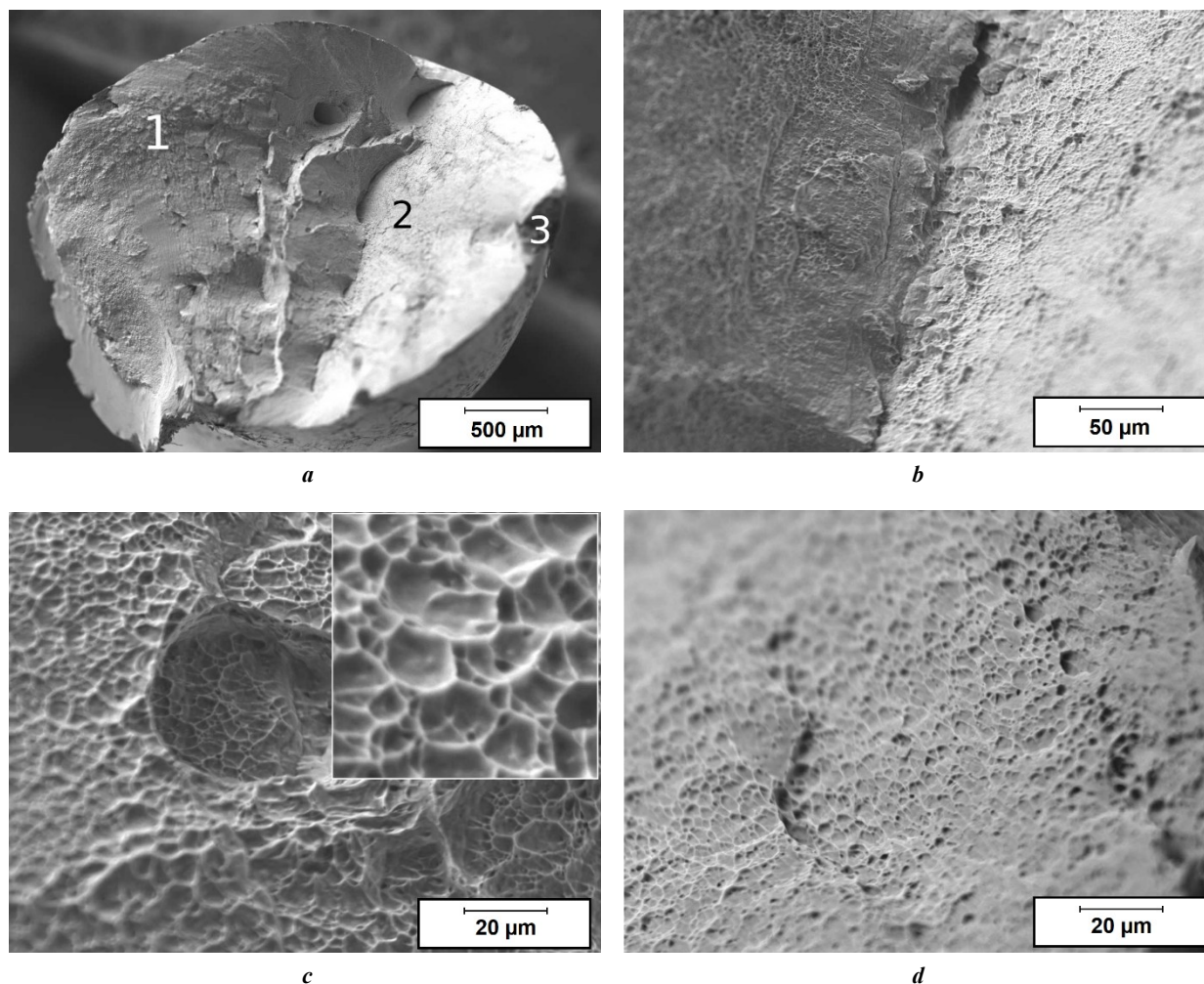
***Fig. 3.*** *Fracture surface of the bending tests sample of the EMCM alloy in the ECAP-C+CD state, SEM:*
***a*** *– fracture surface overview, where 1 – first crack zone, 2 – fracture area zone, 3 – break area zone;*
***b*** *– border between zones 1 and 2;*
***c*** *– the enlarged section of zone 1, as well as even further magnified image of the surface, illustrating the ductile nature of the fracture;*
***d*** *– the enlarged section of the zone 2, it demonstrates smaller, relatively to zone 1, size of the fracture dimples*
***Рис. 3.*** *Поверхность излома образца сплава ЭМКМ в состоянии РКУП-К+ХВ после испытаний на перегибы, СЭМ:*
***a*** *– общий вид поверхности разрушения, где 1 – зона первой трещины, 2 – зона разрушения, 3 – зона отрыва;*
***b*** *– граница между зонами 1 и 2;*
***c*** *– увеличенный участок зоны 1, а также еще более увеличенное изображение поверхности,*
*иллюстрирующее вязкий характер разрушения;*
***d*** *– увеличенный участок зоны 2, на нем видны меньшие относительно зоны 1 размеры ямок*

is a correlation between ductility, bending and wrapping capabilities, since it would allow us to predict the behaviorof aluminium materials with higher precision. Thus, the further discussion will be based on the aforementioned standards. The results of tests (Table 2) were visualized in a point plots, presented in Fig. 4.

Fig. 4 shows notable correlation between bending (and wrapping) and tensile tests. The $C$ value (Fig. 4 a) demonstrates a certain trend of increasing with the increase of the sample's ductility. Increased ductility of the sample provides the means for the material to accumulate higher amount of deformation thus increasing the deformation that the sample can withstand until the first crack. However, in the area of relatively low ductility (below 3 %), the $C$ values of the studied alloys almost merge, showing little to no difference. It should be noted that the $F$ value in most cases

has higher error value, showing that the accumulation of the deformation during the bending tests goes uneven (Fig. 4 b). It also means that the surface defects have a greater role in $F$ value compared to $C$ value. The dependance of the $F$ value from the ductility is notable, contrary to $C$, in the area of lower ductility (below 3 %), where increase in elongation to failure correlates with the increase of $F$ value. In the area of higher ductility, however, such correlation cannot be observed.

The tests, applied to materials studied represent three types of static stresses to which materials can be subjected: tensile, compressive, and shear. The tensile tests involve only tensile stress, while bending tests involve both tensile and compressive stress, simultaneously occurring in the contrary areas of the sample [14]. During the bending and wrapping tests failure usually occurs because the ultimate

*a*



*b*
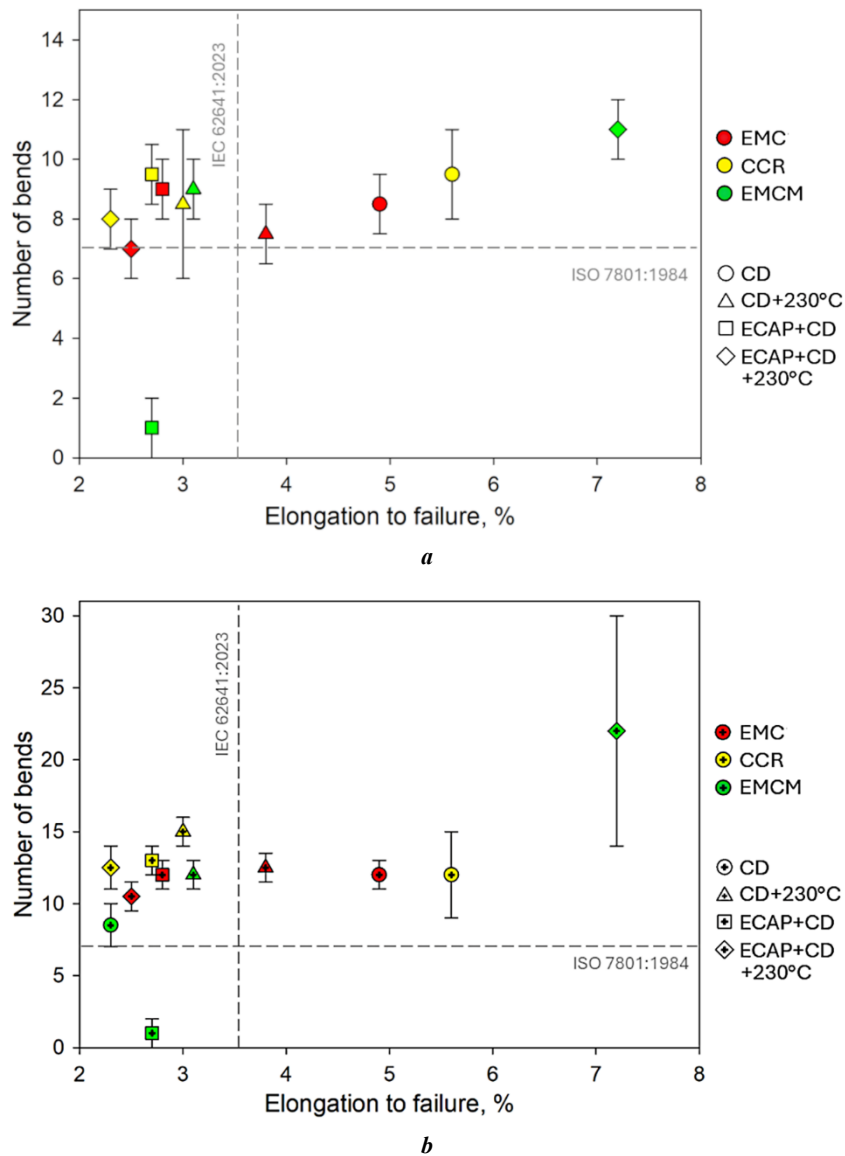
***Fig. 4.*** *Number-of-bends and to elongation-to-failure plot:*
***a*** *– until the first crack, C;* ***b*** *– until complete failure, F.*
*Red markers – EMC state, yellow markers – CCR state, green markers – EMCM state.*
*Circle markers – alloys in CD state, triangle markers – alloys in CD and annealing at 230 °C for 1 h state,*
*square markers – alloys in ECAP-C+CD state, diamond markers – alloys in ECAP-C+CD and annealing at 230 °C for 1 h state*
*[The error bars show the error values in multiple samples within one state. Gray dotted lines show the thresholds according*
*to IEC 62641:2023 and ISO 7801-1984]*
***Рис. 4.*** *Соотношение количества перегибов и величины удлинения до разрушения:*
***a*** *– до первой трещины, Т;* ***b*** *– до полного разрушения, Р.*
*Красные маркеры – состояние ЭМК, желтые маркеры – состояние НЛиП, зеленые маркеры – состояние ЭМКМ.*
*Круглые маркеры – сплавы в состоянии ХВ, треугольные маркеры – сплавы в состоянии ХВ после отжига при 230 °C*
*в течение 1 ч, квадратные маркеры – сплавы в состоянии РКУП-К+ХВ,*
*ромбовидные маркеры – сплавы в состоянии РКУП-К+ХВ после отжига при 230 °C в течение 1 ч*
*[Планки погрешностей показывают значения в нескольких образцах в пределах одного состояния. Серые пунктирные линии*
*показывают пороговые значения согласно IEC 62641:2023 и ISO 7801-1984]*

tensile strength of the outer areas of the specimen has been exceeded. This results in cleavage, or a first crack *C*, in which separation rather than slip occurs along certain crystallographic planes [15].

Thus, there is a difference in the loading schemes (simple vs complex) and even loading type (dynamic vs static) of bending (and wrapping) and tensile tests. This drastic difference doesn't allow to analytically evaluate the rela-

tionship between them, meaning that for the complex assessment of the wires behavior all three tests should be made, making the established correlation strictly experimental.

Despite the noted correlation, a certain anomaly was detected, and it is the behavior of the EMCM alloy. It may be noted that the majority of the specimens meet the requirements of minimum number of bends, equal to 7 (according

to ISO 7801:1984) (Fig. 4), with one exception, being EMCM alloy in ECAP-C+CD state. Interestingly, none of the EMC or CCR samples demonstrated such low *C* and *F* values, even in the ECAP-C+CD state (Table 2). It should be noted that the EMCM sample in the ECAP-C+CD state have also failed to meet the wrapping criteria (Table 2).

It would appear that EMCM alloy in the UFG state (provided by the combined ECAP-C and CD treatments) accumulates deformation much quicker than the other studied materials and states. Since the fracture of the EMCM sample is not fragile, the reason why the samples of the EMCM alloy accumulate significantly higher amount of structural defects lays within their chemical composition: EMCM alloy contains Cu, capable of forming solid solution, clusters, intermetallic particles and grain boundaries segregations. The Cu ions in the EMCM alloy find their way into solid solution and/or grain boundary segregation (similar to one observed in Cu-containing aluminium alloy under similar treatment) during the deformation. In the [16] it was demonstrated that similar deformation treatment can force Cu atoms into grain boundaries, leading to formation of the nano-sized $Al_xCu_y$ precipitates and significantly reducing the ductile properties of the material. Similar effect was also observed in Al alloys with insoluble alloying elements, such as Fe [17]. Though the exact nature of this occurrence is unknown, it is observed regularly. In the [9] it was shown that combined ECAP-C+CD forms in EMCM alloy structural features, that are not presented in the same alloy in CD state.

Thus, the detected discrepancy between the number of bends and the level of ductility of wire samples during the tensile tests made of the EMCM alloy of the Al–Fe system, additionally alloyed with copper, is most likely due to the migration of the Cu ions into the grain boundary regions. This effect can also explain the distinctive inability of the EMCM alloy wire in ECAP-C+CD state withstand the wraps.

## CONCLUSIONS

In this study the analysis of the ductility, bending and wrapping ability of the wires made of Al–Fe and Al–Fe–Cu systems alloys in CD and ECAP-C+CD states were analyzed.

1. For the first time the wires made of Al–0.5 wt. % Fe and Al–0.5 wt. % Fe–0.3 wt. % Cu aluminium alloy, produced using severe plastic deformation methods, subjected to bending and wrapping of tests, were studied. The correspondence of ductility and ability to bend/wrap was established.

2. It was demonstrated that for the low-alloyed aluminium alloys, such as Al–0.5 Fe, the ductility will correlate with the deformation value. In the alloys of higher alloying elements concentration, the chemical composition will have the major role in determining ductile properties. Alloys with soluble elements, such as Cu, will demonstrate the decrease of ductility and maximum number of bends and wraps upon increasing the deformation value.

3. The samples studied demonstrated correlative increase in elongation to failure and maximum number of bends (until the first crack in the high-ductility area and until complete failure in the low-ductility area), thus it is important to study

each characteristic of the material separately, considering the potential application of the produced wires.

4. The presence of the Cu in Al–Fe alloys accelerates the deformation build-up, causing faster failure of the samples in bending and wrapping tests, especially after deformation treatment including ECAP-C. However, thermal treatment allows this effect to diminish.

## REFERENCES

1. Verma R.P., Kumar L.M. A short review on aluminium alloys and welding in structural applications. *Materials Today Proceeding*, 2021, vol. 46, part 20, pp. 10687–10691. DOI: 10.1016/j.matpr.2021.01.447.

2. Shuai Guoliang, Li Zhen, Zhang Diantao, Elhefnawey M., Li Li. On rough set theory on achieving high quality cable material production by green low carbon technology. *Ecological Chemistry and Engineering S*, 2021, vol. 28, no. 1, pp. 49–59. DOI: 10.2478/eces-2021-0005.

3. Wang Shuo, Hou Jiapeng, Li Chenghui et al. Dynamic fatigue damage behaviors and mechanisms of overhead transmission Al wires at elevated temperatures. *International Journal of Fatigue*, 2024, vol. 188, article number 108515. DOI: 10.1016/j.ijfatigue.2024.108515.

4. Kikuchi S., Matsuoka S., Yoshimura T., Ijiri M. Effect of natural aging by multifunction cavitation on plane bending fatigue behaviour of heat-treatable Al-Si7Mg aluminum alloys and its fatigue strength estimation. *International Journal of Fatigue*, 2024, vol. 185, article number 108352. DOI: 10.1016/J.IJFATIGUE.2024.108352.

5. Hergul A.S., Yuce M., Ayaz M., Mese E. Investigation on aluminum alloys as winding materials for alternators in wind turbines. *Emerging Materials Research*, 2020, vol. 9, no. 3, pp. 789–795. DOI: 10.1680/JEMMR.20.00096.

6. Said J., Garcin S., Fouvry S., Cailletaud G., Yang C., Hafid F. A multi-scale strategy to predict fretting-fatigue endurance of overhead conductors. *Tribology International*, 2020, vol. 143, article number 106053. DOI: 10.1016/j.triboint.2019.106053.

7. Kalombo R.B., Reinke G., Miranda T.B., Ferreira J.L.A., Da Silva C.R.M., Araújo J.A. Experimental Study of the Fatigue Performance of Overhead Pure Aluminium Cables. *Procedia Structural Integrity*, 2019, vol. 19, pp. 688–697. DOI: 10.1016/j.prostr.2019.12.075.

8. Yi Huang, Langdon T.G. Advances in ultrafine-grained materials. *Materials Today*, 2013, vol. 16, no. 3, pp. 85–93. DOI: 10.1016/J.MATTOD.2013.03.004.

9. Medvedev A.E., Zhukova O.O., Kazykhanov V.U., Shaikhulova A.F., Motkov M.M., Timofeev V.N., Enikeev N.A., Murashkin M.Yu. Unique properties of the Al-0.5Fe-0.3Cu alloy, obtained by casting into an electromagnetic crystallizer, after equal-channel angular pressing and cold drawing. *Materials Physics and Mechanics*, 2024, vol. 52, no. 3, pp. 58–72. DOI: 10.18149/MPM.5232024_6.

10. Jiang Hongxiang, Li Shixin, Zhang Lili, He Jie, Zheng Qiuji, Song Yan, Li Yanqiang, Zhao Jiuzhou. The influence of rare earth element lanthanum on the microstructures and properties of as-cast 8176

(Al-0.5Fe) aluminum alloy. *Journal of Alloys and Compounds*, 2021, vol. 859, article number 157804. DOI: 10.1016/J.JALLCOM.2020.157804.

11. Chen Peng, Fan Xiangze, Yang Qingbo, Zhang Zhiqing, Jia Zhihong, Liu Qing. Creep behavior and microstructural evolution of 8030 aluminum alloys compressed at intermediate temperature. *Journal of Materials Research and Technology*, 2021, vol. 12, pp. 1755–1761. DOI: 10.1016/J.JMRT.2021.03.052.

12. Zhukova O.O., Medvedev A.E., Kiryanova K.E., Medvedev E.B., Motkov M.M. Properties of bimetallic wire with copper sheath and Al-0.5Fe-0.3Cu alloy core obtained by casting in an electromagnetic crystallizer. *Materials. Technologies. Design*, 2024, vol. 6, no. 3, pp. 27–33. DOI: 10.54708/26587572_2024_631827.

13. Murashkin M., Medvedev A., Kazykhanov V., Krokhin A., Raab G., Enikeev N., Valiev R.Z. Enhanced mechanical properties and electrical conductivity in ultrafine-grained Al 6101 alloy processed via ECAP-conform. *Metals (Basel)*, 2015, vol. 5, no. 4, pp. 2148–2164. DOI: 10.3390/met5042148.

14. Hou Jia-Peng, Wang Qiang, Yang Hua-Jie, Wu Xi-Mao, Li Chun-He, Zhang Zhe-Feng, Li Xiao-Wu. Fatigue and Fracture behavior of a Cold-Drawn Commercially pure aluminum wire. *Materials*, 2016, vol. 9, no. 9, article number 764. DOI: 10.3390/ma9090764.

15. Kuokkala V.T., Hokka M., Isakov M. Dynamic plasticity of metals. *Dynamic Behavior of Materials: Fundamentals, Material Models, and Microstructure Effects*, 2024, pp. 15–49. DOI: 10.1016/B978-0-323-99153-7.00005-0.

16. Shuai Linfei, Huang Tianlin, Yu Tianbo, Wu Guilin, Hansen N., Huang Xiaoxu. Segregation and precipitation stabilizing an ultrafine lamellar-structured Al–0.3%Cu alloy. *Acta Materialia*, 2021, vol. 206, article number 116595. DOI: 10.1016/j.actamat.2020.116595.

17. Medvedev A.E., Zhukova O.O., Fedotova D.D., Murashkin M.Yu. The mechanical properties, electrical conductivity, and thermal stability of a wire made of Al–Fe alloys produced by casting into an electromagnetic crystallizer. *Frontier Materials & Technologies*, 2022, no. 3-1, pp. 96–105. DOI: 10.18323/2782-4039-2022-3-1-96-105.

**СПИСОК ЛИТЕРАТУРЫ**

1. Verma R.P., Kumar L.M. A short review on aluminium alloys and welding in structural applications // Materials Today Proceeding. 2021. Vol. 46. Part 20. P. 10687–10691. DOI: 10.1016/j.matpr.2021.01.447.

2. Shuai Guoliang, Li Zhen, Zhang Diantao, Elhefnawey M., Li Li. On rough set theory on achieving high quality cable material production by green low carbon technology // Ecological Chemistry and Engineering S. 2021. Vol. 28. № 1. P. 49–59. DOI: 10.2478/eces-2021-0005.

3. Wang Shuo, Hou Jiapeng, Li Chenghui et al. Dynamic fatigue damage behaviors and mechanisms of overhead transmission Al wires at elevated temperatures // International Journal of Fatigue. 2024. Vol. 188. Article number 108515. DOI: 10.1016/j.ijfatigue.2024.108515.

4. Kikuchi S., Matsuoka S., Yoshimura T., Ijiri M. Effect of natural aging by multifunction cavitation on plane bending fatigue behaviour of heat-treatable Al-Si7Mg aluminum alloys and its fatigue strength estimation // International Journal of Fatigue. 2024. Vol. 185. Article number 108352. DOI: 10.1016/J.IJFATIGUE.2024.108352.

5. Hergul A.S., Yuce M., Ayaz M., Mese E. Investigation on aluminum alloys as winding materials for alternators in wind turbines // Emerging Materials Research. 2020. Vol. 9. № 3. P. 789–795. DOI: 10.1680/JEMMR.20.00096.

6. Said J., Garcin S., Fouvry S., Cailletaud G., Yang C., Hafid F. A multi-scale strategy to predict fretting-fatigue endurance of overhead conductors // Tribology International. 2020. Vol. 143. Article number 106053. DOI: 10.1016/j.triboint.2019.106053.

7. Kalombo R.B., Reinke G., Miranda T.B., Ferreira J.L.A., Da Silva C.R.M., Araújo J.A. Experimental Study of the Fatigue Performance of Overhead Pure Aluminium Cables // Procedia Structural Integrity. 2019. Vol. 19. P. 688–697. DOI: 10.1016/j.prostr.2019.12.075.

8. Yi Huang, Langdon T.G. Advances in ultrafine-grained materials // Materials Today. 2013. Vol. 16. № 3. P. 85–93. DOI: 10.1016/J.MATTOD.2013.03.004.

9. Medvedev A.E., Zhukova O.O., Kazykhanov V.U., Shaikhulova A.F., Motkov M.M., Timofeev V.N., Enikeev N.A., Murashkin M.Yu. Unique properties of the Al-0.5Fe-0.3Cu alloy, obtained by casting into an electromagnetic crystallizer, after equal-channel angular pressing and cold drawing // Materials Physics and Mechanics. 2024. Vol. 52. № 3. P. 58–72. DOI: 10.18149/MPM.5232024_6.

10. Jiang Hongxiang, Li Shixin, Zhang Lili, He Jie, Zheng Qiuji, Song Yan, Li Yanqiang, Zhao Jiuzhou. The influence of rare earth element lanthanum on the microstructures and properties of as-cast 8176 (Al-0.5Fe) aluminum alloy // Journal of Alloys and Compounds. 2021. Vol. 859. Article number 157804. DOI: 10.1016/J.JALLCOM.2020.157804.

11. Chen Peng, Fan Xiangze, Yang Qingbo, Zhang Zhiqing, Jia Zhihong, Liu Qing. Creep behavior and microstructural evolution of 8030 aluminum alloys compressed at intermediate temperature // Journal of Materials Research and Technology. 2021. Vol. 12. P. 1755–1761. DOI: 10.1016/J.JMRT.2021.03.052.

12. Жукова О.О., Медведев А.Е., Кирьянова К.Э., Медведев Е.Б., Мотков М.М. Свойства биметаллической проволоки с медной оболочкой и сердечником из сплава Al-0,5Fe-0,3Cu, полученного литьем в электромагнитный кристаллизатор // Materials. Technologies. Design. 2024. Т. 6. № 3. С. 27–33. DOI: 10.54708/26587572_2024_631827.

13. Murashkin M., Medvedev A., Kazykhanov V., Krokhin A., Raab G., Enikeev N., Valiev R.Z. Enhanced mechanical properties and electrical conductivity in ultrafine-grained Al 6101 alloy processed via ECAP-conform // Metals (Basel). 2015. Vol. 5. № 4. P. 2148–2164. DOI: 10.3390/met5042148.

14. Hou Jia-Peng, Wang Qiang, Yang Hua-Jie, Wu Xi-Mao, Li Chun-He, Zhang Zhe-Feng, Li Xiao-Wu. Fatigue and

Fracture behavior of a Cold-Drawn Commercially pure aluminum wire // Materials. 2016. Vol. 9. № 9. Article number 764. DOI: 10.3390/ma9090764.

15. Kuokkala V.T., Hokka M., Isakov M. Dynamic plasticity of metals // Dynamic Behavior of Materials: Fundamentals, Material Models, and Microstructure Effects. 2024. P. 15–49. DOI: 10.1016/B978-0-323-99153-7.00005-0.

16. Shuai Linfei, Huang Tianlin, Yu Tianbo, Wu Guilin, Hansen N., Huang Xiaoxu. Segregation and precipitation stabilizing an ultrafine lamellar-structured Al–0.3%Cu alloy // Acta Materialia. 2021. Vol. 206. Article number 116595. DOI: 10.1016/j.actamat.2020.116595.

17. Медведев А.Е., Жукова О.О., Федотова Д.Д., Мурашкин М.Ю. Механические свойства, электропроводность и термостабильность проволоки из сплавов системы Al–Fe, полученных литьем в электромагнитный кристаллизатор // Frontier Materials & Technologies. 2022. № 3-1. С. 96–105. DOI: 10.18323/2782-4039-2022-3-1-96-105.

# Соотношение пластичности, способности к перегибам и навивам проволок из ультрамелкозернистых сплавов Al–0,5Fe и Al–0,5Fe–0,3Cu, полученных литьем в электромагнитный кристаллизатор

*Медведев Андрей Евгеньевич*[*,1,3], кандидат физико-математических наук, старший научный сотрудник
*Жукова Ольга Олеговна*[1,4], инженер-исследователь
*Федотова Дарья Дмитриевна*[1,5], магистр , оператор 4-го разряда
НИЛ «Металлы и сплавы при экстремальных воздействиях»
*Хафизова Эльвира Динифовна*[1,6], кандидат физико-математических наук, старший научный сотрудник
*Мотков Михаил Михайлович*[2,7], кандидат технических наук, старший научный сотрудник
*Мурашкин Максим Юрьевич*[1,8], кандидат технических наук, старший научный сотрудник

[1]*Уфимский университет науки и технологий, Уфа (Россия)*
[2]*Сибирский федеральный университет, Красноярск (Россия)*

*E-mail:** medvedevandreyrf@gmail.com

[3]ORCID: https://orcid.org/0000-0002-8616-0042
[4]ORCID: https://orcid.org/0000-0002-1879-9389
[5]ORCID: https://orcid.org/0009-0000-7526-8309
[6]ORCID: https://orcid.org/0000-0002-4618-412X
[7]ORCID: https://orcid.org/0009-0007-1272-3993
[8]ORCID: https://orcid.org/0000-0001-9950-0336

*Аннотация:* В исследованиях таких функциональных свойств сплавов Al–Fe и Al–Fe–Cu, как способность к перегибам и навивам, а также пластичность проводов из этих сплавов, имеет место значительная степень неопределенности. Способность к перегибам и навивам определяется промышленными стандартами, однако попыток изучить связь между ними и пластичностью проводов из алюминиевых сплавов не предпринималось. Еще меньше внимания уделено проводам с ультрамелкозернистой структурой на основе алюминия, полученным электромагнитным литьем и равноканальным угловым прессованием. В данном исследовании использовались сплавы с двумя различными химическими составами (Al–0,5 вес. % Fe и Al–0,5 вес. % Fe–0,3 вес. % Cu) и двумя различными способами литья (литье в электромагнитный кристаллизатор и непрерывное литье и прокатка). Часть проводов для исследования была изготовлена методом холодного волочения (ХВ), другая – комбинацией равноканального углового прессования по схеме «Конформ» и холодного волочения (РКУП-К+ХВ) для получения крупнозернистой и ультрамелкозернистой структур соответственно. Для оценки термической стабильности проволок проводили отжиг при температуре 230 °C в течение 1 ч. Показано, что соотношение между пластичностью (удлинением до разрушения), числом навивов и числом перегибов (как до первой трещины, так и до полного разрушения образца) может различаться в зависимости от схемы деформации, типа и количества легирующих элементов в сплаве, а также способности образовывать твердые растворы.

*Ключевые слова:* алюминиевый сплав; Al–Fe; Al–Fe–Cu; электромагнитное литье; непрерывное литье и прокатка; равноканальное угловое прессование; холодное волочение; удлинение до разрушения; пластичность; технологические перегибы; технологические навивы; фрактографический анализ.

*Благодарности:* Работа выполнена за счет гранта Российского научного фонда № 20-79-10133, https://rscf.ru/project/20-79-10133/.

Исследовательская часть работы выполнена на оборудовании ЦКП «Нанотех» Уфимского университета науки и технологий.

Авторы выражают благодарность профессору В.Н. Тимофееву (Сибирский федеральный университет) за предоставленный материал исследования.

*Для цитирования:* Медведев А.Е., Жукова О.О., Федотова Д.Д., Хафизова Э.Д., Мотков М.М., Мурашкин М.Ю. Соотношение пластичности, способности к перегибам и навивам проволок из ультрамелкозернистых сплавов Al–0,5Fe и Al–0,5Fe–0,3Cu, полученных литьем в электромагнитный кристаллизатор // Frontier Materials & Technologies. 2025. № 2. С. 29–38. DOI: 10.18323/2782-4039-2025-2-72-3.

# Mechanical and corrosion anisotropy of magnesium single crystal

***Dmitry L. Merson*** *[1,3], Doctor of Sciences (Physics and Mathematics), Professor,
Director of the Research Institute of Advanced Technologies
***Sergey Ya. Betsofen*** [2,4], Doctor of Sciences (Engineering), Professor, professor of Chair
“Technologies and Systems for Computer-Aided Design of Metallurgical Processes”
***Evgeny D. Merson*** [1,5], PhD (Physics and Mathematics), senior researcher
of the Research Institute of Advanced Technologies
***Vitaly A. Poluyanov*** [1,6], PhD (Engineering), junior researcher
of the Research Institute of Advanced Technologies
***Pavel N. Myagkikh*** [1,7], PhD (Engineering), junior researcher
of the Research Institute of Advanced Technologies
***Aleksey V. Danyuk*** [1,8], PhD (Physics and Mathematics), senior researcher
of the Research Institute of Advanced Technologies
***Vladimir A. Danilov*** [1,9], PhD (Engineering), junior researcher
of the Research Institute of Advanced Technologies
***Ekaterina I. Maksimenko*** [2], postgraduate student
***Aleksandr I. Brilevskiy*** [1,10], PhD (Engineering), junior researcher
of the Research Institute of Advanced Technologies*

[1]*Togliatti State University, Togliatti (Russia)*
[2]*Moscow Aviation Institute, Moscow (Russia)*

**\*E-mail:** d.merson@tltsu.ru

[3]ORCID: https://orcid.org/0000-0001-5006-4115
[4]ORCID: https://orcid.org/0000-0003-0931-2839
[5]ORCID: https://orcid.org/0000-0002-7063-088X
[6]ORCID: https://orcid.org/0000-0002-0570-2584
[7]ORCID: https://orcid.org/0000-0002-7530-9518
[8]ORCID: https://orcid.org/0000-0002-7352-9947
[9]ORCID: https://orcid.org/0000-0001-5099-6940
[10]ORCID: https://orcid.org/0000-0002-5780-6094

*Abstract:* Magnesium and its alloys are promising materials for medical use due to their ability to dissolve safely in the human body. However, the rate of dissolution of bioresorbable implants should be in a narrow enough range. The difficulty in ensuring this condition is that the corrosion process in magnesium alloys is influenced by many factors, including natural (single-crystal) and technological (production scheme) anisotropy. By carrying out technological operations on thermomechanical treatment, it is possible to control the process of formation of the semi-finished product texture and to create artificially a preferred orientation of crystallites in the structure of magnesium alloys and thus control their corrosion resistance. This requires precise knowledge of the relationship between corrosion processes and certain crystallographic directions, which can be most reliably obtained in experiments on single crystals. In this work, mechanical (compression and tension) and corrosion tests were carried out for the first time on the same magnesium single crystal on samples with different crystallographic orientations. The Kearns coefficients calculated from the X-ray diffraction patterns of the single crystal specimen faces by the inverse pole figure method were used as a quantitative criterion of the natural texture. The specimens were subjected to compression tests in the $< 0001 >$, $< 1\bar{1}00 >$ and $< 11\bar{2}0 >$ directions, and to tension tests in the $< 0001 >$ direction. The specimen surfaces with orientations close to the $(0001)$, $(10\bar{1}0)$, $(2\bar{1}\bar{1}0)$, and $(10\bar{1}1)$ crystallographic planes were subjected to corrosion testing. It was found that the Young's modulus and the Kearns coefficient for the basal and pyramidal faces were 48.6 GPa and 0.81; 45.3 GPa and 0.04, respectively. The shape of the stress curves depended significantly on the sample orientation and was determined by the degree of involvement of various mechanisms in the overall plastic deformation process. The rate of corrosion in a physiological aqueous solution of 0.9 % NaCl on a 72-h basis for the $(0001)$, $(10\bar{1}0)$, $(2\bar{1}\bar{1}0)$, and $(10\bar{1}0)$ surfaces was 0.51, 0.76, 0.71 and 0.98 mm/year, respectively. In this case, the $(2\bar{1}\bar{1}0)$ plane experienced only uniform corrosion, the $(0001)$ plane experienced uniform corrosion with minor localised corrosion; the most intense localised corrosion is observed in the $(10\bar{1}0)$ direction, and the maximum intensity of the combination of localised and uniform corrosion is in the $<10\bar{1}1>$ direction.

*Keywords:* magnesium single crystal; crystallographic directions; anisotropy; Kearns coefficient; mechanical diagrams; corrosion rate.

## INTRODUCTION

The study and design of magnesium alloys is one of the up-to-date areas of modern materials science, since these materials have a set of unique properties, such as the best strength-to-weight ratio and excellent biocompatibility: pure magnesium is absorbed by a living organism with a minimal risk of negative effects [1; 2]. One of the main problems when using magnesium alloys is their low corrosion resistance that has a galvanic nature [3], and often manifests itself in the form of localised corrosion [4], which can be significantly affected by the composition and structural state of the material. It is well known that Mg and its alloys are characterised by significant anisotropy of mechanical properties due to the features of the deformation mechanism and the formation of an intense basal texture in sheet semi-finished products, and an intense prismatic texture in extruded rods [5; 6].

Understanding the nature of the corrosion anisotropy of magnesium and its alloys will help determine the structural and textural factors affecting the rate and uniformity of the corrosion process. Consequently, knowledge of the target structure and texture of the material will allow choosing the method of deformation treatment of the product (semi-finished product), or its surface at the final stage of manufacture to produce a material with high-quality and guaranteed parameters of the corrosion process. The rate and uniformity of corrosion are understood as quality parameters. The use of magnesium alloys as a material for the manufacture of temporary implants capable of self-absorbing after fulfilling their intended service is currently a relevant up-to-date sector at the junction of materials science and medicine. Therefore, understanding the corrosion process of magnesium materials and managing it is extremely important for the creation of bioresorbable medical materials with an accurately predictable service life. The same applies to structural magnesium alloys used to manufacture power elements in the aviation and automotive industries. Such elements are made in most cases from semi-finished products manufactured by various methods of metal pressure processing (extrusion, rolling, methods of severe plastic deformation, etc.), the consequence of which is the inevitable formation of a corresponding texture in the processed metal, the parameters of which can significantly affect the corrosion processes. In other words, the corrosion resistance of products made from a material with identical chemical and even phase composition may differ essentially depending on the production technology. Therefore, understanding the cause-and-effect relationships between the structural and textural parameters of magnesium alloys and corrosion processes is of great scientific and applied importance.

However, studies of the effect of texture on the corrosion properties of magnesium alloys have not received due attention in the literature for a long time. Only after 2010, a pronounced trend towards conducting such studies emerged [7–10]. In the work [7], the microstructure, texture, mechanical properties and corrosion behaviour of extruded Mg–4Zn alloy were studied. Samples with an orientation close to the basis showed lower corrosion rates compared to the orientation of samples with a predominance of prismatic planes. In [8–10], similar results were obtained for the AZ31 alloy. Corrosion anisotropy has been experimentally found both in pure magnesium [11] and in deformable magnesium alloys. For example, work [12] presents the results of corrosion rate assessment in various technological directions after rolling of AZ80 alloy, and shows that the corrosion rate determined by the mass method can differ by 1.7 times in the normal direction (ND) and in the extrusion direction (ED). Such a difference in corrosion rate is quite significant and must be taken into account, especially when creating bioresorbable structures for medical purposes.

It is generally accepted that corrosion anisotropy associated with crystallographic orientation is determined by the surface atomic-binding energy and the packing density of atoms [13]. Obviously, such a binding can be most correctly revealed during corrosion tests of single crystals. Surprisingly few such studies have been performed on single crystals of metals with a hexagonal close-packed (hcp) lattice, especially on magnesium. In the earliest work [14], it was found for magnesium single crystals that in a chlorine-containing environment, the (0001) basal plane exhibits the lowest corrosion resistance, and the corrosion itself has a filiform, i. e. it spreads in a direction rather than chaotically, and this direction is determined largely by the crystallographic orientation. In [15], where the corrosion process was studied on single-crystal magnesium planes with the widest possible range of directions, the (0001) orientation, on the contrary, showed the highest corrosion resistance. It should be noted that in most known cases it is the (0001) basal plane that exhibits maximum resistance to corrosion, for example, such a conclusion was made in [11] using the example of a study of a polycrystal of pure magnesium with a large grain.

Along with corrosion anisotropy, magnesium and its alloys are even more characterised by mechanical anisotropy, which is expressed in sharply different mechanical behaviour depending on the crystallographic direction of loading. It is worth noting that there are only a few more experimental studies of mechanical anisotropy performed on magnesium single crystals than studies that cover corrosion anisotropy. The earliest ones include studies [16; 17], in which magnesium single crystals were tested for compression in various directions and only the initial region including the transition from the elastic to the plastic stage was studied. Perhaps the most interesting study of the mechanical behaviour of magnesium single crystals also under compression,

but up to failure, was conducted in [18]. This work convincingly demonstrated the fundamental difference in the compression diagrams of single crystals tested in different crystallographic directions, which is explained by the different combination of twinning and slip deformation mechanisms under starting stresses.

Note that we are not aware of any work in which mechanical and corrosion anisotropy would be simultaneously studied on samples of the same magnesium single crystal.

The purpose of the study is to evaluate and compare corrosion and mechanical anisotropy performed on the same magnesium single crystal.

## METHODS

A magnesium single crystal with 99.98 % purity and dimensions of 30×19×62 mm was produced at the Magnesium Technology Innovation Center, School of Materials Science and Engineering, Seoul National University, using the Bridgman method.

The following samples were prepared from the magnesium single crystal by the electrical discharge machining (EDM) using a Sodick AG400L LN2W electric spark wire-cutting machine: (1) in the form of parallelepipeds with dimensions of 6.5×6.0×5.5 mm for compression testing and (2) in the form of specimens of a dog bone shape with cross-section dimensions of 4.0×3.0 mm and a gauge part length of 9.0 mm for tensile testing. Due to the small size of the original single crystal, tensile specimens were prepared for only one $<10\bar{1}1>$ orientation. The drawing and orientation of the tensile specimens are shown in Fig. 1.

The orientation of the samples was determined using a SIGMA scanning electron microscope (Zeiss) equipped with an electron backscatter diffraction detector (EBSD).

The mechanical tests of magnesium samples were carried out at room temperature using a miniature Kammrath & Weiss testing machine with a strain rate of $0.83 \cdot 10^{-3}$ s$^{-1}$ for both compression and tension.

The texture was studied by the X-ray diffraction method using a SHIMADZU XRD-6000 vertical 2Θ-Θ X-ray diffractometer (Japan) in monochromatic copper radiation. The texture was estimated by the method of inverse pole figures (IPF) obtained from X-ray patterns for the faces of the specimens parallel to the basal planes, using normalisation that takes into account the uneven distribution of reflections on the projection sphere using the $A_i$ coefficients. The values of the pole densities $P_i$ for reflections $i=hkl$ were determined by the relation

$$P_i = \frac{I_i / R_i}{\sum_{i=1}^{n} A_i \left( I_i / R_i \right)} , \qquad (1)$$

where $A_i$ is the ratio of the surface area of the stereographic triangle around the normal $(i=hkl)$ limited by large circles dividing in half the angular distances between adjacent normals;
$n$ is the number of experimental reflections ($n$=17);
$I_i$ and $R_i$ are the intensities of reflections $i=hkl$ of textured and textureless specimens.

As a quantitative criterion of texture, the Kearns coefficients (*f*-factors) were used, which are usually used as
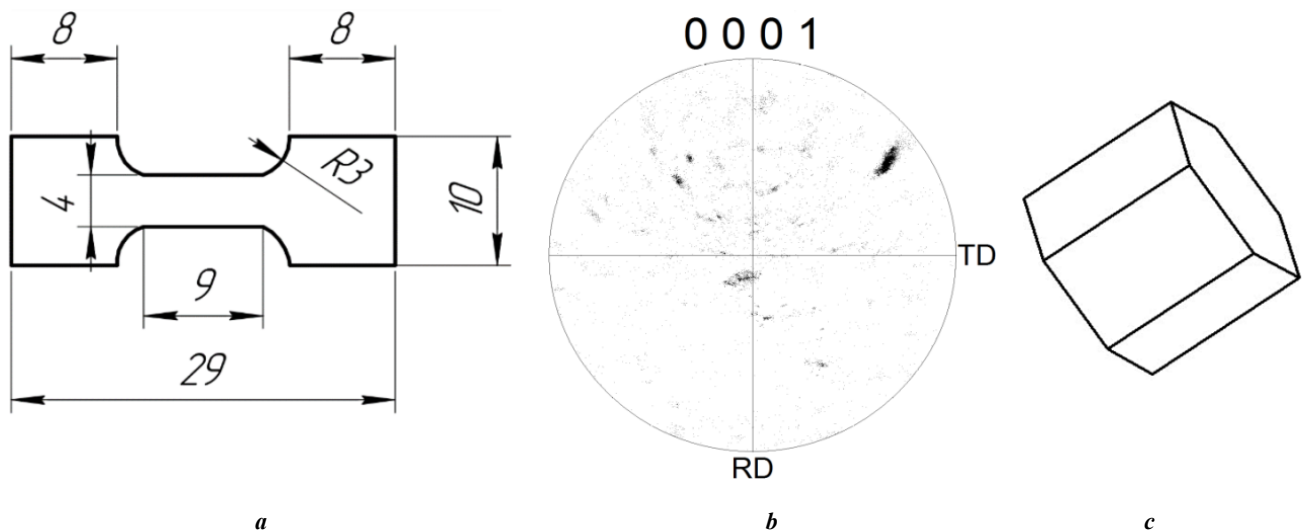


*Fig. 1. Drawing of single crystal magnesium tensile specimens (**a**),*
*steriographic projection of the <0001> crystallographic direction (**b**)*
*and lattice orientation against the longitudinal axis (**c**)*
***Рис. 1.** Чертеж образцов монокристалла магния на растяжение (**a**),*
*стериографическая проекция кристаллографического направления <0001> (**b**)*
*и ориентация решетки по отношению к продольной оси (**c**)*

texture parameters in relation to Zr and Ti [19] alloys. The Kearns coefficients are estimated from the inverse pole figures for the $X$ direction of the specimen:

$$f_x = \sum_{i=1}^{n} Ai\, P_i^x f_i, \qquad (2)$$

where $i=hkl$;
$\gamma_i$ is the angle between the normal to $(hkl)$ and the $c$-axis of the hcp magnesium lattice.

The Kearns coefficient ($f_i$) varies from zero for any directions in the basal plane to unity for the normal to the basal plane ($c$-axis).

Moreover, the data on texture obtained as an inverse pole figure were used to calculate the Young's modulus in the direction for which this pole figure was obtained, taking into account the reference values of single-crystal moduli of the material. Young's moduli for hcp of crystals depend only on the $\gamma$ angle with the $c$-axis:

$$E\gamma = \left[S_{11} - \cos^2\gamma\left(2S_{11} - 2S_{13} - S_{44}\right) + \right.$$
$$\left. + \cos^4\gamma\left(S_{11} + S_{33} - 2S_{13} - S_{44}\right)\right]^{-1} \cdot \qquad (3)$$

Then the value of Young's modulus in an arbitrary $x$ direction can be determined from the relation

$$E_x = \sum_{i=1}^{n} P_i^x A_i E_i. \qquad (4)$$

The values of single-crystal compliance moduli for Mg are given in Table 1 [20].

To study the relationship between corrosion processes and the crystallographic directions of the magnesium crystal lattice, parallelepiped-shaped samples were cut from a single crystal using EDM cutting. The orientation of certain faces of the parallelepipeds was close to the orientations of the (0001), $(10\bar{1}0)$, $(2\bar{1}\bar{1}0)$, and $(10\bar{1}1)$ crystallographic planes, respectively, for samples numbered 1, 2, 3, and 4. Before testing, the working faces of the samples were polished sequentially using alcohol diamond suspensions with particle sizes of 3, 1, and 0.25 µm, and then subjected to ion polishing in a flow of ionised argon using a Hitachi IM4000 Plus machine (Japan). After that, using EBSD method, the crystallographic orientation of the working surface of the samples was precisely determined (shown in the inverse pole figure in Fig. 2).

Corrosion tests of samples 1–4 of the magnesium single crystal were carried out using an original corrosion unit [21] for 72 h. During the test, only the area of the sample working surface limited by a sealing ring with an internal diameter of 4 mm was in contact with the corrosion solution. A physiological aqueous solution of 0.9 % NaCl was used as the corrosion medium. Maintaining the temperature in the cell at the level of 37±0.2 °C, as well as mixing the liquid, was ensured by circulating the corrosion solution using a peristaltic pump and a glass heat exchanger immersed in a thermostat tank with distilled water.

After testing, corrosion products were removed from the sample surface by immersing the sample for 2 min in a standard aqueous solution of 20 % $CrO_3$ + 1 % $AgNO_3$. Then, the samples were washed with alcohol, dried with compressed air, and the surface of the single-crystal samples damaged by corrosion was examined using a LEXT OLS4000 confocal laser scanning microscope (CLSM) (Olympus, Japan). Imaging was performed at a magnification of 400× with a scanning step along the $Z$-axis of 0.8 µm. A panoramic image of 6×6 frames was built for the entire sample. The size of one frame was 640×640 µm. In order to remove optical noise after imaging, a digital

***Table 1.** Values of the ductility moduli of Mg [21]*
***Таблица 1.** Значения модулей податливости Mg [21]*

| Unit of measurement / direction | $S_{11}$ | $S_{12}$ | $S_{13}$ | $S_{33}$ | $S_{44}$ |
|---|---|---|---|---|---|
| $10^{-2}$ GPa$^{-1}$ | 2.21 | −0.78 | −0.49 | 1.99 | 6.03 |
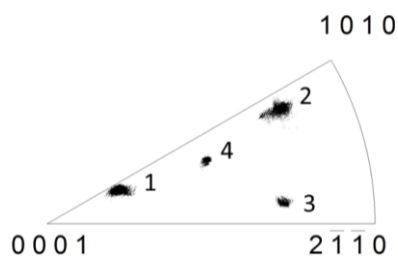


***Fig. 2.** Inverse pole figure indicating the crystallographic orientation*
*of the working surface of magnesium single crystal samples 1–4*
***Рис. 2.** Обратная полюсная фигура с указанием кристаллографической ориентации*
*рабочей поверхности образцов монокристалла магния 1–4*

pre-measurement filter built into the microscope software was applied to all the obtained images. After filtering, taking the surface of the sample that was not in contact with the corrosive environment as the base reference point, the volume of metal lost in the area of the sample damaged by corrosion was measured. The corrosion rate was determined by formula using CLSM data [22]:

$$P = \frac{87600 \cdot V}{S \cdot t} \text{ (mm/year)}, \qquad (5)$$

where $V$ is the volume of lost metal;
$S$ is the area of the sample;
$t$ is the test time.

## RESULTS

### Texture study

Fig. 3 a, 3 b show X-ray diffraction patterns of a magnesium single crystal indicating that it is indeed a single crystal. Additional confirmation of this is provided by the results of recording rocking curves (Fig. 3 c), according to which the block misorientation value $\Delta\alpha$ is 0.8 and 1.8°, indicating very low fragmentation of the subgrain structure.

Tables 2 and 3 show the results of texture intensity assessment for the single crystal, which correspond to the X-ray diffraction patterns obtained for the basal and prismatic faces (Fig. 3 a and 3 b), respectively.

The Kearns coefficient for normals to the basal face is 0.81, which is impossible to obtain on polycrystals. The Young's modulus is 48.6 GPa (Table 2), which, according to equation (3), is achieved at angles with the $c$-axis of 15°. For the lateral prismatic plane $(1\bar{1}00)$ (Fig. 3 b), the Young's modulus is 45.3 GPa, the Kearns coefficient is 0.04, which corresponds to this orientation. The Kearns coefficient is zero for the prismatic plane.

### Mechanical tests

#### Compression test

The compression test of parallelepiped-shaped magnesium single crystal samples was carried out in three mutually perpendicular orientation directions: $<0001>$, $<1\bar{1}00>$, and $<11\bar{2}0>$. The choice and sequence of the crystallographic direction of external stress application were made in the order from suppression to gradual activation of deformation systems (slip and twinning) with the lowest shear stresses. For the $<0001>$ direction, the easy slip systems in the basal plane are completely blocked, and slip along
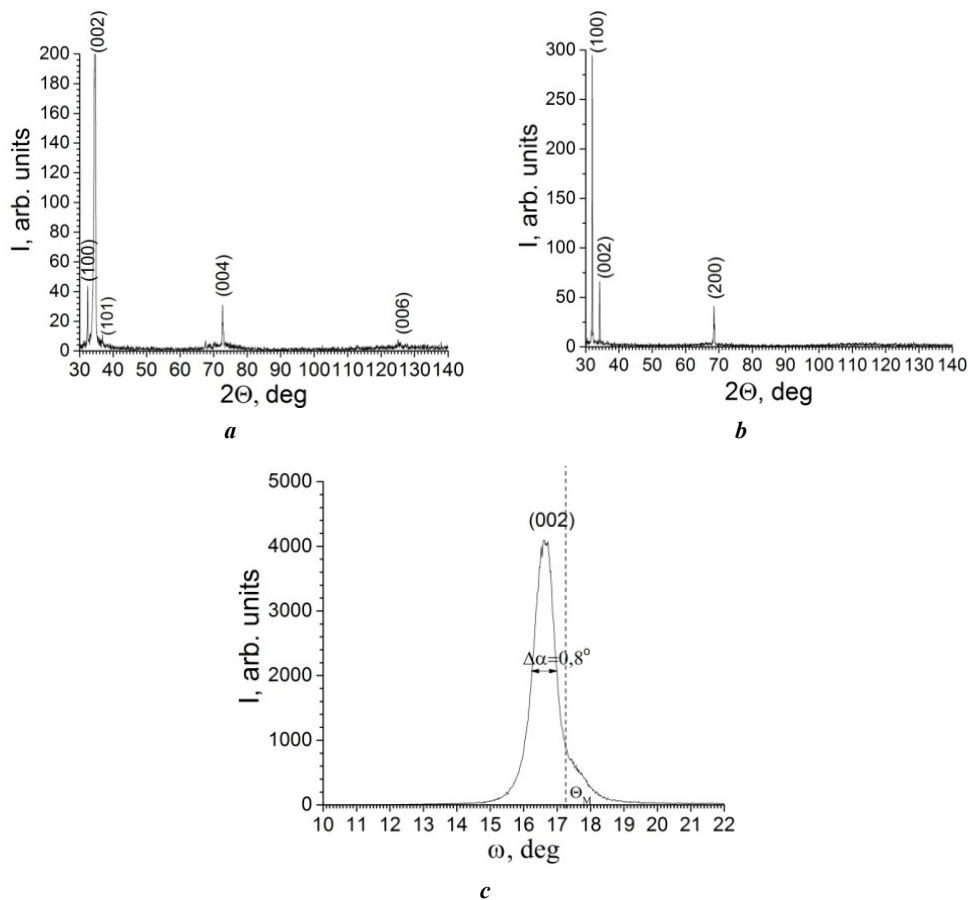


*Fig. 3. X-ray diffraction patterns of faces parallel to: **a** – basal (0001) and **b** – prismatic* $(1\bar{1}00)$ *planes;*
*c – ω-scans of a face parallel to the (0001) basal plane*
***Рис. 3.** Рентгенограммы граней, параллельных: **a** – базисной (0001) и **b** – призматической* $(1\bar{1}00)$ *плоскости;*
*c – ω-сканирования грани, параллельной базисной плоскости (0001)*

***Table 2.*** *Scheme for calculating the Young's modulus and the Kearns coefficient (f-factor) for the basal face*
***Таблица 2.*** *Схема расчета модуля Юнга и коэффициента Кернса (f-фактор) для базисной грани*

| *hkl* | *γ*, degree | $E_{hkl}$, GPa | *f* | $P_{hkl}$ | $A_{hkl}$ | $P_{hkl}xAxE_{hkl}$ | $P_{hkl}xf_{hkl}$ |
|---|---|---|---|---|---|---|---|
| 100 | 90.0 | 45.2 | 0.00 | 1.29 | 0.044 | 2.6 | 0.00 |
| 002 | 0.0 | 50.3 | 1.00 | 48.33 | 0.016 | 38.9 | 0.77 |
| 101 | 61.9 | 43.3 | 0.22 | 0.11 | 0.044 | 0.2 | 0.00 |
| 102 | 43.2 | 43.4 | 0.53 | 0.00 | 0.059 | 0.0 | 0.00 |
| 110 | 90.0 | 45.2 | 0.00 | 0.00 | 0.027 | 0.0 | 0.00 |
| 103 | 32.0 | 45.0 | 0.72 | 0.00 | 0.048 | 0.0 | 0.00 |
| 112 | 58.4 | 43.1 | 0.27 | 0.42 | 0.039 | 0.7 | 0.00 |
| 201 | 75.1 | 44.5 | 0.07 | 0.51 | 0.058 | 1.3 | 0.00 |
| 104 | 25.1 | 46.4 | 0.82 | 0.00 | 0.042 | 0.0 | 0.00 |
| 203 | 51.3 | 43.0 | 0.39 | 0.00 | 0.050 | 0.0 | 0.00 |
| 120 | 90.0 | 45.2 | 0.00 | 0.00 | 0.051 | 0.0 | 0.00 |
| 121 | 78.6 | 44.8 | 0.04 | 0.00 | 0.120 | 0.0 | 0.00 |
| 114 | 39.1 | 43.8 | 0.60 | 0.00 | 0.096 | 0.0 | 0.00 |
| 122 | 68.1 | 43.8 | 0.14 | 0.00 | 0.103 | 0.0 | 0.00 |
| 105 | 20.6 | 47.4 | 0.88 | 0.00 | 0.062 | 0.0 | 0.00 |
| 123 | 58.8 | 43.1 | 0.27 | 1.11 | 0.104 | 5.0 | 0.030 |
| 302 | 70.4 | 44.1 | 0.11 | 0.00 | 0.039 | 0.0 | 0.00 |
|  |  |  |  |  |  | $E_{ND}$=48.6 GPa | $F_{ND}$=0.81 |

*Note. hkℓ is Miller index describing the planes of the crystal lattice;*
*γ is an angle between the normal to (hkl) and the c-axis of the hpc magnesium lattice;*
*f is Kearns coefficient;*
*$E_{hkl}$ is Young's modulus in the hkl direction;*
*$P_{hkl}$ is pole density of reflections;*
*$A_{hkl}$ is the ratio of the surface area of a stereographic triangle around the normal (i=hkl) limited by large circles dividing in half the angular distances between adjacent normals;*
*$E_{ND}$ is Young's modulus in the direction of the normal to the rolling plane;*
*$F_{ND}$ is Kearns coefficient in the direction of the normal to the rolling plane.*

***Table 3.*** *Calculation scheme for Young's modulus and Kearns coefficient (f-factor) for a prismatic face*
***Таблица 3.*** *Схема расчета модуля Юнга и коэффициента Кернса (f-фактор) для призматической грани*

| *hkl* | *γ*, degree | $E_{hkl}$, GPa | *f* | $P_{hkl}$ | $A_{hkl}$ | $P_{hkl}xAxE_{hkl}$ | $P_{hkl}xf_{hkl}$ |
|---|---|---|---|---|---|---|---|
| 100 | 90.0 | 45.2 | 0.00 | 21.71 | 0.044 | 43.2 | 0.00 |
| 002 | 0.0 | 50.3 | 1.00 | 2.48 | 0.016 | 2.0 | 0.04 |
| 101 | 61.9 | 43.3 | 0.22 | 0.04 | 0.044 | 0.1 | 0.00 |
| 102 | 43.2 | 43.4 | 0.53 | 0.00 | 0.059 | 0.0 | 0.00 |
| 110 | 90.0 | 45.2 | 0.00 | 0.00 | 0.027 | 0.0 | 0.00 |
| 103 | 32.0 | 45.0 | 0.72 | 0.00 | 0.048 | 0.0 | 0.00 |

| 112 | 58.4 | 43.1 | 0.27 | 0.00 | 0.039 | 0.0 | 0.00 |
|-----|------|------|------|------|-------|-----|------|
| 201 | 75.1 | 44.5 | 0.07 | 0.00 | 0.058 | 0.0 | 0.00 |
| 104 | 25.1 | 46.4 | 0.82 | 0.00 | 0.042 | 0.0 | 0.00 |
| 203 | 51.3 | 43.0 | 0.39 | 0.00 | 0.050 | 0.0 | 0.00 |
| 120 | 90.0 | 45.2 | 0.00 | 0.00 | 0.051 | 0.0 | 0.00 |
| 121 | 78.6 | 44.8 | 0.04 | 0.00 | 0.120 | 0.0 | 0.00 |
| 114 | 39.1 | 43.8 | 0.60 | 0.00 | 0.096 | 0.0 | 0.00 |
| 122 | 68.1 | 43.8 | 0.14 | 0.00 | 0.103 | 0.0 | 0.00 |
| 105 | 20.6 | 47.4 | 0.88 | 0.00 | 0.062 | 0.0 | 0.00 |
| 123 | 58.8 | 43.1 | 0.27 | 0.00 | 0.104 | 0.0 | 0.00 |
| 302 | 70.4 | 44.1 | 0.11 | 0.00 | 0.039 | 0.0 | 0.00 |
| | | | | | | $E_{ND}$=45.3 GPa | $F_{ND}$=0.04 |

*Note. hkℓ is Miller index describing the planes of the crystal lattice;*
*γ is an angle between the normal to (hkl) and the c-axis of the hpc magnesium lattice;*
*f is Kearns coefficient;*
*$E_{hkl}$ is Young's modulus in the hkl direction;*
*$P_{hkl}$ is pole density of reflections;*
*$A_{hkl}$ is the ratio of the surface area of a stereographic triangle around the normal (i=hkl) limited by large circles dividing in half the angular distances between adjacent normals;*
*$E_{ND}$ is Young's modulus in the direction of the normal to the rolling plane;*
*$F_{ND}$ is Kearns coefficient in the direction of the normal to the rolling plane.*

a limited number of pyramidal systems outside the basal plane is greatly hindered. The <1$\bar{1}$00> and <11$\bar{2}$0> configurations are close to each other in the implementation of slip of prismatic and pyramidal planes in the directions lying in the basal plane and twinning of the "stretching" type, but differ in their more favourable arrangement for activation for the <11$\bar{2}$0> direction. Fig. 4 shows three diagrams of compression tests (one for each orientation) in the "Stress (engineering) – Strain (engineering)" coordinates, where the compressive stresses are conventionally given in the positive direction.

Analysis of the diagrams displayed in Fig. 4 shows that, as expected, the orientation of the single crystal to the direction of the applied uniaxial load has a decisive influence on the type of diagrams, or more precisely, on the mechanisms of plastic deformation realised in certain crystallographic directions. This influence has been well studied in [16–18], so here we will only note the following. When testing samples in all three directions, the Schmid factor for basal slip is zero, so deformation can be carried out by twinning or <c+a> slip.

When testing samples in the <0001> direction, the {10$\bar{1}$2}<10$\bar{1}$1> light tensile twinning cannot act, while the maximum possible strain hardening and rapid exhaustion of the possibility of plastic deformation occur. A similar effect for this orientation was observed in [18] and interpreted as <c+a> slip.

When testing samples in the <1$\bar{1}$00> direction, first there is a stage of deformation with low strain hardening, after which the loading curve rushes sharply upward, and its appearance becomes completely identical to the previous case. This can be easily explained by the action of {10$\bar{1}$2}<10$\bar{1}$1> slight tensile twinning, which for this orientation produces a transfer of the orientation of the single crystal to an orientation located 3° from the c-axis. In accordance with the magnitude of the shear for this type of twinning, a deformation of ~6 % is required for complete re-twinning of all grains, which is observed for the stage with low strain hardening (Fig. 4). After this, compression occurs in the <0001> direction, respectively, similar to the previous case.

When testing samples in the <11$\bar{2}$0> direction, {10$\bar{1}$2}<10$\bar{1}$1> light tensile twinning is also active, but unlike the previous case, the orientation of the twinned single crystal is characterized by a deviation from the c-axis by an angle of ~30°. Such an orientation is favourable for basal slip, which for magnesium has a minimum value of the critical shear stress. However, a high level of plasticity is realized stimulating the formation of a texture that coincides with the slip plane for compression, i. e., a basal texture is formed. Therefore, with increasing deformation, the compression axis approaches the c-axis, which reduces the Schmid factor for basal slip and, accordingly, increases the flow stress.

The mechanical properties of a single crystal of pure magnesium found during compression testing in different directions are given in Table 4.
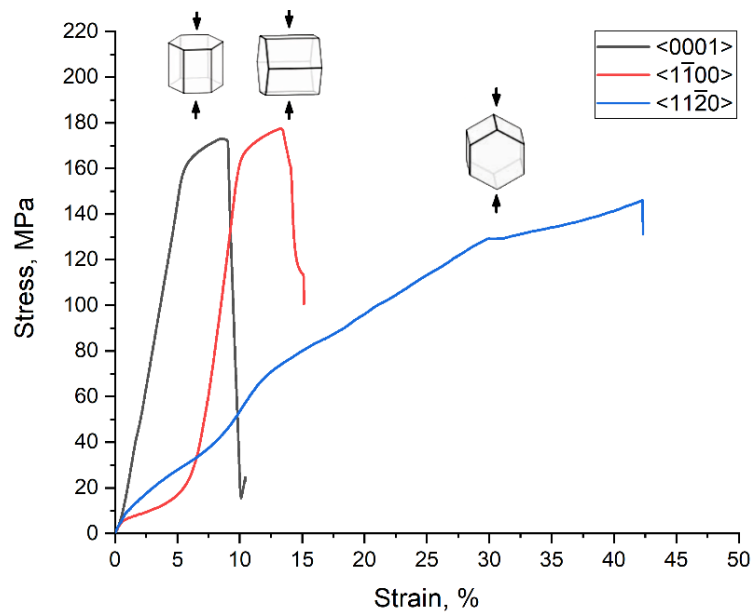
***Fig. 4.*** *Diagrams of compression test of samples of pure magnesium single crystal for three orientations*
***Рис. 4.*** *Диаграммы испытаний образцов монокристалла чистого магния*
*на сжатие для трех ориентаций*

### Tension test

The diagram of the tensile test of a magnesium single crystal in the $<1\bar{1}00>$ direction is shown in Fig. 5. This direction of loading the single crystal by activation of the deformation systems of the hcp crystal lattice is characterised by high activity of basal slip and "tensile" twinning and, to a lesser extent, slip in prismatic and pyramidal planes. The initial strengthening occurs due to the system of the easiest basal slip for an hcp crystal, which is interrupted by the activation of the "tensile" twinning system at a stress of 32.5 MPa and 2 % deformation, forming a "tooth" in the diagram. The subsequent sharp drop in stress is probably associated with the reorientation of the lattice during twinning to easy slip, i. e. the Schmid factor for basal slip increases, due to which the subsequent deformation occurs at a lower stress. In the range of deformation from 4 to 11 %, a slight strain hardening supported by slight sliding occurs, but after 12 % deformation, a stepwise decrease in

strength is observed, which is caused by filling the volume of the sample with intersecting secondary twins with the formation of macrodefects (cracks) at the intersection boundaries. In contrast to compression tests, this direction demonstrates significantly greater plasticity.

Certain standard mechanical properties are given in Table 4.

### Corrosion tests

The study of the surface of single crystal samples damaged by corrosion was carried out using CLSM with the reconstruction of surface profiles based on the areas most damaged by corrosion (Fig. 6).

Analysis of the obtained images and profile diagrams indicates, firstly, that the nature of corrosion damage really strongly depends on the crystallographic orientation of the working surface of the single crystal, and secondly, that the (0001) (Fig. 6 a, 6 b) and $(2\bar{1}\bar{1}0)$ (Fig. 6 e, 6 f) planes are characterised by uniform corrosion, which is evidenced by

***Table 4.*** *Mechanical properties of magnesium single crystal*
***Таблица 4.*** *Механические характеристики монокристалла магния*

| No. | Direction of application of load | Offset yield stress, MPa | Ultimate tensile strength, MPa | Percentage elongation (compression), % |
|-----|----------------------------------|--------------------------|--------------------------------|----------------------------------------|
| 1 | $<0001>$ compression | 2.55±0.05 | 170±4 | 7.5±0.5 |
| 2 | $<1\bar{1}00>$ compression | 2.6±0.05 | 175±5 | 12.5±0.8 |
| 3 | $<11\bar{2}0>$ compression | 2.65±0.05 | 145±4 | 42±5 |
| 4 | $<10\bar{1}1>$ tension | 8.8±0.2 | 33±4 | 34±3 |
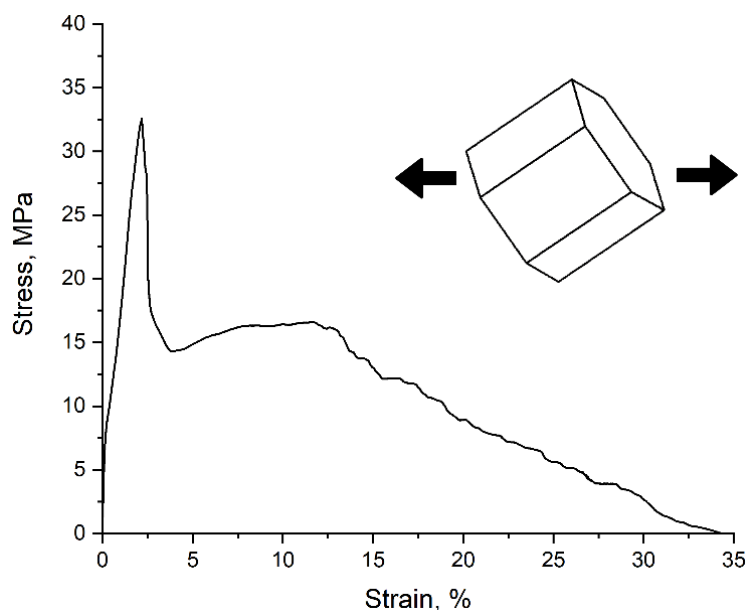
**Fig. 5.** *Diagram of the test of a pure magnesium single crystal sample for uniaxial tension in the* $<10\overline{1}1>$ *direction*
***Рис. 5.*** *Диаграмма испытания образца монокристалла чистого магния*
*на одноосное растяжение в направлении* $<10\overline{1}1>$

significant depth fluctuations along the entire length of the profile diagrams, while the $(10\overline{1}0)$ (Fig. 6 c, 6 d) and $(10\overline{1}1)$ (Fig. 6 g, 6 h) planes, on the contrary, are characterised by localised corrosion with a pit depth of up to 30 μm with minimal damage to the surface between the pits.

According to confocal microscopy data, the corrosion rate based on 72-hour tests was 0.51±0.04, 0.76±0.08, 0.71±0.07, and 0.98±0.10 mm/year for (0001), $(10\overline{1}0)$, $(2\overline{11}0)$, and $(10\overline{1}1)$ planes, respectively.

**DISCUSSION**

According to the obtained results (Table 2), the Young's modulus for the basal plane is 48.6 GPa, which is achieved at angles with the *c*-axis of 15°, which is slightly greater than the Young's modulus for the lateral prismatic plane $(1\overline{1}00)$ – 45.3 GPa.

When testing samples in the $<0001>$ direction, the maximum possible strain hardening occurs, which is associated with the action of $<c+a>$ slip. Compression in the $<1\overline{1}00>$ direction is characterised by low strain hardening at the initial stage as a result of the action of slight tensile $\{10\overline{1}2\}<10\overline{1}1>$ twinning, which for this orientation transfers the single crystal orientation of all grains into an orientation spaced away from the c-axis by 3°. This requires a deformation of ~6 %, which is observed experimentally. After this, compression occurs in the $<0001>$ direction. Under compression in $<11\overline{2}0>$, slight tensile $\{10\overline{1}2\}<10\overline{1}1>$ twinning is also active, but the orientation of the twinned single crystal is characterised by a deviation from the c-axis by an angle of ~30°, and such an orientation is favourable for basal slip, which provides high plasticity. With increasing deformation,

the compression axis approaches the *c*-axis, which reduces the Schmid factor for basal slip and, accordingly, increases the flow stress.

The corrosion process on the surface of magnesium single crystals can be conditionally divided into two components: uniform and localised. The first involves complete dissolution of the surface layer to a certain depth, and the second is the formation of local pits. It is illustrated by the profile diagrams of the corroded surface of differently oriented surfaces of a magnesium single crystal, shown in Fig. 6. Since part of the working surface of the sample was not in contact with the corrosive environment, it was taken as the zero corrosion level (indicated by a dotted line in Fig. 6 b, 6 d, 6 f, 6 h). The dashed line in Fig. 6 b, 6 d, 6 f, 6 h conventionally denotes the maximum depth of uniform corrosion. From Fig. 6, it follows that the minimum depth $h_{un}$ (rate) of uniform corrosion corresponds to the (0001) plane (~6.5 μm, Fig. 6 b), for all the others, it has close values: ~10, 12.5 and 11.5 μm for the $(10\overline{1}0)$, $(2\overline{11}0)$, and $(10\overline{1}1)$ planes, respectively (Fig. 6 d, 6 f, 6 h). In this case, the maximum pit depth $h_{loc}$ took values of 25, 35, 10, and 22 μm for the (0001), $(10\overline{1}0)$, $(2\overline{11}0)$, and $(10\overline{1}1)$ planes, respectively. According to these results, it becomes obvious that in a magnesium single crystal, the $(10\overline{1}0)$ plane has the greatest tendency to pitting (localised) corrosion (Fig. 6 d), and the $(2\overline{11}0)$ plane has the least tendency (Fig. 6 f). A theoretical explanation for this phenomenon has yet to be found.

Based on the above, the previously given values of corrosion rates of 0.51±0.04, 0.76±0.08, 0.71±0.07, and 0.98±0.10 mm/year for the working (0001), $(10\overline{1}0)$, $(2\overline{11}0)$, and $(10\overline{1}1)$ surfaces, respectively, are the result of superposition of uniform and local corrosion rates.

*a*



*b*



*c*



*d*



*e*



*f*



*g*



*h*
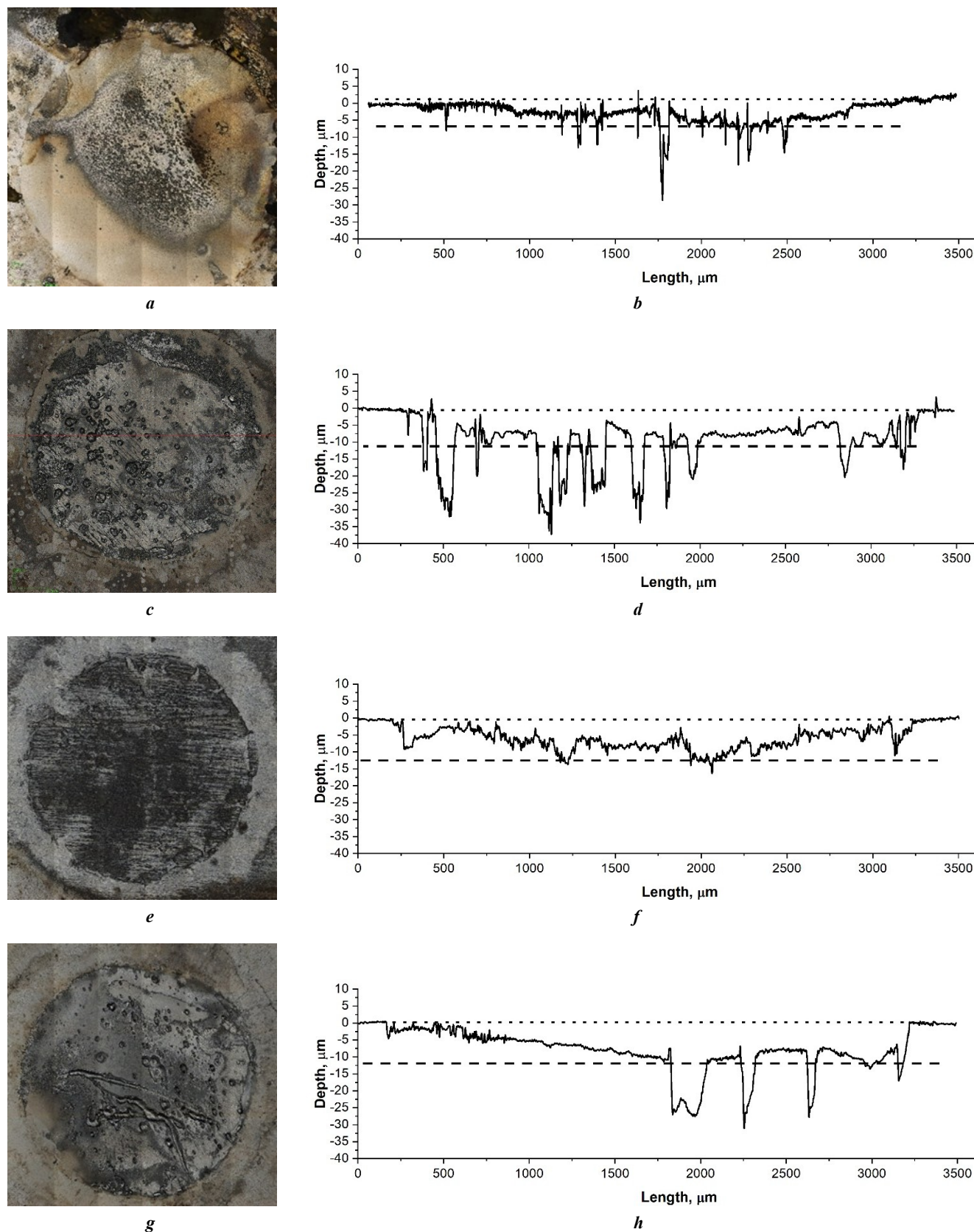
***Fig. 6.*** *Image of corroded surface (**a**, **c**, **e**, **g**) and corresponding profile diagrams (**b**, **d**, **f**, **h**)*
*for working* $(0001)$ *(**a**, **b**), $(10\overline{1}0)$ (**c**, **d**), $(2\overline{1}\overline{1}0)$ (**e**, **f**), and $(10\overline{1}1)$ (**g**, **h**) surfaces according to CLSM data.*
*Dotted line – zero level; dashed line – maximum level of uniform corrosion*

***Рис. 6.*** *Изображение прокорродированной поверхности (**a**, **c**, **e**, **g**) и соответствующие им профилограммы (**b**, **d**, **f**, **h**)*
*для рабочих поверхностей* $(0001)$ *(**a**, **b**), $(10\overline{1}0)$ (**c**, **d**), $(2\overline{1}\overline{1}0)$ (**e**, **f**) и $(10\overline{1}1)$ (**g**, **h**) по данным КЛСМ.*
*Мелкий пунктир – нулевой уровень; средний пунктир – максимальный уровень равномерной коррозии*

It should be noted that, according to the obtained data, the (0001) plane has the lowest average corrosion rate, which is in good agreement with the results of most works by other researchers [11; 15]. At the same time, a detailed analysis of the surface relief shows that the low value of the average corrosion rate of this plane is primarily caused by the low rate of uniform corrosion, while the depth of local corrosion damage in this plane is higher than, for example, in the $(2\bar{1}\bar{1}0)$ and $(10\bar{1}1)$ planes. Thus, at a significantly lower average corrosion rate, the (0001) plane has a rather high tendency to local corrosion compared to other crystallographic planes. It should be considered when designing the microstructure and crystallographic texture of semi-finished and finished products made of magnesium alloys that are planned to be used in contact with aggressive environments. Local corrosion is one of the most dangerous forms of degradation of metallic materials in an aggressive environment, since it can lead to a rapid local decrease in the cross-section of a part and even the occurrence of through damage in thin-walled products. Moreover, corrosion pits formed as a result of the development of this type of corrosion can serve as crack nuclei in stress corrosion cracking. At the same time, until now, corrosion studies on magnesium single crystals have provided data only on the integral assessment of the corrosion rate, which, as shown in this paper, do not always provide a sufficiently complete view of the corrosion resistance of a particular crystallographic plane.

**CONCLUSIONS**

1. The anisotropy of the elastic properties of a magnesium single crystal is insignificant: Young's moduli for the basal and pyramidal directions are 48.6 and 45.3 GPa, respectively, i. e. they differ by less than 7 %. At the same time, the Kearns coefficient, which is a quantitative criterion of texture, is 20 times higher for the basal plane (0.81) than for the pyramidal plane (0.04).

2. The strong anisotropy of the mechanical properties of a pure magnesium single crystal is caused by the structure of the hcp crystal lattice and a complex combination of the work of crystalline deformation systems of slip and twinning, which differ in configuration. Pure single-crystal magnesium demonstrates a wide range of mechanical parameters: yield strength by 3.5 times, ultimate strength by 5 times, and plasticity by 5.6 times with variations in the direction of application of load to a pure magnesium single crystal.

3. The corrosion rate in an aqueous solution of 0.9 % NaCl on a 72-h basis for the (0001), $(10\bar{1}0)$, $(2\bar{1}\bar{1}0)$, and $(10\bar{1}1)$ surfaces of magnesium single crystals was 0.51±0.04, 0.76±0.08, 0.71±0.07, and 0.98±0.10 mm/year, respectively. At the same time, the $(2\bar{1}\bar{1}0)$ plane experiences only uniform corrosion, and the (0001) plane experiences uniform corrosion with minor localised corrosion; localised corrosion is most intense in the $<10\bar{1}0>$ direction, and the maximum intensity of the combination of localised and uniform corrosion is in the $<10\bar{1}1>$ direction.

**REFERENCES**

1. Aljihmani L., Alic L., Boudjemline Y., Hijazi Z.M., Mansoor B., Serpedin E., Qaraqe K. Magnesium-Based Bioresorbable Stent Materials: Review of Reviews. *Journal of Bio- and Tribo-Corrosion*, 2019, vol. 5, article number 26. DOI: 10.1007/s40735-019-0216-x.

2. Gu Xue-Nan, Zheng Yu-Feng. A review on magnesium alloys as bio-degradable materials. *Frontiers of Materials Science in China*, 2010, vol. 4, no. 2, pp. 111–115. DOI: 10.1007/s11706-010-0024-1.

3. Song Guangling, Atrens A. Understanding Magnesium Corrosion – A Framework for Improved Alloy Performance. *Advanced Engineering Materials*, 2003, vol. 5, no. 12, pp. 837–858. DOI: 10.1002/adem.200310405.

4. Schmutz P., Guillaumin V., Lillard R.S., Lillard J.A., Frankel G.S. Influence of Dichromate Ions on Corrosion Processes on Pure Magnesium. *Journal of the Electrochemical Society*, 2003, vol. 150, no. 4, pp. B99–B110. DOI: 10.1149/1.1554721.

5. Betsofen S.Y., Osintsev O.E., Grushin I.A., Petrov A.A., Speranskii K.A. Influence of alloying elements on the deformation mechanism and the texture of magnesium alloys. *Russian Metallurgy (Metally)*, 2019, vol. 2019, no. 4, pp. 346–360. DOI: 10.1134/S0036029519040049.

6. Betsofen S.Y., Osintsev O.E., Grushin I.A., Petrov A.A., Speranskii K.A. Texture and anisotropy of the mechanical properties of magnesium alloys. *Russian Metallurgy (Metally)*, 2019, vol. 2019, no. 4, pp. 361–373. DOI: 10.1134/S0036029519040050.

7. Sabbaghian M., Mahmudia R., Shin K.S. Effect of texture and twinning mechanical properties and corrosion behavior of an extruded biodegradable Mg–4Zn alloy. *Journal of Magnesium and Alloys*, 2019, vol. 7, no. 4, pp. 707–716. DOI: 10.1016/j.jma.2019.11.001.

8. Song Guang-Ling, Mishra R., Xu Zhen Qing. Crystallographic orientation and electrochemical activity of AZ31 Mg alloy. *Electrochemistry Communications*, 2010, vol. 12, no. 8, pp. 1009–1012. DOI: 10.1016/j.elecom.2010.05.011.

9. Jiang Bin, Xiang Qing, Atrens A., Song Jiangfeng, Pan Fusheng. Influence of crystallographic texture and grain size on the corrosion behaviour of as-extruded Mg alloy AZ31 sheets. *Corrosion Science*, 2017, vol. 126, pp. 374–380. DOI: 10.1016/j.corsci.2017.08.004.

10. Xin Renlong, Li Bo, Li Ling, Liu Qing. Influence of texture on corrosion rate of AZ31 Mg alloy in 3.5 wt.% NaCl. *Materials & Design*, 2011, vol. 32, no. 8-9, pp. 4548–4552. DOI: 10.1016/j.matdes.2011.04.031.

11. Liu Ming, Qiu Dong, Zhao Ming-Chun, Song Guangling, Atrens A. The effect of crystallographic orientation on the active corrosion of pure magnesium. *Scripta Materialia*, 2008, vol. 58, no. 5, pp. 421–424. DOI: 10.1016/j.scriptamat.2007.10.027.

12. Jian Quantong, Ma Xiumin, Zhang Kui, Li Yantao, Li Xinggang, Li Yongjun, Ma Minglong, Hou Baorong. Anisotropy of the crystallographic orientation and corrosion performance of high-strength AZ80 Mg alloy. *Journal of Magnesium and Alloys*, 2015, vol. 3, no. 4, pp. 309–314. DOI: 10.1016/j.jma.2015.11.002.

13. Gross A. *Theoretical Surface Science: A Microscopic Perspective*. Berlin, Springer Publ., 2003. 342 p. DOI: 10.1007/978-3-540-68969-0.

14. McCall C.R., Hill M.A., Lillard R.S. Crystallographic Pitting in Magnesium Single Crystals. *Corrosion Engineering Science and Technology*, 2005, vol. 40, pp. 337–343. DOI: 10.1179/174327805X66326.

15. Shin Kwang Seon, Bian Ming Zhe, Nam Nguyen Dang. Effects of Crystallographic Orientation on Corrosion Behavior of Magnesium Single Crystals. *JOM*, 2012, vol. 64, pp. 664–670. DOI: 10.1007/s11837-012-0334-0.

16. Wonsiewicz B.C., Backofen W.A. *Plasticity of magnesium crystals*. Massachusetts, Massachusetts Institute of Technology Publ., 1967. 57 p.

17. Kelley E.W., Hosford W.F. *Plane-Strain Compression of Magnesium and Magnesium Alloy Crystals*. 1968. 242 p.

18. Molodov K.D., Al-Samman T., Molodov D.A. On the Plasticity and Deformation Mechanisms in Magnesium Crystals. *Metals*, 2023, vol. 13, no. 4, article number 640. DOI: 10.3390/met13040640.

19. Dzunovich D.A., Betsofen S.Ya., Panin P.V. Methodological aspects of the quantitative texture analysis of HCP alloy (Ti, Zr) sheet semiproducts. *Russian Metallurgy (Metally)*, 2017, vol. 2017, no. 10, pp. 813–820. DOI: 10.1134/S0036029517100056.

20. Shalin R.E., Svetlov I.L., Kachanov E.B., Toloraiya V.N., Gavrilin O.S. *Monokristally nikelevykh zharoprochnykh splavov* [Single crystals of nickel heat-resistant alloys]. Moscow, Mashinostroenie Publ., 1997. 336 p. EDN: PIYTZX.

21. Merson E.D., Poluyanov V.A., Myagkikh P.N., Sergeev A.A., Merson D.L. Relationship between the anisotropy of corrosion properties of extruded AZ31 and ZK60 with crystallographic texture and volume distribution of second-phase particles. *Russian Journal of Non-ferrous Metals*, 2024, vol. 65, pp. 1–10. DOI: 10.1134/S1067821224600832.

22. Danilov V.A., Merson D.L. Quantitative estimation of the corrosion rate of metallic materials using confocal laser scanning microscopy. *Letters on Materials*, 2021, vol. 11, no. 3, pp. 291–297. DOI: 10.22226/2410-3535-2021-3-291-297.


**СПИСОК ЛИТЕРАТУРЫ**

1. Aljihmani L., Alic L., Boudjemline Y., Hijazi Z.M., Mansoor B., Serpedin E., Qaraqe K. Magnesium-Based Bioresorbable Stent Materials: Review of Reviews // Journal of Bio- and Tribo-Corrosion. 2019. Vol. 5. Article number 26. DOI: 10.1007/s40735-019-0216-x.

2. Gu Xue-Nan, Zheng Yu-Feng. A review on magnesium alloys as bio-degradable materials // Frontiers of Materials Science in China. 2010. Vol. 4. № 2. P. 111–115. DOI: 10.1007/s11706-010-0024-1.

3. Song Guangling, Atrens A. Understanding Magnesium Corrosion – A Framework for Improved Alloy Performance // Advanced Engineering Materials. 2003. Vol. 5. № 12. P. 837–858. DOI: 10.1002/adem.200310405.

4. Schmutz P., Guillaumin V., Lillard R.S., Lillard J.A., Frankel G.S. Influence of Dichromate Ions on Corrosion Processes on Pure Magnesium // Journal of the Electro-chemical Society. 2003. Vol. 150. № 4. P. B99–B110. DOI: 10.1149/1.1554721.

5. Бецофен С.Я., Осинцев О.Е., Грушин И.А., Петров А.А., Сперанский К.А. Влияние легирующих элементов на механизм деформации и текстуру магниевых сплавов // Деформация и разрушение материалов. 2018. № 8. С. 2–17. DOI: 10.31044/1814-4632-2018-8-2-17.

6. Бецофен С.Я., Осинцев О.Е., Грушин И.А., Петров А.А., Сперанский К.А. Закономерности формирования текстуры и анизотропии механических свойств магниевых сплавов // Деформация и разрушение материалов. 2018. № 9. С. 2–15. DOI: 10.31044/1814-4632-2018-9-2-15.

7. Sabbaghian M., Mahmudia R., Shin K.S. Effect of texture and twinning mechanical properties and corrosion behavior of an extruded biodegradable Mg–4Zn alloy // Journal of Magnesium and Alloys. 2019. Vol. 7. № 4. P. 707–716. DOI: 10.1016/j.jma.2019.11.001.

8. Song Guang-Ling, Mishra R., Xu Zhen Qing. Crystallographic orientation and electrochemical activity of AZ31 Mg alloy // Electrochemistry Communications. 2010. Vol. 12. № 8. P. 1009–1012. DOI: 10.1016/j.elecom.2010.05.011.

9. Jiang Bin, Xiang Qing, Atrens A., Song Jiangfeng, Pan Fusheng. Influence of crystallographic texture and grain size on the corrosion behaviour of as-extruded Mg alloy AZ31 sheets // Corrosion Science. 2017. Vol. 126. P. 374–380. DOI: 10.1016/j.corsci.2017.08.004.

10. Xin Renlong, Li Bo, Li Ling, Liu Qing. Influence of texture on corrosion rate of AZ31 Mg alloy in 3.5 wt.% NaCl // Materials & Design. 2011. Vol. 32. № 8-9. P. 4548–4552. DOI: 10.1016/j.matdes.2011.04.031.

11. Liu Ming, Qiu Dong, Zhao Ming-Chun, Song Guang-ling, Atrens A. The effect of crystallographic orientation on the active corrosion of pure magnesium // Scripta Materialia. 2008. Vol. 58. № 5. P. 421–424. DOI: 10.1016/j.scriptamat.2007.10.027.

12. Jian Quantong, Ma Xiumin, Zhang Kui, Li Yantao, Li Xinggang, Li Yongjun, Ma Minglong, Hou Baorong. Anisotropy of the crystallographic orientation and corrosion performance of high-strength AZ80 Mg alloy // Journal of Magnesium and Alloys. 2015. Vol. 3. № 4. P. 309–314. DOI: 10.1016/j.jma.2015.11.002.

13. Gross A. Theoretical Surface Science: A Microscopic Perspective. Berlin: Springer, 2003. 342 p. DOI: 10.1007/978-3-540-68969-0.

14. McCall C.R., Hill M.A., Lillard R.S. Crystallographic Pitting in Magnesium Single Crystals // Corrosion Engineering Science and Technology. 2005. Vol. 40. P. 337–343. DOI: 10.1179/174327805X66326.

15. Shin Kwang Seon, Bian Ming Zhe, Nam Nguyen Dang. Effects of Crystallographic Orientation on Corrosion Behavior of Magnesium Single Crystals // JOM. 2012. Vol. 64. P. 664–670. DOI: 10.1007/s11837-012-0334-0.

16. Wonsiewicz B.C., Backofen W.A. Plasticity of magnesium crystals. Massachusetts: Massachusetts Institute of Technology, 1967. 57 p.

17. Kelley E.W., Hosford W.F. Plane-Strain Compression of Magnesium and Magnesium Alloy Crystals. 1968. 242 p.

18. Molodov K.D., Al-Samman T., Molodov D.A. On the Plasticity and Deformation Mechanisms in Magnesium

Crystals // Metals. 2023. Vol. 13. № 4. Article number 640. DOI: 10.3390/met13040640.

19. Дзунович Д.А., Бецофен С.Я., Панин П.В. Методические аспекты количественного текстурного анализа листовых полуфабрикатов из ГПУ-сплавов (Ti, Zr) // Деформация и разрушение материалов. 2016. № 11. С. 8–16. EDN: XBFIED.

20. Шалин Р.Е., Светлов И.Л., Качанов Е.Б., Толораия В.Н., Гаврилин О.С. Монокристаллы никелевых жаропрочных сплавов. М.: Машиностроение, 1997. 336 с. EDN: PIYTZX.

21. Merson E.D., Poluyanov V.A., Myagkikh P.N., Sergeev A.A., Merson D.L. Relationship between the anisotropy of corrosion properties of extruded AZ31 and ZK60 with crystallographic texture and volume distribution of second-phase particles // Russian Journal of Non-ferrous Metals. 2024. Vol. 65. P. 1–10. DOI: 10.1134/S1067821224600832.

22. Данилов В.А., Мерсон Д.Л. Количественная оценка скорости коррозии металлических материалов с помощью конфокальной лазерной сканирующей микроскопии // Письма о материалах. 2021. Т. 11. № 3. С. 291–297. DOI: 10.22226/2410-3535-2021-3-291-297.

# Механическая и коррозионная анизотропия монокристалла магния

*Мерсон Дмитрий Львович**[1,3], доктор физико-математических наук, профессор,
директор НИИ прогрессивных технологий
*Бецофен Сергей Яковлевич*[2,4], доктор технических наук, профессор, профессор кафедры
«Технологии и системы автоматизированного проектирования металлургических процессов»
*Мерсон Евгений Дмитриевич*[1,5], кандидат физико-математических наук,
старший научный сотрудник НИИ прогрессивных технологий
*Полуянов Виталий Александрович*[1,6], кандидат технических наук,
младший научный сотрудник НИИ прогрессивных технологий
*Мягких Павел Николаевич*[1,7], кандидат технических наук,
младший научный сотрудник НИИ прогрессивных технологий
*Данюк Алексей Валериевич*[1,8], кандидат физико-математических наук,
старший научный сотрудник НИИ прогрессивных технологий
*Данилов Владимир Алексеевич*[1,9], кандидат технических наук,
младший научный сотрудник НИИ прогрессивных технологий
*Максименко Екатерина Игоревна*[2], аспирант
*Брилевский Александр Игоревич*[1,10], кандидат технических наук,
младший научный сотрудник НИИ прогрессивных технологий

[1]*Тольяттинский государственный университет, Тольятти (Россия)*
[2]*Московский авиационный институт, Москва (Россия)*

***E-mail:** d.merson@tltsu.ru

[3]ORCID: https://orcid.org/0000-0001-5006-4115
[4]ORCID: https://orcid.org/0000-0003-0931-2839
[5]ORCID: https://orcid.org/0000-0002-7063-088X
[6]ORCID: https://orcid.org/0000-0002-0570-2584
[7]ORCID: https://orcid.org/0000-0002-7530-9518
[8]ORCID: https://orcid.org/0000-0002-7352-9947
[9]ORCID: https://orcid.org/0000-0001-5099-6940
[10]ORCID: https://orcid.org/0000-0002-5780-6094

*Аннотация:* Магний и его сплавы относятся к перспективным материалам для применения в медицине в связи с их способностью безопасно растворяться в организме человека. Однако скорость растворения биорезорбируемых имплантатов должна находиться в достаточно узком диапазоне. Сложность обеспечения этого условия состоит в том, что на коррозионный процесс в магниевых сплавах оказывают влияние очень многие факторы, в том числе естественная (монокристальная) и технологическая (схема получения) анизотропия. Путем проведения технологических операций по термомеханической обработке можно контролировать процесс формирования текстуры полуфабриката и искусственно создавать преимущественную ориентацию кристаллитов в структуре магниевых сплавов и таким образом управлять их коррозионной стойкостью. Для этого нужны точные знания о связи коррозионных процессов с определенными кристаллографическими направлениями, которые наиболее надежно можно получить в экспериментах на монокристаллах. В настоящей работе впервые на одном и том же монокристалле магния проведены механические (на сжатие и растяжение) и коррозионные испытания на образцах, имеющих различную кристаллографическую ориентацию. В качестве количественного критерия естественной текстуры использовали коэффициенты Кернса, рассчитанные по рентгенограммам граней образцов монокристалла по методу обратных полюсных фигур. Испытания образцов на сжатие проводили в направлениях $< 0001 >$, $< 1\bar{1}00 >$ и $< 11\bar{2}0 >$, а на растяжение – $< 0001 >$. Коррозионному испытанию подвергали поверхности образцов, близкие по ориентации к кристаллографическим плоскостям (0001), $(10\bar{1}0)$, $(2\bar{1}\bar{1}0)$ и $(10\bar{1}1)$. Установлено, что модуль Юнга и коэффициент Кернса для базисной и пирамидальной граней со-

ставляют 48,6 ГПа и 0,81; 45,3 ГПа и 0,04 соответственно. Вид кривых напряжения существенно зависит от ориентации образцов и определяется степенью вовлеченности различных механизмов в общий процесс пластической деформации. Скорость коррозии в физиологическом водном растворе состава 0,9 % NaCl на базе 72 ч для поверхностей (0001), ($10\bar{1}0$), ($2\bar{1}\bar{1}0$) и ($10\bar{1}0$) составила 0,51; 0,76; 0,71 и 0,98 мм/год соответственно, при этом плоскости ($2\bar{1}\bar{1}0$) присуща только равномерная коррозия, плоскости (0001) – равномерная с незначительной локальной; наиболее интенсивно локальная коррозия идет в направлении ($10\bar{1}0$), а максимальная интенсивность сочетания локальной и равномерной – в направлении <$10\bar{1}1$>.

***Ключевые слова:*** монокристалл магния; кристаллографические направления; анизотропия; коэффициент Кернса; механические диаграммы; скорость коррозии.

***Для цитирования:*** Мерсон Д.Л., Бецофен С.Я., Мерсон Е.Д., Полуянов В.А., Мягких П.Н., Данюк А.В., Данилов В.А., Максименко Е.И., Брилевский А.И. Механическая и коррозионная анизотропия монокристалла магния // Frontier Materials & Technologies. 2025. № 2. С. 39–52. 10.18323/2782-4039-2025-2-72-4.

# Effect of ultrasonic treatment on structural transformations and mechanical behaviour of amorphous alloys (REVIEW)

***Inga E. Permyakova**\*1*, Doctor of Science (Physics and Mathematics), Professor,
senior researcher of the Laboratory of Physicochemistry and Mechanics of Metallic Materials
***Elena V. Dyuzheva-Maltseva**2*, postgraduate student
*Baikov Institute of Metallurgy and Materials Science of RAS, Moscow (Russia)*

**\*E-mail:** inga_perm@mail.ru

1ORCID: https://orcid.org/0000-0002-1163-3888
2ORCID: https://orcid.org/0000-0002-7199-487X

*Abstract:* The wide application of amorphous alloys is complicated by a narrow range of their thermal stability, embrittlement at elevated temperatures, difficult machinability, and low tensile plasticity. Ultrasonic treatment is an innovative method for solving these problems. Integration of ultrasonic technology into the technological chain can contribute to the improvement of the operational property of amorphous alloys, the manufacture of parts from them at different scale levels, and high-quality joining with other materials. The effect of ultrasonic vibrations on structural transformations and mechanical behaviour of amorphous alloys is not completely understood. The lack of an integrated scientific basis for the physical processes and accompanying effects in amorphous alloys under ultrasonic excitation prevents the development of the corresponding technology and optimization of its modes. Over the past decade, researchers have proposed various methods of ultrasonic treatment of amorphous alloys to improve their formability, achieve a balance of plasticity and strength, and consolidate with each other and with metals. In addition, certain ideas have been developed about their structure rejuvenation and the possibilities of transformation them to a partially nanocrystalline state under the action of ultrasound. To summarise these developments, the systematic discussion on features, parameters, and modes of ultrasonic treatment applied to ribbon and bulk amorphous alloys to improve their structure-sensitive properties are provided in this review. On this basis, the limitations of current study are discussed. The most promising applications of ultrasonic technologies for rapidly melt-quenched alloys in the near future include: their additive manufacturing, creation of hybrid composites by ultrasonic welding, ultrasonic forming for manufacturing products of complex shapes and geometries, complex multi-stage processing to obtain a unique combination of properties (e.g., melt quenching → laser irradiation → ultrasonic stimulation). This review enhances the existing knowledge on ultrasonic control of the properties and structure of amorphous alloys and facilitates a fast references on this topic for researchers.

*Keywords:* amorphous alloy; ultrasonic treatment; structural transformations; mechanical behaviour; nanocrystal; structure rejuvenation; composite; plasticity; forming.

*Acknowledgements:* The study was supported by the State Assignment No. 075-00319-25-00.

*For citation:* Permyakova I.E., Dyuzheva-Maltseva E.V. Effect of ultrasonic treatment on structural transformations and mechanical behaviour of amorphous alloys (REVIEW). *Frontier Materials & Technologies*, 2025, no. 2, pp. 53–71. DOI: 10.18323/2782-4039-2025-2-72-5.

## INTRODUCTION

Amorphous alloys (AAs) produced by rapid melt quenching or by casting in a copper casting-mold (in the case of bulk amorphous alloys) have unique physical properties, which makes them very promising for many applications in such areas as energy production, electronics, catalysis, medicine, and the aerospace industry [1–3]. Due to their unusual structure with the absence of long-range order and structural defects such as dislocations and grain boundaries, amorphous alloys, compared to their crystalline counterparts, are characterised by an increased elastic limit, high strength, hardness, corrosion and wear resistance, catalytic activity, and some of them – by biocompatibility [4–6]. However, as a kind of metastable material, AAs transform into a more stable energy state under the action of applied stresses, high temperatures, or even under natural conditions. The phenomenon of "aging" of the structure may be accompanied by deterioration of properties. Moreover, amorphous alloys demonstrate almost zero tensile plasticity due to the propagation of main highly localised shear bands, which prevents their use as a structural material [7; 8]. In this regard, the close attention of material scientists is focused on the development of strategies for the structural rejuvenation of AAs, which will contribute to greater disordering of the amorphous matrix and, thus, effective softening [9]. On the other hand, the balance of strength and plasticity can be achieved by forming an optimal proportion of nanocrystals in the volume of AAs, which can prevent crack propagation and initiate an increase in the number of shear bands, due to which plastic deformation in amorphous alloys is realised [10–12]. Numerous approaches are used to modify the structure of AAs,

overcome embrittlement, and improve their thermal stability: annealing and thermal cycling [13–15], electrostatic compression [16; 17], ion irradiation [18; 19], cold rolling [20; 21], and high-pressure torsion [22; 23]. However, these methods usually require a lot of experimental time and high costs, and some have limitations in sample size, which makes their application in production processes quite difficult. Therefore, there is an urgent need to develop an innovative, one-step, convenient approach to the processing of amorphous alloys. The method based on the use of ultrasonic (US) vibration energy with a frequency above 20 kHz is one of the promising methods for processing materials, characterised by ease of control and a fast response time [24–27]. It can directly introduce high energy into the glassy matrix, affecting the response of properties and complex physical processes, including glass transition, structural relaxation, crystallization, strengthening and plasticization mechanisms.

The purpose of this work is to analyse the world experience of using ultrasonic processing to control the structure and improve the properties of amorphous alloys, as well as to carry out technological operations with them.

## METHODS

The search for relevant scientific papers related to the review topic covered the period from the moment of the first publication to the present day. The selection was carried out among papers of peer-reviewed journals, books, conference materials from reliable international abstracting and indexing databases Web of Science and Scopus. Moreover, in order to track current studies, the resources of the Russian Science Citation Index (RSCI) and the patent database of the Russian Federation were used.

The ranking of the found materials was carried out depending on the characteristics of the physical processes and phenomena occurring during ultrasonic treatment, as well as the achievement of specific practical goals. In accordance with this, three areas of research on amorphous alloys during ultrasonic modification were identified:

1) study of the processes of rejuvenation of their structure for the implementation of forming;

2) study of the processes of nanocrystallization of amorphous alloys for the best combination of strength and plasticity;

3) development of the methodology of ultrasonic soldering/welding for effective rapid connection of amorphous alloys with each other or with crystalline materials.

## RESULTS

### 1. Retrospective analysis

When analysing literary sources in retrospect, it is important to note an important fact: the first publications on the use of ultrasonic excitation on amorphous alloys appeared in Russia. In 1992, scientists O.M. Smirnov and A.M. Glezer from the I.P. Bardin Central Research Institute of Ferrous Metallurgy in their paper [28], and a year later in their author's certificate [29], noted the effectiveness of ultrasonic treatment for improving the mechanical properties of Fe–Cr–B amorphous alloys ribbon. Only almost a decade later, in 2003, full-scale studies in this area were launched at the Universities of Osaka and Kagawa [30; 31]. At first, the response of elastic and inelastic properties of bulk zirconium-based $Zr_{55}Cu_{30}Ni_5Al_{10}$ AA under ultrasonic vibrations was studied, and the experiments were carried out in a very wide frequency range of 300–1500 kHz [30]. In 2005, the features of $Pd_{42.5}Ni_{7.5}Cu_{30}P_{20}$ AA crystallization were studied at frequencies of 0.35 MHz [31]. Then, Japanese researchers decided to test the possibility of joining amorphous alloys with each other using ultrasonic welding and in 2008 reported successful consolidation of $Zr_{55}Cu_{30}Ni_5Al_{10}$ using a combination of ultrasonic welding and slight heating (below the glass transition temperature) [32]. Several publications were enough to arouse interest in China and to seize the initiative in conducting fundamental research on the effect of ultrasonic stimulation on the structure and properties of amorphous alloys. Currently, Chinese research groups are the absolute leaders in this area. Attempts to study ultrasonic technologies as applied to amorphous alloys were also made in the USA [33], Belarus [34], Germany [35], and Ukraine [36–39], but only sporadically.

### 2. Structural rejuvenation

#### 2.1. The problem of embrittlement and its solutions

It was found that metallic materials undergo significant softening accompanied by a decrease in strength under the influence of ultrasound (acoustoplasticity effect, or Blaha effect) [40; 41]. Based on these characteristics, the forming technology using ultrasonic vibration was developed. Brittleness remains one of the main disadvantages of amorphous alloys, preventing their wider application. During labour-intensive processes (irradiation, elastostatic loading, cryothermal cycling) when combating the loss of plasticity in AA, reverse relaxation inevitably intervenes, which weakens the effect of structural rejuvenation. Moreover, the rejuvenation mechanism itself is not completely clear. In order to find suitable solutions to the embrittlement problem, in studies in recent years, ultrasonic vibrations have been combined with the process of forming amorphous alloys.

In [42; 43], a significant improvement in the thermoplastic formability of bulk $Zr_{35}Ti_{30}Be_{26.75}Cu_{8.25}$ amorphous alloys was found when using ultrasonic vibrations and its positive correlation with the ultrasound amplitude. In [44], a method of compression using ultrasonic vibration was proposed. By the example of $Zr_{52.5}Cu_{17.9}Ni_{14.6}Al_{10}Ti_5$ alloy, it was shown that this method can achieve rapid (in 10 s) structural rejuvenation, and the alloy itself becomes more heterogeneous with better ability to plastic deformation. Moreover, under ultrasonic compression, plastic deformation occurs on the fracture surface of the alloy, indicating that as the ultrasound amplitude gradually increases, the yield strength of the alloy decreases and the plasticity increases, which can significantly simplify the formability of the alloy at room temperature.

## 2.2. Physical aspects of the rejuvenation process and the accompanying response of mechanical properties

Fig. 1 shows schematically a multilevel landscape of potential energy illustrating the evolution of possible structural states of amorphous alloy. Energy wells and barriers control the thermodynamic stability of the material. The deepest minimum of energy corresponds to stable crystalline phases, and other energy minima represent some metastable glassy states (Fig. 1 a).

Rejuvenation is accompanied by an increase in potential energy and an increase in the free volume concentration. In turn, structural relaxation leads to a decrease in potential energy and a lower free volume content compared to the initial state of amorphous alloy (under conditions of ultrafast cooling during their production) [45]. Annihilation of free volume or loose packing regions during aging leads to the fact that AAs become even more brittle. However, when energy is introduced into amorphous alloy using ultrasonic vibrations at certain values of amplitude and exposure time, they are able to rejuvenate, since they acquire additional free volume and greater plasticity. During ultrasonic treatment, the combined effect of external applied elastic stress, internal converted heat and ultrasonic resonance of atoms can stimulate the movement of loosely packed atoms in the AA to a high-energy state, thereby causing the formation of other regions with free volume and rheological units to improve formability [44; 46].
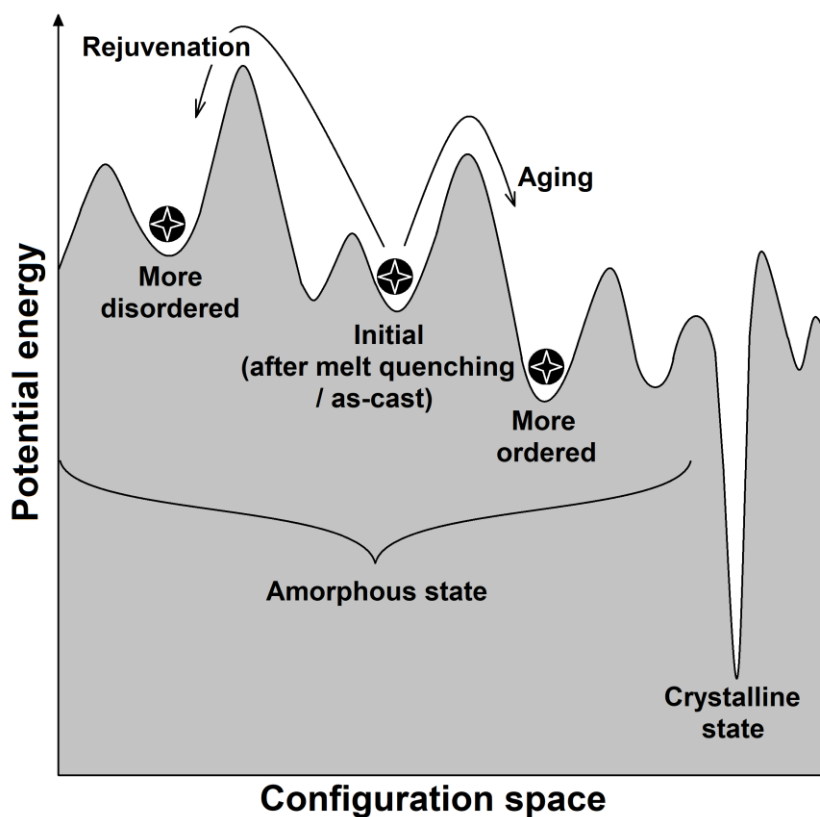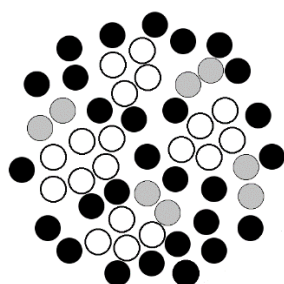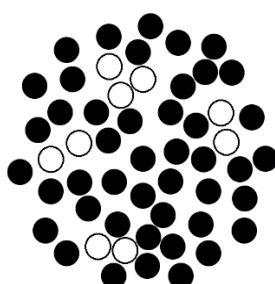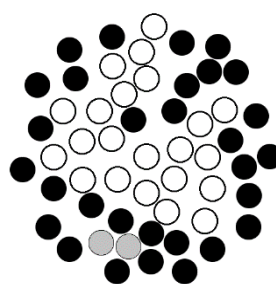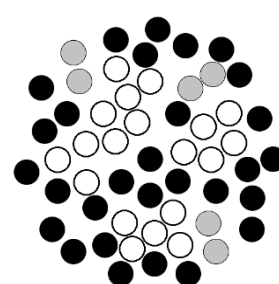


***Fig. 1.*** *Schematic illustrations of the energy states of atoms in the potential landscape (**a**)*
*and the structure evolution of amorphous alloys in initial state (**b**), during aging (**c**),*
*during ultrasonic rejuvenation (**d**) and afterwards (**e**)*
***Рис. 1.*** *Схематические иллюстрации энергетических состояний атомов в потенциальном ландшафте (**a**)*
*и эволюции структуры аморфных сплавов в исходном состоянии (**b**),*
*при старении (**c**), в процессе УЗ омоложения (**d**) и после него (**e**)*

In as-cast and melt-quenched amorphous alloys, reversible and irreversible β-relaxations can occur [47], the behaviour of which can be judged by the configurations of white and grey atoms in Fig. 1 b, respectively. With increasing aging time, the grey regions gradually become black, and the white ones are significantly compressed (Fig. 1 c). Under ultrasonic loading, the structure again becomes loosely packed (Fig. 1 d), so the set of highly mobile white atoms increases, and zones with grey atoms appear again after exposure to ultrasound (Fig. 1 e).

In [48], using atomistic modelling and evaluation of the nanomechanical characteristics of bulk $La_{55}Al_{25}Ni_5Cu_{10}Co_5$, $Pd_{40}Cu_{30}P_{20}Ni_{10}$ and $Zr_{35}Ti_{30}Cu_{8.25}Be_{26.75}$ amorphous alloys, evidence was provided that their significant plastic flow below the glass transition temperature under ultrasonic exposure is explained by dynamic inhomogeneity and cyclically induced atomic-scale expansions (liquefaction) in the amorphous alloys. This leads to significant rejuvenation and final "collapse" of the solid-like amorphous structure.

In [36; 37], the influence of preliminary ultrasonic treatment on the mechanical properties and structural features of bulk $Zr_{52.5}Ti_5Cu_{17.9}Ni_{14.6}Al_{10}$ and $Zr_{46.25}Cu_{45.25}Al_{7.5}Er_1$ amorphous alloys was studied using the acoustic emission method under uniaxial compression. The research results were interpreted within a polycluster model of the AA structure. The analysis of the obtained data allowed substantiating the mechanism of structural changes and a decrease in the strength of amorphous alloys as a result of alternating mechanical loading with an ultrasonic frequency of 20 kHz. The authors substantiated that the resistance to plastic deformation of amorphous alloys is determined by the strength of the intercluster boundaries, which are restructured and "softened" under the action of ultrasonic mechanical loading.

In [49; 50], the mechanical behaviour of $Pd_{40}Cu_{30}P_{20}Ni_{10}$ and $La_{55}Al_{25}Ni_5Cu_{10}Co_5$ amorphous alloys after ultrasonic vibrations was studied by the nanoindentation method. A noticeable softening after ultrasonic treatment was expressed as a decrease in hardness and elastic modulus – by ~25 and 40 %, respectively. It was found that flow defects with a shorter characteristic relaxation time, activated under loading with ultrasonic cycling, promote rapid diffusion of atoms with a low energy barrier. Ultimately, this leads to a noticeable creep displacement and, thus, to greater formability at ambient temperature.

A method for producing amorphous alloys was proposed, which included melting a metal blank in a crucible, melt quenching the on a rapidly rotating disk, but the nuance was that in order to increase the temperature range of plasticity, immediately after removing the ribbon, it was additionally subjected to ultrasonic treatment with an amplitude of alternating stresses [29]. In this case, the ratio of the amplitude of alternating stresses to the Young's modulus of the processed material should be within the range of $(0.135–0.48)\times10^{-3}$. This range was chosen so that the applied alternating stresses of ultrasonic frequency did not exceed the yield strength of

the studied amorphous alloys, did not provoke their subsequent destruction, but contributed to the effective preservation of plasticity and a shift in the embrittlement threshold towards higher temperatures.

In the work [28], using the example of the $Fe_{70}Cr_{15}B_{15}$ AA, it was shown that, depending on the ultrasonic impact parameters, the critical temperature of amorphous alloy embrittlement can shift either upward or downward depending on the amplitude of the ultrasonic vibrations used.

The results of dilatometric studies in the work [38] show an increase in the temperature of crystallization of the $Fe_{76}Ni_4Si_{14}B_6$ AA by 30–50 K after different modes of ultrasonic treatment and the microhardness of the amorphous alloy decreases by 15 %. This indirectly confirms the fact that the percentage content of the crystalline phase in the alloy decreases due to a decrease in the size or dissolution of frozen crystallization centres in the amorphous alloy.

## 2.3. Ultrasonic assisted shear punching

Ma J. et al. used high-frequency vibrations for shear punching of templates, products from bulk and ribbon amorphous alloys of the following systems: Zr–Ti–Cu–Be, Fe–Si–B, La–Al–Ni–Cu–Co, La–Ni–Al, and Cu–Zr [51–53]. Fig. 2 shows a schematic representation of the experimental assembly for this technology.

Under the action of ultrasonic vibration of the punch, the plastic powder melts due to frictional heat generation and viscoelastic thermal effect and continues to flow downwards under the action of the extrusion of the ultrasonic head, plastically deforming the amorphous ribbon or plate. The disordered structure of the amorphous alloys helps them to soften in a localised area during high-frequency vibrations, which leads to low-stress deformations. For example, using ultrasonic vibrations and a molten plastic viscous medium, various forms of AA in the shape of the letters "B", "M", "G" and Chinese characters 工, 大 were produced on an area of 5 mm$^2$ [51]. In [54], to increase the plasticity of amorphous alloys, a method for their forming using ultrasonic vibrations in liquid media (fresh and sea water, alcohol) was proposed. In the process of this treatment, at low stress (300 MPa) and temperatures significantly below the glass transition temperature $T_g$, complex structures such as lattices, gear wheels and hexagons about 5 mm in size were successfully produced from AA in 1 s.

These fast ultrasonic forming methods (from milliseconds to several seconds) help to preserve the amorphous nature. They largely allow avoiding time-dependent crystallization and oxidation processes and thereby bypassing traditional heat treatment, as well as the risk of crystal growth. In order to prevent the AA relaxation, it is possible to adjust the ultrasonic thermal effect by controlling the amplitude and time under compression with ultrasonic vibration, and thereby effectively improve the mechanical properties of amorphous alloys.

Promising ultrasonic methods to improve the plasticity of amorphous alloys at room temperature (ultrasonic assisted shear punching and ultrasonic extrusion forming) can be applied to the rapid manufacture of macro-, micro-,
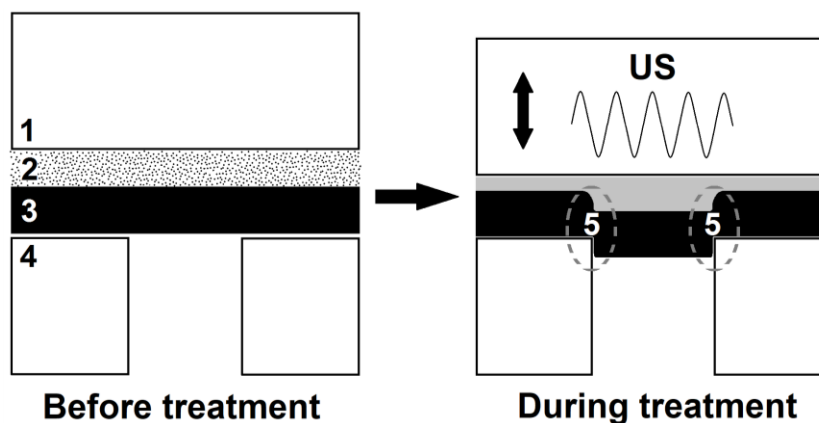
*Fig. 2. Schematic diagram of the ultrasonic assisted micro-shear punching set-up:*
*1 – punch; 2 – polymer powder (e.g., ethylene vinyl acetate);*
*3 – amorphous alloy; 4 – mold cavity;*
*5 – softening zones in amorphous alloy (highlighted by dotted line)*
*Рис. 2. Принципиальная схема установки для УЗ сдвиговой штамповки:*
*1 – пуансон; 2 – полимерный порошок (например, этиленвинилацетат);*
*3 – аморфный сплав; 4 – пресс-форма с полостью;*
*5 – зоны размягчения в аморфном сплаве (выделены пунктиром)*

nanoproducts and devices from amorphous alloys on the surface of metal materials. Forming of AA in liquids opens up exciting opportunities for application in aerospace, energy and marine engineering: in situ repair of ships and containers, polar construction, deep-sea exploration, providing valuable information and paving the way for future advances in underwater processing techniques.

### 3. Nanocrystallization

#### 3.1. Methods for creating an amorphous-nanocrystalline state

When stretched, amorphous alloys demonstrate poor macroscopic plastic deformation at ambient temperature, which is a result of the formation of highly localised shear bands, as well as surface softening, which limits their wide application as construction materials [7; 8]. To solve this problem, methods have been proposed aimed at increasing the heterogeneity of AAs or creating a small number of micrometre-sized [55; 56] and nanosized crystals [57; 58] embedded in amorphous matrices: composition development [59], annealing treatment [60], nitrogen additives [61], and severe plastic deformation [62]. The scientific concept of the listed technologies is to activate the nucleation of shear bands or prevent the propagation of shear bands. Ultrasound induces strong forced vibration action of atoms and/or molecules and nonlinear effects such as acoustic cavitation and acoustic flow, which change the microstructure and properties of various materials. In particular, the introduction of ultrasonic energy into AAs can increase their heterogeneity in atomic rearrangement and even lead to the formation of crystallites. Ultrasonic resonance can modulate the inhomogeneity of AAs and improve the mechanical properties of rejuvenated zones [63]. Ultrasonic vibrations of MHz frequency lead to

partial crystallization of bulk Pd-based AA when it is annealed below the glass transition temperature [31]. In [33], the ultrasonic surface modification method was used to treat $Zr_{44}Ti_{11}Cu_{10}Ni_{10}Be_{10}$ amorphous alloy and it was shown that its fracture strength and deformation were enhanced in a three-point bending experiment.

#### 3.2. Balance of strength and plasticity

An urgent issue arises: can ultrasound overcome the dilemma of compromise between strength and plasticity in amorphous alloys? The introduction of a significant amount of free volume and a small amount of dispersed nanocrystals into AA by means of ultrasonic vibrations can effectively prevent the propagation and expansion of cracks during fracture, thereby improving their strength and plasticity at room temperature [64; 65]. The authors of [65] used intermittent high-frequency vibration loading to control the behaviour of shear deformation and atomic arrangement in bulk $Zr_{41.2}Ti_{13.8}Cu_{12.5}Ni_{10}Be_{22.5}$ AA. It was found that this method allowed increasing very quickly (in 4 s) the plasticity of the alloy (up to 5.3 %) and its strength (up to 2240 MPa) by increasing the content of free volume and forming $CuZr_2$ nanocrystals in the amorphous matrix. However, it was noted that with excess ultrasonic energy, there is a risk of transition from the plastic state to the brittle state if the volume fraction of nanocrystals exceeds the critical limit.

In work [64], amorphous Cu-based composites at room temperature were subjected to elastic preload from 250 to 1000 N and ultrasonic treatment with ultrasound amplitudes from 15 to 50 μm. It was shown that at low values of amplitudes and preloads, the free volume dominates, and nanocrystals do not precipitate. At low amplitudes / medium preloads or at medium amplitudes / low preloads, the free volume and nanocrystals coexist together as integral parts of the structure. At high values of amplitudes and

loads, nanocrystals prevail, and the free volume content decreases sharply. Increasing the amplitude and decreasing the preload improves the efficiency of ultrasonic transmission.

In the work [66], 20 kHz ultrasonic excitation was applied to bulk $Zr_{46.75}Cu_{46.75}Al_{6.5}$ amorphous alloy and its influence on the microstructure evolution and mechanical properties was studied. It is found that $Cu_{10}Zr_7$ nanocrystals can be formed after ultrasonic vibrations. The evolution of nanocrystalline particles leads to an increase in plasticity during compression at room temperature in combination with an increase in the yield strength.

Currently, the construction of gradient structures has become a successful strategy in the development of advanced metallic materials with excellent performance properties. By ultrasonic vibration treatment, it was possible to form a gradient amorphous-nanocrystalline structure in $Zr_{46}Cu_{46}Al_8$ bulk amorphous alloy [67]. Using 20 kHz ultrasonic cyclic loading in the elastic mode, it is possible to obtain gradient structures with different volume fractions of crystallised substance in less than 2 s by adjusting the input ultrasonic energy. This innovative approach has clear advantages: it is extremely fast, requires minimal stress, and allows adjusting easily the degree of structural gradients by fine adjustment of the processing parameters. Nanoindentation tests show higher hardness near the impact surface, which is explained by a higher degree of nanocrystal formation, which gradually decreases with depth. As a result of the gradient dispersion of nanocrystals after ultrasonic treatment, increased plasticity of $Zr_{46}Cu_{46}Al_8$ AA was found, characterised by the formation of multiple shear bands. Microstructural studies show that nanocrystallization induced by ultrasonic treatment occurs due to local atomic rearrangements in phase-separated regions rich in Cu with high diffusion mobility.

The study of the effect of ultrasonic mechanical activation on the structural-phase transformations of $Ti_{50}Ni_{25}Cu_{25}$ AA carried out by the authors of [34] using differential scanning calorimetry (DSC) showed that this method of action affects the crystallization parameters and martensitic transitions. Temperatures and energies of crystallization increase after processing of amorphous ribbons in a longitudinal vibration waveguide. In turn, after processing of AA ribbons in an ultrasonic anvil, crystallization temperatures increase, and the crystallization energy decreases. The study of martensitic transformations showed that processing in an ultrasonic anvil leads to a decrease in characteristic temperatures and the magnitude of thermal effects, which may indicate a decrease in the grain size of the crystalline phase.

Using ultrasonic vibrations, a method for producing a series of composites from La-based amorphous alloys is proposed [68]. By modulating the amplitude and time of ultrasonic action, controlling the input energy of high-frequency vibrations, such composites with different proportions of the crystalline phase can be produced easily and accurately in seconds at low pressure and room temperature. By varying the degree of crystallinity, reduced hardness and better plasticity of AA composites are achieved compared to samples in the cast state.

Combining two technologies (ultrasonic treatment with multiple rolling) as applied to $Fe_{78}Si_{13}B_9$ and $Al_{87}Ni_8Gd_5$ AAs promotes an increase in the amount of free volume in the amorphous phase and leads to a significant acceleration of the AA crystallization processes [69; 70].

In [39], changes in the surface morphology and structure of the $Fe_{73.6}Si_{15.8}B_{7.2}Cu_{1.0}Nb_{2.4}$ ribbon AA (Finemet) as a result of severe deformation using ultrasonic impact treatment at room temperature in air were studied. The AA surface morphology after ultrasonic impact treatment is the result of localised plastic deformation occurring through the formation of a large number of shear bands. The effect of structural-phase transformation in the volume of the Finemet ribbon during ultrasonic impact treatment is caused by an increase in atomic mobility during deformation, which can be sufficient for the formation of nanocrystals by the diffusion mechanism and their uniform distribution in the amorphous matrix.

## 4. Ultrasonic material joining technologies

### 4.1. Alternative consolidation methods

One of the reasons limiting the large-scale application of ribbon and bulk amorphous alloys is their geometric dimensions. The thickness of commercial rapidly melt-quenched AA ribbons typically ranges from 20 to 30 μm, and the width – from 1 to 100 mm. The diameter/thickness of massive amorphous metal rods or plates can vary from 1 to 50 mm, and their length is usually no more than 80 mm. Moreover, AA often needs to be joined with other crystalline alloys in technical applications. Therefore, the development of AA/AA, AA/metal, AA/crystalline alloy joining methods has attracted much attention from researchers. Amorphous alloy can become brittle due to crystallization upon heating [1; 7]. Considering this fact, joining temperatures should be maintained below the glass transition temperature of amorphous alloy. Attempts have been made to use various methods for AA/AA and AA/crystal joining. In particular, spark welding was used to join $Zr_{55}Al_{10}Ni_5Cu_{30}$ AA and crystallization in the joint was successfully avoided [71]. The results showed that the tensile strength of the produced joints was equal to the strength of the original AA. In similar experiments, electron beam welding was used to consolidate the $Zr_{41}Be_{23}Ti_{14}Cu_{12}Ni_{10}$ AA plate with metallic nickel [72]. In [73], friction welding was tested to join $Pd_{40}Ni_{40}P_{20}$ / $Pd_{40}Cu_{30}P_{20}Ni_{10}$, $Zr_{55}Cu_{30}Al_{10}Ni_5$ / $Zr_{41}Be_{23}Ti_{14}Cu_{12}Ni_{10}$ together. It was shown that amorphous alloys could be joined at temperatures approximately 50 K below the glass transition temperature without demonstrating crystallization at the interface.

### 4.2. Ultrasonic soldering

Ultrasonic soldering is a flux-free method that can operate in air. Ultrasonic vibrations help to improve the initial wetting conditions at the solder/substrate interface [74; 75]. In this context, ultrasonic soldering can be used to join some materials that are difficult to wet. Moreover, this type of soldering can realise a connection through the low-temperature eutectic solder/substrate phase [75; 76]. Thus, ultrasonic soldering serves as an effective method for

joining amorphous alloys at temperatures significantly below their crystallization temperatures.

Melt-quenched iron-based amorphous foils are among the superior soft magnetic materials used in amorphous motors. Producing a strong connection between them is a complex technical task when assembling amorphous stators with aluminium shells. The use of ultrasound with a resonant frequency of 27 kHz and a vibration amplitude of 15 μm in the soldering process, it was possible to join qualitatively the $Fe_{77}Si_{14}B_9$ amorphous alloy with an aluminium sheet at temperatures of 250–350 °C for 10 s [77]. Sn–Zn filler was used as a welding filler material. A $FeZn_{13}$ compound was found at the filler metal/amorphous alloy interface. The results showed that the initial wetting of the interface and the refinement of the microstructure were improved under the action of ultrasonic vibrations.

The characteristics of wetting the $Zr_{55}Al_{10}Cu_{30}Ni_5$ amorphous alloy using Sn–Cu–Ni solder were studied using 40 kHz ultrasonic vibrations in open air at 528 K for 90 s [78]. It was found that wetting mainly depends on the collapse of cavitation bubbles on the AA surface, initiating erosion. Such cavitation erosion is effective for immediate removal of the passivation film from the AA surface. The sono-capillary effect, which is also caused by ultrasonic vibration, improves the adhesive properties of the solder.

In [79], the behaviour of wetting pure tin with respect to the $Zr_{50.7}Cu_{28}Ni_9Al_{12.3}$ amorphous alloy was studied under ultrasonic treatment (20 kHz) and a pressure of 0.2 MPa. Heating to 300 °C without ultrasound showed a non-wetting state of Sn for the amorphous alloy. Ultrasonic vibration promoted the wetting of Sn. Before ultrasonic treatment for 30 s, only physical adsorption was observed at the Sn/AA interface. Increasing the ultrasonic treatment time led to a change in the bonding at the Sn/AA interface from a point contact to a local surface contact and a diffusion layer. Two bonding modes were found at the Sn/AA interface. In the order-order bonding mode, slight crystallization occurred inside the amorphous alloy near the interface. The filler metal was bonded to the amorphous alloy through an ordered structure. In the order-disorder bonding mode, the filler metal and the amorphous alloy retained their original structures. The interface was characterised by stepped layers. The Cu content was higher than that of other elements near the bonding boundary. Longer diffusion distances of Sn in the amorphous alloy were obtained at high ultrasound power, high temperature (up to 400 °C), and large immersion depth (up to 3 mm).

### 4.3. Ultrasonic powder consolidation

The work [80] reports the successful production of two-phase composites of $Zr_{55}Cu_{30}Ni_5Al_{10}$ and Al-6061 aluminium alloy using ultrasonic powder consolidation at low temperatures and stresses. A wide range of composites with individual compressive strength and plasticity were obtained by optimizing the mass ratios of $Zr_{55}Cu_{30}Ni_5Al_{10}$ and Al-6061 powders. Mechanical tests showed that increasing the aluminium content improved plasticity while maintaining significant strength. In particular, the composite with a mass ratio of 5:5 demonstrated the best balance of me-

chanical properties, excellent compaction, homogeneity without visible defects, and a relative density in the range from 92 to 99 %. Microstructural analysis revealed the formation of a tightly bonded interface with the diffusion layer. This confirms that high-quality bonding was facilitated by ultrasonic vibration. Moreover, the ultrasonic powder consolidation process has successfully produced complex shapes from materials (star-shaped, toothed). This innovative approach is promising in the development of high-quality lightweight composites to meet the requirements of advanced manufacturing applications.

### 4.4. Ultrasonic welding

There are reports of successful production of "sandwich" composites from $Zr_{35}Ti_{30}Cu_{8.25}Be_{26.75}$ ribbon amorphous alloy and $Al_{80}Li_5Mg_5Zn_5Cu_5$ high-entropy alloy (HEA) [81], as well as from $La_{55}Al_{25}Ni_5Cu_{10}Co_5$ amorphous alloy and $Co_{20}Cr_{20}Fe_{20}Ni_{20}Mn_{20}$ HEA [82] using ultrasonic excitation. The ribbons were first folded together using a clamping force and then subjected to high-frequency (20 kHz) vibrations of an ultrasonic sonotrode that lasted for several seconds. During this process, the amorphous alloys softened and bonded into a bulk mass with the HEA ribbons. This low-temperature low-stress method allowed creating composites that combine the properties of both amorphous and crystalline components. Microscopic studies and computed tomography show good bonding quality without pores and cracks in the composites of AA and HEA. Due to the unique structure combining soft and solid phases, the composite has improved mechanical properties compared to those obtained from a pure single phase.

In the process of ultrasonic welding when joining AAs to each other or to other materials, crystallization of the amorphous structure can be prevented due to the weak thermal effect and the quickness of the process. Other advantages of this technology include energy efficiency and the absence of the need for welding consumables. An important feature is also the ability to join materials with different melting temperatures, since the process occurs in the solid state.

Ultrasonic welding was used to join a sheet of commercial forged aluminium alloy (AA5754) 1 mm thick and a strips of $Zr_{59.3}Cu_{28.8}Al_{10.4}Nb_{1.5}$ commercial bulk amorphous alloy (AMZ4) 0.4 mm thick [35]. The following process parameters were proposed: welding energy was 2000 W·s, displacement amplitude was 41 μm, and welding force was 740 N. The results showed that the AA retains its amorphous structure in the joint, and the joint strength is higher than the strength of the Al sheet. In [83], a technology was considered in which, using a normal pressure of 80 N, a vibration time of 1 s, and a frequency of 20 kHz, three-dimensional plates of $Cu_{54}Zr_{22}Ti_{18}Ni_6$ AA with a thickness of 1 mm were successfully "welded" without any signs of crystallization. In [32], it was similarly shown that ultrasonic welding could be used to consolidate $Zr_{55}Cu_{30}Ni_5Al_{10}$ amorphous alloys with each other, maintaining the bonding zone in an amorphous state. The joint area can be increased by using the gluing condition with external heating to a temperature of 423 K (below the glass transition temperature).

Using ultrasonic welding, joints of bulk $Zr_{62}Cu_{33}Al_4Ti$ AAs with hypoeutectic Zn–3Al filler metal were produced [84]. A thick wavy layer consisting of alternating $Zn_{50}Al_{25}Zr_{25}/Zn_{22}Zr$ sublayers was formed on the surface of the Zr-based AA substrate, which provided a shear strength of about 100 MPa for the welded samples.

It should be separately noted that a method for producing multilayer AA ribbons using ultrasonic welding has been developed. This method can be used as an ultrasonic additive manufacturing process, such as 3D printing, in which thin metal strips are laid layer by layer to obtain thicker metal samples. It can be imagined that if the AA ribbons can be infinitely superimposed on each other under the action of ultrasonic vibrations, then the glass-forming capacity limitation on the AA dimensions will no longer exist. Fig. 3 schematically shows the principle of consolidating samples using ultrasonic welding.

Using ultrasonic welding technology, 4–5 pieces of Fe–Si–B AA ribbons with a joint area of up to 8×8 mm² (each layer thickness was 25 μm) were successfully and quickly (in 220 ms) joined [85]. The operating frequency, ultrasound amplitude, and maximum output power of the ultrasonic welding equipment were 20 kHz, 35 μm, and 4000 W, respectively. Similarly, multilayer $Ni_{82.2}Cr_7B_3Si_{4.8}Fe_3$ AA ribbons were joined using ultrasonic welding, which were laid in 3–4 layers (each layer thickness was 40 μm) [86]. Moreover,

ultrasonic welding was used to prepare composite samples in which two crystalline Al and Cu ribbons were joined with $Ni_{82.2}Cr_7B_3Si_{4.8}Fe_3$ AA ribbons [87]. However, the laminated AA and metal-AA composites produced in the above-mentioned works can be welded only in several layers, and the alternate, unlimited stacking, as in 3D printing, has not yet been achieved [88].

It should be noted that, taking into account the morphology of the joints and the phase stability, ultrasonic welding treatment demonstrates powerful capabilities for consolidating amorphous alloys both in air and in liquid media. In [89], bulk $La_{55}Al_{25}Ni_5Cu_{10}Co_5$, $Zr_{55}Cu_{30}Al_{10}Ni_5$ amorphous alloys and high-entropy Ti–Zr–Hf–Be–Ni amorphous alloy were selected for ultrasonic joining in fresh and sea water, in alcohol, and in liquid nitrogen. It was shown that the technology using ultrasonic vibration eliminates high temperature and problems associated with high current (as in the case of conventional underwater joining methods). Moreover, the samples from the studied amorphous alloys both had no obvious defects in the joined interface and demonstrated excellent mechanical properties and corrosion resistance. This approach both provides an effective underwater joining method for on-the-shelf and marine applications and ensures a feasible joining strategy in extreme conditions such as flammable environments in oil, gas, organic solvents and cryogenic conditions in space.

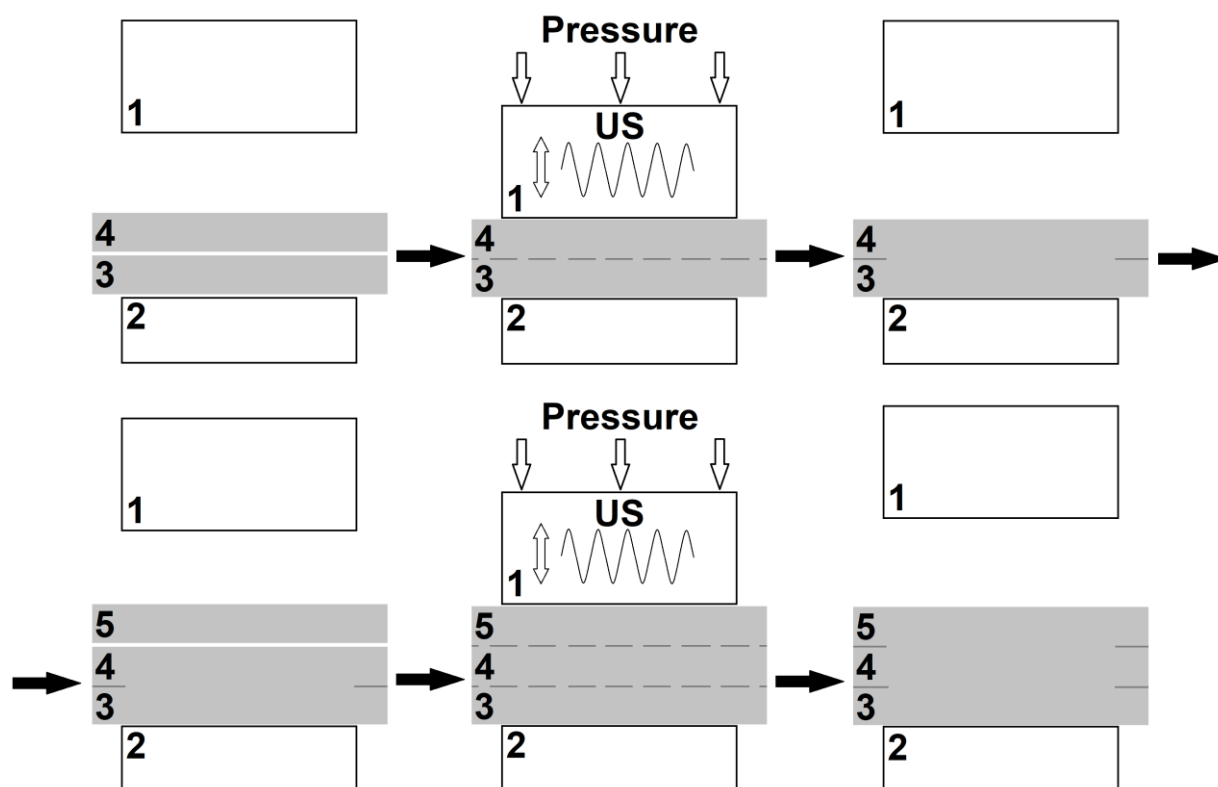***Fig. 3.*** *Schematic diagram of ultrasonic vibration welding:*
*1 – sonotrode; 2 – fixture; 3, 4, 5 – layers of amorphous alloys*
***Рис. 3.*** *Схема УЗ вибрационной сварки:*
*1 – сонотрод; 2 – установочная плита; 3, 4, 5 – слои аморфных сплавов*

## DISCUSSION

In most publications on ultrasonic processing, the object of study is massive amorphous alloys produced in the form of rods, bars, plates. Increased interest clearly implies expanding the boundaries of their use both as a functional and as a construction material. Currently, bulk AAs are integrated into jewellery, sports equipment (for example, golf clubs and tennis rackets), used for the production of biocompatible implants, mobile phone cases, and applied for reinforcement [3; 5; 6]. Ultrasonic forming has broad prospects for overcoming the size limitations of cast amorphous alloys, synthesizing new composites based on them. Nano-, micro- and miniature products of complex shapes currently produced in laboratory conditions using ultrasonic stimulation of bulk AAs will later be able to compete with similar products made of traditional metals and alloys. Moreover, the US and Japan are developing defence industry products, in particular, for the creation of lightweight and durable composite armour plates based on ceramics and bulk AAs, as well as for the replacement of the core material in anti-tank armour-piercing shells with composites made of AAs due to their similar density and performance properties [90].

However, in Russia, bulk amorphous alloys have not yet found their large-scale application due to their difficult machinability; they are cast exclusively for research purposes for fundamental science. Therefore, it is reasonable to adopt the accumulated world experience in the use of ultrasonic technology. Being an effective and convenient method of subsequent processing to improve the final plasticity of bulk AAs, ultrasonic modification will be of great importance for their further development and commercialization in Russia.

In turn, amorphous, amorphous-nanocrystalline ribbons and microwires are manufactured on an industrial scale in Russia. PJSC Ashinsky Metallurgical Plant (Asha), PJSC M-STATOR (Borovichi), and R&D Company GAMMA-MET (Yekaterinburg) are the largest and most well-known manufacturers in the market. Their rapidly melt-quenchered ribbons are best known primarily for a high level of magnetic and corrosion properties and are used in electrical products, transformers, magnetic screens, and as components for protective coatings. In this regard, it is extremely important to continue studying the effect of ultrasound on amorphous alloys with an emphasis on the behaviour of their magnetic and chemical properties. Judging by the literature, it is here that an obvious gap is noticeable. Most of the studies conducted were focused on improving the mechanical response of AAs after ultrasonic vibrations, and the study of corrosion resistance, magnetic behaviour, and catalytic activity was not given due attention. Meanwhile, the use of ultrasonic energy can provide saturation magnetization significantly higher than that achieved with conventional annealing, along with a low coercive force. For manufactured iron-based amorphous alloys, the use of ultrasonic vibrations can promote the balanced formation of uniformly distributed ferromagnetic nanoclusters, which will reduce anisotropy and, thus, increase the soft magnetic properties of the ribbons. Moreover, the effect of ultrasonic vibrations is quite capable of improving the corrosion resistance of AAs in aggressive environments. It should be understood that the corrosion resistance of amorphous alloys both depends on the alloying elements and is closely related to their metastable amorphous structure. As practice has shown, ultrasonic treatment of AAs can produce an amorphous-nanocrystalline state [64; 65; 67], which is characterised by a decrease in the average atomic distance. A more stable structure will lead to some decrease in the chemical potential and will contribute to an increase in corrosion resistance. Thus, it is advisable to initiate scientific studies of the susceptibility of amorphous alloys to chemical action after ultrasonic modification.

Selective ultrasonic stimulation has great potential for adaptation of local nano-, microstructure and properties of amorphous alloys: it is possible to achieve simultaneously rejuvenation in areas of close packing of atoms with a decrease in the elastic modulus and relaxation in areas of loose packing, suppressing the nucleation of the first shear bands. In addition, the size, length and pattern of rejuvenated zones can be adjusted as needed.

Introduction of free volume and a small amount of dispersed nanocrystals into amorphous alloys due to ultrasound treatment allows improving their complex characteristics (increasing plasticity and strength). However, it is important to learn how to obtain controllably the optimal ratio of amorphous and crystalline components, adjusting the efficiency of ultrasound transmission and avoiding the transition from plasticity to brittleness, by controlling the ultrasound amplitude and preliminary loads. The nature of embrittlement and attenuation of ultrasonic waves in such a structural state is not completely clear.

To date, published data on ultrasonic excitation modes as applied to amorphous alloys are not complete, few in number and scattered. It is necessary to accumulate and expand this experimental knowledge for various chemical compositions of both bulk and, to a greater extent, AAs ribbons. Nevertheless, we have attempted to collect the information of interest on the main parameters, distributing it in accordance with the ultimate goal of ultrasonic processing, which the researchers set in their experiments: rejuvenation and forming of amorphous alloys, nanocrystallization from an amorphous state or joining the material by ultrasonic welding/soldering (Table 1). Analysing the obtained data, we can conclude the following.

1. Bulk amorphous alloys are studied more intensively than ribbon ones, and it is expected that there is more information on the main parameters of their ultrasonic excitation.

2. There are two generalised methods of ultrasonic modification of amorphous alloys: a noncontact method, when high-frequency vibrations are transmitted through a liquid medium in an ultrasonic bath, and a contact method, i.e. using an ultrasonic sonotrode directly adjacent to the AA. In most cases, researchers use the second method, since it has proven itself to be faster and more effective in its influence on the AA structure.

3. To implement softening and structural renewal of amorphous alloys, the frequency of ultrasonic treatment $f$ is 20 kHz, the time of exposure $t$ is very short – from 80 to 950 ms, the amplitude $A$ varies from 19 to 44.4 μm.

***Table 1.*** *Modes of ultrasonic treatment for ribbon and bulk amorphous alloys*
***Таблица 1.*** *Режимы УЗ обработки для ленточных и объемных аморфных сплавов*

| Chemical composition of amorphous alloys, at. % | Ultrasonic treatment parameters | | | | | Source |
|---|---|---|---|---|---|---|
| | *f*, kHz | *A*, μm | *t*, s | *E*, J | *W*, W | |
| **Structural rejuvenation and forming** | | | | | | |
| $La_{60}Ni_{15}Al_{25}$ | 20 | 40 | – | – | – | [45] |
| $La_{55}Al_{25}Ni_5Cu_{10}Co_5$<br>$Al_{86}Ni_9La_5$<br>$La_{60}Al_{20}Ni_{20}$<br>$Cu_{50}Zr_{50}$<br>$Pd_{40}Cu_{30}P_{20}Ni_{10}$<br>$Zr_{35}Ti_{30}Cu_{8.25}Be_{26.75}$<br>$Fe_{78}Si_9B_{13}$ ribbons | 20 | 40–44.4 | 1 | – | – | [51]<br>[52]<br>[48] |
| $La_{55}Al_{25}Ni_5Cu_{10}Co_5$ | 20 | – | 0.08–0.24 | 5–30 | – | [91] |
| $Zr_{52.5}Cu_{17.9}Ni_{14.6}Al_{10}Ti_5$ | 20 | 19–36 | – | – | – | [44] |
| $Zr_{46}Cu_{46}Al_8$ | 20 | 40 | 0.6–0.95 | 50–400 | 83–205 | [67] |
| **Partial nanocrystallization** | | | | | | |
| $Cu_{52.71}Ti_{28.06}Zr_{11.59}Ni_{7.54}$ – ZnB amorphous composite | 20 | 15–50 | – | – | – | [64] |
| $Zr_{44}Ti_{11}Cu_{10}Ni_{10}Be_{25}$ | 20 | 24 | – | – | – | [33] |
| $Zr_{46.75}Cu_{46.75}Al_{6.5}$ | 20 | 15 | 7200 | – | – | [66] |
| $Ti_{50}Ni_{25}Cu_{25}$ ribbons | 22 | 10 | 720–1800 | – | – | [34] |
| $La_{64}Al_{14}Cu_{22}$ | 20 | 4–14 | – | 100–700 | – | [68] |
| $Fe_{78}Si_{13}B_9$ ribbons<br>$Al_{87}Ni_8Gd_5$ ribbons | 37 | – | 720–1800 | – | 100 | [69]<br>[70] |
| $Fe_{73.6}Si_{15.8}B_{7.2}Cu_{1.0}Nb_{2.4}$ ribbons | 21 | 25 | 10–60 | – | 600 | [39] |
| **Joining via ultrasonic welding/soldering** | | | | | | |
| $La_{55}Al_{25}Ni_5Cu_{10}Co_5$ / $Zr_{55}Cu_{30}Al_{10}Ni_5$ / TiZrHfBeNi | 20 | 44.4 | – | 300–700 | 2500 | [89] |
| AA5754 aluminum alloy / $Zr_{59.3}Cu_{28.8}Al_{10.4}Nb_{1.5}$ | 20 | 41 | – | 2000 | – | [82] |
| Al / $Fe_{77}Si_{14}B_9$ ribbons | 27 | 15 | 10 | – | – | [77] |
| Sn–Cu–Ni / $Zr_{55}Al_{10}Cu_{30}Ni_5$ | 40 | 5.1–7.4 | 90 | – | – | [78] |
| Sn / $Zr_{50.7}Cu_{28}Ni_9Al_{12.3}$ | 20 | – | 5–3600 | – | – | [79] |
| $Fe_{78}Si_9B_{13}$ ribbons to each other | 20 | 35 | 0.22 | – | 4000 | [85] |
| Al / Cu / $Ni_{82.2}Cr_7B_3Si_{4.8}Fe_3$ ribbons | 35 | – | – | – | 800 | [86] |

*Note. A is the amplitude of ultrasonic vibrations;*
*f is the frequency of ultrasonic vibrations;*
*t is the ultrasonic exposure time;*
*W is the power;*
*E is the energy of ultrasonic equipment.*

*Примечание. А – амплитуда УЗ колебаний;*
*f – частота УЗ колебаний;*
*t – время УЗ воздействия;*
*W – мощность УЗ установки;*
*E – ее энергия.*

At lower amplitudes, AAs usually pass into a state with lower potential energy, similar to the aging effect.

4. To transfer amorphous alloy into a partially nanocrystalline state, a longer ultrasonic treatment is required than for rejuvenation (from 10 s to 2 h). In this case, the frequency range is expanded ($f$=20–37 kHz) along with the amplitude range ($A$=4–50 µm).

5. During ultrasonic welding/soldering of amorphous alloys, the following ranges of ultrasonic characteristics can be noted: $f$=20–40 kHz, $A$=5.1–44.4 µm. As for the time of ultrasonic action, for joining micron AAs ribbons with each other or with another material, it is necessary from 220 ms to 10 s, and for bulk AAs with a thickness of several centimetres, it will take up to 1 h.

6. The highest values of energy $E$ and power $W$ of ultrasonic devices are noted during ultrasonic welding ($E$=300–2000 J, $W$=800–4000 W), average values – during partial nanocrystallization ($E$=100–700 J, $W$=100–600 W), and the lowest – during structural rejuvenation and forming of AAs ($E$=5–400 J, $W$=83–205 W).

An interesting and attractive idea is to build extreme effects, including ultrasonic modification, into one integral technological chain [1]. This can lead to qualitative changes in the nature of the final structure and, consequently, to the possibility of obtaining unique properties of metallic materials subjected to complex effects. With regard to amorphous alloys, individual links of the chain are already successfully implemented: for example, melt quenching (MQ), during which AAs are created, and their subsequent severe plastic deformation (SPD) in a Bridgman chamber, or MQ + laser irradiation (LI), or MQ + ultrasonic treatment (UST), or MQ + cryogenic deformation (CD). For the successful implementation of systemic multi-stage treatment, for example MQ → SPD → CD → LI → UST, it is necessary to "synchronise" the parameters for the material to obtain new structures and structure-sensitive properties. This research layout is innovative, but has not yet been sufficiently reflected in the scientific literature.

## CONCLUSIONS

Processing of amorphous alloys into desired shapes and structures is a prerequisite and basis for their successful commercial application. A promising method of influencing AAs (non-destructive, environmentally friendly and inexpensive) both from a fundamental and from practical point of view is the use of high-frequency ultrasonic vibrations. However, to date, many aspects concerning the physical nature of structure formation in amorphous alloys, the mechanisms of their plastic deformation, crystallization, and the response of physicochemical properties during ultrasonic processing remain unclear.

It is important to continue identifying in detail the relationships between the sequence of structural-phase transformations in amorphous alloys and the parameters of ultrasonic processing. This will expand the existing scientific knowledge in the physics of disordered and nonequilibrium systems, and will allow for a comprehensive formulation of conditions and accurate determination of modes that promote:

– the structure rejuvenation with softening and improvement of thermal stability while maintaining amorphousness;

– partial devitrification of AAs with an optimal combination of the proportion of amorphous and nanocrystalline phases, a compromise balance of strength and plasticity, as well as the preservation of soft magnetic properties;

– cold welding of layers of amorphous alloys different in compositions and properties with high-quality adhesion, i. e. the creation of hybrid materials.

Understanding the scientific principles of these processes using ultrasound is extremely important for the effective management of properties of amorphous alloys and the creation of innovative multifunctional materials based on them.

Studying the influence of ultrasonic treatment on the thermal stability of AAs will allow expanding the temperature ranges of their operation without embrittlement.

Shear punching of amorphous alloys under the influence of high-frequency vibrations is an innovative method of their forming. The method is not limited to the punch profile, and it is possible to manufacture more target products with different shapes. Such advantages as low cost, fast operation speed and good product quality make the process of forming AAs an energy-saving and effective technology with wide application prospects.

The study of the influence of ultrasonic mechanical activation on the structure will help to understand the mechanisms of structural rearrangements, activation of defects in amorphous alloys under the action of ultrasonic vibrations. This, in particular, helps to identify the physical causes of superplastic flow in a glassy system using cold ultrasonic treatment. Ultrasonic forming using the phenomenon of superplasticity of amorphous alloys in a supercooled liquid state can become an advanced method for manufacturing circuits, relief images, parts from AAs with sizes from nanometres to centimetres. This opens up inviting prospects in engineering applications, for example, in microelectronics and nanotechnology, for the creation of components, integrated circuits, chips, printed circuit boards.

The results of cold welding of dissimilar amorphous alloys stimulate further development of high-tech manual design and manufacture of intelligent materials containing several phases and compositions. Ultrasonic forming of AAs will provide a new method for manufacturing structures and large-sized AAs with great potential for future developments. Ultrasonic processing can be used when creating high-speed devices, planar mechanisms, for example, to create actuators in microelectromechanical systems based on crystallization using ultrasonic vibrations of TiNi amorphous thin films with shape memory. The advantage of this method is that the shape memory properties can be spatially distributed taking into account the specified requirements.

## REFERENCES

1. Glezer A.M., Permyakova I.E. *Melt-quenched nanocrystals*. Boca Raton, CRC Press, Taylor & Francis Group Publ., 2013. 369 p. DOI: 10.1201/b15028.

2. Greer A.L., Costa M.B., Houghton O.S. Metallic glasses. *MRS Bulletin*, 2023, vol. 48, pp. 1054–1061. DOI: 10.1557/s43577-023-00586-5.

3. Gao K., Zhu X.G., Chen L. et al. Recent development in the application of bulk metallic glasses. *Journal of Materials Science and Technology*, 2022, vol. 131, pp. 115–121. DOI: 10.1016/j.jmst.2022.05.028.

4. Khan M.M., Nemati A., Rahman Z.U., Shah U.H., Asgar H., Haider W. Recent advancements in bulk metallic glasses and their applications: a review. Critical Reviews in Solid State and Material Sciences, 2018, vol. 43, no. 3, pp. 233–268. DOI: 10.1080/10408436.2017.1358149.

5. Inoue A., Hashimoto K., eds. *Amorphous and nanocrystalline materials: preparation, properties, and applications*. Berlin, Springer Publ., 2001. 206 p. DOI: 10.1007/978-3-662-04426-1.

6. Trexler M.M., Thadhani N.N. Mechanical properties of bulk metallic glasses. Progress in Materials Science, 2010, vol. 55, no. 8, pp. 759–839. DOI: 10.1016/j.pmatsci.2010.04.002.

7. Glezer A.M., Permyakova I.E., Gromov V.E., Kovalenko V.V. *Mekhanicheskoe povedenie amorfnykh splavov* [Mechanical behavior of amorphous alloys]. Novokuznetsk, SibGIU Publ., 2006. 416 p.

8. Dong Quan, Tan Jun, Li Caiju, Sarac B., Eckert J. Room-temperature plasticity of metallic glass composites: a review. Composites Part B: Engineering, 2024, vol. 280, article number 111453. DOI: 10.1016/j.compositesb.2024.111453.

9. Zhang M., Chen Y., Li W. On the origin of softening in the plastic deformation of metallic glasses. *International Journal of Plasticity*, 2019, vol. 116, pp. 24–38. DOI: 10.1016/j.ijplas.2018.12.004.

10. Hufnagel T.C., Schuh C.A., Falk M.L. Deformation of metallic glasses: recent developments in theory, simulations, and experiments. *Acta Materialia*, 2016, vol. 109, pp. 375–393. DOI: 10.1016/j.actamat.2016.01.049.

11. Permyakova I., Glezer A. Mechanical behavior of Fe- and Co-based amorphous alloys after thermal action. *Metals*, 2022, vol. 12, no. 2, article number 297. DOI: 10.3390/met12020297.

12. Maaß R., Löffler J.F. Shear-band dynamics in metallic glasses. *Advanced Functional Materials*, 2015, vol. 25, no. 16, pp. 2353–2368. DOI: 10.1002/adfm.201404223.

13. Shelyakov A., Sitnikov N., Zaletova I., Borodako K., Tabachkova N. Study of structure and phase transformations in rejuvenated rapidly quenched TiNiCu alloys. *Metals*, 2023, vol. 13, no. 7, article number 1175. DOI: 10.3390/met13071175.

14. Priezjev N.V. The effect of thermal history on the atomic structure and mechanical properties of amorphous alloys. *Computational Materials Science*, 2020, vol. 174, article number 109477. DOI: 10.1016/j.commatsci.2019.109477.

15. Di Siyi, Zhou Jing, Cai Mingjuan, Cui Jingxian, Li Xuesong, Shen Baolong, Ke Haibo, Wang Qianqian. Improved ductility of annealed Fe-based metallic glass with good soft magnetic property by cryogenic thermal cycling. *Journal of Alloys and Compounds*, 2023, vol. 960, article number 170686. DOI: 10.1016/j.jallcom.2023.170686.

16. Sohrabi S., Sun B.Y., Mahmoodan M., Sun Y.H., Gholamipour R., Wang W.H. Rejuvenation by compressive elasto-static loading: the role of static stress on a Zr-based metallic glass. *Journal of Alloys and Com-*

pounds*, 2023, vol. 933, article number 167715. DOI: 10.1016/j.jallcom.2022.167715.

17. Zhang Sailong, Shi Bo, Wang Jinhui, Xu Yuanli, Jin Peipeng. Rejuvenation of a naturally aged bulk metallic glass by elastostatic loading. *Materials Science and Engineering: A*, 2021, vol. 806, article number 140843. DOI: 10.1016/j.msea.2021.140843.

18. Khademorezaian S., Tomut M., Peterlechner M., da Silva Pinto M.W., Rösner H., Divinski S., Wilde G. Extreme rejuvenation of a bulk metallic glass at the nanoscale by swift heavy ion irradiation. *Journal of Alloys and Compounds*, 2024, vol. 980, article number 173571. DOI: 10.1016/j.jallcom.2024.173571.

19. Boukhemkhem W., Izerrouken M., Ghidelli M., Pardoen T., Sari A., Khereddine A.Y., Meftah A. Swift heavy ion irradiation effect on structural, morphological and mechanical properties of $Zr_{70}Ni_{30}$ metallic glass. *Physica Scripta*, 2023, vol. 98, no. 8, article number 085311. DOI: 10.1088/1402-4896/ace387.

20. Zhang C.Y., Zhu Z.W., Li S.T., Wang Y.Y., Li Z.K., Li H., Yuan G., Zhang H.F. Shear band evolution and mechanical behavior of cold-rolled Zr-based amorphous alloy sheets: an in-situ study. *Journal of Materials Science and Technology*, 2024, vol. 181, pp. 115–127. DOI: 10.1016/j.jmst.2023.09.022.

21. Stolpe M., Kruzic J.J., Busch R. Evolution of shear bands, free volume and hardness during cold rolling of a Zr-based bulk metallic glass. *Acta Materialia*, 2014, vol. 64, pp. 231–240. DOI: 10.1016/j.actamat.2013.10.035.

22. Permyakova I., Glezer A. Amorphous-nanocrystalline composites prepared by high-pressure torsion. *Metals*, 2020, vol. 10, no. 4, article number 511. DOI: 10.3390/met10040511.

23. Bazlov A.I., Parkhomenko M.S., Ubyivovk E.V., Zanaeva E.N., Bazlova T.A., Gunderov D.V. Severe plastic deformation influence on the structure transformation of the amorphous $Zr_{62.5}Cu_{22.5}Al_{10}Fe_5$ alloy. *Intermetallics*, 2023, vol. 152, article number 107777. DOI: 10.1016/j.intermet.2022.107777.

24. Yang Zhichao, Zhu Lida, Zhang Guixiang, Ni Chenbing, Lin Bin. Review of ultrasonic vibration-assisted machining in advanced materials. *International Journal of Machine Tools and Manufacture*, 2020, vol. 156, article number 103594. DOI: 10.1016/j.ijmachtools.2020.103594.

25. Behal J., Maru M.S., Katwal R., Pathak D., Kumar V. Ultrasonic assisted green synthesis approach for nanotechnological materials. *Journal of Alloys and Compounds Communications*, 2024, vol. 3, article number 100013. DOI: 10.1016/j.jacomc.2024.100013.

26. Yang Jingwei, Xie Chuhao, Zhang Jie, Qiao Jian. Design strategies for enhancing strength and toughness in ultrasonic welding of dissimilar metals: a review. *Materials Today Communications*, 2025, vol. 42, article number 111502. DOI: 10.1016/j.mtcomm.2025.111502.

27. Gallego-Juárez J.A., Graff K.F., eds. *Power ultrasonics: Applications of high-intensity ultrasound*. Oxford, Woodhead Publ., 2023. 946 p. DOI: 10.1016/C2019-0-00783-2.

28. Smirnov O.M., Glezer A.M. Effect of ultrasonic treatment on embrittlement of amorphous alloys during heat treatment. *Fizika i khimiya obrabotki materialov*, 1992, no. 3, pp. 131–134.

29. Smirnov O.M., Glezer A.M., Ovcharov V.P., Khudyakova E.V. *Sposob polucheniya amorfnykh splavov* [Method for the producing amorphous alloys], opisanie izobreteniya k avtorskomu svidetelstvu no. SU 1787665 A1, 1993, 3 p. EDN: PGXVAV.

30. Ichitsubo T., Kai S., Ogi H., Hirao M., Tanaka K. Elastic and anelastic behavior of $Zr_{55}Al_{10}Ni_5Cu_{30}$ bulk metallic glass around the glass transition temperature under ultrasonic excitation. *Scripta Materialia*, 2003, vol. 49, no. 4, pp. 267–271. DOI: 10.1016/S1359-6462(03)00294-X.

31. Ichitsubo T., Matsubara E., Yamamoto T., Chen H.S., Nishiyama N., Saida J., Anazawa K. Microstructure of fragile metallic glasses inferred from ultrasoundaccelerated crystallization in Pd-based metallic glasses. *Physical Review Letters*, 2005, vol. 95, article number 245501. DOI: 10.1103/PhysRevLett.95.245501.

32. Maeda M., Takahashi Y., Fukuhara M., Xinmin Wang, Inoue A. Ultrasonic bonding of $Zr_{55}Cu_{30}Ni_5Al_{10}$ metallic glass. *Materials Science and Engineering: B*, 2008, vol. 148, no. 1-3, pp. 141–144. DOI: 10.1016/j.mseb.2007.09.028.

33. Ma Chi, Qin Haifeng, Ren Zhencheng, O'Keeffe S.C., Stevick J., Doll G.L., Dong Yalin, Winiarski B., Ye Chang. Increasing fracture strength in bulk metallic glasses using ultrasonic nanocrystal surface modification. *Journal of Alloys and Compounds*, 2017, vol. 718, pp. 246–253. DOI: 10.1016/j.jallcom.2017.05.056.

34. Nepomnyashchaya V.V., Rubanik V.V. The influence of ultrasonic mechanical activation on crystallization kinetics and martensitic transformations of TiNi-based amorphous alloys. *Vektor nauki Tolyattinskogo gosudarstvennogo universiteta*, 2017, no. 3, pp. 90–96. DOI: 10.18323/2073-5073-2017-3-90-96.

35. Becker M., Kuball A., Ghavimi A., Adam B., Busch R., Gallino I., Balle F. Solid state joining of a cold rolled Zr-based bulk metallic glass to a wrought aluminum alloy by power ultrasonics. *Materials*, 2022, vol. 15, no. 21, article number 7673. DOI: 10.3390/ma15217673.

36. Bakai S.A., Volchok O.I., Stoev P.I., Kamyshanchenko N.V., Kungurtsev E.S. Effect of the ultrasound action on the acoustic emission and mechanical properties of zirconium-based bulk metallic glasses. *Acoustical Physics*, 2012, vol. 58, no. 3, pp. 277–280. DOI: 10.1134/S1063771012020029.

37. Bakai S.A., Bulatov A.S., Klochko V.S., Korniets A.V., Fateev M.P. On the low-temperature absorption of longitudinal ultrasound in $Zr_{52.5}Ti_5Cu_{17.9}Ni_{14.6}Al_{10}$ bulk metallic glass. *Low Temperature Physics*, 2012, vol. 38, no. 10, pp. 948–951. DOI: 10.1063/1.4758778.

38. Tsaregradskaya T.L., Kozachenko V.V., Kuryliuk A.M., Turkov O.V., Saenko G.V. Effect of ultrasonic treatment on phase formation processes in amorphous alloy $Fe_{76}Ni_4Si_{14}B_6$. *Journal of Nano- and Electronic Physics*, 2019, vol. 11, no. 3, article number 03031. DOI: 10.21272/jnep.11(3).03031.

39. Vasilev M.A., Tinkov V.A., Petrov Yu.N., Voloshko S.M., Galstyan G.G., Cherepin V.T., Khodakovskiy A.S. Nanocrystallization of amorphous alloy $Fe_{73.6}Si_{15.8}B_{7.2}Cu_{1.0}Nb_{2.4}$ (Finemet) under ultrasonic impact treatment. *Metallofizika i noveyshie tekhnologii*, 2013, vol. 35, no. 5, pp. 667–675.

40. Blaha F., Langenecker B. Dehnung von zink-kristallen unter ultraschalleinwirkung. *Naturwissenschaften*, 1955, vol. 42, no. 20, pp. 556–557. DOI: 10.1007/BF00623773.

41. Langenecker B. Effects of ultrasound on deformation characteristics of metals. *IEEE Transactions on Sonics and Ultrasonics*, 1966, vol. 13, no. 1, pp. 1–8. DOI: 10.1109/T-SU.1966.29367.

42. Li Ning, Xu Xiaona, Zheng Zhizhen, Liu Lin. Enhanced formability of a Zr-based bulk metallic glass in a supercooled liquid state by vibrational loading. *Acta Materialia*, 2014, vol. 65, pp. 400–411. DOI: 10.1016/j.actamat.2013.11.009.

43. Han Guangchao, Peng Zhuo, Xu Linhong, Li Ning. Ultrasonic vibration facilitates the micro-formability of a Zr-based metallic glass. *Materials*, 2018, vol. 11, no. 12, article number 2568. DOI: 10.3390/ma11122568.

44. Lou Yan, Liu Xiao, Yang Xiaole, Ge Yang, Zhao Dandan, Wang Hao, Zhang Lai-Chang, Liu Zhiyuan. Fast rejuvenation in bulk metallic glass induced by ultrasonic vibration precompression. *Intermetallics*, 2020, vol. 118, no. 5, article number 106687. DOI: 10.1016/j.intermet.2019.106687.

45. Chen Zhe, Ren Shuai, Zhao Rui et al. Plasticity and rejuvenation of aged metallic glasses by ultrasonic vibrations. *Journal of Materials Science and Technology*, 2024, vol. 181, pp. 231–239. DOI: 10.1016/j.jmst.2023.09.029.

46. Li Ning, Chen Wen, Liu Lin. Thermoplastic microforming of bulk metallic glasses: a review. *JOM*, 2016, vol. 68, no. 4, pp. 1246–1261. DOI: 10.1007/s11837-016-1844-y.

47. Zhao R., Jiang H.Y., Luo P., Shen L.Q., Wen P., Sun Y.H., Bai H.Y., Wang W.H. Reversible and irreversible β-relaxations in metallic glasses. *Physical Review B*, 2020, vol. 101, no. 9, article number 094203. DOI: 10.1103/PhysRevB.101.094203.

48. Li X., Wei D., Zhang J.Y. et al. Ultrasonic plasticity of metallic glass near room temperature. *Applied Materials Today*, 2020, vol. 21, no. 3, article number 100866. DOI: 10.1016/j.apmt.2020.100866.

49. Yuan Chenchen, Liu Rui, Lv Zhuwei, Li Xin, Pang Changmeng, Yang Can, Ma Jiang, Wang Weihua. Softening in an ultrasonic-vibrated Pd-based metallic glass. *Intermetallics*, 2022, vol. 144, article number 107527. DOI: 10.1016/j.intermet.2022.107527.

50. Yuan C.C., Lv Z.W., Li X. et al. Ultrasonic-promoted defect activation and structural rejuvenation in a La-based metallic glass. *Intermetallics*, 2023, vol. 153, article number 107803. DOI: 10.1016/j.intermet.2022.107803.

51. Li Hongzhen, Yan Yuqiang, Sun Fei, Li Kangsen, Luo Feng, Ma Jiang. Shear punching of amorphous alloys under high-frequency vibrations. *Metals*, 2019, vol. 9, no. 11, article number 1158. DOI: 10.3390/met9111158.

52. Ma Jiang, Liang Xiong, Wu Xiaoyu, Liu Zhiyuan, Gong Feng. Sub-second thermoplastic forming of bulk metallic glasses by ultrasonic beating. *Scientific Reports*, 2015, vol. 5, article number 17844. DOI: 10.1038/srep17844.

53. Luo Feng, Sun Fei, Li Kangsen, Gong Feng, Liang Xiong, Wu Xiaoyu, Ma Jiang. Ultrasonic assisted micro-shear punching of amorphous alloy. *Materials Research Letters*, 2018, vol. 6, no. 10, pp. 545–551. DOI: 10.1080/21663831.2018.1500399.

54. Li Xin, Li Luyao, Sohrabi S. et al. Ultrasonic vibration enabled under-liquid forming of metallic glasses. *Science Bulletin*, 2024, vol. 69, no. 2, pp. 163–166. DOI: 10.1016/j.scib.2023.11.049.

55. González S., Sort J., Louzguine-Luzgin D.V., Perepezko J.H., Baró M.D., Inoue A. Tuning the microstructure and mechanical properties of Al-based amorphous/crystalline composites by addition of Pd. *Intermetallics*, 2010, vol. 18, no. 12, pp. 2377–2384. DOI: 10.1016/j.intermet.2010.08.036.

56. Song Wenli, Wu Yuan, Wang Hui, Liu Xiongjun, Chen Houwen, Guo Zhenxi, Lu Zhaoping. Microstructural control via copious nucleation manipulated by in situ formed nucleants: large-sized and ductile metallic glass composites. *Advanced Materials*, 2016, vol. 28, no. 37, pp. 8156–8161. DOI: 10.1002/adma.201601954.

57. Khademian N., Gholamipour R., Shahri F., Tamizifar M. Effect of vanadium substitution for zirconium on the glass forming ability and mechanical properties of a $Zr_{65}Cu_{17.5}Ni_{10}Al_{7.5}$ bulk metallic glass. *Journal of Alloys and Compounds*, 2013, vol. 546, pp. 41–47. DOI: 10.1016/j.jallcom.2012.08.035.

58. Jang J.S.C., Wu K.C., Jian S.R., Hsieh P.J., Huang J.C., Liu C.T. A Ni-free Zr-based bulk metallic glass with remarkable plasticity. *Journal of Alloys and Compounds*, 2011, vol. 509, pp. S109–S114. DOI: 10.1016/j.jallcom.2011.01.209.

59. Wu Y., Wang H., Liu X.J., Chen X.H., Hui X.D., Zhang Y., Lu Z.P. Designing bulk metallic glass composites with enhanced formability and plasticity. *Journal of Materials Science and Technology*, 2014, vol. 30, no. 6, pp. 566–575. DOI: 10.1016/j.jmst.2014.03.028.

60. Zhao Yan Chun, Ma Wen Long, Yuan Xiao Peng, Zhao Zhi Ping, Huang Ming Yuan, Kou Sheng Zhong, Li Chun Yan. Influence of annealing treatment on microstructure and mechanical properties of Fe-Cu-Si-Al amorphous composites. *Materials Science Forum*, 2016, vol. 849, pp. 71–75. DOI: 10.4028/www.scientific.net/MSF.849.71.

61. Lee J.I., Kim S.Y., Park E.S. In-situ synthesis and mechanical properties of Zr-based bulk metallic glass matrix composites manipulated by nitrogen additions. *Intermetallics*, 2017, vol. 91, pp. 70–77. DOI: 10.1016/j.intermet.2017.08.005.

62. Wang Tuo, Wu Yidong, Si Jiajia, Liu Yanhui, Hui Xidong. Plasticizing and work hardening in phase separated Cu-Zr-Al-Nb bulk metallic glasses by deformation induced nanocrystallization. *Materials and Design*, 2018, vol. 142, pp. 74–82. DOI: 10.1016/j.matdes.2018.01.003.

63. Wang D.P., Yang Y., Niu X.R., Lu J., Yang G.N., Wang W.H., Liu C.T. Resonance ultrasonic actuation and local structural rejuvenation in metallic glasses. *Physical Review B*, 2017, vol. 95, article number 235407. DOI: 10.1103/PhysRevB.95.235407.

64. Yu Jiangtao, Lou Yan, Wang Zhaoyi, Yang Lingyun, Huang Guijian, Ma Jiang. Revealing the mechanical responses and accommodation mechanisms of Cu-based amorphous composites under elastic preload and ultrasonic vibration treatment. *Journal of Non-Crystalline Solids*, 2024, vol. 629, article number 122875. DOI: 10.1016/j.jnoncrysol.2024.122875.

65. Lou Yan, Yang Lingyun, Xv Shenpeng, Ma Jiang. Fast increase in ductility and strength of Zr-based bulk amorphous alloys induced by intermittent high-frequency vibration loading. *Intermetallics*, 2022, vol. 142, article number 107467. DOI: 10.1016/j.intermet.2022.107467.

66. Zhai W., Nie L.H., Hui X.D., Xiao Y., Wang T., Wei B. Ultrasonic excitation induced nanocrystallization and toughening of $Zr_{46.75}Cu_{46.75}Al_{6.5}$ bulk metallic glass. *Journal of Materials Science and Technology*, 2020, vol. 45, pp. 157–161. DOI: 10.1016/j.jmst.2019.10.035.

67. Zhang Yu, Sohrabi Sajad, Li Xin, Ren Shuai, Ma Jiang. Tailored gradient nanocrystallization in bulk metallic glass via ultrasonic vibrations. *Journal of Materials Science and Technology*, 2025, vol. 210, pp. 109–120. DOI: 10.1016/j.jmst.2024.05.027.

68. Zhang Y., Zhao H., Yan Y.Q., Tong X., Ma Jiang, Ke Haibo, Wang Weihua. Ultrasonic-assisted fabrication of metallic glass composites. *Journal of Non-Crystalline Solids*, 2022, vol. 597, article number 121894. DOI: 10.2139/ssrn.4039426.

69. Chirkova V.V., Abrosimova G.E., Pershina E.A., Volkov N.A., Aronin A.S. Influence of a Ta Coating on the Crystallization of Deformed Amorphous Alloys $Fe_{78}Si_{13}B_9$ and $Al_{87}Ni_8Gd_5$. *Journal of Surface Investigation: X-ray, Synchrotron and Neutron Techniques*, 2023, vol. 17, pp. 1192–1198. DOI: 10.1134/S1027451023060083.

70. Abrosimova G., Chirkova V., Matveev D., Pershina E., Volkov N., Aronin A. Influence of a protective coating on the crystallization of an amorphous $Fe_{78}Si_{13}B_9$ alloy. *Metals*, 2023, vol. 13, no. 6, article number 1090. DOI: 10.3390/met13061090.

71. Kawamura Y., Ohno Y. Spark welding of $Zr_{55}Al_{10}Ni_5Cu_{30}$ bulk metallic glass. *Scripta Materialia*, 2001, vol. 45, no. 2, pp. 127–132. DOI: 10.1016/S1359-6462(01)01003-X.

72. Kim J., Kawamura Y. Electron beam welding of Zr-based BMG/Ni joints: effect of beam irradiation position on mechanical and microstructural properties. *Journal of Materials Processing Technology*, 2008, vol. 207, no. 1-3, pp. 112–117. DOI: 10.1016/j.jmatprotec.2007.12.090.

73. Shoji T., Kawamura Y., Ohno Y. Friction welding of bulk metallic glasses to different ones. *Materials Science and Engineering: A*, 2004, vol. 375–377, pp. 394–398. DOI: 10.1016/j.msea.2003.10.183.

74. Xu Z., Ma L., Yang J., Zhang J., Yan J. Ultrasonic-induced rising and wetting of a Sn-Zn filler in an aluminum joint. *Welding Journal*, 2016, vol. 95, pp. 264–272.

75. Xu Zhiwu, Ma Lin, Yan Jiuchun, Yang Shiqin, Du Shanyi. Wetting and oxidation during ultrasonic soldering of an alumina reinforced aluminum–copper–magnesium (2024 Al) matrix composite. *Composites Part A: Applied Science and Manufacturing*, 2012, vol. 43, no. 3, pp. 407–414. DOI: 10.1016/j.compositesa.2011.12.006.

76. Lai Zhiwei, Xie Ruishan, Pan Chuan, Chen Xiaoguang, Liu Lei, Wang Wenxian, Zou Guisheng. Ultrasound-assisted transient liquid phase bonding of magnesium alloy using brass interlayer in air. *Journal of Materials Science and Technology*, 2017, vol. 33, no. 6, pp. 567–572. DOI: 10.1016/j.jmst.2016.11.002.

77. Ji Hongjun, Li Long, Wang Lijie, Li Mingyu. Microstructures and properties of the Fe-based amorphous foil/aluminum dissimilar joint by ultrasonic-assisted

soldering. *Welding in the World*, 2015, vol. 59, pp. 623–628. DOI: 10.1007/s40194-015-0237-0.

78. Tamura S., Tsunekawa Y., Okumiya M., Hatakeyama M. Ultrasonic cavitation treatment for soldering on Zr-based bulk metallic glass. *Journal of Materials Processing Technology*, 2008, vol. 206, no. 1-3, pp. 322–327. DOI: 10.1016/j.jmatprotec.2007.12.032.

79. Xu Zhiwu, Li Zhengwei, Zhong Shijiang, Ma Zhipeng, Yan Jiuchun. Wetting mechanism of Sn to $Zr_{50.7}Cu_{28}Ni_9Al_{12.3}$ bulk metallic glass assisted by ultrasonic treatment. *Ultrasonics Sonochemistry*, 2018, vol. 48, no. 1, pp. 207–217. DOI: 10.1016/j.ultsonch.2018.05.036.

80. Wang Jiahao, Liu Senji, Huang Pengyu, Liu Junsheng, Zhang Yu, Liang Xiong, Sohrabi Sajad, Ma Jiang. Ultrasonic powder consolidation of metallic glass/Al-6061 composites. *Intermetallics*, 2024, vol. 174, article number 108462. DOI: 10.1016/j.intermet.2024.108462.

81. Liang Xiong, Zhu XiaoLong, Li Xin, Mo RuoDong, Liu YongJing, Wu Kai, Ma Jiang. High-entropy alloy and amorphous alloy composites fabricated by ultrasonic vibrations. *Science China: Physics, Mechanics and Astronomy*, 2020, vol. 63, no. 11, article number 116111. DOI: 10.1007/s11433-020-1560-4.

82. Liang Xiong, Wu Kai, Fu Jianan et al. Fabrication of amorphous and high-entropy biphasic composites using high-frequency ultrasonic vibration. *Journal of Non-Crystalline Solids*, 2022, vol. 582, article number 121458. DOI: 10.1016/j.jnoncrysol.2022.121458.

83. Kim J. Weld ability of $Cu_{54}Zr_{22}Ti_{18}Ni_6$ bulk metallic glass by ultrasonic welding processing. *Materials Letters*, 2014, vol. 130, pp. 160–163. DOI: 10.1016/j.matlet.2014.05.056.

84. Zhang Xingyi, Xiao Yong, Wang Ling, Wan Chao, Wang Qiwei, Sheng Hongchao, Li Mingyu. Ultrasound-induced liquid/solid interfacial reaction between Zn-3Al alloy and Zr-based bulk metallic glasses. *Ultrasonics Sonochemistry*, 2018, vol. 45, pp. 86–94. DOI: 10.1016/j.ultsonch.2018.03.006.

85. Song Xiao Cun, Zhu Zheng Qiang, Chen Yan Fei. Ultrasonic welding of $Fe_{78}Si_9B_{13}$ metallic glass. *Materials Science Forum*, 2014, vol. 809, pp. 348–353. DOI: 10.4028/www.scientific.net/MSF.809-810.348.

86. Wu Wenzheng, Jiang Jili, Li Guiwei, Fuh Jerry Ying His, Jiang Hao, Gou Pengwei, Zhang Longjian, Liu Wei, Zhao Ji. Ultrasonic additive manufacturing of bulk Ni-based metallic glass. *Journal of Non-Crystalline Solids*, 2019, vol. 506, pp. 1–5. DOI: 10.1016/j.jnoncrysol.2018.12.008.

87. Li Guiwei, Zhao Ji, Fuh Jerry Ying His, Wu Wenzheng, Jiang Jili, Wang Tianqi, Chang Shuai. Experiments on the ultrasonic bonding manufacturing of metallic glass and crystalline metal composite. *Materials*, 2019, vol. 12, no. 18, article number 2975. DOI: 10.3390/ma12182975.

88. Li Z., Huang Z., Sun F., Li X., Ma J. Forming of metallic glasses: mechanisms and processes. *Materials Today Advances*, 2020, vol. 7, article number 100077. DOI: 10.1016/j.mtadv.2020.100077.

89. Li Luyao, Li Xin, Huang Zhiyuan et al. Joining of metallic glasses in liquid via ultrasonic vibrations. *Nature Communications*, 2023, vol. 14, no. 1, article number 6305. DOI: 10.1038/s41467-023-42014-x.

90. Telford M. The case for bulk metallic glass. *Materials Today*, 2004, vol. 7, no. 3, pp. 36–43. DOI: 10.1016/S1369-7021(04)00124-5.

91. Li W., Wang C., Li L.Y. et al. Manipulating defects in metallic glasses via ultrasonic treatment. *International Journal of Mechanical Sciences*, 2025, vol. 287, article number 109960. DOI: 10.1016/j.ijmecsci.2025.109960.

**СПИСОК ЛИТЕРАТУРЫ**

1. Glezer A.M., Permyakova I.E. Melt-quenched nanocrystals. Boca Raton: CRC Press, Taylor & Francis Group, 2013. 369 p. DOI: 10.1201/b15028.

2. Greer A.L., Costa M.B., Houghton O.S. Metallic glasses // MRS Bulletin. 2023. Vol. 48. P. 1054–1061. DOI: 10.1557/s43577-023-00586-5.

3. Gao K., Zhu X.G., Chen L. et al. Recent development in the application of bulk metallic glasses // Journal of Materials Science and Technology. 2022. Vol. 131. P. 115–121. DOI: 10.1016/j.jmst.2022.05.028.

4. Khan M.M., Nemati A., Rahman Z.U., Shah U.H., Asgar H., Haider W. Recent advancements in bulk metallic glasses and their applications: a review // Critical Reviews in Solid State and Material Sciences. 2018. Vol. 43. № 3. P. 233–268. DOI: 10.1080/10408436.2017.1358149.

5. Amorphous and nanocrystalline materials: preparation, properties, and applications / eds. A. Inoue, K. Hashimoto. Berlin: Springer, 2001. 206 p. DOI: 10.1007/978-3-662-04426-1.

6. Trexler M.M., Thadhani N.N. Mechanical properties of bulk metallic glasses // Progress in Materials Science. 2010. Vol. 55. № 8. P. 759–839. DOI: 10.1016/j.pmatsci.2010.04.002.

7. Глезер А.М., Пермякова И.Е., Громов В.Е., Коваленко В.В. Механическое поведение аморфных сплавов. Новокузнецк: СибГИУ, 2006. 416 с.

8. Dong Quan, Tan Jun, Li Caiju, Sarac B., Eckert J. Room-temperature plasticity of metallic glass composites: a review // Composites Part B: Engineering. 2024. Vol. 280. Article number 111453. DOI: 10.1016/j.compositesb.2024.111453.

9. Zhang M., Chen Y., Li W. On the origin of softening in the plastic deformation of metallic glasses // International Journal of Plasticity. 2019. Vol. 116. P. 24–38. DOI: 10.1016/j.ijplas.2018.12.004.

10. Hufnagel T.C., Schuh C.A., Falk M.L. Deformation of metallic glasses: recent developments in theory, simulations, and experiments // Acta Materialia. 2016. Vol. 109. P. 375–393. DOI: 10.1016/j.actamat.2016.01.049.

11. Permyakova I., Glezer A. Mechanical behavior of Fe- and Co-based amorphous alloys after thermal action // Metals. 2022. Vol. 12. № 2. Article number 297. DOI: 10.3390/met12020297.

12. Maaß R., Löffler J.F. Shear-band dynamics in metallic glasses // Advanced Functional Materials. 2015. Vol. 25. № 16. P. 2353–2368. DOI: 10.1002/adfm.201404223.

13. Shelyakov A., Sitnikov N., Zaletova I., Borodako K., Tabachkova N. Study of structure and phase transformations in rejuvenated rapidly quenched TiNiCu alloys //

Metals. 2023. Vol. 13. № 7. Article number 1175. DOI: 10.3390/met13071175.

14. Priezjev N.V. The effect of thermal history on the atomic structure and mechanical properties of amorphous alloys // Computational Materials Science. 2020. Vol. 174. Article number 109477. DOI: 10.1016/j.commatsci.2019.109477.

15. Di Siyi, Zhou Jing, Cai Mingjuan, Cui Jingxian, Li Xuesong, Shen Baolong, Ke Haibo, Wang Qianqian. Improved ductility of annealed Fe-based metallic glass with good soft magnetic property by cryogenic thermal cycling // Journal of Alloys and Compounds. 2023. Vol. 960. Article number 170686. DOI: 10.1016/j.jallcom.2023.170686.

16. Sohrabi S., Sun B.Y., Mahmoodan M., Sun Y.H., Gholamipour R., Wang W.H. Rejuvenation by compressive elasto-static loading: the role of static stress on a Zr-based metallic glass // Journal of Alloys and Compounds. 2023. Vol. 933. Article number 167715. DOI: 10.1016/j.jallcom.2022.167715.

17. Zhang Sailong, Shi Bo, Wang Jinhui, Xu Yuanli, Jin Peipeng. Rejuvenation of a naturally aged bulk metallic glass by elastostatic loading // Materials Science and Engineering: A. 2021. Vol. 806. Article number 140843. DOI: 10.1016/j.msea.2021.140843.

18. Khademorezaian S., Tomut M., Peterlechner M., da Silva Pinto M.W., Rösner H., Divinski S., Wilde G. Extreme rejuvenation of a bulk metallic glass at the nanoscale by swift heavy ion irradiation // Journal of Alloys and Compounds. 2024. Vol. 980. Article number 173571. DOI: 10.1016/j.jallcom.2024.173571.

19. Boukhemkhem W., Izerrouken M., Ghidelli M., Pardoen T., Sari A., Khereddine A.Y., Meftah A. Swift heavy ion irradiation effect on structural, morphological and mechanical properties of $Zr_{70}Ni_{30}$ metallic glass // Physica Scripta. 2023. Vol. 98. № 8. Article number 085311. DOI: 10.1088/1402-4896/ace387.

20. Zhang C.Y., Zhu Z.W., Li S.T., Wang Y.Y., Li Z.K., Li H., Yuan G., Zhang H.F. Shear band evolution and mechanical behavior of cold-rolled Zr-based amorphous alloy sheets: an in-situ study // Journal of Materials Science and Technology. 2024. Vol. 181. P. 115–127. DOI: 10.1016/j.jmst.2023.09.022.

21. Stolpe M., Kruzic J.J., Busch R. Evolution of shear bands, free volume and hardness during cold rolling of a Zr-based bulk metallic glass // Acta Materialia. 2014. Vol. 64. P. 231–240. DOI: 10.1016/j.actamat.2013.10.035.

22. Permyakova I., Glezer A. Amorphous-nanocrystalline composites prepared by high-pressure torsion // Metals. 2020. Vol. 10. № 4. Article number 511. DOI: 10.3390/met10040511.

23. Bazlov A.I., Parkhomenko M.S., Ubyivovk E.V., Zanaeva E.N., Bazlova T.A., Gunderov D.V. Severe plastic deformation influence on the structure transformation of the amorphous $Zr_{62.5}Cu_{22.5}Al_{10}Fe_5$ alloy // Intermetallics. 2023. Vol. 152. Article number 107777. DOI: 10.1016/j.intermet.2022.107777.

24. Yang Zhichao, Zhu Lida, Zhang Guixiang, Ni Chenbing, Lin Bin. Review of ultrasonic vibration-assisted machining in advanced materials // International Journal of Machine Tools and Manufacture. 2020. Vol. 156. Article number 103594. DOI: 10.1016/j.ijmachtools.2020.103594.

25. Behal J., Maru M.S., Katwal R., Pathak D., Kumar V. Ultrasonic assisted green synthesis approach for nanotechnological materials // Journal of Alloys and Compounds Communications. 2024. Vol. 3. Article number 100013. DOI: 10.1016/j.jacomc.2024.100013.

26. Yang Jingwei, Xie Chuhao, Zhang Jie, Qiao Jian. Design strategies for enhancing strength and toughness in ultrasonic welding of dissimilar metals: a review // Materials Today Communications. 2025. Vol. 42. Article number 111502. DOI: 10.1016/j.mtcomm.2025.111502.

27. Power ultrasonics: Applications of high-intensity ultrasound / eds. J.A. Gallego-Juárez, K.F. Graff. Oxford: Woodhead Publishing, 2023. 946 p. DOI: 10.1016/C2019-0-00783-2.

28. Смирнов О.М., Глезер А.М. Влияние ультразвуковой обработки на охрупчивание аморфных сплавов при термообработке // Физика и химия обработки материалов. 1992. № 3. С. 131–134.

29. Смирнов О.М., Глезер А.М., Овчаров В.П., Худякова Е.В. Способ получения аморфных сплавов: описание изобретения к авторскому свидетельству № SU 1787665 A1, 1993. 3 с. EDN: PGXVAV.

30. Ichitsubo T., Kai S., Ogi H., Hirao M., Tanaka K. Elastic and anelastic behavior of $Zr_{55}Al_{10}Ni_5Cu_{30}$ bulk metallic glass around the glass transition temperature under ultrasonic excitation. // Scripta Materialia. 2003. Vol. 49. № 4. P. 267–271. DOI: 10.1016/S1359-6462(03)00294-X.

31. Ichitsubo T., Matsubara E., Yamamoto T., Chen H.S., Nishiyama N., Saida J., Anazawa K. Microstructure of fragile metallic glasses inferred from ultrasoundaccelerated crystallization in Pd-based metallic glasses // Physical Review Letters. 2005. Vol. 95. Article number 245501. DOI: 10.1103/PhysRevLett.95.245501.

32. Maeda M., Takahashi Y., Fukuhara M., Xinmin Wang, Inoue A. Ultrasonic bonding of $Zr_{55}Cu_{30}Ni_5Al_{10}$ metallic glass // Materials Science and Engineering: B. 2008. Vol. 148. № 1-3. P. 141–144. DOI: 10.1016/j.mseb.2007.09.028.

33. Ma Chi, Qin Haifeng, Ren Zhencheng, O'Keeffe S.C., Stevick J., Doll G.L., Dong Yalin, Winiarski B., Ye Chang. Increasing fracture strength in bulk metallic glasses using ultrasonic nanocrystal surface modification // Journal of Alloys and Compounds. 2017. Vol. 718. P. 246–253. DOI: 10.1016/j.jallcom.2017.05.056.

34. Непомнящая В.В., Рубаник В.В. Влияние ультразвуковой механоактивации на кинетику кристаллизации и мартенситные превращения аморфного сплава на основе TiNi // Вектор науки Тольяттинского государственного университета. 2017. № 3. С. 90–96. DOI: 10.18323/2073-5073-2017-3-90-96.

35. Becker M., Kuball A., Ghavimi A., Adam B., Busch R., Gallino I., Balle F. Solid state joining of a cold rolled Zr-based bulk metallic glass to a wrought aluminum alloy by power ultrasonics // Materials. 2022. Vol. 15. № 21. Article number 7673. DOI: 10.3390/ma15217673.

36. Бакай С.А., Волчок О.И., Стоев П.И., Камышанченко Н.В., Кунгурцев Е.С. Влияние ультразвукового воздействия на акустическую эмиссию и механические свойства объемных металлических стекол на основе циркония // Акустический журнал. 2012. Т. 58. № 3. С. 304–307. EDN: OXXVET.

37. Бакай С.А., Булатов А.С., Клочко В.С., Корниец А.В., Фатеев М.П. О низкотемпературном поглощении продольного ультразвука в объемном металлическом стекле $Zr_{52,5}Ti_5Cu_{17,9}Ni_{14,6}Al_{10}$ // Физика низких температур. 2012. Т. 38. № 10. С. 1197–1201. EDN: PCRCYT.

38. Tsaregradskaya T.L., Kozachenko V.V., Kuryliuk A.M., Turkov O.V., Saenko G.V. Effect of ultrasonic treatment on phase formation processes in amorphous alloy $Fe_{76}Ni_4Si_{14}B_6$ // Journal of Nano- and Electronic Physics. 2019. Vol. 11. № 3. Article number 03031. DOI: 10.21272/jnep.11(3).03031.

39. Васильев М.А., Тиньков В.А., Петров Ю.Н., Волошко С.М., Галстян Г.Г., Черепин В.Т., Ходаковский А.С. Нанокристаллизация аморфного сплава $Fe_{73,6}Si_{15,8}B_{7,2}Cu_{1,0}Nb_{2,4}$ (Finemet) под действием ультразвуковой ударной обработки // Металлофизика и новейшие технологии. 2013. Т. 35. № 5. С. 667–675.

40. Blaha F., Langenecker B. Dehnung von zink-kristallen unter ultraschalleinwirkung // Naturwissenschaften. 1955. Vol. 42. № 20. P. 556–557. DOI: 10.1007/BF00623773.

41. Langenecker B. Effects of ultrasound on deformation characteristics of metals // IEEE Transactions on Sonics and Ultrasonics. 1966. Vol. 13. № 1. P. 1–8. DOI: 10.1109/T-SU.1966.29367.

42. Li Ning, Xu Xiaona, Zheng Zhizhen, Liu Lin. Enhanced formability of a Zr-based bulk metallic glass in a supercooled liquid state by vibrational loading // Acta Materialia. 2014. Vol. 65. P. 400–411. DOI: 10.1016/j.actamat.2013.11.009.

43. Han Guangchao, Peng Zhuo, Xu Linhong, Li Ning. Ultrasonic vibration facilitates the micro-formability of a Zr-based metallic glass // Materials. 2018. Vol. 11. № 12. Article number 2568. DOI: 10.3390/ma11122568.

44. Lou Yan, Liu Xiao, Yang Xiaole, Ge Yang, Zhao Dandan, Wang Hao, Zhang Lai-Chang, Liu Zhiyuan. Fast rejuvenation in bulk metallic glass induced by ultrasonic vibration precompression // Intermetallics. 2020. Vol. 118. № 5. Article number 106687. DOI: 10.1016/j.intermet.2019.106687.

45. Chen Zhe, Ren Shuai, Zhao Rui et al. Plasticity and rejuvenation of aged metallic glasses by ultrasonic vibrations // Journal of Materials Science and Technology. 2024. Vol. 181. P. 231–239. DOI: 10.1016/j.jmst.2023.09.029.

46. Li Ning, Chen Wen, Liu Lin. Thermoplastic microforming of bulk metallic glasses: a review // JOM. 2016. Vol. 68. № 4. P. 1246–1261. DOI: 10.1007/s11837-016-1844-y.

47. Zhao R., Jiang H.Y., Luo P., Shen L.Q., Wen P., Sun Y.H., Bai H.Y., Wang W.H. Reversible and irreversible β-relaxations in metallic glasses // Physical Review B. 2020. Vol. 101. № 9. Article number 094203. DOI: 10.1103/PhysRevB.101.094203.

48. Li X., Wei D., Zhang J.Y. et al. Ultrasonic plasticity of metallic glass near room temperature // Applied Materials Today. 2020. Vol. 21. № 3. Article number 100866. DOI: 10.1016/j.apmt.2020.100866.

49. Yuan Chenchen, Liu Rui, Lv Zhuwei, Li Xin, Pang Changmeng, Yang Can, Ma Jiang, Wang Weihua. Softening in an ultrasonic-vibrated Pd-based metallic glass // Intermetallics. 2022. Vol. 144. Article number 107527. DOI: 10.1016/j.intermet.2022.107527.

50. Yuan C.C., Lv Z.W., Li X. et al. Ultrasonic-promoted defect activation and structural rejuvenation in a La-based metallic glass // Intermetallics. 2023. Vol. 153. Article number 107803. DOI: 10.1016/j.intermet.2022.107803.

51. Li Hongzhen, Yan Yuqiang, Sun Fei, Li Kangsen, Luo Feng, Ma Jiang. Shear punching of amorphous alloys under high-frequency vibrations // Metals. 2019. Vol. 9. № 11. Article number 1158. DOI: 10.3390/met9111158.

52. Ma Jiang, Liang Xiong, Wu Xiaoyu, Liu Zhiyuan, Gong Feng. Sub-second thermoplastic forming of bulk metallic glasses by ultrasonic beating // Scientific Reports. 2015. Vol. 5. Article number 17844. DOI: 10.1038/srep17844.

53. Luo Feng, Sun Fei, Li Kangsen, Gong Feng, Liang Xiong, Wu Xiaoyu, Ma Jiang. Ultrasonic assisted micro-shear punching of amorphous alloy // Materials Research Letters. 2018. Vol. 6. № 10. P. 545–551. DOI: 10.1080/21663831.2018.1500399.

54. Li Xin, Li Luyao, Sohrabi S. et al. Ultrasonic vibration enabled under-liquid forming of metallic glasses // Science Bulletin. 2024. Vol. 69. № 2. P. 163–166. DOI: 10.1016/j.scib.2023.11.049.

55. González S., Sort J., Louzguine-Luzgin D.V., Perepezko J.H., Baró M.D., Inoue A. Tuning the microstructure and mechanical properties of Al-based amorphous/crystalline composites by addition of Pd // Intermetallics. 2010. Vol. 18. № 12. P. 2377–2384. DOI: 10.1016/j.intermet.2010.08.036.

56. Song Wenli, Wu Yuan, Wang Hui, Liu Xiongjun, Chen Houwen, Guo Zhenxi, Lu Zhaoping. Microstructural control via copious nucleation manipulated by in situ formed nucleants: large-sized and ductile metallic glass composites // Advanced Materials. 2016. Vol. 28. № 37. P. 8156–8161. DOI: 10.1002/adma.201601954.

57. Khademian N., Gholamipour R., Shahri F., Tamizifar M. Effect of vanadium substitution for zirconium on the glass forming ability and mechanical properties of a $Zr_{65}Cu_{17.5}Ni_{10}Al_{7.5}$ bulk metallic glass // Journal of Alloys and Compounds. 2013. Vol. 546. P. 41–47. DOI: 10.1016/j.jallcom.2012.08.035.

58. Jang J.S.C., Wu K.C., Jian S.R., Hsieh P.J., Huang J.C., Liu C.T. A Ni-free Zr-based bulk metallic glass with remarkable plasticity // Journal of Alloys and Compounds. 2011. Vol. 509. P. S109–S114. DOI: 10.1016/j.jallcom.2011.01.209.

59. Wu Y., Wang H., Liu X.J., Chen X.H., Hui X.D., Zhang Y., Lu Z.P. Designing bulk metallic glass composites with enhanced formability and plasticity // Journal of Materials Science and Technology. 2014. Vol. 30. № 6. P. 566–575. DOI: 10.1016/j.jmst.2014.03.028.

60. Zhao Yan Chun, Ma Wen Long, Yuan Xiao Peng, Zhao Zhi Ping, Huang Ming Yuan, Kou Sheng Zhong, Li Chun Yan. Influence of annealing treatment on microstructure and mechanical properties of Fe-Cu-Si-Al amorphous composites // Materials Science Forum. 2016. Vol. 849. P. 71–75. DOI: 10.4028/www.scientific.net/MSF.849.71.

61. Lee J.I., Kim S.Y., Park E.S. In-situ synthesis and mechanical properties of Zr-based bulk metallic glass matrix composites manipulated by nitrogen additions // Intermetallics. 2017. Vol. 91. P. 70–77. DOI: 10.1016/j.intermet.2017.08.005.

62. Wang Tuo, Wu Yidong, Si Jiajia, Liu Yanhui, Hui Xidong. Plasticizing and work hardening in phase separated Cu-Zr-Al-Nb bulk metallic glasses by deformation induced nanocrystallization // Materials and Design. 2018. Vol. 142. P. 74–82. DOI: 10.1016/j.matdes.2018.01.003.

63. Wang D.P., Yang Y., Niu X.R., Lu J., Yang G.N., Wang W.H., Liu C.T. Resonance ultrasonic actuation and local structural rejuvenation in metallic glasses // Physical Review B. 2017. Vol. 95. Article number 235407. DOI: 10.1103/PhysRevB.95.235407.

64. Yu Jiangtao, Lou Yan, Wang Zhaoyi, Yang Lingyun, Huang Guijian, Ma Jiang. Revealing the mechanical responses and accommodation mechanisms of Cu-based amorphous composites under elastic preload and ultrasonic vibration treatment // Journal of Non-Crystalline Solids. 2024. Vol. 629. Article number 122875. DOI: 10.1016/j.jnoncrysol.2024.122875.

65. Lou Yan, Yang Lingyun, Xv Shenpeng, Ma Jiang. Fast increase in ductility and strength of Zr-based bulk amorphous alloys induced by intermittent high-frequency vibration loading // Intermetallics. 2022. Vol. 142. Article number 107467. DOI: 10.1016/j.intermet.2022.107467.

66. Zhai W., Nie L.H., Hui X.D., Xiao Y., Wang T., Wei B. Ultrasonic excitation induced nanocrystallization and toughening of $Zr_{46.75}Cu_{46.75}Al_{6.5}$ bulk metallic glass // Journal of Materials Science and Technology. 2020. Vol. 45. P. 157–161. DOI: 10.1016/j.jmst.2019.10.035.

67. Zhang Yu, Sohrabi Sajad, Li Xin, Ren Shuai, Ma Jiang. Tailored gradient nanocrystallization in bulk metallic glass via ultrasonic vibrations // Journal of Materials Science and Technology. 2025. Vol. 210. P. 109–120. DOI: 10.1016/j.jmst.2024.05.027.

68. Zhang Y., Zhao H., Yan Y.Q., Tong X., Ma Jiang, Ke Haibo, Wang Weihua. Ultrasonic-assisted fabrication of metallic glass composites // Journal of Non-Crystalline Solids. 2022. Vol. 597. Article number 121894. DOI: 10.2139/ssrn.4039426.

69. Чиркова В.В., Абросимова Г.Е., Першина Е.А., Волков Н.А., Аронин А.С. Влияние покрытия танталом на кристаллизацию деформированных аморфных сплавов $Fe_{78}Si_{13}B_9$ и $Al_{87}Ni_8Gd_5$ // Поверхность. Рентгеновские, синхротронные и нейтронные исследования. 2023. № 11. С. 16–23. DOI: 10.31857/S1028096023110080.

70. Abrosimova G., Chirkova V., Matveev D., Pershina E., Volkov N., Aronin A. Influence of a protective coating on the crystallization of an amorphous $Fe_{78}Si_{13}B_9$ alloy // Metals. 2023. Vol. 13. № 6. Article number 1090. DOI: 10.3390/met13061090.

71. Kawamura Y., Ohno Y. Spark welding of $Zr_{55}Al_{10}Ni_5Cu_{30}$ bulk metallic glass // Scripta Materialia. 2001. Vol. 45. № 2. P. 127–132. DOI: 10.1016/S1359-6462(01)01003-X.

72. Kim J., Kawamura Y. Electron beam welding of Zr-based BMG/Ni joints: effect of beam irradiation position on mechanical and microstructural properties // Journal of Materials Processing Technology. 2008. Vol. 207. № 1-3. P. 112–117. DOI: 10.1016/j.jmatprotec.2007.12.090.

73. Shoji T., Kawamura Y., Ohno Y. Friction welding of bulk metallic glasses to different ones // Materials Science and Engineering: A. 2004. Vol. 375–377. P. 394–398. DOI: 10.1016/j.msea.2003.10.183.

74. Xu Z., Ma L., Yang J., Zhang J., Yan J. Ultrasonic-induced rising and wetting of a Sn-Zn filler in an aluminum joint // Welding Journal. 2016. Vol. 95. P. 264–272.

75. Xu Zhiwu, Ma Lin, Yan Jiuchun, Yang Shiqin, Du Shanyi. Wetting and oxidation during ultrasonic soldering of an alumina reinforced aluminum–copper–magnesium (2024 Al) matrix composite // Composites Part A: Applied Science and Manufacturing. 2012. Vol. 43. № 3. P. 407–414. DOI: 10.1016/j.compositesa.2011.12.006.

76. Lai Zhiwei, Xie Ruishan, Pan Chuan, Chen Xiaoguang, Liu Lei, Wang Wenxian, Zou Guisheng. Ultrasound-assisted transient liquid phase bonding of magnesium alloy using brass interlayer in air // Journal of Materials Science and Technology. 2017. Vol. 33. № 6. P. 567–572. DOI: 10.1016/j.jmst.2016.11.002.

77. Ji Hongjun, Li Long, Wang Lijie, Li Mingyu. Microstructures and properties of the Fe-based amorphous foil/aluminum dissimilar joint by ultrasonic-assisted soldering // Welding in the World. 2015. Vol. 59. P. 623–628. DOI: 10.1007/s40194-015-0237-0.

78. Tamura S., Tsunekawa Y., Okumiya M., Hatakeyama M. Ultrasonic cavitation treatment for soldering on Zr-based bulk metallic glass // Journal of Materials Processing Technology. 2008. Vol. 206. № 1-3. P. 322–327. DOI: 10.1016/j.jmatprotec.2007.12.032.

79. Xu Zhiwu, Li Zhengwei, Zhong Shijiang, Ma Zhipeng, Yan Jiuchun. Wetting mechanism of Sn to $Zr_{50.7}Cu_{28}Ni_9Al_{12.3}$ bulk metallic glass assisted by ultrasonic treatment // Ultrasonics Sonochemistry. 2018. Vol. 48. № 1. P. 207–217. DOI: 10.1016/j.ultsonch.2018.05.036.

80. Wang Jiahao, Liu Senji, Huang Pengyu, Liu Junsheng, Zhang Yu, Liang Xiong, Sohrabi Sajad, Ma Jiang. Ultrasonic powder consolidation of metallic glass/Al-6061 composites // Intermetallics. 2024. Vol. 174. Article number 108462. DOI: 10.1016/j.intermet.2024.108462.

81. Liang Xiong, Zhu XiaoLong, Li Xin, Mo RuoDong, Liu YongJing, Wu Kai, Ma Jiang. High-entropy alloy and amorphous alloy composites fabricated by ultrasonic vibrations // Science China: Physics, Mechanics and Astronomy. 2020. Vol. 63. № 11. Article number 116111. DOI: 10.1007/s11433-020-1560-4.

82. Liang Xiong, Wu Kai, Fu Jianan et al. Fabrication of amorphous and high-entropy biphasic composites using high-frequency ultrasonic vibration // Journal of Non-Crystalline Solids. 2022. Vol. 582. Article number 121458. DOI: 10.1016/j.jnoncrysol.2022.121458.

83. Kim J. Weld ability of $Cu_{54}Zr_{22}Ti_{18}Ni_6$ bulk metallic glass by ultrasonic welding processing // Materials Letters. 2014. Vol. 130. P. 160–163. DOI: 10.1016/j.matlet.2014.05.056.

84. Zhang Xingyi, Xiao Yong, Wang Ling, Wan Chao, Wang Qiwei, Sheng Hongchao, Li Mingyu. Ultrasound-induced liquid/solid interfacial reaction between Zn-3Al alloy and Zr-based bulk metallic glasses // Ultrasonics Sonochemistry. 2018. Vol. 45. P. 86–94. DOI: 10.1016/j.ultsonch.2018.03.006.

85. Song Xiao Cun, Zhu Zheng Qiang, Chen Yan Fei. Ultrasonic welding of $Fe_{78}Si_9B_{13}$ metallic glass // Materials Science Forum. 2014. Vol. 809. P. 348–353. DOI: 10.4028/www.scientific.net/MSF.809-810.348.

86. Wu Wenzheng, Jiang Jili, Li Guiwei, Fuh Jerry Ying His, Jiang Hao, Gou Pengwei, Zhang Longjian, Liu Wei, Zhao Ji. Ultrasonic additive manufacturing of bulk Ni-based metallic glass // Journal of Non-Crystalline Solids. 2019. Vol. 506. P. 1–5. DOI: 10.1016/j.jnoncrysol.2018.12.008.

87. Li Guiwei, Zhao Ji, Fuh Jerry Ying His, Wu Wenzheng, Jiang Jili, Wang Tianqi, Chang Shuai. Experiments on the ultrasonic bonding manufacturing of metallic glass and crystalline metal composite // Materials. 2019. Vol. 12. № 18. Article number 2975. DOI: 10.3390/ma12182975.

88. Li Z., Huang Z., Sun F., Li X., Ma J. Forming of metallic glasses: mechanisms and processes // Materials Today Advances. 2020. Vol. 7. Article number 100077. DOI: 10.1016/j.mtadv.2020.100077.

89. Li Luyao, Li Xin, Huang Zhiyuan et al. Joining of metallic glasses in liquid via ultrasonic vibrations // Nature Communications. 2023. Vol. 14. № 1. Article number 6305. DOI: 10.1038/s41467-023-42014-x.

90. Telford M. The case for bulk metallic glass // Materials Today. 2004. Vol. 7. № 3. P. 36–43. DOI: 10.1016/S1369-7021(04)00124-5.

91. Li W., Wang C., Li L.Y. et al. Manipulating defects in metallic glasses via ultrasonic treatment // International Journal of Mechanical Sciences. 2025. Vol. 287. Article number 109960. DOI: 10.1016/j.ijmecsci.2025.109960.

# Влияние ультразвуковой обработки на структурные превращения и механическое поведение аморфных сплавов (ОБЗОР)

*Пермякова Инга Евгеньевна*[*1], доктор физико-математических наук, профессор,
ведущий научный сотрудник лаборатории физикохимии и механики металлических материалов
*Дюжева-Мальцева Елена Вадимовна*[2], аспирант
*Институт металлургии и материаловедения им. А.А. Байкова РАН, Москва (Россия)*

*E-mail: inga_perm@mail.ru

[1]ORCID: https://orcid.org/0000-0002-1163-3888
[2]ORCID: https://orcid.org/0000-0002-7199-487X

*Аннотация:* Широкое применение аморфных сплавов осложнено узким диапазоном их термической стабильности, охрупчиванием при повышенных температурах, труднообрабатываемостью, низкой пластичностью при растяжении. Ультразвуковая обработка является инновационным методом для решения этих проблем. Встраивание в технологическую цепочку ультразвуковой технологии может способствовать совершенствованию эксплуатационных характеристик аморфных сплавов, изготовлению из них деталей на разных масштабных уровнях, а также качественному соединению с другими материалами. Влияние ультразвуковых вибраций на структурные превращения и механическое поведение аморфных сплавов изучено не в полной мере. Отсутствие целостного научного обоснования физических процессов и сопутствующих эффектов в аморфных сплавах при ультразвуковом возбуждении препятствует развитию соответствующей технологии и оптимизации ее режимов. За последнее десятилетие исследователи предложили различные методики ультразвуковой обработки аморфных сплавов для улучшения их формуемости, достижения баланса пластичности и прочности, консолидирования друг с другом и с металлами. Кроме того, развиты определенные представления об омоложении их структуры, о возможностях перевода в частично нанокристаллическое состояние под действием ультразвука. Чтобы подвести итог этим разработкам, приводится систематическое обсуждение особенностей, параметров и режимов ультразвуковой обработки применительно к ленточным и объемным аморфным сплавам для улучшения их структурочувствительных свойств. На этой основе рассматриваются ограничения текущих исследований. К наиболее перспективным применениям ультразвуковых технологий для быстрозакаленных сплавов в ближайшем будущем следует отнести: их аддитивное производство, создание гибридных композитов за счет ультразвуковой сварки, ультразвуковое формование для изготовления изделий сложных форм и геометрии, комплексную многоэтапную обработку для получения уникального сочетания свойств (например, закалка из расплава → лазерное облучение → ультразвуковое стимулирование). Настоящий обзор расширяет существующие знания об ультразвуковом управлении свойствами, структурой аморфных сплавов и облегчает исследователям быстрый поиск ссылок по данной тематике.

*Ключевые слова:* аморфный сплав; ультразвуковая обработка; структурные превращения; механическое поведение; нанокристалл; омоложение структуры; композит; пластичность; формование.

**The Publishing Center** (until November 1, 2011 – the Editorial and Publishing Center) is a structural subdivision of Togliatti State University, which takes an important place in providing the educational process with high-quality instructional, educational, methodological, and scientific literature.
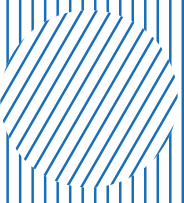
### TSU Publishing Center today

– Publishing center includes an editorial office and a printing shop. In recent years, the base of computer equipment, printing and post-printing equipment has been almost completely updated.

– It publishes books and electronic textbooks for students, graduate students, lecturers, and specialists in almost all branches of modern scientific knowledge, as well as popular science and reference literature, fiction, books of reports (papers) of conferences. Published literature corresponds to all areas of the educational cycles of the university disciplines.

– A considerable volume of printing job is the prompt execution of promotional and information products.

– The publishing center team is a collaboration of highly skilled professionals with wide work experience and young motivated employees.

– Publishing center employees participate in practical seminars to become acquainted with new opportunities in the field of printing technologies and equipment, as well as with advanced materials for digital printing.

### Main areas of activity

– Publication of paper-based educational and scientific literature, production of electronic educational and scientific aids.

– Implementation of editorial and publishing cycle stages: editing, production of original layouts, replication, pre-printing and post-printing treatment.

– Methodological and advisory work with the university departments on the issue of educational and scientific publications.

– Interaction with the Russian Book Chamber on the assignment of ISBNs to publications issued by Togliatti State University.

– Preparation of publications issued by Togliatti State University for state registration and sending of statutory copies.

– Markup of papers published in the TSU journals in the Articulus program to place on the eLibrary platform.

### Main achievements

– The results of the work were awarded with diplomas of the winners of the annual interregional and all-Russian University Book competitions.

– Publishing center regularly participates in the academic book exhibition of publishing activities "University – Science – City".

# Interrelation between the microstructure and impact toughness of the interface of welded joints of 32HGMA and 40HN2MA steels produced by rotary friction welding

*Elena Yu. Priymak*\*[1,2,4], PhD (Engineering), Associate Professor,
Head of the Laboratory of Metal Science and Heat Treatment,
Director of Research and Educational Center of New Materials and Advanced Technologies
*Artem S. Atamashkin*[2,5], PhD (Engineering), senior researcher
of Research and Educational Center of New Materials and Advanced Technologies
*Irina L. Yakovleva*[3,6], Doctor of Sciences (Engineering), chief researcher
of the Laboratory of Physical Metallurgy
*Andrey P. Fot*[1,7], Doctor of Sciences (Engineering), Professor,
Chief Scientific Secretary – Head of Department of Dissertation Councils

[1]*ZBO Drill Industries, Inc., Orenburg (Russia)*
[2]*Orenburg State University, Orenburg (Russia)*
[3]*M.N. Mikheev Institute of Metal Physics of the Ural Branch of RAS, Yekaterinburg (Russia)*

**\*E-mail:** e.prijmak@zbo.ru

[4]ORCID: https://orcid.org/0000-0002-4571-2410
[5]ORCID: https://orcid.org/0000-0003-3727-8738
[6]ORCID: https://orcid.org/0000-0001-8918-3066
[7]ORCID: https://orcid.org/0000-0002-2971-7908

*Abstract:* This paper covers the assessment of the influence of the morphological features of the microstructure of medium-carbon alloyed steels, formed at different forces in the process of rotary friction welding (RFW), on the impact toughness of their interface. The paper presents the results of an experimental study of a joint produced by welding tubular billets of 32HGMA and 40HN2MA steels with an outer diameter of 73 mm and a wall thickness of 9 mm with a change in force at the stage of friction (heating) of the billets. The studies of the microstructure, microhardness and impact toughness on samples with a V-notch of welded joints were carried out in the initial state after welding and after tempering at a temperature of 550 °C. Macro- and microfractographic analysis of the destroyed samples was carried out. The study shows that the friction force affects the kinetics of phase transformations, phase composition and microstructure homogeneity in the steel junction zone. With a decrease in this parameter of rotational friction welding, the microstructure heterogeneity associated with the occurrence of upper bainite areas with uneven precipitation of large carbide particles increases, which has a negative effect on the viscosity of the steel interface both in the initial state and after tempering; the fracture mechanism is quasi-cleavage. At higher values of the friction force, the density of high-angle boundaries and the dispersion of the bainite microstructure increase, which ensures higher viscosity and energy capacity of destruction with the formation of a pitted microrelief. The obtained results open up space for regulating the visco-plastic properties of welded joints even at the welding stage without subsequent recrystallisation of the weld zone.

*Keywords:* rotary friction welding; medium-carbon alloyed steels; welded joint interface; martensite; bainite; impact toughness.

*For citation:* Priymak E.Yu., Atamashkin A.S., Yakovleva I.L., Fot A.P. Interrelation between the microstructure and impact toughness of the interface of welded joints of 32HGMA and 40HN2MA steels produced by rotary friction welding. *Frontier Materials & Technologies*, 2025, no. 2, pp. 73–85. DOI: 10.18323/2782-4039-2025-2-72-6.

## INTRODUCTION

The efficiency of geological exploration and major repairs of oil wells depends on the reliability of the drill string. Development of deep wells requires a reduction in the weight of drill pipes, which can be achieved by using stronger steels with a decrease in wall thickness. 26H1MF, 32HMA, 32HGMA and other low- and medium-carbon steels alloyed with Cr, Mo and Mn to achieve an optimal combination of strength and ductility are widely used as the material for the drill pipe body [1–3]. As the material for locking parts, steels with a high carbon content are commonly used to further increase the strength, rigidity and wear resistance of the threaded connections used to assemble the drill string. They include 40HN, 40HN2MA and other steels [4; 5].

The connection of the lock part to the pipe body is usually carried out by means of rotary friction welding (RFW). This method allows joining difficult-to-weld materials, which include medium-carbon alloyed steels used for drill pipes. RFW has a number of technological advantages; the key ones are high productivity, the degree of automation and stability of the quality of welded joints [6–8].

Currently, there are two RFW methods: continuous drive friction welding (conventional), and inertia friction welding. The main difference between these options is the method of supplying the energy required for welding.

During continuous drive RFW, one of the billets is rotated by an electric motor shaft. The billet is rotated at a constant speed and is pressed against a stationary billet with a certain force, resulting in heating of the contact surfaces. When a certain degree of deformation (upset) is reached or after a specified time, the rotating billet quickly stops, and an increased axial forging force is applied to the billets. Cooling after welding is carried out in still air. The resulting burr is removed by mechanical treatment both from the outside and from the inside.

It is known that during rotary friction welding of steels, the billets are heated to the temperature of austenite formation, which undergoes a $\gamma \rightarrow \alpha$ transformation upon completion of the process [9; 10]. The degree of transformation is determined by both the chemical composition of steels and the technological parameters of welding. It is obvious that the applied force during friction of the billets will determine the heating temperature and the degree of deformation during welding, and, therefore, will affect the kinetics of austenite transformation in the thermomechanical influence area of welded joints and the mechanical properties of the joints that determine the reliability of drill pipes.

An analysis of literary sources has shown the existence of great interest in assessing the influence of the RFW parameters on the mechanical properties of joints of both homogeneous and dissimilar metals [6; 11; 12]. However, despite the abundance of published works, the information on rotary friction welding of carbon alloyed steels is limited. There are individual publications containing the results of studies of the microstructure and properties of welded joints of drill pipes made of N80 steels after normalisation with 42CrMo4 steel after quenching and tempering [13], AISI 8630 steel [9],

welded joints of ASTM A 106 Grade B steel in the hot-rolled condition and AISI 4140 steel after normalisation and after quenching and tempering [5; 10]. These works indicate that the mechanical properties of welded joints during tensile tests with correctly selected welding conditions are not inferior to, and in some cases even surpass, the mechanical properties of the least durable of the mating materials. However, except for the tensile properties, an important issue for drill pipes is the assessment of brittle fracture resistance, namely the impact toughness of welded joints. Little attention is paid to the study of this parameter in the presented publications. For example, in the work [5], it is noted that the weld seam has lower impact toughness values compared to the original ASTM A 106 Grade B and AISI 4140 steels. However, no studies of the influence of the RFW parameters on the impact toughness value are presented in the analysed publication. In the work [9], the impact toughness values of AISI 8630 steel joints obtained with different parameters of inertia friction welding are presented. However, no comparison with microstructural changes in the weld zone is given.

It is known that the visco-plastic properties of steels largely depend on the morphological features of the phase microstructure components [14–16], which, as shown above, are determined by the welding parameters.

The aim of this work is to evaluate the influence of the structural-phase state formed in the joint area of steels under different friction forces during rotary friction welding on the impact toughness and the mechanism of destruction of welded joints of 32HGMA and 40HN2MA steels used for the production of drill pipes.

## METHODS

The ingoing materials in this work were 32HGMA steel of S strength group according to API 5DP and 40HN2MA steel in the form of hot-rolled seamless pipes with an outside diameter of 73 mm and a wall thickness of 9 mm. The chemical composition of the selected steels, obtained using a Labspark 1000 optical emission spectrometer, is given in Table 1.

For 32HGMA steel, preliminary heat treatment included quenching from 870 °C and tempering at 580 °C with water cooling in a sprayer. For 40HN2MA steel, heat treatment consisted of normalisation at 880 °C, quenching from 860 °C with cooling in a water-polymer mixture, tempering at 580 °C with air cooling. The mechanical properties of the materials after heat treatment are given in Table 2.

Friction welding was performed using a 60-ton machine manufactured by Thompson Friction Welding company. The welding modes are given in Table 3. In this work, the friction force was varied while the forging force, rotation speed, and axial shortening were kept constant.

Some of the friction-welded samples were tempered at 550 °C for an hour in an SNOL chamber furnace.

The microstructure was studied on transverse sections after etching with a 4 % solution of nitric acid in ethanol. The macrostructure was studied using an Olympus DSX1000 optical microscope (Japan). The microstructure

| Steel grade | C | Mn | Si | S | P | Cr | Ni | Cu | Mo |
|---|---|---|---|---|---|---|---|---|---|
| 32HGMA | 0.32 | 0.82 | 0.36 | 0.005 | 0.010 | 0.98 | 0.15 | 0.14 | 0.31 |
| 40HN2MA | 0.44 | 0.49 | 0.25 | 0.005 | 0.008 | 0.72 | 1.24 | 0.20 | 0.14 |

**Table 2.** *Mechanical properties of 32HGMA and 40HN2MA steels after heat treatment*
**Таблица 2.** *Механические свойства сталей 32ХГМА и 40ХН2МА после термической обработки*

| Steel | Yield strength, MPa | Ultimate strength, MPa | Relative elongation, % | KCV, J/cm$^2$ |
|---|---|---|---|---|
| 32HGMA | 777–792 | 894–907 | 14.5–15.5 | 87.5–92.4 |
| 40HN2MA | 870–885 | 984–998 | 10.5–11.0 | 73.8–78.9 |

**Table 3.** *Rotary friction welding parameters*
**Таблица 3.** *Параметры ротационной сварки трением*

| Mode (sample) No. | Force during friction, kN | Rotation frequency during friction, rpm | Force during forging, kN | Upset during welding, mm |
|---|---|---|---|---|
| 1 | 100 | 600 | 220 | 7 |
| 2 | 145 | | | |

and fractographic analysis of the samples after impact bending tests were studied using a Tescan Mira 3 scanning electron microscope (Japan) at an accelerating voltage of 5 kV. The analysis of the steel interface using the electron backscatter diffraction (EBSD) method was carried out on a ThermoScience Scios 2 LoVac scanning electron microscope (Japan) with an Oxford Instrument Symmetry EBSD Detector attachment (Japan) using the AZtec software package. The microscope parameters at the time of shooting were as follows: accelerating voltage is 20 kV, probe current is 410 nA, and scanning step is 0.1 μm.

To determine the proportion of residual austenite in samples near the welded joint, X-ray structural analysis was used. The studies were carried out on a DRON-3M diffractometer (Russia) using copper $K_\alpha$ radiation at an accelerating voltage of 40 kV, a current force of 30 A, in the angular range of 30...90° with automatic data recording. The volume fraction of austenite was calculated from the ratio of the integral intensities of the diffraction lines $J$(III) of austenite and $J$(II0) of ferrite using the formula:

$$A_{res}, \% = \frac{100}{\dfrac{J(\text{II0})\alpha}{J(\text{III})\gamma} \times 0.742 + 1},$$

where $A_{res}$ is the fraction of residual austenite;
$J$(II0)α is the intensity of the ferrite diffraction line;
$J$(III)γ is the intensity of the austenite diffraction line.

Charpy impact bending tests on samples with a *V*-type stress concentrator were carried out on a WANCE PIT-100 pendulum impact tester (China). The samples for determining impact toughness had dimensions of 5×10×55 mm. The stress concentrator was applied in the zone of junction of two steels. Impact toughness values were determined as the average value of three identical samples.

## RESULTS

### Microstructure

Fig. 1 shows photographs of the macrostructure of welded joints produced with different friction forces. Approximately the same volume of upset metal (burr) on the side of both steels indicates their similar mechanical properties at elevated temperatures. In both samples, three characteristic zones are distinguished in the welding area: the joint zone, the thermomechanically affected zone (TMAZ), and the heat-affected zone (HAZ). This is followed by the base metal zone. The thermomechanical effect zone is characterised by structural heterogeneity caused by the influence of the thermo-deformation cycle
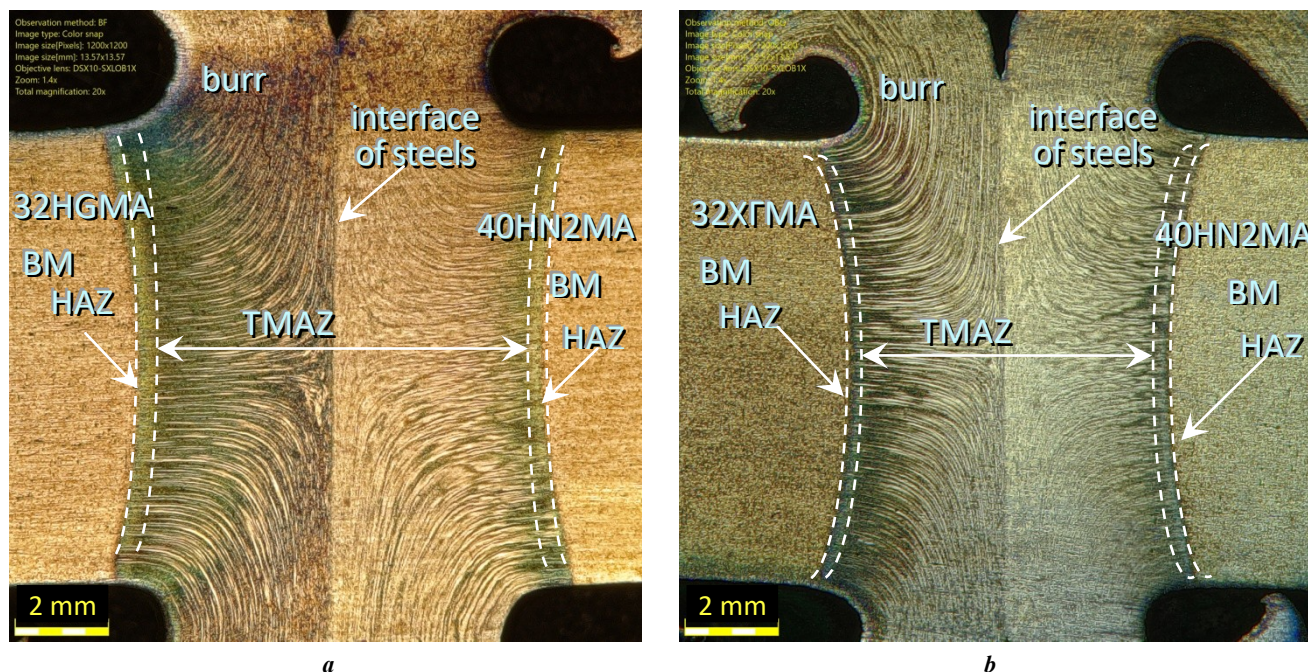
*Fig. 1. Macrostructure of welded joint of 32HGMA and 40HN2MA steels produced by rotary friction welding:*
*a – sample No. 1; b – sample No. 2.*
*BM – base metal; TMAZ – thermomechanically affected zone; HAZ – heat-affected zone*
***Рис. 1.*** *Макроструктура сварного соединения сталей 32ХГМА и 40ХН2МА,*
*полученного ротационной сваркой трением: **a** – образец № 1; **b** – образец № 2.*
*BM – основной металл; TMAZ – зона термомеханического влияния; HAZ – зона термического влияния*

of welding, as well as by plastic deformation of the metal during welding and the texture of the metal of the original pipes produced by hot rolling. Near the joint, an area with a parallel arrangement of fibres relative to the plane of contact of the billets can be distinguished. It is followed by a partially deformed zone where the texture threads are curved. This zone is followed by a zone with texture lines parallel to the rolling plane of the pipe billet. Such a structure of the welded joint was also observed in [10]. With increasing friction force, the total TMAZ length decreased from 7.7 mm in sample No. 1 to 6.7 mm in sample No. 2.

Fig. 2 and 3 show photographs of the microstructure of the welded joint interface. It is evident that there is no clear boundary between the steels, which in turn indicates the formation of common austenite grains during joint recrystallisation during welding. The resulting microstructure is predominantly acicular, indicating that the austenite transformation occurred in the low-temperature region. The size of the former austenite grain reaches 40 μm. At the same time, the inner structure of the austenite grains is highly fragmented; it consists of individual sections of crystallites elongated in one direction. The presence of a developed substructure is caused by the processes of dynamic recrystallisation of austenite during welding.

The kinetics of the deformed austenite transformation in the studied samples differs due to differences in the morphology of the phase components of the formed microstructure. In the microstructure of sample No. 1 obtained with a lower friction force, the microstructure of upper bainite

and martensite was formed within one austenite grain (Fig. 2 d). Martensite areas are characterised by an acicular structure and strong misorientation of crystallites. Obviously, the γ→α transformation in them occurred at the final stage in carbon-rich areas.

The nucleation and growth of martensite crystals occurred both from the boundaries and from the sub-boundaries of deformed austenite. The formation of upper bainite is observed mainly on the side of 32HGMA steel. Morphologically, two types of upper bainite can be identified in the microstructure, differing in the structural features of the carbide phase. In one case, it has an elongated plate-like shape and is continuously located at the boundaries of ferrite laths. In the other case, the carbide phase is concentrated inside the grains of bainitic ferrite with a particle size of 0.1–0.2 μm. Obviously, in the first case, bainite has a coarser structure and is formed at higher transformation temperatures.

In sample No. 2 obtained with a higher friction force, only two morphological components of the α-phase are present in the microstructure of the interface: lamellar bainite and lath martensite. Elongated crystals of lath bainite, 5–15 μm in size, grouped into packets, formed in the lower temperature range of the γ→α transformation are morphologically close to martensite. The microstructure on the side of both steels is identical.

The study using EBSD analysis allowed identifying that the formation of a bainitic microstructure at low values of friction force led to a decrease in the proportion of high-angle boundaries (Fig. 2 c). A developed substructure of a reticular structure formed by low-angle boundaries is
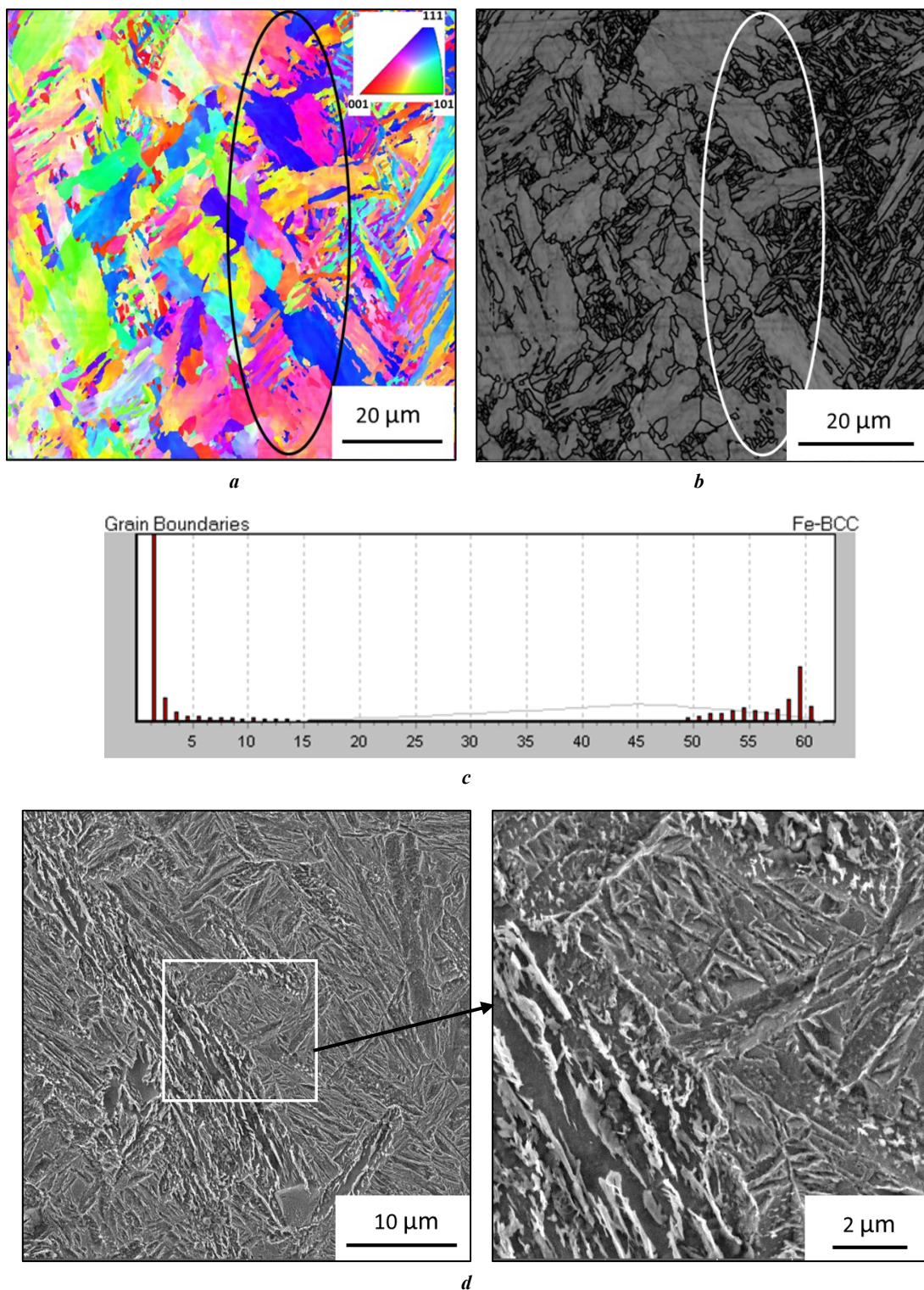
***Fig. 2.*** *Microstructure of the interface of 32HGMA and 40HN2MA steels in a welded joint*
*produced by rotary friction welding, mode No. 1:*
***a*** *– crystallographic misorientation map;* ***b*** *– microstructure with high-angle boundaries (15°);*
***c*** *– spectra of  intercrystalline boundaries;* ***d*** *– SEM image*
***Рис. 2.*** *Микроструктура зоны сопряжения сталей 32ХГМА и 40ХН2МА в сварном соединении,*
*полученном ротационной сваркой трением, режим № 1:*
***a*** *– карта кристаллографических разориентировок;* ***b*** *– микроструктура с нанесением большеугловых границ (15°);*
***c*** *– спектры межкристаллитных границ;* ***d*** *– СЭМ-изображение*
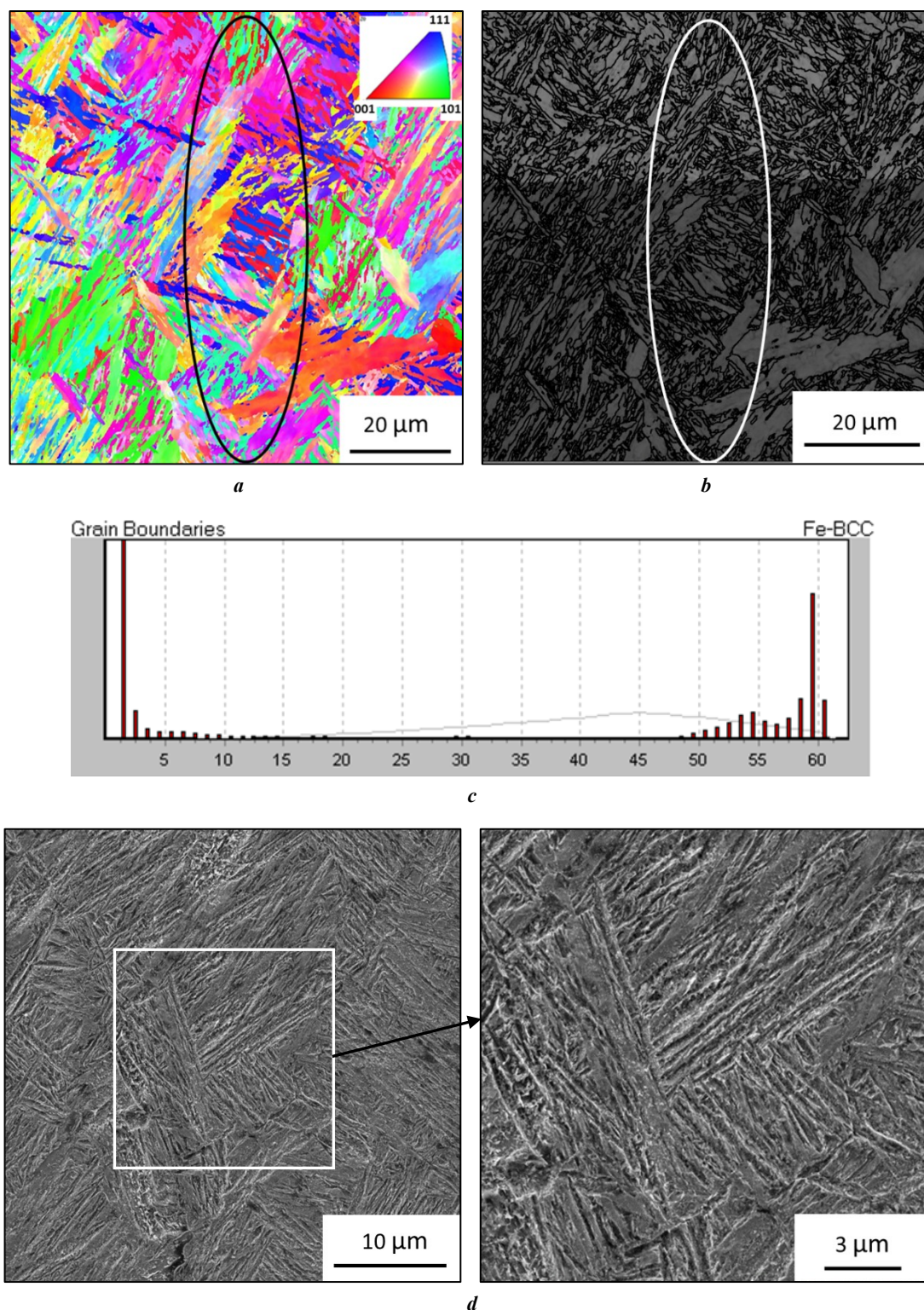
***Fig. 3.** Microstructure of the interface of 32HGMA and 40HN2MA steels in a welded joint
produced by rotary friction welding, mode No. 2:
**a** – crystallographic misorientation map; **b** – microstructure with high-angle boundaries (15°);
**c** – spectra of intercrystalline boundaries; **d** – SEM image*
***Рис. 3.** Микроструктура зоны сопряжения сталей 32ХГМА и 40ХН2МА в сварном соединении,
полученном ротационной сваркой трением, режим № 2:
**a** – карта кристаллографических разориентировок; **b** – микроструктура с нанесением большеугловых границ (15°);
**c** – спектры межкристаллитных границ; **d** – СЭМ-изображение*

observed inside the bainitic ferrite grains. At the same time, the lath morphology of the α-phase microstructure formed at higher friction force values is characterised by a higher density of high-angle boundaries located at misorientation angles from 49 to 60° (Fig. 3 c).

The proportion of residual austenite in the steel interface was determined by X-ray structural analysis. It was found that residual austenite in the amount of 2–3 % was detected in sample No. 2 welded at a higher friction force. In sample No. 1, the proportion of residual austenite is less than 1 %.

Post-welding tempering resulted in the development of diffusion processes with additional formation of carbide phases both inside and along the boundaries of the initial α-phase (Fig. 4, 5). In the structure of the upper bainite of tempered sample No. 1, a breakdown and partial coagulation of long cementite plates is observed (Fig. 4). In the martensitic microstructure areas, finely dispersed carbide particles precipitated. Thus, the structure of this sample after tempering is characterised by a combination of areas of a coarse bainitic structure with large carbides and areas of a more homogeneous dispersed structure.

In the microstructure of the mating zone of tempered sample No. 2, areas of a coarse structure are absent (Fig. 5). In the bainitic structure, a developed subgrain structure is observed in the α-phase crystals. The microstructure is homogeneous. Carbide particles are located both along the boundaries of the initial α-phase and inside the crystallites.

## Microhardness

Fig. 6 shows the microhardness profiles in welded joints in the initial state and after tempering.

In the TMAZ, the microhardness changes abruptly, which is caused by the heterogeneity of the microstructure due to the presence of isolated areas of austenite decomposition products of different morphology. The highest microhardness values are observed in the TMAZ on the side of 40HN2MA steel in the as-welded state. In this case, the maximum value of 677 HV was recorded in the sample produced with a higher friction force. A tendency towards a decrease in microhardness is observed with distance from the mating zone. In the HAZ, the microhardness values are virtually identical to the values of the original steels, which were 271–288 HV for 32HGMA steel and 310–347 HV for 40HN2MA steel. The influence of tempering results in a decrease in microhardness in the TMAZ to values in the range of 256–424 HV, which is associated with a decrease in the tetragonality of the martensite crystal lattice and the precipitation of carbide particles.

## Impact toughness

The results of determining the impact toughness in the steel interface zone are shown in Table 4, and the fractograms of the tested samples are shown in Fig. 7.

In the as-welded state, the steel interface zone has a low toughness reserve, which is determined by the brittleness of the microstructures formed in this zone. In all cases, fracture occurred along the body of the former austenite grain. However, some differences are observed in the morphology of the fracture surface of the samples produced with different friction forces. The fracture surface of the sample produced using mode No. 1 has virtually no traces of plastic deformation. The fracture mechanism is cleaving (Fig. 7 a). The facets of the transcrystalline cleavage are relatively flat areas disordered relative to the adjacent facets by a certain angle. Secondary cracks extending deep into the sample are revealed perpendicular to the direction of growth of the main crack.
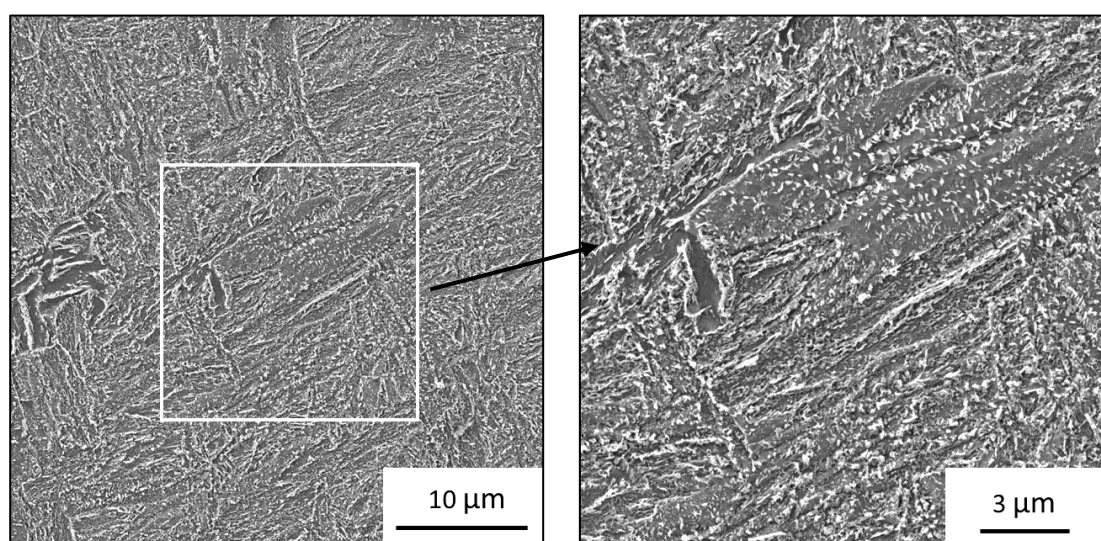


***Fig. 4.** Microstructure of the interface of the welded joint of 32HGMA and 40HN2MA steels
after tempering at 550 °C for 1 h, welding mode No. 1*
***Рис. 4.** Микроструктура зоны сопряжения сварного соединения сталей 32ХГМА и 40ХН2МА
после отпуска при 550 °C в течение 1 ч, режим сварки № 1*
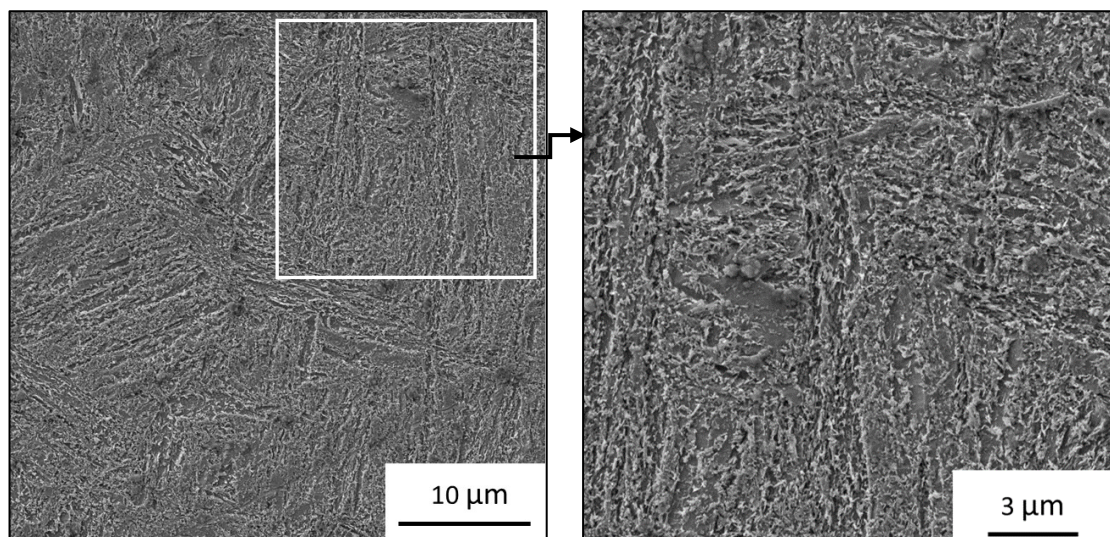
***Fig. 5.*** *Microstructure of the interface of the welded joint of 32HGMA and 40HN2MA steels*
*after tempering at 550 °C for 1 h, welding mode No. 2*
***Рис. 5.*** *Микроструктура зоны сопряжения сварного соединения сталей 32ХГМА и 40ХН2МА*
*после отпуска при 550 °С в течение 1 ч, режим сварки № 2*
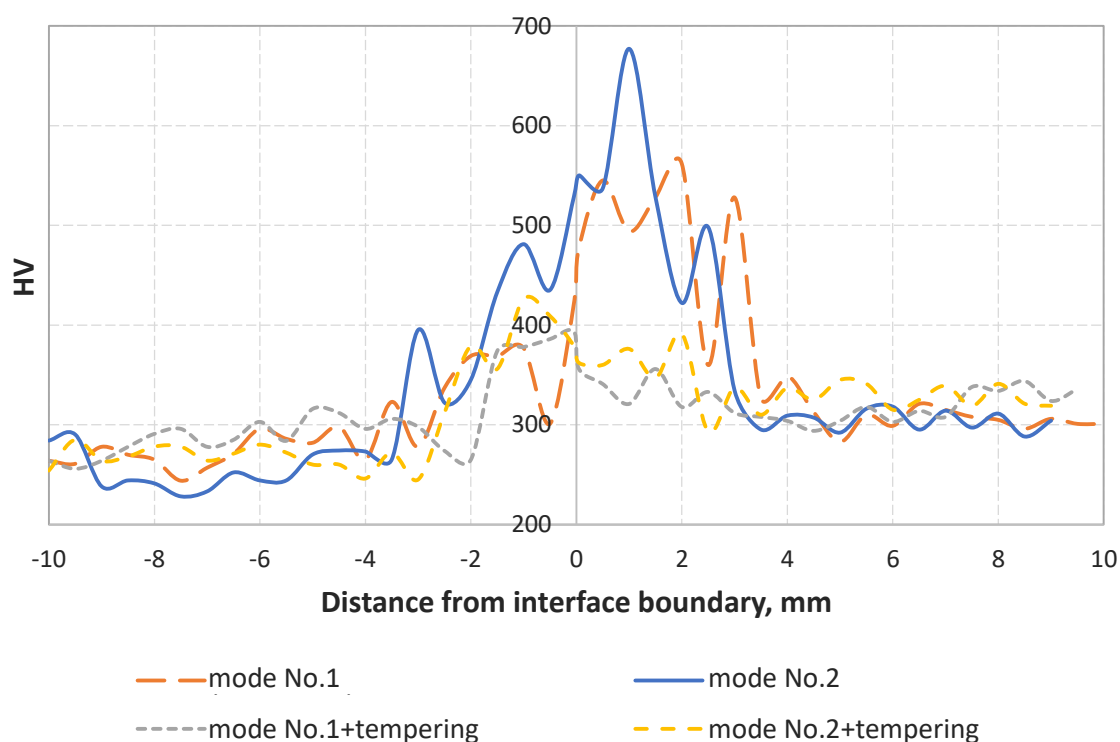


***Fig. 6.*** *Microhardness profiles in welded joints in the initial state and after tempering*
***Рис. 6.*** *Профили микротвердости в сварных соединениях в исходном состоянии и после отпуска*

The sample produced using mode No. 2 fractured with a greater share of plastic deformation. The fracture macrostructure is characterised by the formation of a small contraction at the edges. In the microrelief, the quasi-cleavage micromechanism dominates. The quasi-cleavage facets alternate with the dimple structure (Fig. 7 c).

Tempering contributed to an increase in the impact toughness of the welded joints. In this case, the maximum value of KCV=53.5 J/cm$^2$ is recorded in sample No. 2 produced with a higher friction force. Traces of macroplastic deformation in the form of the formation of shear lips are observed on the fracture surface of this sample (Fig. 7 d).

***Table 4.*** *Impact toughness of the interface in welded joints of 32HGMA and 40HN2MA steels*
***Таблица 4.*** *Ударная вязкость зоны сопряжения в сварных соединениях сталей 32ХГМА и 40ХН2МА*

| Welding mode | No. 1 | No. 2 | No. 1 + tempering | No. 2 + tempering |
|---|---|---|---|---|
| KCV, J/cm$^2$ | 11.3 | 18.0 | 19.3 | 53.5 |
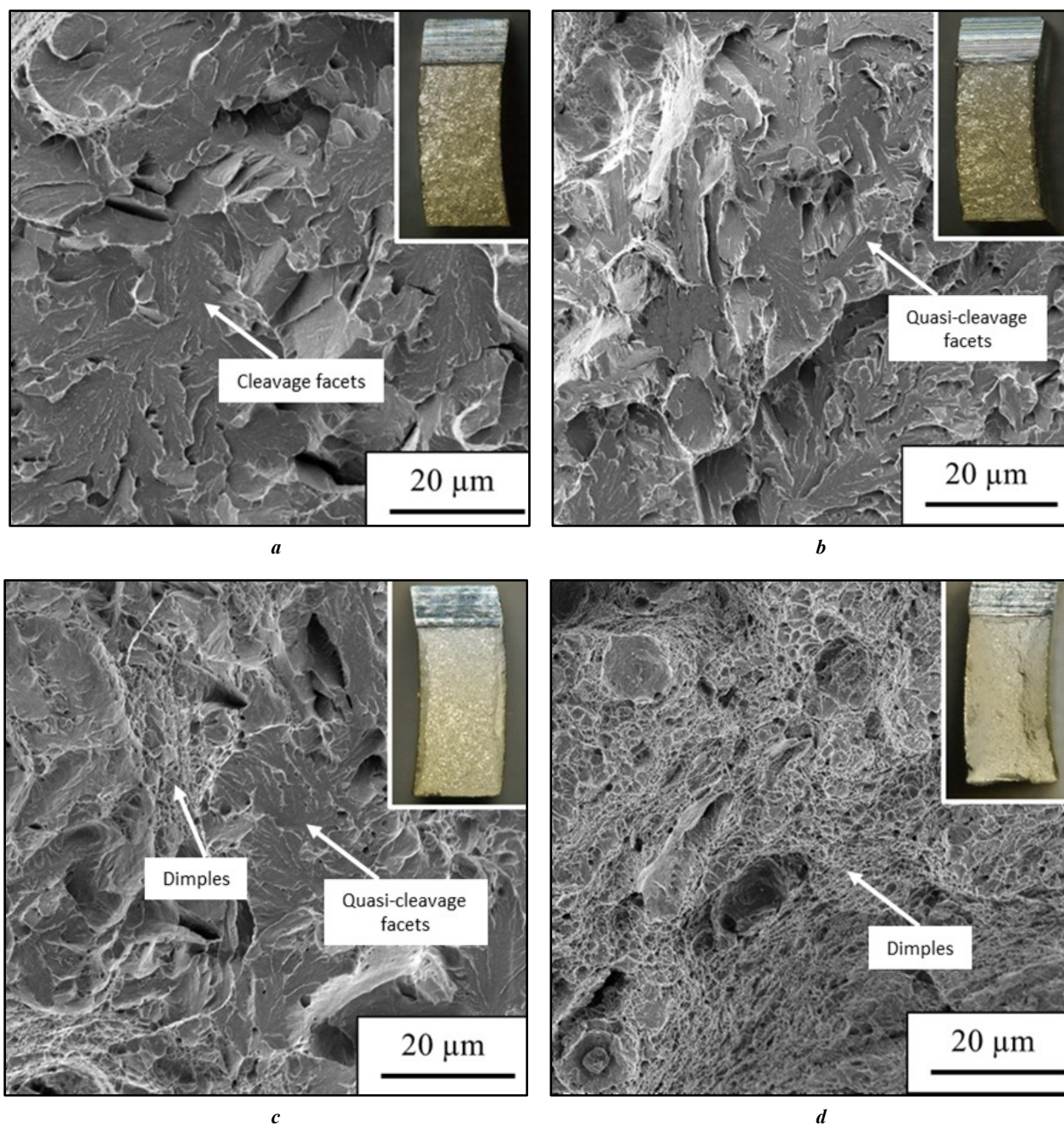


***Fig. 7.*** *Fractograms of samples of welded joint of 32HGMA and 40HN2MA steels*
*after impact bending tests:*
***a*** *– mode No. 1;* ***b*** *– mode No. 1 + tempering;* ***c*** *– mode No. 2;* ***d*** *– mode No. 2 + tempering*
***Рис. 7.*** *Фрактограммы образцов сварных соединений сталей 32ХГМА и 40ХН2МА*
*после испытаний на ударный изгиб:*
***a*** *– режим № 1;* ***b*** *– режим № 1 + отпуск;* ***c*** *– режим № 2;* ***d*** *– режим № 2 + отпуск*

The fracture morphology is completely represented by dimples of ductile fracture. Against the background of a fine-dimple microrelief, individual large dimples are observed, the centres of origin of which are large particles.

In the tempered sample of the welded joint produced with a lower friction force, the impact toughness increased insignificantly compared to the initial state. The crack propagated in this case according to the quasi-cleavage mechanism (Fig. 7 b). The fracture surface has a more developed surface structure compared to the state of this sample after welding and more pronounced ridges of separation in the locations of high-angle boundaries. No secondary cracks were detected.

## DISCUSSION

The results of the conducted studies confirmed the assumption about the influence of the RFW parameter (force at the friction stage) on the microstructure and toughness of the mating zone of medium-carbon alloyed steels. This is related to the fact that with an increase in the friction force, the temperature and degree of deformation of the near-contact zones of the billets increase, which is consistent with the results of modelling the RFW process presented in works [17–19]. These conditions, apparently, led to the suppression of the formation of coarse-acicular bainite in the upper temperature range of the transformation. The formation of a coarse microstructure of upper bainite with a large number of large cementite particles, obtained at a lower force during friction of the billets, causes brittleness of the microstructure, which is not eliminated by subsequent high-temperature tempering. The negative effect of upper bainite on impact toughness was previously noted in studies [20–22]. The authors of the work [5] note as well the relationship between low impact toughness in the joint interface and the presence of coarse carbide particles at the interface, which does not contradict the results obtained in this work.

Thus, an increase in the force of friction of the billets at the stage of their heating in the RFW process leads to an increase in the visco-plastic properties of the interface of steels after high-temperature tempering of welded joints. This effect is achieved due to the formation of a more homogeneous fine-grained microstructure of tempered martensite and lower bainite with a developed subgrain structure.

## CONCLUSIONS

1. In welded joints of 32HGMA and 40HN2MA medium-carbon alloyed steels produced by rotary friction welding, a microstructure consisting of sections of martensite and bainite of various morphologies is formed in the steel interface. The morphology of the bainitic component of the microstructure depends on the welding parameters and the kinetics of the transformation of supercooled austenite.

2. It was found that at reduced values of the force during friction of the billets after the completion of welding, in the steel interface, a coarse microstructure of upper bainite with uneven precipitation of large carbide particles is formed, which negatively affects the visco-plastic properties of the steel interface.

3. With an increase in the force at the stage of friction of the billets after the completion of welding, the formation of a more dispersed structure of lath bainite and an increase in the density of high-angle boundaries occur. After high tempering, such a microstructure provides high impact toughness in the interface of steels due to the transformation into a tempered bainite structure with a developed subgrain structure.

4. The toughness of the interface of steels can be controlled by welding modes, avoiding the need for complete subsequent recrystallisation of the weld zone (quenching and tempering), which significantly reduces the cost of manufacturing of high-strength drill pipes.

## REFERENCES

1. Ovchinnikov D.V., Sofrygina O.A., Zhukova S.Y., Pyshmintsev I.Y., Bityukov S.M. Influence of microalloying with boron on the structure and properties of high-strength oil pipe. *Steel in Translation*, 2011, vol. 41, no. 4, pp. 356–360. DOI: 10.3103/S0967091211040188.

2. Sofrygina O.A., Zhukova S.Y., Bityukov S.M., Pyshmintsev I.Y. Economical steels for the manufacture of high-strength oil pipe (according to the API Spec5CT standard). *Steel in Translation*, 2010, vol. 40, no. 7, pp. 616–621. DOI: 10.3103/S0967091210070041.

3. Zaselskiy E.M., Tikhontseva N.T., Savchenko I.P., Sofrygina O.A. Development and implementation of materials in the production of high-strength drill pipes with special properties. *Problemy chernoy metallurgii i materialovedeniya*, 2021, no. 2, pp. 37–40. EDN: XBMMOL.

4. Still J.R. Welding of AISI 4130 and 4140 steels for drilling systems. *Welding Journal*, 1997, vol. 76, no. 6, pp. 37–42.

5. Khadeer Sk.A., Babu P.R., Kumar B.R., Kumar A.S. Evaluation of friction welded dissimilar pipe joints between AISI 4140 and ASTM A 106 Grade B steels used in deep exploration drilling. *Journal of Manufacturing Processes*, 2020, vol. 56, part A, pp. 197–205. DOI: 10.1016/j.jmapro.2020.04.078.

6. Maalekian M. Friction Welding-Critical Assessment of Literature. *Science and Technology of Welding and Joining*, 2007, no. 12, pp. 738–759. DOI: 10.1179/174329307X249333.

7. Vill V.I. *Svarka metallov treniem* [Friction welding of metals]. Moscow, Mashinostroenie Publ., 1970. 176 p.

8. Li Wenya, Vairis A., Preuss M., Ma Tiejun. Linear and Rotary Friction Welding Review. *International Materials Reviews*, 2016, no. 61, pp. 71–100. DOI: 10.1080/09506608.2015.1109214.

9. Banerjee A., Ntovas M., Da Silva L., Rahimi S., Wynne B. Inter relationship between microstructure evolution and mechanical properties in inertia friction welded 8630 low-alloy steel. *Archives of Civil and Mechanical Engineering*, 2021, vol. 21, article number 149. DOI: 10.1007/s43452-021-00300-9.

10. Kumar A.S., Khadeer Sk.A., Rajinikanth V., Pahari S., Kumar B.R. Evaluation of bond interface characteristics of rotary friction welded carbon steel to low alloy steel pipe joints. *Materials Science & Engineering A*, 2021, vol. 824, article number 141844. DOI: [10.1016/j.msea.2021.141844](10.1016/j.msea.2021.141844).

11. Shete N., Deokar S.U. A Review Paper on Rotary Friction Welding. *International Conference on Ideas, Impact and Innovation in Mechanical Engineering*, 2017, vol. 5, no. 6, pp. 1557–1560.

12. Cai Wayne, Daehn G., Vivek A., Li Jingjing, Khan H., Mishra R.S., Komarasamy M. A State of the Art Review on Solid-State Metal Joining. *Journal of Manufacturing Science and Engineering*, 2019, vol. 141, no. 3, article number 031012. DOI: [10.1115/1.4041182](10.1115/1.4041182).

13. Emre H.E., Kaçar R. Effect of Post Weld Heat Treatment Process on Microstructure and Mechanical Properties of Friction Welded Dissimilar Drill Pipe. *Materials Research*, 2015, vol. 18, no. 3, pp. 503–508. DOI: [10.1590/1516-1439.308114](10.1590/1516-1439.308114).

14. Kaletin A.Y., Kaletina Y.V., Ryzhkov A.G. Enhancement of impact toughness of structural steels upon formation of carbide-free bainite. *Physics of Metals and Metallography*, 2015, vol. 116, no. 1, pp. 109–114. DOI: [10.1134/S0031918X15010068](10.1134/S0031918X15010068).

15. Maisuradze M.V., Kuklina A.A., Nazarova V.V., Ryzhkov M.A., Antakov E.V. Microstructure and mechanical property formation of heat treated low-carbon chromium-nickel-molybdenum steels. *Metallurgist*, 2024, vol. 68, no. 3, pp. 322–335. DOI: [10.1007/s11015-024-01732-3](10.1007/s11015-024-01732-3).

16. Panin V.E., Shulepov I.A., Derevyagina L.S., Panin S.V., Gordienko A.I., Vlasov I.V. Nanoscale mesoscopic structural states in low-alloy steels for martensitic phase formation and low-temperature toughness enhancement. *Physical mesomechanics*, 2020, vol. 23, no. 5, pp. 376–383. DOI: [10.1134/S1029959920050021](10.1134/S1029959920050021).

17. Celik S., Ersozlu I. Investigation of the mechanical properties and microstructure of friction welded joints between AISI 4140 and AISI 1050 steels. *Materials and Design*, 2009, vol. 30, no. 4, pp. 970–976. DOI: [10.1016/j.matdes.2008.06.070](10.1016/j.matdes.2008.06.070).

18. Nan Xujing, Xiong Jiangtao, Jin Feng, Li Xun, Liao Zhongxiang, Zhang Fusheng, Li Jinglong. Modeling of rotary friction welding process based on maximum entropy production principle. *Journal of Manufacturing Processes*, 2019, vol. 37, pp. 21–27. DOI: [10.1016/j.jmapro.2018.11.016](10.1016/j.jmapro.2018.11.016).

19. Geng Peihao, Qin Guoliang, Zhou Jun. Numerical and experimental investigation on friction welding of austenite stainless steel and middle carbon steel. *Journal of Manufacturing Processes*, 2019, vol. 47, pp. 83–97. DOI: [10.1016/j.jmapro.2019.09.016](10.1016/j.jmapro.2019.09.016).

20. Kaletin A.Yu., Schastlivtsev V.M., Kareva N.T., Smirnov M.A. Embrittlement of structural steel with bainitic structure during tempering. *Fizika metallov i metallovedenie*, 1983, vol. 56, no. 2, pp. 366–371. EDN: [TBDJOQ](TBDJOQ).

21. Zikeev V.N., Chevskaya O.N., Mishet'yan A.R., Filippov V.G., Korostelev A.B. Effect of high strength structural steel structural state on fracture resistance.

*Metallurgist*, 2021, vol. 65, no. 3-4, pp. 375–388. DOI: [10.1007/s11015-021-01167-0](10.1007/s11015-021-01167-0).

22. Kaletin A.Yu., Kaletina Yu.V., Simonov Yu.N. Retained austenite and impact strength of structural steels with carbide-free bainite. *Bulletin of PNRPU. Mechanical engineering, materials science,* 2022, vol. 24, no. 4, pp. 49–55. EDN: [UZSBWG](UZSBWG).

## СПИСОК ЛИТЕРАТУРЫ

1. Ovchinnikov D.V., Sofrygina O.A., Zhukova S.Y., Pyshmintsev I.Y., Bityukov S.M. Influence of microalloying with boron on the structure and properties of high-strength oil pipe // Steel in Translation. 2011. Vol. 41. № 4. P. 356–360. DOI: [10.3103/S0967091211040188](10.3103/S0967091211040188).

2. Sofrygina O.A., Zhukova S.Y., Bityukov S.M., Pyshmintsev I.Y. Economical steels for the manufacture of high-strength oil pipe (according to the API Spec5CT standard) // Steel in Translation. 2010. Vol. 40. № 7. P. 616–621. DOI: [10.3103/S0967091210070041](10.3103/S0967091210070041).

3. Засельский Е.М., Тихонцева Н.Т., Савченко И.П., Софрыгина О.А. Разработка и освоение материалов в производстве высокопрочных бурильных труб со специальными свойствами // Проблемы черной металлургии и материаловедения. 2021. № 2. С. 37–40. EDN: [XBMMOL](XBMMOL).

4. Still J.R. Welding of AISI 4130 and 4140 steels for drilling systems // Welding Journal. 1997. Vol. 76. № 6. P. 37–42.

5. Khadeer Sk.A., Babu P.R., Kumar B.R., Kumar A.S. Evaluation of friction welded dissimilar pipe joints between AISI 4140 and ASTM A 106 Grade B steels used in deep exploration drilling // Journal of Manufacturing Processes. 2020. Vol. 56. Part A. P. 197–205. DOI: [10.1016/j.jmapro.2020.04.078](10.1016/j.jmapro.2020.04.078).

6. Maalekian M. Friction Welding-Critical Assessment of Literature // Science and Technology of Welding and Joining. 2007. № 12. P. 738–759. DOI: [10.1179/174329307X249333](10.1179/174329307X249333).

7. Вилль В.И. Сварка металлов трением. М.: Машиностроение, 1970. 176 с.

8. Li Wenya, Vairis A., Preuss M., Ma Tiejun. Linear and Rotary Friction Welding Review // International Materials Reviews. 2016. № 61. P. 71–100. DOI: [10.1080/09506608.2015.1109214](10.1080/09506608.2015.1109214).

9. Banerjee A., Ntovas M., Da Silva L., Rahimi S., Wynne B. Inter relationship between microstructure evolution and mechanical properties in inertia friction welded 8630 low-alloy steel // Archives of Civil and Mechanical Engineering. 2021. Vol. 21. Article number 149. DOI: [10.1007/s43452-021-00300-9](10.1007/s43452-021-00300-9).

10. Kumar A.S., Khadeer Sk.A., Rajinikanth V., Pahari S., Kumar B.R. Evaluation of bond interface characteristics of rotary friction welded carbon steel to low alloy steel pipe joints // Materials Science & Engineering A. 2021. Vol. 824. Article number 141844. DOI: [10.1016/j.msea.2021.141844](10.1016/j.msea.2021.141844).

11. Shete N., Deokar S.U. A Review Paper on Rotary Friction Welding // International Conference on Ideas, Im-

pact and Innovation in Mechanical Engineering. 2017. Vol. 5. № 6. P. 1557–1560.

12. Cai Wayne, Daehn G., Vivek A., Li Jingjing, Khan H., Mishra R.S., Komarasamy M. A State of the Art Review on Solid-State Metal Joining // Journal of Manufacturing Science and Engineering. 2019. Vol. 141. № 3. Article number 031012. DOI: 10.1115/1.4041182.

13. Emre H.E., Kaçar R. Effect of Post Weld Heat Treatment Process on Microstructure and Mechanical Properties of Friction Welded Dissimilar Drill Pipe // Materials Research. 2015. Vol. 18. № 3. P. 503–508. DOI: 10.1590/1516-1439.308114.

14. Калетин А.Ю., Рыжков А.Г., Калетина Ю.В. Повышение ударной вязкости конструкционных сталей при образовании бескарбидного бейнита // Физика металлов и металловедение. 2015. Т. 116. № 1. С. 114–120. DOI: 10.7868/S0015323015010064.

15. Майсурадзе М.В., Куклина А.А., Назарова В.В., Рыжков М.А., Антаков Е.В. Формирование микроструктуры и механических свойств при термической обработке низкоуглеродистых хромоникельмолибденовых сталей // Металлург. 2024. № 3. С. 21–30. DOI: 10.52351/00260827_2024_3_21.

16. Панин В.Е., Шулепов И.А., Деревягина Л.С., Панин С.В., Гордиенко А.И., Власов И.В. Создание наномасштабных мезоскопических структурных состояний для образования мартенситных фаз в низколегированной стали с целью получения высокой низкотемпературной ударной вязкости // Физическая мезомеханика. 2019. Т. 22. № 6. С. 5–13. EDN: ZGEIOJ.

17. Celik S., Ersozlu I. Investigation of the mechanical properties and microstructure of friction welded joints between AISI 4140 and AISI 1050 steels // Materials and Design. 2009. Vol. 30. № 4. P. 970–976. DOI: 10.1016/j.matdes.2008.06.070.

18. Nan Xujing, Xiong Jiangtao, Jin Feng, Li Xun, Liao Zhongxiang, Zhang Fusheng, Li Jinglong. Modeling of rotary friction welding process based on maximum entropy production principle // Journal of Manufacturing Processes. 2019. Vol. 37. P. 21–27. DOI: 10.1016/j.jmapro.2018.11.016.

19. Geng Peihao, Qin Guoliang, Zhou Jun. Numerical and experimental investigation on friction welding of austenite stainless steel and middle carbon steel // Journal of Manufacturing Processes. 2019. Vol. 47. P. 83–97. DOI: 10.1016/j.jmapro.2019.09.016.

20. Калетин А.Ю., Счастливцев В.М., Карева Н.Т., Смирнов М.А. Охрупчивание конструкционной стали с бейнитной структурой при отпуске // Физика металлов и металловедение. 1983. Т. 56. № 2. С. 366–371. EDN: TBDJOQ.

21. Зикеев В.Н., Чевская О.Н., Мишетьян А.Р., Филиппов В.Г., Коростелев А.Б. Влияние структурного состояния конструкционных высокопрочных сталей на сопротивление разрушению // Металлург. 2021. № 4. С. 15–25. DOI: 10.52351/00260827_2021_04_15.

22. Калетин А.Ю., Калетина Ю.В., Симонов Ю.Н. Остаточный аустенит и ударная вязкость конструкционных сталей с бескарбидным бейнитом // Вестник Пермского национального исследовательского политехнического университета. Машиностроение, материаловедение. 2022. Т. 24. № 4. С. 49–55. EDN: UZSBWG.

# Взаимосвязь микроструктуры и ударной вязкости зоны сопряжения сварных соединений сталей 32ХГМА и 40ХН2МА, полученных ротационной сваркой трением

**Приймак Елена Юрьевна**[*,1,2,4], кандидат технических наук, доцент,
заведующий лабораторией металловедения и термической обработки,
директор научно-образовательного центра новых материалов и перспективных технологий
**Атамашкин Артём Сергеевич**[2,5], кандидат технических наук,
старший научный сотрудник научно-образовательного центра новых материалов и перспективных технологий
**Яковлева Ирина Леонидовна**[3,6], доктор технических наук,
главный научный сотрудник лаборатории физического металловедения
**Фот Андрей Петрович**[1,7], доктор технических наук, профессор,
главный ученый секретарь – начальник отдела диссертационных советов

[1]АО «Завод бурового оборудования», Оренбург (Россия)
[2]Оренбургский государственный университет, Оренбург (Россия)
[3]Институт физики металлов имени М.Н. Михеева Уральского отделения РАН, Екатеринбург (Россия)

**\*E-mail:** e.prijmak@zbo.ru

[4]ORCID: https://orcid.org/0000-0002-4571-2410
[5]ORCID: https://orcid.org/0000-0003-3727-8738
[6]ORCID: https://orcid.org/0000-0001-8918-3066
[7]ORCID: https://orcid.org/0000-0002-2971-7908

*Аннотация:* Настоящая работа посвящена оценке влияния морфологических особенностей микроструктуры среднеуглеродистых легированных сталей, сформированной при различном усилии в процессе ротационной сварки трением (РСТ), на ударную вязкость их зоны сопряжения. Приведены результаты экспериментального исследования соединения, полученного при сварке трубных заготовок из сталей 32ХГМА и 40ХН2МА с внешним диаметром 73 мм и толщиной стенки 9 мм при изменении силы на этапе трения (разогрева) заготовок. Исследования микроструктуры, микротвердости и ударной вязкости на образцах с *V*-образным надрезом сварных соединений были проведены в исходном состоянии после сварки и после отпуска при температуре 550 °C. Проведен макро- и микрофрактографический анализ разрушенных образцов. Показано, что сила при трении оказывает влияние на кинетику фазовых превращений, фазовый состав и однородность микроструктуры в зоне сопряжения сталей. С уменьшением данного параметра РСТ возрастает неоднородность микроструктуры, связанная с возникновением участков верхнего бейнита с неравномерными выделениями крупных карбидных частиц, что оказывает негативное влияние на вязкость зоны сопряжения сталей как в исходном состоянии, так и после отпуска; механизм разрушения – квазискол. При более высоких значениях силы при трении повышается плотность большеугловых границ и дисперсность микроструктуры бейнита, что обеспечивает более высокую вязкость и энергоемкость разрушения с формированием ямочного микрорельефа. Полученные результаты открывают возможности регулирования вязкопластических свойств сварных соединений уже на этапе сварки без последующей перекристаллизации зоны сварного шва.

*Ключевые слова:* ротационная сварка трением; среднеуглеродистые легированные стали; зона сопряжения сварных соединений; мартенсит; бейнит; ударная вязкость.

The journal publishes two versions of papers: in Russian and in English. The data of manuscript has to be original and never submitted or published before in other journals. All submitted papers are checked in the Anti-Plagiarism system ("Antiplagiat" system).

For publication, authors need to submit an application to the editorial office by sending the materials to the e-mail of the journal vektornaukitgu@yandex.ru or by uploading them to their personal account on the website https://www.vektornaukitech.ru.

### Required structural elements of the manuscript

– *UDC identifier*;
– *the title* of the scientific manuscript;
– *copyright sign and year*;
– *information about the authors*: surname and initials of the author, academic degree, academic status, occupation; company, city, country; ORCID. The author corresponding to the editorial staff should provide his/her E-mail;
– *abstract* (200–250 words) should contain a brief summary of the paper's concept in order to interest a potential reader;
– *keywords* (the main criterion of choosing keywords is their potential value to summarize the content of the document or to help the readers to find the document);
– *acknowledgements* to individuals, granting organizations;
– *the text of the manuscript* structured in accordance with the rules;
– *references* (at least 20 sources).

### Article structure

The structure of the article should conform to the IMRAD (Introduction, Methods, Results, and Discussion) standard, applied by Science World Community:

– INTRODUCTION
– METHODS
– RESULTS
– DISCUSSION
– CONCLUSIONS

### Tables and figures formatting
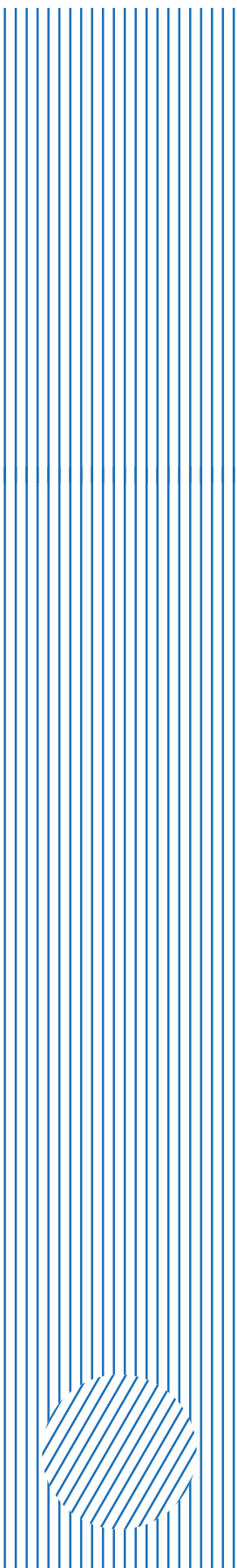
Tables and figures should not fall outside the page layout. The use of landscape pages is not allowed. The titles of the tables and figures captures are required. If the text contains figures, diagrams, and tables from other literary sources, it is necessary to indicate where they were taken from..

### Formulas typing

Formulas are edited in Microsoft Equation 3 formula editor. Formulas should not be longer than 80 mm. The size of the formula is 100 %. Converting formulas to figures is not allowed.

### References and citations formatting

References are listed in the order of citation in the article. Reference list should not include the sources not cited in the article. In the journal it is not common to cite textbooks and study guides, except the flagship in their respective field, thesis papers and synopsis of a thesis. Not less than a quarter of the sources listed in the reference list should be published in the last 3–5 years. References to print publications only are acceptable (excluding e-journals). References to internet sites are not accepted. Not more than 20 % of the sources can be references on the own author's publications. If a cited source has a DOI, the DOI should be indicated at the end of bibliographic description of this source. All DOIs should be valid links

# The influence of cavitational synthesis nanodiamonds on the tribological properties of a water-oil-based cooling lubricant

*Evgeny V. Fominov*[*1,3], PhD (Engineering), Associate Professor
*Maksim V. Kovtun*[2,4], Head of Research and Technology Center
*Sergey A. Kurlovich*[2,5], Director
*Dmitry I. Gladkikh*[1,6], postgraduate student
*Tatyana V. Lavrenova*[1,7], senior lecturer

[1]*Don State Technical University, Rostov-on-Don (Russia)*
[2]*Trading and Industrial Company SYNTEZ, Rostov-on-Don (Russia)*

*\*E-mail:* fominoff83@mail.ru

[3]ORCID: https://orcid.org/0000-0002-0165-7536
[4]ORCID: https://orcid.org/0009-0003-1489-8333
[5]ORCID: https://orcid.org/0009-0002-3606-6311
[6]ORCID: https://orcid.org/0000-0003-2292-256X
[7]ORCID: https://orcid.org/0000-0002-8283-7730

*Abstract:* This paper deals with the study of the influence of nanosized diamonds produced by the cavitational synthesis method on the tribological properties of a commercial water-oil-based cooling lubricant. The study is aimed at assessing the prospects for application of this type of nanodiamonds as an antifriction and antiwear additive. Tribological tests were carried out using the "indenter on a disk" friction scheme at a constant load and sliding speed. High-speed P18 steel for the indenter and 30HGSA steel for the rotating counterbody (disk) were used as friction couple materials. The studies were carried out for the base lubricant and two variants of its composition modifications using colloidal dispersion (distilled water with dispersed nanodiamonds) with a final additive concentration of 0.5 and 2.5 %. It was experimentally found that both variants of modification of the base water-oil emulsion resulted in increase of the bearing capacity of lubricating layers, decreasing the total linear wear of friction couple elements by 1.8–2.4 times. The presence of nanodiamonds in the composition enhanced as well the shielding effect of the cutting coolant. A decrease in visible damage to friction surfaces was recorded using optical microscopy. Analysis of profile diagrams of worn areas in the transverse direction showed a decrease in the size of a groove on the counterbody against the background of a decrease in roughness from $Ra$=0.49 μm in the basic variant to $Ra$=0.29–0.34 μm. Evaluation of the loss in counterbody weight for nanodiamond concentrations of 0.5 and 2.5 % showed a decrease in their value by 1.3 and 1.9 times, respectively; for the indenter, the decrease in this parameter was 1.2 and 1.5 times. Thus, the use of cavitational synthesis nanodiamonds as an additive may become a promising direction for increasing the antiwear properties of water-oil-based cooling lubricants.

*Keywords:* cavitational synthesis nanodiamonds; water-oil emulsion; cooling lubricant; boundary friction; wear resistance; friction ratio.

*For citation:* Fominov E.V., Kovtun M.V., Kurlovich S.A., Gladkikh D.I., Lavrenova T.V. The influence of cavitational synthesis nanodiamonds on the tribological properties of a water-oil-based cooling lubricant. *Frontier Materials & Technologies*, 2025, no. 2, pp. 87–94. DOI: 10.18323/2782-4039-2025-2-72-7.

## INTRODUCTION

The use of various types of additives is an effective way to control the tribological properties of liquid lubricants. In the last decade, nanoparticles of various metals, metal and non-metal oxides, sulfides and carbonates have been widely used for this purpose [1; 2]. Modification of the base lubricant by introducing such additives, as a rule, leads to a significant improvement in its antifriction and/or antiwear properties [3; 4]. Among nanosized additives, fully carbon particles (graphenes, fullerenes, carbon nanotubes) are in high demand, allowing improving significantly the tribological properties of base lubricants [5–7].

Among carbon nanoadditives, the use of nanodiamonds (ND) is especially promising, due to their high hardness, thermal conductivity, chemical stability and compatibility with other additives [8]. To date, many detailed studies on the tribological characteristics of various types of lubricants containing ND have been conducted. Thus, the authors of the work [9] note a significant improvement in the tribological characteristics of motor oils containing ND particles and in the quality of friction surfaces. When studying the friction process in a polyalphaolefin oil environment with the ND addition, a decrease in the friction coefficients and an increase in the antiwear effect of the lubricating film for the composition with the additive were found as well

[10]. In [11], a 3-fold decrease in the friction force and a 2-fold increase in the wear resistance of titanium hip implants were recorded when adding less than 0.2 % of ND in a weight concentration to the body fluid imitation.

An important advantage of ND is their solubility in water, which opens up opportunities for modifying both pure water and water-based lubricants. In this regard, the study of the tribological properties of aqueous suspensions with ND is an up-to-date area of scientific research. For example, a study [12] showed that the introduction of ND significantly improved the poor lubricating properties of water, reducing friction forces and wear by 70 and 88 %, respectively. A similar antifriction effect and antiwear action of water modified with ND are also noted in the works [13; 14].

A widespread category of lubricants is water-oil emulsion cooling lubricants used in cutting metals and their processing by plastic deformation methods. One of the ways for improving the operational characteristics of cooling lubricants is the introduction of various nanosized additives into the composition, enhancing their anti-scuffing effect, improving antifriction and thermophysical properties [15–17].

Currently, there are many different methods for producing ND. Examples of the most attractive of them in terms of industrial reproduction are the method of pulsed laser ablation of a specially prepared carbon target [18], the method of detonation of explosives in closed chambers [19], and some others. The method of hydrodynamic cavitation is also promising and in demand for industrial application. It consists of passing water with dispersed high-purity graphite powder through special-geometry microfluidic channels with feeding into the zone where, due to the collapse/deflation of cavitation caverns, destructive cumulative jets are formed, a buffer layer with subsequent additional effect on the collapsing caverns of fields with supercritical parameters.

This method is of the greatest interest in terms of the applicability of nanodiamonds produced with its use as a modifying additive in aqueous systems, such as gypsum, cooling lubricants, galvanics, and concrete. The advantages of the method consist in producing ND with high homogeneity of the main characteristic indicators: size, shape, charge, and functional cover. Cavitational synthesis nanodiamonds (CND-NS – Cavitation NanoDiamonds produced by the NanoSystems Company) manufactured by this method do not require additional chemical cleaning, centrifugation and other preparatory operations. Immediately after synthesis, the aqueous dispersion of ND is ready for industrial use, since ND dispersed in distilled water are completely hydrated. At present, studies have already been conducted on the influence of CND-NS on the physical and mechanical properties of building concrete. These studies have recorded a significant increase in compressive and bending strength when adding CND-NS particles to the base mixture [20].

The purpose of this study is to evaluate the influence of nanosized diamonds produced by cavitation synthesis on the tribological properties of a commercial water-oil-based cooling lubricant.

## METHODS

Comparative tribological tests were carried out using the "indenter on disk" friction scheme at a constant sliding speed of $V$=0.4 m/s and a load of $P$=20 N on a T-11 tribometer (Poland). The material of the cylindrical indenter with a diameter of 4 mm and a length of 10 mm was high-speed P18 steel (HRC 65). The rotating counterbody (disk) with a diameter of 25.4 mm and a thickness of 6 mm was made of 30HGSA steel (HRC 35), the initial roughness of the friction surfaces was $Ra$=0.16 μm. This friction couple imitates frictional interaction during cutting (smoothing) of a difficult-to-machine structural material. At the same time, according to the previous experimental experience of the authors, the friction process without lubricating these materials is characterised by strong adhesive seizure. During testing, the friction force $F$(N) and the indenter displacement relative to the counterbody Δ (μm) were recorded in real time. The friction path length was $L$=400 m. A Mitutoyo Surftest SJ-210 profilograph-profilometer (Japan) was used to evaluate the relief of friction tracks and measure roughness. The worn surfaces of the samples were examined using a LaboMet-I4 metallographic inverted microscope (Russia). The shielding effect of the lubricating fluid was assessed based on a comparison of the wear of the softer counterbody material. An LV 210-A analytical balance (Russia) was used to measure the mass loss Δm of the samples.

The friction process was carried out in three variants of lubricating media. In the first basic case, a commercial Modus-M cooling lubricant (Trading and Industrial Company SINTEZ, Rostov-on-Don, Russia) was used. This semisynthetic water-soluble cooling lubricant in the working solution is a 5 % water-oil emulsion and contains the least amount of oil and other environmentally hazardous functional additives. In the two subsequent versions, the emulsion was modified with a colloidal dispersion consisting of ND dispersed in distilled water. The dispersion was prepared using CND-NS synthesised by Research and Production Company Nanosystems, LLC (Rostov-on-Don, Russia), which are spheroidal nanocrystals with a negative zeta potential of $\zeta$=−44 mV. They were synthesised by the hydrodynamic cavitation method from high-purity graphite powder dispersed in distilled water with additional exposure of the system to alternating fields with supercritical parameters. By the dynamic light scattering method, it was found that the colloidal solution of the produced ND has high monodispersity with a maximum of 1 to 3 nm (Fig. 1).

To assess the influence of CND-NS ND on the tribological properties of commercial cooling lubricant, 0.5 and 2.5 % of CND-NS colloidal dispersion were added to its composition. The concentration of the aqueous colloidal dispersion of CND-NS was determined photometrically using an Expert-003 photometer by passing through a quartz cuvette with an optical path length of 1 mm and a transmission laser wavelength of 375 nm. The optical density was adjusted by diluting the concentrated CND-NS-2772 dispersion with distilled water.
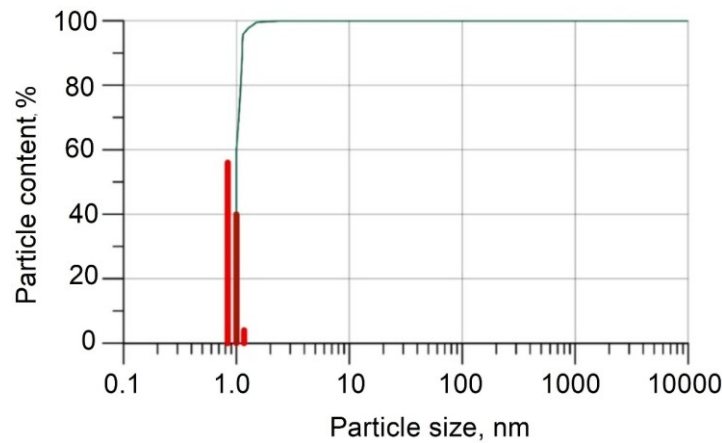
*Fig. 1. Particle size distribution of nanodiamonds [24]*
*Рис. 1. Распределение размеров частиц наноалмазов [24]*

Lubricants were supplied directly to the friction track using the drop-by-drop method with a flow rate of about 2 ml/min. The number of experiment implementations for each lubrication option was 5 experiments, statistical processing of the results was carried out using reliability theory methods in the MathCAD program. To calculate the values of the confidence limits for the estimated parameters, the Student's method was used at a specified reliability level of 95 %.

## RESULTS

Evaluation of the tribological properties of the lubricant samples showed that both variants of CND-NS concentration in the base cooling lubricant lead to an increase in the average values of friction forces. Fig. 2

shows examples of the evolution of the friction ratios $f$ during the experiments. According to the results of statistical processing, the average value of the friction ratio for the base lubricant variant was $f_{av}=0.08$; with the addition of 0.5 and 2.5 % of CND-NS, the value of this parameter increased to 0.11 and 0.13, respectively (Table 1).

Evaluation of the change in the tribocontact geometry relative to the initial position using the $\Delta(L)$ curves showed that the addition of additives contributed to a slowdown in the convergence of the friction couple elements due to wear processes (Fig. 3).

The lowest total linear wear of the tribo-couple elements was recorded at a concentration of 2.5 % and averaged $\delta_3 \approx 3.4$ µm, while for the base cooling lubricant this value reached $\delta_1 \approx 7.8$ µm.



*Fig. 2. Change in friction ratios f(L) in various environments:*
*1 – base cooling lubricant; 2 – cooling lubricant + 0.5 % of CND-NS; 3 – cooling lubricant + 2.5 % of CND-NS*
*Рис. 2. Изменение коэффициентов трения f(L) в различных средах:*
*1 – базовая СОЖ; 2 – СОЖ + 0,5 % КНА-НС; 3 – СОЖ + 2,5 % КНА-НС*

*Table 1. Tribological characteristics of the friction process in various lubricating environments*
*Таблица 1. Трибологические характеристики процесса трения в различных смазочных средах*

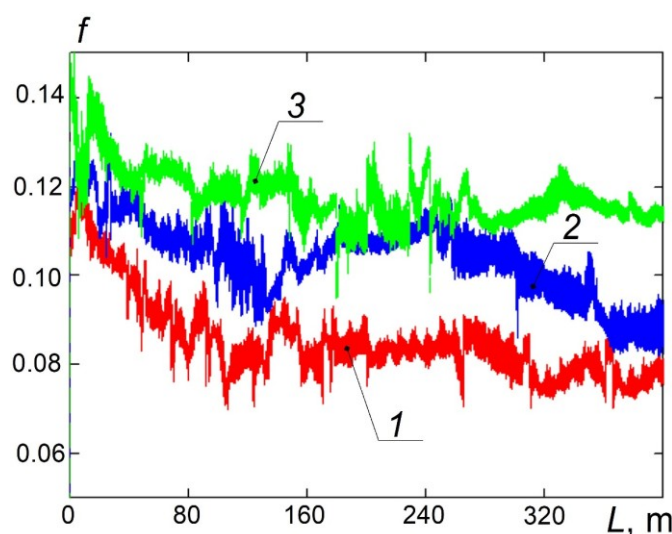| Lubricant type | $F_{av}$ | Counterbody | | | | Indenter |
|---|---|---|---|---|---|---|
| | | $\delta$, μm | $h_{max}$, μm | $\Delta m_c \cdot 10^{-3}$, g | $Ra$, μm | $\Delta m_{in} \cdot 10^{-4}$, g |
| **Base cooling lubricant** | 0.08±0.02 | 7.88±0.99 | 7.49±1.67 | 3.21±0.64 | 0.49±0.16 | 9.2±0.75 |
| **Cooling lubricant + 0.5 % of ND** | 0.11±0.03 | 4.45±0.59 | 4.81±0.86 | 2.33±0.56 | 0.34±0.07 | 7.6±0.81 |
| **Cooling lubricant + 2.5 % of ND** | 0.13±0.02 | 3.41±0.46 | 3.22±0.73 | 1.67±0.40 | 0.29±0.05 | 5.8±0.98 |

The greatest damage was suffered by the surface of the samples during friction in unmodified cooling lubricant (Fig. 4 a). The width of the friction tracks in thiscase reached 1000 μm, the wear depth was $h_{max} \approx 7.5$ μm, and the roughness of the friction tracks in the transverse direction was $Ra$=0.49 μm. Evaluation of the mass losses of the samples also showed the highest values of these parameters during friction in the base cooling lubricant (Table 1).

The surfaces of the samples are damaged to a lesser extent during frictional interaction in the cooling lubricant + 2.5 % of CND-NS environment. The width of the friction track in this lubrication option does not exceed 600 μm; the depth of the worn area is $h_{max} \approx 3.2$ μm. The roughness of the friction tracks for this concentration was $Ra$=0.29 μm. A high shielding effect is found as well when adding a much smaller amount of additive – at a concentration of 0.5 % of CND-NS (Fig. 4 b). In this case, an improvement in all the studied tribological indicators is also observed (Table 1, Fig. 4 c).

## DISCUSSION

The introduction of CND-NS nanoclusters into a water-oil emulsion in various concentrations significantly reduces the wear rate relative to the basic tribosystem configuration, but leads to an increase in friction forces. At the same time, the values of the friction ratios in all cases show that the boundary lubrication condition is maintained in the tribosystem.

The method and mode of producing ND, which determine their shape, average size and other statistical indicators of geometric characteristics, significantly affect the tribological behaviour of the lubricant when these particles are introduced into it. The antifriction effect of adding ND, according to the results of modern studies, is mainly associated with a partial replacement of sliding friction with rolling friction due to the presence of particles in the gap that are large enough in comparison with the sizes of surface microasperities, close to a spherical shape [21]. Smaller ND particles, being in the lubricant and penetrating into surface microasperities,
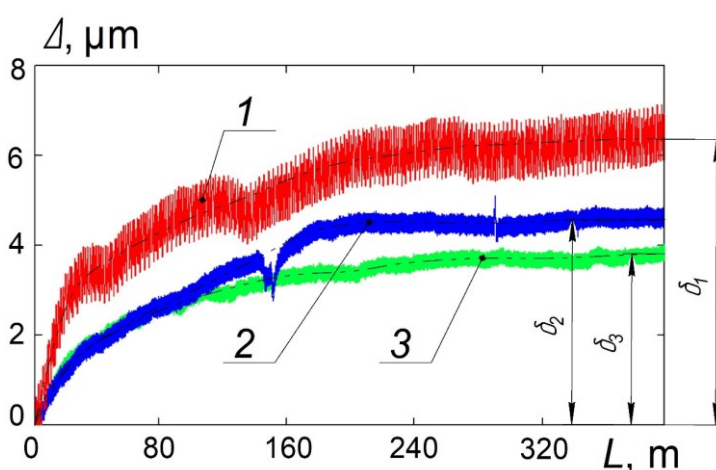


*Fig. 3. Total linear wear of tribocouple elements:*
*1 – base cooling lubricant; 2 – cooling lubricant + 0.5 % of CND-NS; 3 – cooling lubricant +2.5 % of CND-NS*
*Рис. 3. Суммарный линейный износ элементов трибопары:*
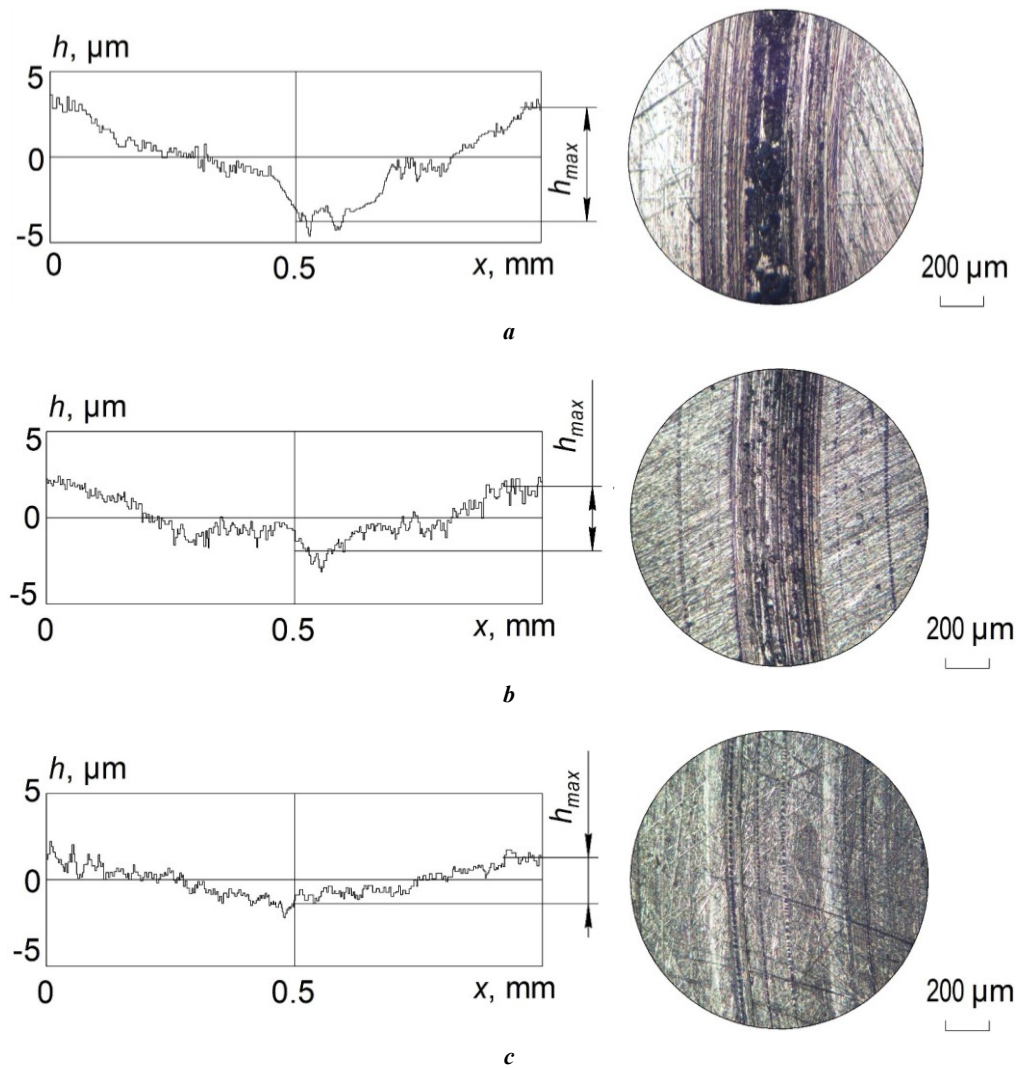*1 – базовая СОЖ; 2 – СОЖ + 0,5 % КНА-НС; 3 – СОЖ + 2,5 % КНА-НС*

**Fig. 4.** *Worn surfaces of disks during friction in various environments:*
***a** – base cooling lubricant; **b** – cooling lubricant + 0.5 % of CND-NS; **c** – cooling lubricant +2.5 % of CND-NS*
***Рис. 4.** Изношенные поверхности дисков при трении в различных средах:*
***a** – базовая СОЖ; **b** – СОЖ + 0,5 % КНА-НС; **c** – СОЖ + 2,5 % КНА-НС*

microasperities, can have a polishing effect. In this case, on the areas of surfaces separated by the lubricant, the presence of ND leads to the formation of a homoge-neous and thick tribofilm, which reduces the wear of the contacting bodies [10; 21]. These mechanisms of action on the tribological properties of the lubricant have been proven for particles obtained by the detonation method; they are most often studied as additives [21]. In comparison with CND-NS, these ND usually have a larger size range. Thus, when adding detonation ND, the lubricant contains particles close to a spherical (oval) shape within the range of 5–10 nm. For ND with a dia-meter in this range, the ball-bearing effect has been proven, including by molecular modelling [12].

When introducing CND-NS, which are significantly smaller in diameter, characterised by higher mono-dispersity, the ball-bearing effect from the use of ND de-creases, giving way to other mechanisms of action. Small-diameter diamond particles (1–3 nm) will fill surface microasperities more easily and remain fixed in them. This

type of introduction, on the one hand, protects the faces of the tribo-couple elements from destruction due to the pres-ence of a periodically regenerated protective layer of ND on them; on the other hand, the frictional interaction of surfac-es with hard inclusions, accompanied by a polishing effect, is the cause of the increase in the friction force. Concurrent-ly, the ND particles modify the lubricating film, promoting its compaction, increasing abrasion resistance and shear resistance, which leads to an increase in the friction ratio even with the addition of 0.5 % of CND-NS.

Further saturation of the cooling lubricant with nanodiamond particles enhances to an even greater degree the effect of the antiwear and polishing action of CND-NS. The increase in the average friction ratio relative to a con-centration of 0.5 % in this case, taking into account the va-lues of the confidence limits, can be considered insignifi-cant (Table 1). Thus, the properties, shape and size of cavi-tation nanodiamond particles, as well as their high mono-dispersity, allow achieving significant antiwear and polish-ing (smoothing) effects when modifying water-oil-based

cooling lubricants with them against the background of a slight decrease in anti-friction properties, which generally makes the application of CND-NS as an antiwear additive promising.

## CONCLUSIONS

1. Addition of diamond nanoclusters to the studied water-based cooling lubricant resulted in a significant change in the tribological characteristics of the friction system. Modification of the lubricating layers contributed to an increase in their load-bearing capacity, which ensured a decrease in the total linear wear of the friction-couple elements by 1.8 and 2.4 times at colloidal dispersion concentrations of 0.5 and 2.5 %, respectively.

2. Intermediate layers containing CND-NS increased the shielding effect of the lubricant in comparison with the base version, reducing the average roughness of the friction tracks by 1.4 and 1.6 times, which indicates an improvement in the surface quality after using the modified cooling lubricants.

3. Addition of nanosized diamonds enhanced the anti-wear properties of the lubricant. The reduction in mass losses of the rotating counterbody for colloidal dispersion concentrations of 0.5 and 2.5 % was 1.3 and 1.9 times, respectively, for the indenter – 1.2 and 1.5 times. The observed reduction in wear of the friction-couple elements was accompanied by an increase in the shear resistance of the lubricating layer, contributing to an increase in the friction force in the system by 1.4 times even with the addition of 0.5 % of nanodiamonds. A further increase in the amount of additive to 2.5 % led to an insignificant increase in the friction ratio relative to the minimum concentration of nanodiamonds.

The use of cavitational synthesis nanodiamonds as an additive in water-oil-based cooling lubricants can become a promising direction for further improvement of tribological properties and enhancement of their performance characteristics. The development of new compositions of cooling lubricants based on the studied commercial brand with the addition of nanocrystalline diamonds in various concentrations and subsequent studies of the performance characteristics of these experimental compositions in various metal cutting operations, plastic deformation processing, and knurling are considered as up-to-date sectors of further research in this area. The expected effects from the lubricant modification in this case will be an increase in the service life of the tools used and an improvement in the quality of the microrelief of the treated surfaces.

## REFERENCES

1. Chen Yan, Renner P., Liang Hong. Dispersion of Nanoparticles in Lubricating Oil: A Critical Review. *Lubricants*, 2019, vol. 7, no. 1, article number 7. DOI: 10.3390/lubricants7010007.

2. Gulzar M., Masjuki H.H., Kalam M.A., Varman M., Zulkifli N.W.M., Mufti R.A., Zahid R. Tribological performance of nanoparticles as lubricating oil additives. *Journal of Nanoparticle Research*, 2016, vol. 18, article number 223. DOI: 10.1007/s11051-016-3537-4.

3. Xia Wenzhen, Zhao Jingwei, Wu Hui et al. Effects of oil-in-water based nanolubricant containing TiO$_2$ nanoparticles in hot rolling of 304 stainless steel. *Journal of Materials Processing Technology*, 2018, vol. 262, pp. 149–156. DOI: 10.1016/j.jmatprotec.2018.06.020.

4. Kim Hyun-Joon, Seo Kuk-Jin, Kang Kyeong Hee, Kim Dae-Eun. Nano-lubrication: A review. *International Journal of Precision Engineering and Manufacturing*, 2016, vol. 17, pp. 829–841. DOI: 10.1007/s12541-016-0102-0.

5. Ali I., Basheer A.A., Kucherova A. et al. Advances in carbon nanomaterials as lubricants modifiers. *Journal of Molecular Liquids*, 2019, vol. 279, pp. 251–266. DOI: 10.1016/j.molliq.2019.01.113.

6. Zhai Wenzheng, Srikanth N., Kong Ling Bing, Zhou Kun. Carbon nanomaterials in tribology. *Carbon*, 2017, vol. 119, pp. 150–171. DOI: 10.1016/j.carbon.2017.04.027.

7. Gong Zhenbin, Shi Jing, Zhang Bin, Zhang Junyan. Graphene nano scrolls responding to superlow friction of amorphous carbon. *Carbon*, 2017, vol. 116, pp. 310–317. DOI: 10.1016/j.carbon.2017.01.106.

8. Morshed A., Wu Hui, Jiang Zhengyi. A Comprehensive Review of Water-Based Nanolubricants. *Lubricants*, 2021, vol. 9, article number 89. DOI: 10.3390/lubricants9090089.

9. Ivanov M., Shenderova O. Nanodiamond-based nanolubricants for motor oils. *Current Opinion in Solid State and Materials Science*, 2017, vol. 21, no. 1, pp. 17–24. DOI: 10.1016/j.cossms.2016.07.003.

10. Piya A.K., Yang L., Omar A.A.S., Emami N., Morina A. Synergistic lubrication mechanism of nanodiamonds with organic friction modifier. *Carbon*, 2024, vol. 218, article number 118742. DOI: 10.1016/j.carbon.2023.118742.

11. Shirani A., Nunn N., Shenderova O., Osawa E., Berman D. Nanodiamonds for improving lubrication of titanium surfaces in simulated body fluid. *Carbon*, 2019, vol. 143, pp. 890–896. DOI: 10.1016/j.carbon.2018.12.005.

12. Mirzaamiri R., Akbarzadeh S., Ziaei-Rad S., Shin Dong-Gap, Kim Dae-Eun. Molecular dynamics simulation and experimental investigation of tribological behavior of nanodiamonds in aqueous suspensions. *Tribology International*, 2021, vol. 156, article number 106838. DOI: 10.1016/j.triboint.2020.106838.

13. Alias A.A., Kinoshita H., Fujii M. Tribological properties of diamond nanoparticle additive in water under a lubrication between steel plate and tungsten carbide ball. *Journal of Advanced Mechanical Design, Systems, and Manufacturing*, 2015, vol. 9, no. 1, article number JAMDSM0006. DOI: 10.1299/jamdsm.2015jamdsm0006.

14. Wu Pu, Chen Xinchun, Zhang Chenhui, Luo Jianbin. Synergistic tribological behaviors of graphene oxide and nanodiamond as lubricating additives in water. *Tribology International*, 2019, vol. 132, pp. 177–184. DOI: 10.1016/j.triboint.2018.12.021.

15. Hu Shuguo, Li Changhe, Zhou Zongming et al. Nanoparticle-enhanced coolants in machining: mechanism, application, and prospects. *Frontiers of Mechanical*

*Engineering*, 2023, vol. 18, article number 53. DOI: 10.1007/s11465-023-0769-8.

16. Wang Xiaoming, Song Yuxiang, Lim Changhe et al. Nanofluids application in machining: a comprehensive review. *The International Journal of Advanced Manufacturing*, 2024, vol. 131, pp. 3113–3164. DOI: 10.1007/s00170-022-10767-2.

17. Kumar A.S., Deb S., Paul S. Tribological characteristics and micromilling performance of nanoparticle enhanced water based cutting fluids in minimum quantity lubrication. *Journal of Manufacturing Processes*, 2020, vol. 56, part A, pp. 766–776. DOI: 10.1016/j.jmapro.2020.05.032.

18. Antipov A.A., Arakelyan S.M., Kutrovskaya S.V., Kucherik A.O., Nogtev D.S., Osipov A.V., Garnov S.V. Laser ablation of carbon targets placed in a liquid. *Quantum Electronics*, 2015, vol. 45, no. 8, pp. 731–735. DOI: 10.1070/QE2015v045n08ABEH015681.

19. Vityaz P.A. *Nanoalmazy detonatsionnogo sinteza: poluchenie i primenenie* [Detonation synthesis nanodiamonds: production and application]. Minsk, Belaruskaya navuka Publ., 2013. 381 p.

20. Beskopylny A.N., Stel'makh S.A., Shcherban' E.M. et al. Performance and mechanism of the structure formation and physical-mechanical properties of concrete by modification with nanodiamonds. *Construction and Building Materials*, 2024, vol. 452, article number 138994. DOI: 10.1016/j.conbuildmat.2024.138994.

21. Xia Yue, Lu Yunxiang, Yang Guoyong et al. Application of Nano-Crystalline Diamond in Tribology. *Materials*, 2023, vol. 16, no. 7, article number 2710. DOI: 10.3390/ma16072710.

## СПИСОК ЛИТЕРАТУРЫ

1. Chen Yan, Renner P., Liang Hong. Dispersion of Nanoparticles in Lubricating Oil: A Critical Review // Lubricants. 2019. Vol. 7. № 1. Article number 7. DOI: 10.3390/lubricants7010007.

2. Gulzar M., Masjuki H.H., Kalam M.A., Varman M., Zulkifli N.W.M., Mufti R.A., Zahid R. Tribological performance of nanoparticles as lubricating oil additives // Journal of Nanoparticle Research. 2016. Vol. 18. Article number 223. DOI: 10.1007/s11051-016-3537-4.

3. Wenzhen Xia, Jingwei Zhao, Hui Wu et al. Effects of oil-in-water based nanolubricant containing TiO$_2$ nanoparticles in hot rolling of 304 stainless steel // Journal of Materials Processing Technology. 2018. Vol. 262. P. 149–156. DOI: 10.1016/j.jmatprotec.2018.06.020.

4. Kim Hyun-Joon, Seo Kuk-Jin, Kang Kyeong Hee, Kim Dae-Eun. Nano-lubrication: A review // International Journal of Precision Engineering and Manufacturing. 2016. Vol. 17. P. 829–841. DOI: 10.1007/s12541-016-0102-0.

5. Ali I., Basheer A.A., Kucherova A. et al. Advances in carbon nanomaterials as lubricants modifiers // Journal of Molecular Liquids. 2019. Vol. 279. P. 251–266. DOI: 10.1016/j.molliq.2019.01.113.

6. Zhai Wenzheng, Srikanth N., Kong Ling Bing, Zhou Kun. Carbon nanomaterials in tribology // Carbon. 2017. Vol. 119. P. 150–171. DOI: 10.1016/j.carbon.2017.04.027.

7. Gong Zhenbin, Shi Jing, Zhang Bin, Zhang Junyan. Graphene nano scrolls responding to superlow friction of amorphous carbon // Carbon. 2017. Vol. 116. P. 310–317. DOI: 10.1016/j.carbon.2017.01.106.

8. Morshed A., Wu Hui, Jiang Zhengyi. A Comprehensive Review of Water-Based Nanolubricants // Lubricants. 2021. Vol. 9. Article number 89. DOI: 10.3390/lubricants9090089.

9. Ivanov M., Shenderova O. Nanodiamond-based nanolubricants for motor oils // Current Opinion in Solid State and Materials Science. 2017. Vol. 21. № 1. P. 17–24. DOI: 10.1016/j.cossms.2016.07.003.

10. Piya A.K., Yang L., Omar A.A.S., Emami N., Morina A. Synergistic lubrication mechanism of nanodiamonds with organic friction modifier // Carbon. 2024. Vol. 218. Article number 118742. DOI: 10.1016/j.carbon.2023.118742.

11. Shirani A., Nunn N., Shenderova O., Osawa E., Berman D. Nanodiamonds for improving lubrication of titanium surfaces in simulated body fluid // Carbon. 2019. Vol. 143. P. 890–896. DOI: 10.1016/j.carbon.2018.12.005.

12. Mirzaamiri R., Akbarzadeh S., Ziaei-Rad S., Shin Dong-Gap, Kim Dae-Eun. Molecular dynamics simulation and experimental investigation of tribological behavior of nanodiamonds in aqueous suspensions // Tribology International. 2021. Vol. 156. Article number 106838. DOI: 10.1016/j.triboint.2020.106838.

13. Alias A.A., Kinoshita H., Fujii M. Tribological properties of diamond nanoparticle additive in water under a lubrication between steel plate and tungsten carbide ball // Journal of Advanced Mechanical Design, Systems, and Manufacturing. 2015. Vol. 9. № 1. Article number JAMDSM0006. DOI: 10.1299/jamdsm.2015jamdsm0006.

14. Wu Pu, Chen Xinchun, Zhang Chenhui, Luo Jianbin. Synergistic tribological behaviors of graphene oxide and nanodiamond as lubricating additives in water // Tribology International. 2019. Vol. 132. P. 177–184. DOI: 10.1016/j.triboint.2018.12.021.

15. Hu Shuguo, Li Changhe, Zhou Zongming et al. Nanoparticle-enhanced coolants in machining: mechanism, application, and prospects // Frontiers of Mechanical Engineering. 2023. Vol. 18. Article number 53. DOI: 10.1007/s11465-023-0769-8.

16. Wang Xiaoming, Song Yuxiang, Lim Changhe et al. Nanofluids application in machining: a comprehensive review // The International Journal of Advanced Manufacturing. 2024. Vol. 131. P. 3113–3164. DOI: 10.1007/s00170-022-10767-2.

17. Kumar A.S., Deb S., Paul S. Tribological characteristics and micromilling performance of nanoparticle enhanced water based cutting fluids in minimum quantity lubrication // Journal of Manufacturing Processes. 2020. Vol. 56. Part A. P. 766–776. DOI: 10.1016/j.jmapro.2020.05.032.

18. Антипов А.А., Аракелян С.М., Гарнов С.В., Кутровская С.В., Кучерик А.О., Ногтев Д.С., Осипов А.В. Лазерная абляция углеродных мишеней, помещенных в жидкость // Квантовая электроника. 2015. Т. 45. № 8. С. 731–735. EDN: UGUZNP.

19. Витязь П.А. Наноалмазы детонационного синтеза: получение и применение. Минск: Беларуская навука, 2013. 381 с.

20. Beskopylny A.N., Stel'makh S.A., Shcherban' E.M. et al. Performance and mechanism of the structure formation and physical-mechanical properties of concrete by modification with nanodiamonds // Construction and Building Materials. 2024. Vol. 452. Article number 138994. DOI: 10.1016/j.conbuildmat.2024.138994.

21. Xia Yue, Lu Yunxiang, Yang Guoyong et al. Application of Nano-Crystalline Diamond in Tribology // Materials. 2023. Vol. 16. № 7. Article number 2710. DOI: 10.3390/ma16072710.

# Влияние наноалмазов кавитационного синтеза на трибологические свойства смазывающе-охлаждающей жидкости на водомасляной основе

**Фоминов Евгений Валерьевич**\*[1,3], кандидат технических наук, доцент
**Ковтун Максим Витальевич**[2,4], руководитель научно-технического центра
**Курлович Сергей Анатольевич**[2,5], директор
**Гладких Дмитрий Игоревич**[1,6], аспирант
**Лавренова Татьяна Владимировна**[1,7], старший преподаватель

[1]*Донской государственный технический университет, Ростов-на-Дону (Россия)*
[2]*ТПК «СИНТЕЗ», Ростов-на-Дону (Россия)*

\***E-mail:** fominoff83@mail.ru

[3]ORCID: https://orcid.org/0000-0002-0165-7536
[4]ORCID: https://orcid.org/0009-0003-1489-8333
[5]ORCID: https://orcid.org/0009-0002-3606-6311
[6]ORCID: https://orcid.org/0000-0003-2292-256X
[7]ORCID: https://orcid.org/0000-0002-8283-7730

*Аннотация:* Статья посвящена изучению влияния наноразмерных алмазов, полученных методом кавитационного синтеза, на трибологические характеристики коммерческой смазывающе-охлаждающей жидкости на водомасляной основе. Исследование направлено на оценку перспектив применения наноалмазов данного типа в качестве антифрикционной и противоизносной присадки. Трибологические испытания проводились по схеме трения «индентор по диску» при постоянной нагрузке и скорости скольжения. В качестве материалов пары трения использованы быстрорежущая сталь Р18 для индентора и сталь 30ХГСА для вращающегося контртела (диска). Исследования проведены для базового смазочного материала и двух вариантов модификаций его состава коллоидной дисперсией (дистиллированная вода с диспергированными наноалмазами) с окончательной концентрацией присадки 0,5 и 2,5 %. Экспериментально установлено, что оба варианта модификации базовой водомасляной эмульсии привели к увеличению несущей способности смазочных слоев, снизив суммарный линейный износ элементов пары трения в 1,8–2,4 раза. Присутствие наноалмазов в составе также усилило экранирующий эффект смазочно-охлаждающей жидкости. Посредством оптической микроскопии было зафиксировано снижение видимых повреждений поверхностей трения. Анализ профилограмм изношенных участков в поперечном направлении показал уменьшение размеров борозды на контртеле на фоне снижения шероховатости с $Ra=0,49$ мкм в базовом варианте до $Ra=0,29$–$0,34$ мкм. Оценка потери массы контртел для концентраций наноалмазов 0,5 и 2,5 % показала снижение их величины в 1,3 и 1,9 раза соответственно, для индентора уменьшение этого параметра составило 1,2 и 1,5 раза. Таким образом, использование наноалмазов кавитационного синтеза в качестве присадки может стать перспективным направлением повышения противоизносных свойств смазывающе-охлаждающих жидкостей на водомасляной основе.

*Ключевые слова:* наноалмазы кавитационного синтеза; водомасляная эмульсия; смазывающе-охлаждающая жидкость; граничное трение; износостойкость; коэффициент трения.

*Для цитирования:* Фоминов Е.В., Ковтун М.В., Курлович С.А., Гладких Д.И., Лавренова Т.В. Влияние наноалмазов кавитационного синтеза на трибологические свойства смазывающе-охлаждающей жидкости на водомасляной основе // Frontier Materials & Technologies. 2025. № 2. С. 87–94. DOI: 10.18323/2782-4039-2025-2-72-7.

# The influence of hardening heat treatment modes
# on the crack propagation resistance of 5H2SMF die steel

*Karen Yu. Shakhnazarov*\*[1], Doctor of Sciences (Engineering),
professor of Chair of Materials Science and Technology of Artistic Products
*Artur R. Rafikov*[2], postgraduate student
of Chair of Materials Science and Technology of Artistic Products
*Empress Catherine II Saint Petersburg Mining University, St. Petersburg (Russia)*

\*E-mail: mthi@spmi.ru,
karen812@yandex.ru

[1]ORCID: https://orcid.org/0000-0001-7501-6590
[2]ORCID: https://orcid.org/0009-0001-9881-9115

*Abstract:* In the literature, there are virtually no data on the effect of quenching with holding in the pearlite and bainitic regions and subsequent low and high tempering of different durations on the crack propagation resistance of die steels, and the available data are contradictory. Meanwhile, a "softer" quenching with holding in the intermediate regions reduces significantly the risk of quenching cracks and deformation of dies and die tooling. In this work, samples of 5H2SMF die steel with a sharp notch and artificially induced cracks were subjected to heat treatment, including standard quenching at 910 °C in oil and quenching from 910 °C with steps at 650 °C and 340 °C with different types of tempering (200, 560, 600, and 640 °C) and different durations of time – 1, 3, 5, 7, and 14 h (for 200 °C) in order to increase the crack propagation resistance. The conducted studies allowed identifying that the data on crack propagation resistance after step quenching with holding in the pearlite transformation region and subsequent high tempering at 560, 600 and 640 °C are comparable with standard quenching in oil and high tempering at the same temperatures. The hardness after step quenching in the bainitic transformation region (340 °C) is significantly lower in all cases under different tempering conditions; therefore, it is not possible to compare crack propagation resistance with standard quenching. The optimal holding time (3 and 5 h) from the point of view of increasing crack propagation resistance after standard quenching from 910 °C in oil and low tempering at 200 °C was found.

*Keywords:* die steel; quenching; tempering; hardness; crack propagation resistance.

*For citation:* Shakhnazarov K.Yu., Rafikov A.R. The influence of hardening heat treatment modes on the crack propagation resistance of 5H2SMF die steel. *Frontier Materials & Technologies*, 2025, no. 2, pp. 95–101. DOI: 10.18323/2782-4039-2025-2-72-8.

## INTRODUCTION

Heat treatment is one of the key processes significantly affecting mechanical properties, therefore the correct choice of the quenching mode, during which the alloying elements are redistributed, the grain size changes, carbides dissolve, etc., ultimately determines the operational properties of steel products.

Step quenching used to reduce quenching stresses and deformation is known from the report "On the Preparation of Steel Armour-Piercing Projectiles" of D.K. Chernov in 1885 [1]. Despite the fact that this method has now been studied quite well, in the literature, there are contradictory data on the influence of step quenching on the mechanical properties of steels after various modes of tempering [2–4]. Step cooling of metastable austenite in the pearlite area without decomposition into a ferrite-carbide mixture led to the discovery of interesting effects [5; 6]. A comparison of conventional quenching with quenching with isothermal holding at 560–680 °C shows that for 6H6M1, 5F3B and 6H6M3F steels, processes leading to an increase in hardness occur in supercooled austenite. These processes are associated with the forma-

tion of equilibrium regions of 10–15 Å in size in martensite resulted from step quenching, having an increased content of carbon, vanadium and molybdenum, with the same lattice as the matrix. During subsequent tempering, these microheterogeneities act as nuclei for the formation of carbides, providing them with high dispersion and uniformity of distribution, which leads to an increase in the heat resistance of the dies [5; 7; 8].

A study of the patterns of structural transformations occurring during quenching with holding in the bainitic transformation region of the 30HSNMFB and 30H3N3MFB steels showed that at the early stages of such holding, agglomerates (clusters or mixed zones) of alloying element atoms (vanadium and carbon) are formed by analogy with the processes occurring at the initial stages of aging of many steels [9; 10]. The authors believe that these clusters also contain molybdenum and chromium atoms [9; 11]. The presence of such clusters of atoms exhibits the resistance to destruction and thereby strengthens the steel.

The processes of both high and low tempering of quenched steel occurring at different temperatures have

been studied quite well. However, in the literature, there are practically no data on the influence of tempering duration on the properties of steels. A number of studies provide non-monotonic dependencies of mechanical properties on tempering duration [12–14]. The identified non-monotonic, sawtooth nature of the "resistance to crack propagation – time" curves is presented without any comments [14; 15].

5H2SMF die steel is used mainly for the manufacture of hot deformation dies, but since in the low-tempered state the hardness is in the range of 58–60 HRC, it can also be used for cold deformation dies [16; 17]. In this regard, in the presented work, a comparative study of the dependence of the resistance to crack propagation and hardness of 5H2SMF steel after standard quenching (in oil), and quenching with holding in the pearlite and bainitic regions with subsequent low and high tempering, as well as low tempering of different durations, is carried out.

The purpose of this study is to develop hardening heat treatment modes for industrially used 5H2SMF die steel, including quenching with holding in the pearlite and bainitic regions and tempering at different temperatures of different durations, increasing the resistance to crack propagation.

## METHODS

For the study, 5H2SMF die steel [18] was selected. The chemical composition of the steel is given in Table 1.

The heat treatment of the studied samples with dimensions of 10×11×55 mm was carried out in salt baths of AO Obukhovski Plant (JSC). Termooil-26 oil was used as a quenching medium. Tests for each heat treatment mode were carried out on 7 samples. Three quenching modes were studied: 1 – 910 °C, 15 min, cooling in oil; 2 – 910 °C, 15 min – 340 °C, 15 min, cooling in oil; 3 – 910 °C, 15 min – 650 °C, 7 min, cooling in oil; subsequent tempering: 200, 560, 600, and 640 °C for 2 h for each quenching mode. A study was conducted as well on the duration of low tempering. The samples after quenching according to the standard mode (910 °C, 15 min, cooling in oil) were subjected to low tempering (200 °C) of different durations: 1, 3, 5, 7, and 14 h.

The blanks of the samples for determining the mechanical properties were prepared with a grinding allowance of 0.5 mm. After quenching, the dimensions were brought to the finished ones (10×10×55 mm), which allowed, excluding the influence of decarburisation occurring during heating for quenching, on the hardness of the samples.

The maximum achievable force ($P_c$) required for complete destruction of the sample during static three-point bending was taken as the evaluation criterion.

The experiment was carried out on samples for impact toughness testing according to KCT with a *V*-shaped notch 1.5 mm deep and a concentrator radius *R* of 0.25±0.025 (GOST 9454-78, Fig. 3). According to clause 1.4 of GOST 9454-78 and clause 1.6 of GOST 25.506-85, a fatigue crack 1.5 mm deep was initiated by the cyclic loading method with a number of cycles of at least 3000 on a Drozdovsky resonant vibrator (Russia). The maximum residual deflection formed when applying a T-type concentrator to the samples did not exceed 0.25 mm.

Static bending tests were carried out on a POWERTEST T testing machine (Spain) (distance between supports is 45 mm) with a loading rate of no more than 2 mm/min.

Due to the fact that when initiating a fatigue crack on a Drozdovsky vibrator, some deviation of the depth from the required one is possible, after testing the fractures of all samples, the total depth of the crack and notch ($L_{cr}$) was measured using an MPB-2 counting microscope (Russia). The analysis of the obtained experimental data on crack propagation resistance and hardness after various heat treatment modes was carried out taking into account the actual total crack and notch depth. Hardness was measured on a TK-2M hardness tester (Russia).

## RESULTS

### Hardness and crack propagation resistance after low and high tempering

Table 2 shows that the maximum values of hardness and crack resistance ($P_{cr}$) after low tempering (200 °C) were obtained after standard oil quenching. Quenching with holding in the pearlite region (mode 3) with an insignificant (by 0.5 HRC) decrease in hardness and a 0.03 mm less total crack and notch depth ($L_{cr}$) leads to an insignificant (by 64 kN/cm$^2$) decrease in crack resistance. Crack resistance is maximum after the mode with a step at 340 °C, but at the same time the hardness in the low-tempered state decreases significantly (by 5 HRC), which indicates the occurrence of partial bainitic decomposition.

Hardness after quenching according to mode 3 and tempering at 560 °C has maximum values (49 HRC) with minimum total crack and notch depth (3.16 mm versus 3.4 and 3.34 mm after standard quenching and with holding at 340 °C, respectively), while this mode has minimum values of crack propagation resistance ($P_{cr}$) (Table 3). Samples

*Table 1. Chemical composition of 5H2SMF [18]*
*Таблица 1. Химический состав 5X2СМФ [18]*

| Steel grade | C, % | Mn, % | Si, % | Cr, % | Mo, % | V, % |
|---|---|---|---|---|---|---|
| 5H2SMF | 0.56 | 0.47 | 0.72 | 2.48 | 0.23 | 0.27 |

*Table 2. Maximum ($P_{max}$), average ($P_{av}$) and minimum ($P_{min}$) values of crack propagation resistance,
hardness after quenching (HRC$_{quen}$) and tempering (HRC$_{temp}$) and total depth of crack and notch ($L_{cr}$)
of 5H2SMF steel quenched by different modes and tempered at 200 °C*
***Таблица 2.*** *Максимальное ($P_{max}$), среднее ($P_{av}$) и минимальное ($P_{min}$) значение сопротивления развитию трещины,
твердость после закалки (HRC$_{quen}$) и отпуска (HRC$_{temp}$) и суммарная глубина трещины
и надреза ($L_{cr}$) стали 5Х2СМФ, закаленной по различным режимам, отпуск при 200 °C*

| Mode No. | Quenching mode | Crack propagation resistance ($P_{cr}$), kN/cm² | | | Hardness, HRC | | Total depth of crack and notch ($L_{cr}$), mm |
|---|---|---|---|---|---|---|---|
| | | $P_{cr\ max}$ | $P_{cr\ av}$ | $P_{cr\ min}$ | HRC$_{quen}$ | HRC$_{temp}$ | |
| **1** | 910 °C in oil | 735 | 667 | 590 | 61.0 | 58.5 | 3.27 |
| **2** | 910 °C – 340 °C in oil | 770 | 727 | 630 | 54.0 | 53.5 | 3.62 |
| **3** | 910 °C – 650 °C in oil | 670 | 603 | 500 | 60.5 | 58.0 | 3.24 |

*Table 3. Maximum ($P_{max}$), average ($P_{av}$) and minimum ($P_{min}$) values of crack propagation resistance,
hardness after quenching (HRC$_{quen}$) and tempering (HRC$_{temp}$) and total depth of crack and notch ($L_{cr}$)
of 5H2SMF steel quenched by different modes and tempered at 560 °C*
***Таблица 3.*** *Максимальное ($P_{max}$), среднее ($P_{av}$) и минимальное ($P_{min}$) значение сопротивления развитию трещины,
твердость после закалки (HRC$_{quen}$) и отпуска (HRC$_{temp}$) и суммарная глубина трещины
и надреза ($L_{cr}$) стали 5Х2СМФ, закаленной по различным режимам, отпуск при 560 °C*

| Mode No. | Quenching mode | Crack propagation resistance ($P_{cr}$), kN/cm² | | | Hardness, HRC | | Total depth of crack and notch ($L_{cr}$), mm |
|---|---|---|---|---|---|---|---|
| | | $P_{cr\ max}$ | $P_{cr\ av}$ | $P_{cr\ min}$ | HRC$_{quen}$ | HRC$_{temp}$ | |
| **1** | 910 °C in oil | 1180 | 1170 | 1060 | 62.0 | 48.5 | 3.40 |
| **2** | 910 °C – 340 °C in oil | 1515 | 1381 | 1292 | 53.5 | 46.5 | 3.34 |
| **3** | 910 °C – 650 °C in oil | 920 | 840 | 730 | 61.5 | 49.0 | 3.16 |

quenched according to mode 2, compared to standard quenching with a decrease in hardness (by 2 HRC) and a 0.06 mm less total crack and notch depth ($L_{cr}$), have maximum (more than 200 kN/cm² compared to standard quenching) crack propagation resistance ($P_{cr}$) (Table 3). The hardness after tempering at 600 °C, as in the previous experiment, has maximum values after quenching with a step at 650 °C, but the value of crack propagation resistance ($P_{cr}$) is minimal (Table 4). The values of crack propagation resistance ($P_{cr}$) after mode 2 and standard quenching with some decrease in hardness (by 1.5 HRC) at approximately the same total crack and notch depth (3.38 and 3.37 mm) are comparable (2410 and 2420 kN/cm², respectively) (Table 4).

After heat treatment according to mode 3, the maximum hardness values (38 HRC) were obtained, while unlike the mode of tempering at 600 °C (Table 4), such a large difference in crack propagation resistance ($P_{cr}$) is not observed at an equal total crack and notch depth (3.3 mm) compared to standard quenching (Table 5). The decrease in hardness after tempering at 640 °C and quenching according to mode 2 does not increase the value of crack propagation resistance ($P_{cr}$) compared to standard quenching and

quenching according to mode 3, even despite the minimum (3.2 mm) total crack and notch depth ($L_{cr}$) (Table 5).

**Hardness and crack propagation resistance
after tempering (200 °C) of different durations**

Table 6 shows that increasing the holding time from 1 to 14 h of low tempering leads to an insignificant (by 1.5 HRC) decrease in the hardness of 5H2SMF steel samples.

Tempering for 3 h leads to maximum (667 kN/cm²) crack propagation resistance ($P_{cr}$) values at maximum hardness (58 HRC) and maximum (3.37 mm) total crack and notch depth ($L_{cr}$). With tempering for 5 h, a minimum (55 kN/cm²) difference can be observed between the maximum and minimum crack propagation resistance ($P_{cr}$), while for other modes it is more than 135 kN/cm². The values of crack propagation resistance ($P_{cr}$) at equal hardness (57.5 HRC) and maximum (3.37 mm) total crack and notch depth ($L_{cr}$) are comparable with other modes (Table 6).

Conducting tempering for 1 h leads to minimum values of crack propagation resistance ($P_{cr}$), which is probably associated with the fact that one-hour tempering does not eliminate the brittleness specific for freshly quenched martensite.

***Table 4.*** *Maximum ($P_{max}$), average ($P_{av}$) and minimum ($P_{min}$) values of crack propagation resistance,*
*hardness after quenching ($HRC_{quen}$) and tempering ($HRC_{temp}$) and total depth of crack and notch ($L_{cr}$)*
*of 5H2SMF steel quenched by different modes and tempered at 600 °C*
***Таблица 4.*** *Максимальное ($P_{max}$), среднее ($P_{av}$) и минимальное ($P_{min}$) значение сопротивления развитию трещины,*
*твердость после закалки ($HRC_{quen}$) и отпуска ($HRC_{temp}$) и суммарная глубина трещины*
*и надреза ($L_{cr}$) стали 5Х2СМФ, закаленной по различным режимам, отпуск при 600 °C*

| Mode No. | Quenching mode | Crack propagation resistance ($P_{cr}$), kN/cm² | | | Hardness, HRC | | Total depth of crack and notch ($L_{cr}$), mm |
|---|---|---|---|---|---|---|---|
| | | $P_{cr\ max}$ | $P_{cr\ av}$ | $P_{cr\ min}$ | $HRC_{quen}$ | $HRC_{temp}$ | |
| **1** | 910 °C in oil | 2600 | 2420 | 2120 | 61.0 | 43.5 | 3.37 |
| **2** | 910 °C – 340 °C in oil | 2550 | 2410 | 2040 | 54.0 | 42.0 | 3.38 |
| **3** | 910 °C – 650 °C in oil | 1280 | 1188 | 1085 | 60.5 | 45.0 | 3.35 |

***Table 5.*** *Maximum ($P_{max}$), average ($P_{av}$) and minimum ($P_{min}$) values of crack propagation resistance,*
*hardness after quenching ($HRC_{quen}$) and tempering ($HRC_{temp}$) and total depth of crack and notch ($L_{cr}$)*
*of 5H2SMF steel quenched by different modes and tempered at 640 °C*
***Таблица 5.*** *Максимальное ($P_{max}$), среднее ($P_{av}$) и минимальное ($P_{min}$) значение сопротивления развитию трещины,*
*твердость после закалки ($HRC_{quen}$) и отпуска ($HRC_{temp}$) и суммарная глубина трещины*
*и надреза ($L_{cr}$) стали 5Х2СМФ, закаленной по различным режимам, отпуск при 640 °C*

| Mode No. | Quenching mode | Crack propagation resistance ($P_{cr}$), kN/cm² | | | Hardness, HRC | | Total depth of crack and notch ($L_{cr}$), mm |
|---|---|---|---|---|---|---|---|
| | | $P_{cr\ max}$ | $P_{cr\ av}$ | $P_{cr\ min}$ | $HRC_{quen}$ | $HRC_{temp}$ | |
| **1** | 910 °C in oil | 2600 | 2451 | 2100 | 61.0 | 36.5 | 3.3 |
| **2** | 910 °C – 340 °C in oil | 2290 | 2150 | 2070 | 53.5 | 35.0 | 3.2 |
| **3** | 910 °C – 650 °C in oil | 2530 | 2272 | 2100 | 60.5 | 38.0 | 3.3 |

***Table 6.*** *Maximum ($P_{max}$), average ($P_{av}$) and minimum ($P_{min}$) values of crack propagation resistance,*
*hardness after quenching ($HRC_{quen}$) and tempering ($HRC_{temp}$) and total depth of crack and notch ($L_{cr}$)*
*of 5H2SMF steel quenched under the standard mode (910 °C in oil),*
*tempering at 200 °C with different durations*
***Таблица 6.*** *Максимальное ($P_{max}$), среднее ($P_{av}$) и минимальное ($P_{min}$) значение сопротивления развитию трещины,*
*твердость после закалки ($HRC_{quen}$) и отпуска ($HRC_{temp}$) и суммарная глубина трещины*
*и надреза ($L_{cr}$) стали 5Х2СМФ, закаленной по стандартному режиму (910 °C в масло),*
*отпуск при 200 °C разной продолжительности*

| Holding time at tempering at 200 °C, h | Crack propagation resistance ($P_{cr}$), kN/cm² | | | Hardness, HRC | | Total depth of crack and notch ($L_{cr}$), mm |
|---|---|---|---|---|---|---|
| | $P_{cr\ max}$ | $P_{cr\ av}$ | $P_{cr\ min}$ | $HRC_{quen}$ | $HRC_{temp}$ | |
| **1** | 595 | 528 | 460 | 59.5 | 58.5 | 3.27 |
| **3** | 735 | 667 | 595 | 59.5 | 58.0 | 3.37 |
| **5** | 650 | 625 | 595 | 59.5 | 57.5 | 3.37 |
| **7** | 695 | 617 | 535 | 59.0 | 57.0 | 3.28 |
| **14** | 725 | 638 | 585 | 59.5 | 57.0 | 3.34 |

## DISCUSSION

Step quenching with holding at a temperature of 650 °C allows obtaining crack propagation resistance values comparable to standard quenching (in oil) and high tempering at approximately equal values of hardness and total crack and notch depth. This is in good agreement with the study conducted by the authors [13; 16]. They associate the positive effect of step quenching with the formation of microheterogeneities in martensite that have an increased content of carbon, vanadium and molybdenum, which, with subsequent high tempering, are nuclei for the formation of carbides, providing them with high dispersion and uniformity of distribution, thereby increasing the crack propagation resistance [13].

Compared with standard quenching, quenching with a step at 340 °C leads to a significant decrease in hardness, which indicates partial bainitic decomposition. The resistance to crack propagation regardless of the tempering temperature (low, high tempering) is lower than that of the samples after standard quenching. "Bainite brittleness" is probably associated with the formation of upper bainite crystals in the structure, reinforced with cementite-type carbide plates associated with the matrix [19]. It should be noted that there are isolated studies arguing this, for example [14]. Thus, when quenching 5H2SMF die steel, it is necessary to achieve increased stability of supercooled austenite in the intermediate region, thereby preventing bainite precipitation.

A study of the dependence of hardness and crack resistance on the duration (1, 3, 5, 7, and 14 h) of low tempering (200 °C) of 5H2SMF steel showed that with an increase in the holding time from 1 to 14 h, a decrease in hardness is observed. In this case, the maximum crack resistance ($P_{cr}$) does not correspond to the minimum hardness, which confirms the data on the non-monotonic, saw-tooth nature of the "crack resistance – time" dependence [14]. Attempts to link the non-monotonicity of this dependence with structural transformations are hypothetical, which is understandable if we cite the following quote: "With the development of the foil method and diffraction electron microscopy, it became possible to identify carbide precipitates by microdiffraction. However, it should be recognised that these possibilities have not yet been used, and the available data are contradictory" [20, p. 143]. In this regard, at this stage of the study, experimental data on the effect of the duration of low tempering were accumulated.

## CONCLUSIONS

1. Quenching of 5H2SMF die steel with holding at 650 °C allows obtaining values for crack propagation resistance at approximately equal hardness values comparable with standard quenching and high tempering of dies.

2. A significant decrease in hardness during quenching with a step at 340 °C compared to standard quenching regardless of the tempering temperature (low, high tempering) does not allow recommending this mode for industrial application.

3. Heat treatment modes with holding times of 3 and 5 h can be recommended as standard, since they provide the maximum value of crack propagation resistance after standard quenching and low tempering at 200 °C.

## REFERENCES

1. Chernov D.K. *O prigotovlenii stalnykh broneprobivayu-shchikh snaryadov: soobshchenie D.K. Chernova v Imperatorskom Russkom tekhnologicheskom obshchestve, 10 maya 1885 g.* [On the preparation of steel armor-piercing shells]. Sankt-Petersburg, tip. br. Panteleevykh Publ., 1885. 33 p.

2. Kostin N.A. Features of hardening of 5KhGS and 5Kh3GS die steels carburized to hypereutectoid concentrations. *Chernye metally*, 2020, no. 5, pp. 31–36. EDN: YCAHQN.

3. Tsukanov D.V., Smirnova D.L., Petkova A.P., Shtertser V.V. Modeling of cooling mode during hardening of a large-sized rotor blank made of Cr-Ni-Mo-V steel. *Chernye metally*, 2024, no. 9, pp. 29–36. DOI: 10.17580/chm.2024.09.05.

4. Rakhshtadt A.G. About structural transformations in supercooled austenite of vanadium containing steels. *Izvestiya AN SSSR. Metally*, 1984, no. 2, pp. 102–107.

5. Bazhin V.Yu., Issa B. Influence of heat treatment on the microstructure of steel coils of a heating tube furnace. *Journal of Mining Institute*, 2021, vol. 249, pp. 393–400. DOI: 10.31897/PMI.2021.3.8.

6. Pryakhin E.I., Pribytkova D.A. The influence of the quality of surface preparation of pipes for heating networks on their corrosion resistance during operation in underground conditions. *Chernye metally*, 2023, no. 11, pp. 97–102. DOI: 10.17580/chm.2023.11.15.

7. Yakubovich E.A. Analysis of the heat treatment modes influence on the life of the tool for hot forming. *Zhurnal peredovykh issledovaniy v oblasti estestvoznaniya*, 2020, no. 11, pp. 37–42. DOI: 10.26160/2572-4347-2020-11-37-42.

8. Ermakov B.S., Ermakov S.B., Vologzhanina S.A., Khuznakhmetov R.M. Relationship between operating conditions and the emergence of nano and ultradispersed grain boundary defects in weld joints. *Tsvetnye metally*, 2023, no. 8, pp. 80–85. DOI: 10.17580/tsm.2023.08.13.

9. Sivenkov A.V., Konchus D.A., Gareev D.V., Pryakhin E.I. Application of Cr - Ni coatings by chemical-thermal treatment from lowmelting metal solutions. *Chernye metally*, 2024, no. 12, pp. 101–106. DOI: 10.17580/chm.2024.12.14.

10. Krylova S.E., Romashkov E.V. Features of heat treatment of a new steel for the manufacture of hot deformation dies. *Chernye metally*, 2021, no. 1, pp. 54–60. DOI: 10.17580/chm.2021.01.08.

11. Zambrano O.A. A Review on the Effect of Impact Toughness and Fracture Toughness on Impact-Abrasion Wear. *Journal of Materials Engineering and Performance*, 2021, vol. 30, pp. 7101–7116. DOI: 10.1007/s11665-021-05960-5.

12. Shneyderman A.Sh. On the tempering of the bainite structure. *Metallovedenie i termicheskaya obrabotka metallov*, 1978, no. 12, pp. 12–15.

13. Edneral A.F., Rusanenko V.V., Smirnova A.V. Structural transformations during heat treatment of chromium-molybdenum steel. *Metallovedenie i termicheskaya obrabotka metallov*, 1982, no. 9, pp. 4–8.

14. Kramarov M.A., Vinogradov S.I. Effect of tempering mode on static and cyclic crack resistance of steels.

*Metallovedenie i termicheskaya obrabotka metallov*, 1986, no. 3, pp. 14–17.

15. Pryakhin E.I., Azarov V.A. Comparative analysis of the use of epoxy and fluoroplastic polymer compositions as internal smooth coatings of the inner cavity of steel main gas pipelines. *CIS Iron and Steel Review*, 2024, vol. 28, pp. 93–98. DOI: 10.17580/cisisr.2024.02.16.

16. Petkova A.P., Zlotin V.A. Analysis of the efficiency of reducing hydrogen losses in a pipeline made of various austenitic stainless steels. *Chernye metally*, 2024, no. 9, pp. 50–54. DOI: 10.17580/chm.2024.09.08.

17. Xu Wen-hua, Li Yang, Xiao Gui-yong, Gu Guo-chao, Lu Yu-peng. Effects of quenching and partitioning on microstructure and properties of high-silicon and high-aluminum medium carbon alloy steels. *Materials Today: Communications*, 2023, vol. 34, article number 105031. DOI: 10.1016/j.mtcomm.2022.105031.

18. Shakhnazarov K.Yu., Kasatonov V.F., Vasilev A.P., Akifev S.K., Kudryavtsev R.S., Panteleev V.I., Astrakhantsev G.N. *Shtampovaya stal* [Stamping steel], avtorskoe svidetelstvo no. 1671726 A1 SSSR. 2 p. EDN: VVISEL.

19. Tishaev S.I., Orlov M.R., Kolesnikov V.A. On the nature of "bainite brittleness" of secondary-hardening steels. *Izvestiya AN SSSR*, 1984, no. 4, pp. 32–37.

20. Kurdyumov G.V., Utevskiy L.M., Entin R.I. *Prevrashchenie v zheleze i stali* [Transformation in iron and steel]. Moscow, Metallurgiya Publ., 1978. 392 p.

**СПИСОК ЛИТЕРАТУРЫ**

1. Чернов Д.К. О приготовлении стальных бронепробивающих снарядов: сообщение Д.К. Чернова в Императорском Русском технологическом обществе, 10 мая 1885 г. СПб.: тип. бр. Пантелеевых, 1885. 33 с.

2. Костин Н.А. Особенности закалки штамповых сталей 5ХГС и 5Х3ГС, науглероженных до заэвтектоидных концентраций // Черные металлы. 2020. № 5. С. 31–36. EDN: YCAHQN.

3. Цуканов Д.В., Смирнова Д.Л., Петкова А.П., Штерцер В.В. Моделирование режима охлаждения при закалке крупногабаритной заготовки ротора из Cr-Ni-Mo-V-стали // Черные металлы. 2024. № 9. С. 29–36. DOI: 10.17580/chm.2024.09.05.

4. Рахштадт А.Г. О структурных превращениях в переохлажденном аустените ванадий содержащих сталей // Известия АН СССР. Металлы. 1984. № 2. С. 102–107.

5. Бажин В.Ю., Исса Б. Влияние термической обработки на микроструктуру стальных змеевиков нагревательной трубчатой печи // Записки Горного института. 2021. Т. 249. С. 393–400. DOI: 10.31897/PMI.2021.3.8.

6. Пряхин Е.И., Прибыткова Д.А. Влияние качества подготовки поверхности труб для теплосетей на их коррозионную стойкость при эксплуатации в условиях подземного залегания // Черные металлы. 2023. № 11. С. 97–102. DOI: 10.17580/chm.2023.11.15.

7. Якубович Е.А. Анализ влияния режимов термической обработки на стойкость инструмента для горя-

чей штамповки // Журнал передовых исследований в области естествознания. 2020. № 11. С. 37–42. DOI: 10.26160/2572-4347-2020-11-37-42.

8. Ермаков Б.С., Ермаков С.Б., Вологжанина С.А., Хузнахметов Р.М. Влияние условий эксплуатации на формирование нано- и ультрадисперсных зернограничных дефектов в сварных соединениях // Цветные металлы. 2023. № 8. С. 80–85. DOI: 10.17580/tsm.2023.08.13.

9. Сивенков А.В., Кончус Д.А., Гареев Д.В., Пряхин Е.И. Применение покрытий Cr – Ni методом химико-термической обработки из растворов легкоплавких металлов // Черные металлы. 2024. № 12. С. 101–106. DOI: 10.17580/chm.2024.12.14.

10. Крылова С.Е., Ромашков Е.В. Особенности термической обработки новой стали для изготовления штампов горячего деформирования // Черные металлы. 2021. № 1. С. 54–60. DOI: 10.17580/chm.2021.01.08.

11. Zambrano O.A. A Review on the Effect of Impact Toughness and Fracture Toughness on Impact-Abrasion Wear // Journal of Materials Engineering and Performance. 2021. Vol. 30. P. 7101–7116. DOI: 10.1007/s11665-021-05960-5.

12. Шнейдерман А.Ш. Об отпуске бейнитной структуры // Металловедение и термическая обработка металлов. 1978. № 12. С. 12–15.

13. Еднерал А.Ф., Русаненко В.В., Смирнова А.В. Структурные превращения при термической обработке хромомолибденовой стали // Металловедение и термическая обработка металлов. 1982. № 9. С. 4–8.

14. Крамаров М.А., Виноградов С.И. Влияние режима отпуска на статическую и циклическую трещиностойкость сталей // Металловедение и термическая обработка металлов. 1986. № 3. С. 14–17.

15. Pryakhin E.I., Azarov V.A. Comparative analysis of the use of epoxy and fluoroplastic polymer compositions as internal smooth coatings of the inner cavity of steel main gas pipelines // CIS Iron and Steel Review. 2024. Vol. 28. P. 93–98. DOI: 10.17580/cisisr.2024.02.16.

16. Петкова А.П., Злотин В.А. Анализ эффективности снижения потерь водорода в трубопроводе из различных аустенитных нержавеющих сталей // Черные металлы. 2024. № 9. С. 50–54. DOI: 10.17580/chm.2024.09.08.

17. Xu Wen-hua, Li Yang, Xiao Gui-yong, Gu Guo-chao, Lu Yu-peng. Effects of quenching and partitioning on microstructure and properties of high-silicon and high-aluminum medium carbon alloy steels // Materials Today: Communications. 2023. Vol. 34. Article number 105031. DOI: 10.1016/j.mtcomm.2022.105031.

18. Шахназаров К.Ю., Касатонов В.Ф., Васильев А.П., Акифьев С.К., Кудрявцев Р.С., Пантелеев В.И., Астраханцев Г.Н. Штамповая сталь: авторское свидетельство № 1671726 A1 СССР. 2 с. EDN: VVISEL.

19. Тишаев С.И., Орлов М.Р., Колесников В.А. О природе «бейнитной хрупкости» вторичнотвердеющих сталей // Известия АН СССР. 1984. № 4. С. 32–37.

20. Курдюмов Г.В., Утевский Л.М., Энтин Р.И. Превращение в железе и стали. М.: Металлургия, 1978. 392 с.

# Влияние режимов упрочняющей термической обработки на сопротивление развитию трещины штамповой стали 5Х2СМФ

**Шахназаров Карэн Юрьевич**\*[1], доктор технических наук,
профессор кафедры материаловедения и технологии художественных изделий
**Рафиков Артур Русланович**[2], аспирант
кафедры материаловедения и технологии художественных изделий
*Санкт-Петербургский горный университет императрицы Екатерины II, Санкт-Петербург (Россия)*

\***E-mail:** mthi@spmi.ru,
karen812@yandex.ru

[1]ORCID: https://orcid.org/0000-0001-7501-6590
[2]ORCID: https://orcid.org/0009-0001-9881-9115

*Аннотация:* В литературных источниках практически отсутствуют данные о влиянии закалки с выдержками в перлитной и бейнитной областях и последующего низкого и высокого отпуска разной продолжительности на сопротивление развитию трещины штамповых сталей, а имеющиеся данные противоречивы. Между тем более «мягкая» закалка с выдержками в промежуточных областях существенно снижает риск образования закалочных трещин и деформацию штампов и штамповой оснастки. В работе образцы из штамповой стали 5Х2СМФ с острым надрезом и искусственно нанесенными трещинами были подвергнуты термической обработке, включающей в себя стандартную закалку 910 °C в масло и закалку от 910 °C со ступенями при 650 и 340 °C с разными видами отпуска (200, 560, 600 и 640 °C) и разной продолжительностью по времени – 1, 3, 5, 7 и 14 ч (для 200 °C) с целью повышения сопротивления развитию трещины. Проведенные исследования позволили установить, что данные по сопротивлению развитию трещины после ступенчатой закалки с выдержкой в области перлитного превращения и последующего высокого отпуска при 560, 600 и 640 °C сопоставимы со стандартной закалкой в масло и высоким отпуском при тех же температурах. Твердость после ступенчатой закалки в области бейнитного превращения (340 °C) во всех случаях значительно ниже при различных режимах отпуска, поэтому сравнить сопротивление развитию трещины со стандартной закалкой не представляется возможным. Установлено оптимальное с точки зрения повышения сопротивления развитию трещины время выдержки (3 и 5 ч) после стандартной закалки от 910 °C в масло и низкого отпуска при 200 °C.

*Ключевые слова:* штамповая сталь; закалка; отпуск; твердость; сопротивление развитию трещины.

*Для цитирования:* Шахназаров К.Ю., Рафиков А.Р. Влияние режимов упрочняющей термической обработки на сопротивление развитию трещины штамповой стали 5Х2СМФ // Frontier Materials & Technologies. 2025. № 2. С. 95–101. DOI: 10.18323/2782-4039-2025-2-72-8.

# OUR AUTHORS

**Atamashkin Artem Sergeevich**, PhD (Engineering),
senior researcher of Research and Educational Center
of New Materials and Advanced Technologies.
Address: Orenburg State University,
460018, Russia, Orenburg, Prospekt Pobedy, 13.
E-mail: atamashkin2017@yandex.ru

**Betsofen Sergey Yakovlevich**, Doctor of Sciences (Engineering), Professor,
professor of Chair "Technologies and Systems
for Computer-Aided Design of Metallurgical Processes".
Address: Moscow Aviation Institute,
125993, Russia, Moscow, Volokolamskoye Shosse, 4.
E-mail: s.betsofen@gmail.com

**Brilevskiy Aleksandr Igorevich**, junior researcher
of the Research Institute of Advanced Technologies.
Address: Togliatti State University,
445020, Russia, Togliatti, Belorusskaya Street, 14.
E-mail: alexandrbril@yandex.ru

**Danilov Vladimir Alekseevich**, PhD (Engineering),
junior researcher of the Research Institute of Advanced Technologies.
Address: Togliatti State University,
445020, Russia, Togliatti, Belorusskaya Street, 14.
E-mail: v.dani1ov@yandex.ru

**Danyuk Aleksey Valerievich**, PhD (Physics and Mathematics),
senior researcher of the Research Institute of Advanced Technologies.
Address: Togliatti State University,
445020, Russia, Togliatti, Belorusskaya Street, 14.
E-mail: alexey.danyuk@gmail.com

**Dorogov Maksim Vladimirovich**, PhD (Physics and Mathematics),
assistant professor of Institute of Advanced Data Transfer Systems.
Address: ITMO University,
197101, Russia, St. Petersburg, Kronverksky Pr. 49, bldg. A.
E-mail: mvdorogov@itmo.ru

**Dyuzheva-Maltseva Elena Vadimovna**, postgraduate student.
Address: Baikov Institute of Metallurgy and Materials Science of RAS,
119334, Russia, Moscow, Leninsky Prospekt, 49.
E-mail: elena.dujewa@yandex.ru

**Elsukov Sergey Konstantinovich**, PhD (Engineering),
assistant professor of Chair "Welding Production Equipment and Technology".
Address: Volgograd State Technical University,
400005, Russia, Volgograd, Lenin Prospekt, 28.
E-mail: serzh.elsukov@yandex.ru

**Fedotova Darya Dmitrievna**, master, 4th category operator
of the Research Laboratory "Metals and Alloys under Extreme Conditions".
Address: Ufa University of Science and Technology,
450076, Russia, Ufa, Zaki Validi Street, 32.
E-mail: dariafedotowa@mail.ru

**Fominov Evgeny Valeryevich**, PhD (Engineering), Associate Professor.
Address: Don State Technical University,
344010, Russia, Rostov-on-Don, Gagarin Square, 1.
E-mail: fominoff83@mail.ru

# AUTHORS

**Fot Andrey Petrovich**, Doctor of Sciences (Engineering), Professor,
Chief Scientific Secretary – Head of Department of Dissertation Councils.
Address: ZBO Drill Industries, Inc.,
460026, Russia, Orenburg, Prospekt Pobedy, 118.
E-mail: andreas.voht@mail.ru

**Gladkikh Dmitry Igorevich**, postgraduate student.
Address: Don State Technical University,
344010, Russia, Rostov-on-Don, Gagarin Square, 1.
E-mail: ya.gladckih-dmitriy@yandex.ru

**Kalganov Dmitrii Alexandrovich**, junior researcher
of Laboratory of Diffraction Methods
for Investigation of Real Crystal-Structures.
Address: Ioffe Institute of the RAS,
194021, Russia, St. Petersburg, Polytekhnicheskaya Street, 26.
E-mail: kalganov@itmo.ru

**Kaminskii Vladimir Vladimirovich**, PhD (Physics and Mathematics),
Head of laboratory of Institute of Advanced Data Transfer Systems.
Address 1: ITMO University,
197101, Russia, St. Petersburg, Kronverksky Pr. 49, bldg. A.
Address 2: Ioffe Institute of the RAS,
194021, Russia, St. Petersburg, Polytekhnicheskaya Street, 26.
E-mail: kam-vladimiro@yandex.ru

**Khafizova Elvira Dinifovna**, PhD (Physics and Mathematics),
senior researcher.
Address: Ufa University of Science and Technology,
450076, Russia, Ufa, Zaki Validi Street, 32.
E-mail: ela.90@mail.ru

**Kovtun Maksim Vitalyevich**, Head of Research and Technology Center.
Address: Trading and Industrial Company SYNTEZ,
344033, Russia, Rostov-on-Don, Portovaya Street, 543.
E-mail: 79185530688@ya.ru

**Kurlovich Sergey Anatolyevich**, Director.
Address: Trading and Industrial Company SYNTEZ,
344033, Russia, Rostov-on-Don, Portovaya Street, 543.
E-mail: mtdos@mail.ru

**Lavrenova Tatyana Vladimirovna**, senior lecturer.
Address: Don State Technical University,
344010, Russia, Rostov-on-Don, Gagarin Square, 1.
E-mail: bys_ka87@mail.ru

**Maksimenko Ekaterina Igorevna**, postgraduate student.
Address: Moscow Aviation Institute,
125993, Russia, Moscow, Volokolamskoye Shosse, 4.
E-mail: ek.maximencko@yandex.ru

**Medvedev Andrey Evgenievich**, PhD (Physics and Mathematics),
senior researcher.
Address: Ufa University of Science and Technology,
450076, Russia, Ufa, Zaki Validi Street, 32.
E-mail: medvedevandreyrf@gmail.com

**Merson Dmitry Lvovich,** Doctor of Sciences (Physics and Mathematics), Professor,
Director of the Research Institute of Advanced Technologies.
Address: Togliatti State University,
445020, Russia, Togliatti, Belorusskaya Street, 14.
E-mail: d.merson@tltsu.ru

---

# AUTHORS

**Merson Evgeny Dmitrievich**, PhD (Physics and Mathematics),
senior researcher of the Research Institute of Advanced Technologies.
Address: Togliatti State University,
445020, Russia, Togliatti, Belorusskaya Street, 14.
E-mail: mersoned@gmail.com

**Motkov Mikhail Mikhailovich**, PhD (Engineering), senior researcher.
Address: Siberian Federal University,
660041, Russia, Krasnoyarsk, Svobodny Prospekt, 79.
E-mail: mikhail145@mail.ru

**Murashkin Maksim Yurievich**, PhD (Engineering), senior researcher.
Address: Ufa University of Science and Technology,
450076, Russia, Ufa, Zaki Validi Street, 32.
E-mail: m.murashkin.70@gmail.com

**Myagkikh Pavel Nikolaevich**, junior researcher
of the Research Institute of Advanced Technologies.
Address: Togliatti State University,
445020, Russia, Togliatti, Belorusskaya Street, 14.
E-mail: p.myagkikh@tltsu.ru

**Nesin Dmitry Sergeevich**, postgraduate student.
Address: Volgograd State Technical University,
400005, Russia, Volgograd, Lenin Prospekt, 28.
E-mail: nesdmiser2000@mail.ru

**Permyakova Inga Evgenyevna**, Doctor of Science (Physics and Mathematics), Professor,
senior researcher of the Laboratory of Physicochemistry and Mechanics of Metallic Materials.
Address: Baikov Institute of Metallurgy and Materials Science of RAS,
119334, Russia, Moscow, Leninsky Prospekt, 49.
E-mail: inga_perm@mail.ru

**Philippov Sergei Anatolievich**, researcher
of Laboratory of Diffraction Methods for Investigation of Real Crystal-Structures,
assistant professor of Higher School of Mechanics and Control Processes.
Address 1: Ioffe Institute of the RAS,
194021, Russia, St. Petersburg, Polytekhnicheskaya Street, 26.
Address 2: Peter the Great St. Petersburg Polytechnic University,
195251, Russia, St. Petersburg, Polytekhnicheskaya Street, 29.
E-mail: filippov_sa@spbstu.ru

**Poluyanov Vitaly Aleksandrovich**, PhD (Engineering),
junior researcher of the Research Institute of Advanced Technologies.
Address: Togliatti State University,
445020, Russia, Togliatti, Belorusskaya Street, 14.
E-mail: vitaliy.poluyanov@gmail.com

**Priymak Elena Yurievna**, PhD (Engineering), Associate Professor,
Head of the Laboratory of Metal Science and Heat Treatment,
Director of Research and Educational Center
of New Materials and Advanced Technologies.
Address 1: ZBO Drill Industries, Inc.,
460026, Russia, Orenburg, Prospekt Pobedy, 118.
Address 2: Orenburg State University,
460018, Russia, Orenburg, Prospekt Pobedy, 13.
E-mail: e.prijmak@zbo.ru

**Rafikov Artur Ruslanovich**, postgraduate student
of Chair of Materials Science and Technology of Artistic Products.
Address: Empress Catherine II Saint Petersburg Mining University,
199106, Russia, St. Petersburg, Vasilyevsky Island, 21st Line, 2.
E-mail: artur.mankevich.99@mail.ru

# AUTHORS

**Romanov Alexey Evgenievich**, Doctor of Sciences (Physics and Mathematics), Professor,
chief researcher of Institute of Advanced Data Transfer Systems.
Address 1: ITMO University,
197101, Russia, St. Petersburg, Kronverksky Pr. 49, bldg. A.
Address 2: Togliatti State University,
445020, Russia, Togliatti, Belorusskaya Street, 14.
E-mail: alexey.romanov@niuitmo.ru

**Shakhnazarov Karen Yurievich**, Doctor of Sciences (Engineering),
professor of Chair of Materials Science and Technology of Artistic Products.
Address: Empress Catherine II Saint Petersburg Mining University,
199106, Russia, St. Petersburg, Vasilyevsky Island, 21st Line, 2.
E-mail: karen812@yandex.ru

**Yakovleva Irina Leonidovna**, Doctor of Sciences (Engineering),
chief researcher of the Laboratory of Physical Metallurgy.
Address: M.N. Mikheev Institute of Metal Physics of the Ural Branch of RAS,
620108, Russia, Yekaterinburg, Sofya Kovalevskaya Street, 18.
E-mail: labmet@imp.uran.ru

**Zhukova Olga Olegovna**, engineer-researcher.
Address: Ufa University of Science and Technology,
450076, Russia, Ufa, Zaki Validi Street, 32.
E-mail: baykeeva.olga@yandex.ru

**Zorin Ilya Vasilyevich**, Doctor of Sciences (Engineering), Associate Professor,
professor of Chair "Welding Production Equipment and Technology".
Address: Volgograd State Technical University,
400005, Russia, Volgograd, Lenin Prospekt, 28.
E-mail: zorin.iv@vstu.ru

# НАШИ АВТОРЫ

**Атамашкин Артём Сергеевич**, кандидат технических наук, старший научный сотрудник научно-образовательного центра новых материалов и перспективных технологий.
Адрес: Оренбургский государственный университет,
460018, Россия, г. Оренбург, пр-т Победы, 13.
E-mail: atamashkin2017@yandex.ru

**Бецофен Сергей Яковлевич**, доктор технических наук, профессор, профессор кафедры «Технологии и системы автоматизированного проектирования металлургических процессов».
Адрес: Московский авиационный институт,
125993, Россия, г. Москва, Волоколамское шоссе, 4.
E-mail: s.betsofen@gmail.com

**Брилевский Александр Игоревич**, младший научный сотрудник НИИ прогрессивных технологий.
Адрес: Тольяттинский государственный университет,
445020, Россия, г. Тольятти, ул. Белорусская, 14.
E-mail: alexandrbril@yandex.ru

**Гладких Дмитрий Игоревич**, аспирант.
Адрес: Донской государственный технический университет,
344010, Россия, г. Ростов-на-Дону, пл. Гагарина, 1.
E-mail: ya.gladckih-dmitriy@yandex.ru

**Данилов Владимир Алексеевич**, кандидат технических наук, младший научный сотрудник НИИ прогрессивных технологий.
Адрес: Тольяттинский государственный университет,
445020, Россия, г. Тольятти, ул. Белорусская, 14.
E-mail: v.dani1ov@yandex.ru

**Данюк Алексей Валериевич**, кандидат физико-математических наук, старший научный сотрудник НИИ прогрессивных технологий.
Адрес: Тольяттинский государственный университет,
445020, Россия, г. Тольятти, ул. Белорусская, 14.
E-mail: alexey.danyuk@gmail.com

**Дорогов Максим Владимирович**, кандидат физико-математических наук, доцент института перспективных систем передачи данных.
Адрес: Университет ИТМО,
197101, Россия, г. Санкт-Петербург, Кронверкский пр-т, 49, лит. А.
E-mail: mvdorogov@itmo.ru

**Дюжева-Мальцева Елена Вадимовна**, аспирант.
Адрес: Институт металлургии и материаловедения им. А.А. Байкова РАН,
119334, Россия, г. Москва, Ленинский пр-т, 49.
E-mail: elena.dujewa@yandex.ru

**Елсуков Сергей Константинович**, кандидат технических наук, доцент кафедры «Оборудование и технология сварочного производства».
Адрес: Волгоградский государственный технический университет,
400005, Россия, г. Волгоград, пр-т им. В.И. Ленина, 28.
E-mail: serzh.elsukov@yandex.ru

**Жукова Ольга Олеговна**, инженер-исследователь.
Адрес: Уфимский университет науки и технологий,
450076, Россия, г. Уфа, ул. Заки Валиди, 32.
E-mail: baykeeva.olga@yandex.ru

**Зорин Илья Васильевич**, доктор технических наук, доцент,
профессор кафедры «Оборудование и технология сварочного производства».
Адрес: Волгоградский государственный технический университет,
400005, Россия, г. Волгоград, пр-т им. В.И. Ленина, 28.
E-mail: zorin.iv@vstu.ru

**Калганов Дмитрий Александрович**, младший научный сотрудник лаборатории
дифракционных методов исследования реальной структуры кристаллов.
Адрес: Физико-технический институт им. А.Ф. Иоффе РАН,
194021, Россия, г. Санкт-Петербург, ул. Политехническая, 26.
E-mail: kalganov@itmo.ru

**Каминский Владимир Владимирович**, кандидат физико-математических наук,
заведующий лабораторией института перспективных систем передачи данных.
Адрес 1: Университет ИТМО,
197101, Россия, г. Санкт-Петербург, Кронверкский пр-т, 49, лит. А.
Адрес 2: Физико-технический институт им. А.Ф. Иоффе РАН,
194021, Россия, г. Санкт-Петербург, ул. Политехническая, 26.
E-mail: kam-vladimiro@yandex.ru

**Ковтун Максим Витальевич**, руководитель научно-технического центра.
Адрес: ТПК «СИНТЕЗ»,
344033, Россия, г. Ростов-на-Дону, ул. Портовая, 543.
E-mail: 79185530688@ya.ru

**Курлович Сергей Анатольевич**, директор.
Адрес: ТПК «СИНТЕЗ»,
344033, Россия, г. Ростов-на-Дону, ул. Портовая, 543.
E-mail: mtdos@mail.ru

**Лавренова Татьяна Владимировна**, старший преподаватель.
Адрес: Донской государственный технический университет,
344010, Россия, г. Ростов-на-Дону, пл. Гагарина, 1.
E-mail: bys_ka87@mail.ru

**Максименко Екатерина Игоревна**, аспирант.
Адрес: Московский авиационный институт,
125993, Россия, г. Москва, Волоколамское шоссе, 4.
E-mail: ek.maximencko@yandex.ru

**Медведев Андрей Евгеньевич**, кандидат физико-математических наук,
старший научный сотрудник.
Адрес: Уфимский университет науки и технологий,
450076, Россия, г. Уфа, ул. Заки Валиди, 32.
E-mail: medvedevandreyrf@gmail.com

**Мерсон Дмитрий Львович**, доктор физико-математических наук, профессор,
директор НИИ прогрессивных технологий.
Адрес: Тольяттинский государственный университет,
445020, Россия, г. Тольятти, ул. Белорусская, 14.
E-mail: d.merson@tltsu.ru

**Мерсон Евгений Дмитриевич**, кандидат физико-математических наук,
старший научный сотрудник НИИ прогрессивных технологий.
Адрес: Тольяттинский государственный университет,
445020, Россия, г. Тольятти, ул. Белорусская, 14.
E-mail: mersoned@gmail.com

**Мотков Михаил Михайлович**, кандидат технических наук,
старший научный сотрудник.
Адрес: Сибирский федеральный университет,
660041, Россия, г. Красноярск, пр-т Свободный, 79.
E-mail: mikhail145@mail.ru

**Филиппов Сергей Анатольевич**, научный сотрудник лаборатории дифракционных методов исследования реальной структуры кристаллов, доцент высшей школы механики и процессов управления.
Адрес 1: Физико-технический институт им. А.Ф. Иоффе РАН,
194021, Россия, г. Санкт-Петербург, ул. Политехническая, 26.
Адрес 2: Санкт-Петербургский политехнический университет Петра Великого,
195251, Россия, г. Санкт-Петербург, ул. Политехническая, 29.
E-mail: filippov_sa@spbstu.ru

**Фоминов Евгений Валерьевич**, кандидат технических наук, доцент.
Адрес: Донской государственный технический университет,
344010, Россия, г. Ростов-на-Дону, пл. Гагарина, 1.
E-mail: fominoff83@mail.ru

**Фот Андрей Петрович**, доктор технических наук, профессор,
главный ученый секретарь – начальник отдела диссертационных советов.
Адрес: АО «Завод бурового оборудования»,
460026, Россия, г. Оренбург, пр-т Победы, 118.
E-mail: andreas.voht@mail.ru

**Хафизова Эльвира Динифовна**, кандидат физико-математических наук,
старший научный сотрудник.
Адрес: Уфимский университет науки и технологий,
450076, Россия, г. Уфа, ул. Заки Валиди, 32.
E-mail: ela.90@mail.ru

**Шахназаров Карэн Юрьевич**, доктор технических наук,
профессор кафедры материаловедения и технологии художественных изделий.
Адрес: Санкт-Петербургский горный университет императрицы Екатерины II,
199106, Россия, г. Санкт-Петербург, Васильевский остров, 21-я линия, 2.
E-mail: karen812@yandex.ru

**Яковлева Ирина Леонидовна**, доктор технических наук,
главный научный сотрудник лаборатории физического металловедения.
Адрес: Институт физики металлов имени М.Н. Михеева Уральского отделения РАН,
620108, Россия, г. Екатеринбург, ул. Софьи Ковалевской, 18.
E-mail: labmet@imp.uran.ru